Development and Performance Analyses of Non-Pneumatic Wheels with Honeycomb Spokes

Zhou Zheng

A Thesis

in

The Department

of

Mechanical and Industrial Engineering

Presented in Partial Fulfillment of the Requirements

For the Degree of

Doctor of Philosophy (Mechanical Engineering)

at Concordia University

Montréal, Québec, Canada

April 2022

CONCORDIA UNIVERSITY
SCHOOL OF GRADUATE STUDIES

This is to certify that the thesis proposal prepared

By: Zhou Zheng

Entitled: Development and Performance Analyses of Non-Pneumatic Wheels with Honeycomb Spokes

and submitted in partial fulfillment of the requirements for the degree of

Doctor of Philosophy (Mechanical Engineering)

complies with the regulations of this University and meets the accepted standards with respect to originality and quality.

Signed by the final examining committee:

_____ Dr. A Mohammadi, Chair

_____ Dr. Y.P. He, External to Program

_____ Dr. K. Galal, External Examiner

_____ Dr. A. Ince, Examiner

_____ Dr. C.Y. Su, Examiner

_____ Dr. S. Rakheja, Co-Supervisor

_____ Dr. R. Sedaghati, Co-Supervisor

Approved by _____

Dr. Ivan Contreras, Graduate Program Director

June 16, 2022 _____

Dr. Mourad Debbabi, Dean

Gina Cody School of Engineering and Computer Science

ABSTRACT

Development and Performance Analyses of Non-Pneumatic Wheels with Honeycomb Spokes

Zhou Zheng,

Concordia University, 2022

The dynamic performance of a ground vehicle is predominantly influenced by interactions of the tires with the terrain. The designs of pneumatic tires has evolved over the past many decades to satisfy multiple performance demands such as transfer of tractive/braking forces with minimal energy losses, ease of handling and directional control, ride comfort and road holding. Despite their proven superior performance, the pneumatic tires exhibit deficiencies such as loss of vehicle performance and directional control in the event of severe air leakage or bursting, high maintenance, complex manufacturing process, and fire hazards and environmental risks of used tires. In recent years, concepts in non-pneumatic wheels (NPWs) with different spokes' designs have emerged, which potentially offer many advantages over the pneumatic tires, particularly the elimination of the road safety risks and the routine maintenance induced by the inflation pressure loss. The reported studies on NPWs with honeycomb spokes have mostly focused on their static and dynamic responses to normal wheel loads, such as vertical deflection, modes of vibration and rolling resistance. Only minimal efforts, however, are evident in view of their out-of-plane responses such as cornering force and self-aligning moment, which are vital for adequate handling and directional control of the vehicle.

This dissertation research is focused on design and development honeycomb NPWs with an objective to achieve in-plane and out-of-plane force-deflection and force-slip characteristics comparable to those of the pneumatic tires so as to be considered as their potential substitute in general vehicular applications. Three-dimensional finite element (FE) models of the honeycomb NPW with different spokes' configurations are initially developed using ABAQUS software in order to predict their static and dynamic responses. A mesh convergence study is conducted to determine nearly optimal element sizes for each component, which permitted convergence of responses with least computational cost. The validity of these wheel models is verified by comparisons of predicted responses with the available results.

The verified NPW models are subsequently employed to evaluate their feasibility and relative merits through comparisons of in-plane as well as out-of-plane properties with those of a reference pneumatic tire (205/55R16). These include the multi-axis stiffness properties as well as cornering force and self-aligning moment characteristics. It is shown that the honeycomb NPW designs could be easily tuned with to achieve vertical and longitudinal stiffness as those of the reference pneumatic tire, while its lateral and cornering stiffness are substantially higher, irrespective of the spokes' configurations considered. The considerably higher cornering stiffness of the NPW designs may cause rapid saturation of the cornering force under very low side slip conditions and thus side slippage of the wheel under higher side slip angles.

Efficient parametric studies using Taguchi and response surface methodologies are further performed using the verified NPW models so as to investigate the influences of multiple design parameters and the two-factor interactions on their multi-axis and cornering stiffness characteristics as well as natural frequencies of important vibration modes. The natural frequencies are extracted for the stationary NPW with vertically movable spindle and ground contact. The results from the experiment designs are used to develop guidance for design tuning of the NPW in order to achieve desired stiffness and modal properties. The results reveal that the design parameters of the honeycomb NPW can be tuned to achieve significantly lower lateral and cornering stiffness, which are comparable to those of the reference pneumatic tire. These designs, however, in general are coupled with higher thickness of the core layer and tread, which tend to lower the longitudinal stiffness.

A novel design concept, called "symmetric helical honeycomb spokes" is subsequently proposed for the NPW. The relative merits of the proposed helical spokes design are evaluated in terms of multi-axis and cornering stiffness properties of the wheel using the verified NPW models by varying the helix angle of the spokes. The results show that introducing the "symmetric helical honeycomb spokes" offer notable reductions in both lateral and cornering stiffness and higher longitudinal stiffness with only slight increase in mass of the NPW.

Acknowledgements

First and foremost I would like to appreciate my supervisors, Dr. Subhash Rakheja and Dr. Ramin Sedaghati, for their invaluable guidance and continuous support throughout every stage of the research project. Their passion and determination for perfection have inspired me a lot. I extend thanks to colleagues, faculty and staff of the Mechanical Engineering Department.

Financial support from China Scholarship Council, Concordia University and Mechanical Engineering Department are gratefully acknowledged.

I am extremely grateful to my parents and my sister for their endless love and support.

Finally, I would like to express my special thanks to my fiancée, Shanshan Chen, for the unconditional love and the patience she showed during my absence.

Table of Contents

List of Figures

List of Tables

Nomenclature

$A\times B$	interaction between factors A and B
A_c	contact area of a wheel with the road
C_{10}, C_{01}	Elastic constants in Neo-Hookean material model
D_i	model parameter (compressibility-related) of Ogden strain energy potential
E	Young's modulus
E_{eq}	equivalent elastic modulus of the sandwich beam
E_X	effective elastic modulus of a 2D honeycomb spoke along X-axis (circumferential)
E_Z	effective elastic modulus of a 2D honeycomb spoke along Z-axis (radial)
E_{0a}	initial elastic modulus of the annular beam or core layer
E_{0c}	initial elastic modulus of the cell-wall material
E_{0r}	(initial) elastic modulus of the reinforcements
E_{0t}	initial elastic modulus of the tread
f	natural frequency
f^*	natural frequency predicted by regression model
Factor A	thickness of the cell-wall
Factor B	initial elastic modulus of the cell-wall
Factor C	thickness of the annular beam or core layer or annular layer
Factor D	initial elastic modulus of the annular beam or core layer or annular layer
Factor E	thickness of the tread
Factor F	initial elastic modulus of the tread
$\mathrm{F_{y\alpha}}$	cornering force
$\mathrm{F_s}$	side force
g_i	i^{th} Prony series parameter
G	shear modulus
$G_R(t)$	time-dependent shear relaxation modulus
G_{ZX}	in-plane effective shear modulus of a 2D honeycomb spoke
h	average height of the honeycomb cell-walls
h_i	heights of the cell-walls

J^{el}	elastic volume ratio
K_x	longitudinal stiffness of a wheel
K_y	lateral stiffness of a wheel
K_z	vertical stiffness of a wheel
K_0	initial bulk modulus
K_α	cornering stiffness of a wheel
$\overline{K_\alpha}$	average cornering stiffness
K_φ	yaw stiffness of a wheel
K_α^*	(regression) model-predicted cornering stiffness
$[K]$	stiffness matrix
l	average length of the honeycomb cell-walls
l_i	lengths of the cell-walls
$m_{\eta i}^{\text{eff}}$	modal effective mass of vibration mode η in i-direction
M_Z	self-aligning moment
$[M]$	mass matrix
N	number of spokes
$\bar{p}$	mean contact pressure
p_c^{max}	peak contact pressure
R	outer radius of the shear beam
R_1	radius of the inner reinforcement or the steel ring connected to spokes
R_2	radius of the rim
t	thickness of the shear beam
t_a	thickness of the annular beam or core layer
t_c	cell-wall thickness
t_r	thickness of the reinforcements
t_t	thickness of the tread
T_i	rigid body response in i-direction
U	Ogden strain energy density

v_x	forward velocity
v_y	side velocity
α	side-slip angle
a_R	mass-proportional damping factor
α_i	model parameter of Ogden strain energy potential
α_j, α_{jj}	parameters of regression model for natural frequency
β	helix angle
β_j, β_{jj}	parameters of quadratic regression model for cornering stiffness
$\gamma_{\eta i}$	modal participation factor of vibration mode η in i-direction
$(\gamma_{pl})_{ZX}$	in-plane effective shear yield strain
ε_j	fraction of the critical damping for a given mode j
θ	average angle of the honeycomb cell
θ_i	angles of the honeycomb cell
θ_x	rotation about x-direction
θ_y	rotation about y-direction
θ_z	rotation about z-direction
$\bar{\lambda}_i$	deviatoric principal stretches
μ_0	initial shear modulus
μ_i	model parameter (shear modulus-related) of Ogden strain energy potential
υ	Poisson's ratio
ρ	density of cell-wall constituent material
ρ^*	effective density of a 2D honeycomb spoke
σ_{ys}	yield strength of cell-wall constituent material
$(\tau_{pl})_{ZX}$	in-plane effective shear yield strength
τ_i	i^{th} Prony series parameter
ϕ_η	eigenvector of vibration mode η
ϕ_η^{T}	transpose of eigenvector ϕ_η
ω_j	natural frequency for a given mode j

ω_η	eigenvalue of vibration mode η

Acronyms

ANOVA	analysis of variance
CCD	central composite design
CMT	cellular materials theory
DoF	degrees-of-freedom
FE	finite element
ME	mechano-elastic
MEMF	modal effective mass fraction
NPW	non-pneumatic wheel
NFORC	nodal forces
RSM	response surface method

Chapter 1

Literature Review and Scope of the Dissertation

1.1 Introduction

With four critical characteristics, namely, the lower contact pressure, lower vertical stiffness, lower energy loss on rough road surfaces and the lower mass per unit load carried, the pneumatic tires had substituted the traditional rigid wheels in most rolling transport fields shortly after its invention [1]. The pneumatic tires, however, exhibit inherent shortcomings in view of durability, reliability and maintenance. The punctures or bursting of the pneumatic tires, in-particular, could cause potential loss of vehicle directional control, leading to severe body injuries and property losses [1-3]. Besides, the design space of the pneumatic tires is quite restricted by the constraints imposed by the mechanics of the pneumatic system. The airless wheels, developed for NASA's Lunar Rover, have stimulated concerted efforts in NPWs for general vehicular applications. In recent years, a number of design concepts of NPWs have evolved, the majority of which may be grouped in three categories, namely, Tweels [1], mechano-elastic (ME) wheels [4], and honeycomb NPWs [5]. These designs exhibit very similar principles, which, invariably, replace air in the pneumatic tires by radial flexible spokes [1,4] or honeycomb structure spokes [5,6]. These NPW designs not only exhibit essential characteristics of the pneumatic tires but can also eliminate the road safety risks and the routine maintenance associated with the inflation pressure. Moreover, such wheels are more environmentally friendly and sustainable as compared to the pneumatic tires [7].

The performance characteristics of NPWs relative to the conventional tires, especially the out-of-plane properties, however, have not yet been fully investigated. Reported studies have mostly focused on the response characteristics of stationary and rolling NPWs subjected to in-plane forces and moments excitations (e.g., normal loads) via either analytical or FE methods [6,8,9]. The horizontal response analyses such as traction/braking and cornering properties, however, have been attempted in a few studies limited only to ME-wheels with metal hinge-unit spokes [10-12]. Moreover, only limited knowledge exits on the modal properties of NPWs when compared to those concerning the pneumatic tires, which determine the dynamic responses of these wheels and thus reflect the performance characteristics of the vehicles [13-15]. In addition, reported studies have also shown that hexagonal honeycomb spokes of positive cell angle (regular)

could offer relatively uniform wheel-road contact pressure [16], high load carrying capacity [16-18], low rolling resistance [16] and good ride quality [18].

This dissertation research aims to establish design guidance for a NPW with regular honeycomb spokes in view of its stiffness and road contact characteristics as well as modal properties, using numerical techniques. As a first step, FE models of the honeycomb NPW with different spokes configurations are developed and validated by comparing predicted wheel responses with the available data, considering both non-rolling and rolling conditions. The multi-axis and cornering stiffness properties of these wheel models are initially compared with those of a reference pneumatic tire (205/55R16) in order to gain insight into the feasibility and relative merits of the NPW. Parametric studies are subsequently conducted using Taguchi and response surface methods so as to evaluate the influences of essential design parameters as well as their two-factor interactions on road contact characteristics, multi-axis stiffness, cornering stiffness and modal properties of the NPW in an efficient manner. The results serve as essential guidance for design tuning to realize desired performance measures. Finally, a novel design concept of the honeycomb spokes with higher out-of-plane flexibility, called "symmetric helical honeycomb spokes", is proposed for the NPW and its in-plane as well as out-of-plane response characteristics are assessed under both stationary and rolling conditions.

1.2 Literature review

The state-of-the-art development in designs, analyses methods and performance analyses of NPWs have been reviewed to build the essential background and the scope of the proposed research. The reported studies grouped under specific topics are briefly summarized in the following subsections focusing on: design concepts for the spokes of NPWs; performance analysis of NPWs; and important performance measures concerning ride comfort and directional control and stability of the vehicles, including stiffness characteristics as well as modal properties.

1.2.1 Design of the spokes for NPWs

NPWs employ high stiffness and high resilience spokes that replace compressed air in the pneumatic tires and undergo cyclic tension-compression loading. Stiffness and resilience, however, are conflicting parameters for most conventional materials. The solution is thus sought from the perspective of geometric design of the spokes. The reported spoke designs mostly include curved

radial flexible spokes as in Tweels [1,2], hinge-unit spokes in mechano-elastic (ME) wheels [4] and polygonal lattice spokes in honeycomb NPWs [6]. The majority of the reported works on the spokes' designs, however, have focused on honeycomb structures. The review is thus limited to polygon lattice spokes, with particular focus on the design and in-plane properties of hexagonal honeycomb spokes.

Honeycomb structures, owing to their high out-of-plane stiffness to weight ratio, have been widely used for designs of ultra-light weight sandwich cores [19,20]. The triangular, kagome, and diamond cell honeycombs are stretch-dominated structures, which are known to yield high modulus structure design. The bending-dominated square and hexagonal cell honeycombs are considered well-suited for designing flexible structures [19-22]. The hexagonal honeycombs can provide target in-plane properties by adjusting the geometric parameters. These have been derived using the cellular materials theory (CMT) together with Timoshenko beam theory in the linear elasticity range [23,24], such that:

$$\frac{E_Z}{E} = (t_c/l)^3 \frac{\cos\theta}{(h/l+\sin\theta)\sin^2\theta}; \frac{E_X}{E} = (t_c/l)^3 \frac{(h/l+\sin\theta)}{\cos^3\theta} \tag{1.1}$$

$$\frac{G_{ZX}}{E} = (t_c/l)^3 \frac{(h/l+\sin\theta)}{(h/l)^2(1+2h/l)\cos\theta}; \frac{\rho^*}{\rho} = \frac{(t_c/l)(h/l+2)}{2\cos\theta(h/l+\sin\theta)} \tag{1.2}$$

$$(\tau_{pl})_{ZX} = \frac{1}{4}\sigma_{ys}(t_c/l)^2 \frac{1}{h/l\cos\theta}; (\gamma_{pl})_{ZX} = \frac{1}{4}\frac{\sigma_{ys}}{G_{ZX}}(t_c/l)^2 \frac{1}{h/l\cos\theta} \tag{1.3}$$

where E_Z, E_X, G_{ZX} and ρ^* are in-plane effective moduli and density of the hexagonal honeycomb, respectively; $(\tau_{pl})_{ZX}$ and $(\gamma_{pl})_{ZX}$ denote in-plane effective shear yield strength and shear yield strain, respectively; E, ρ and σ_{ys} are the isotropic Young's modulus, density and yield strength of the constituent material of the hexagonal honeycomb structure, respectively. The subscripts 'Z' and 'X' denote the axis system, as shown in Fig. 1.1. The figure also shows the cell angle (θ), height (h), length (l) and cell-wall thickness (t_c) of the regular and auxetic hexagonal honeycomb cells.

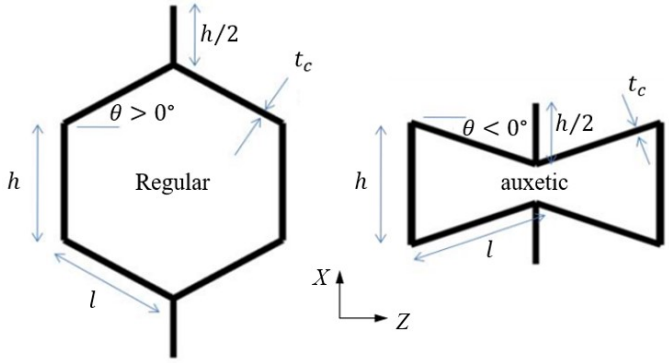

Figure 1.1: Unit cell geometry of regular and auxetic hexagonal honeycombs [19]

Reported studies have mostly focused on the in-plane flexibility of hexagonal honeycomb structures for realizing NPW designs stimulated by the NASA's Lunar Rover [19-22]. Owing to the high cost of manufacturing cellular structures with various geometric options, parametric studies using analytical models developed for small deformations (linear) or FE based models for large deformations are generally preferred over the physical experiments in the initial design stage. Ju et al. [19-21] conducted parametric studies using an analytical model based on CMT to achieve a functional design of hexagonal honeycomb structure with target shear moduli and maximum shear strains. The studies showed that auxetic hexagonal honeycombs exhibit lower effective shear moduli and higher maximum shear strains. In [19], the cell height, length, angle and cell-wall thickness were selected as design variables to achieve target shear properties. These parameters, however, yield coupled effects, which makes it difficult to obtain target levels of shear modulus and shear strain simultaneously. Berglind et al. [22] proposed effective height and horizontal separation as the design variables to achieve a target shear modulus independent of the shear flexibility. Based on the Prony series of the generalized Maxwell model and CMT, Ju et al. [23] proposed a viscoelastic analytical model to investigate the hysteretic energy dissipation of regular and auxetic hexagonal honeycombs of identical thickness. The results showed that auxetic honeycombs may be better candidates for energy efficient structural designs for their relatively less energy loss over the regular counterparts.

1.2.2 Development and performance analysis of NPWs

Compared with the pneumatic tires, the NPWs can eliminate the potential loss of inflation pressure due to punctures and routine inflation pressure maintenance. The vehicle handling and ride performance measures impose opposing design requirements for tires. Low vertical stiffness and

high lateral stiffness are desirable for improved ride and handling, respectively. The lateral, longitudinal, and vertical elastic properties of a pneumatic tire, however, are strongly coupled by the inflation pressure. The NPW designs offer flexibility in minimizing the coupling among the multi-axis stiffness and thus offer a good potential for improved handing and ride comfort performances of the vehicles [1]. During the last decade, a range of NPW designs have evolved, which were stimulated by the wheels designed for space exploration vehicles. The vast majority of the reported designs of NPWs can be represented on the basis of their structure and load bearing elements as: Tweels, honeycomb NPW and ME-wheel. This section is thus limited only to these three types of NPWs, with particular focus on the design, and static and dynamic properties.

Tweels

The Tweels, developed by Michelin [1], consists of a circular beam connected to the wheel hub by uniformly and discretely distributed thin deformable elastic spoke pairs with very low critical buckling load, as illustrated in Fig. 1.2. The circular beam comprises at least two inextensible membrane reinforcements made of orthotropic elastic material, which are separated by relatively low modulus elastic material, e.g., polyurethane (PU). The viscoelastic property of the PU is considerably smaller than the synthetic rubber, which potentially leads to lower rolling resistance. The application of the sandwich structure and low modulus material make the circular beam deform almost entirely in shear instead of bending. The circular beam is thus referred to as a shear beam or shear ring.

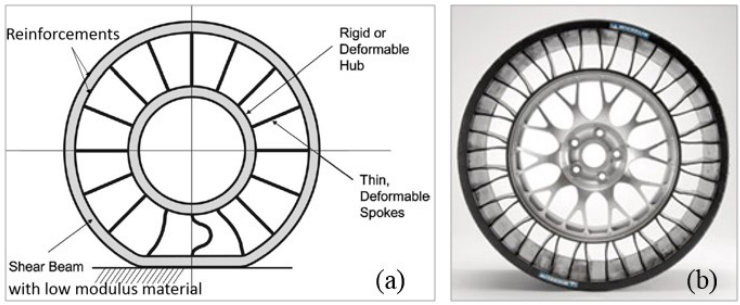

Figure 1.2: (a) Schematic representation of a deformed Tweel; and (b) Porotype Tweel structure [1]

The contact pressure $\bar{p}$ of the Tweel is related to shear modulus of the elastic material G and thickness of the shear beam t, as [1]:

$$\bar{p} \cong \frac{Gt}{R} \tag{1.4}$$

where R is outer radius of the shear beam. The design permits low contact pressure to achieve greater tire-road adhesion, reduced pavement damage potential and longer service life. Since the reinforcements are almost inextensible and the spokes are flexible, loading causes the diameter of the Tweel to increase, as shown in Fig. 1.3(a). The vertical load is supported by the tension force in the spokes out of the contact region caused by extension of the spokes together with increase in diameter. The absence of the sidewalls and beads yields lower mass and rolling resistance of the Tweels compared to the conventional tires.

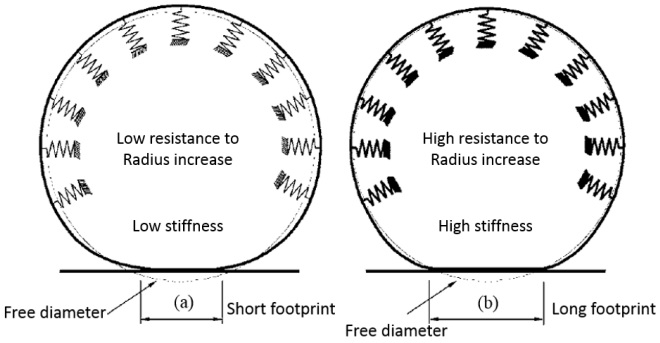

Figure 1.3: Schematic representation of the change in diameter and footprint length [1]

Besides, with the rubber tread bonded to the shear beam, the Tweel may be able to provide sufficient traction for handling and stability control. The manufacturing process of the Tweel, however, yields considerable residual thermal stresses and thus pretension exists in the spokes. Furthermore, the prototype Tweel has shown high-level noise under high speed operations [2]. A few studies have attempted to identify the sources of the noise and reduce the noise level. Manga [2] investigated vibration characteristics of the spokes using a 2D FE model and concluded that both the rolling speed and spoke thickness have only slight effect on spokes' vibration. The resulting noise was attributed to self-excitation of the spokes entering the contact area, and buckle and snap back into tension while exiting the contact region. Ramachandran [3] explored the effects of spoke geometric parameters on its vibration characteristics using a 2D FE model, and suggested that scalloping spoke edges and altering spoke width could significantly reduce the vibration amplitudes of spokes. These variations, however, showed only minimal effects on the dominant frequencies, while altering the spoke curvature significantly affected both the vibration amplitudes and frequencies. Using orthogonal arrays, efficient in achieving an optimal combination of design variables, Rutherford et al. [25] studied the effects of geometric design parameters, namely, spoke thickness, spoke length, spoke curvature, shear beam thickness, and inside and outside coverage,

on the Tweel's vibration characteristics. The study concluded that the spoke length and curvature are the most important design parameters, and shorter spokes with larger curvature resulted in low amplitudes of spoke and ground interaction vibration. Bezgam [26] proposed a 2D FE model with tread rubber to explore methods for reducing the spoke and ground interaction vibration amplitudes. The study concluded that, compared with spoke length and curvature, the inner and outer DeRad (deviation from radial lines as defined in [26]) affect the spoke and ground interaction vibration only slightly. The author also proposed an "alternating spoke pair design concept" in which even numbered spoke pairs have different geometric properties from the odd number pairs. Combining thin spokes with large curvature and thick spokes with small curvature for alternating spoke pairs could reduce both spoke and ground interaction vibration.

A number of studies have investigated the rolling resistance of the NPWs [27-30]. Using a 2D FE model, Veeramurthy et al. [27] conducted parametric studies, design of experiments and sensitivity analysis to investigate the effects of spoke and shear band (core layer) thickness on the rolling resistance of the Tweel. The study employed spokes with an eccentricity of 0.773 mm from the straight plane instead of a curvature, making the spokes easier to buckle in the contact area, as illustrated Fig. 1.4. Increasing the shear band and spoke thickness resulted in higher resistant to shear and thus lower rolling resistance. A constrained design optimization was performed to identify optimal spoke and shear band thickness to obtain minimum rolling resistance with constraint on the vertical stiffness. Veeramurthy et al. [28] further investigated optimal geometry (spoke and shear band thickness) and material property (shear modulus of PU) to minimize rolling resistance subject to constraints on the vertical stiffness and maximum contact pressure. It was concluded that the shear modulus of PU is most prominent design parameter, and the optimal design resulted in 25-32% reduction in the rolling resistance.

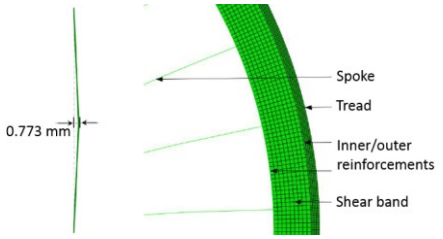

Figure 1.4: 2D FE model of Tweel [27]

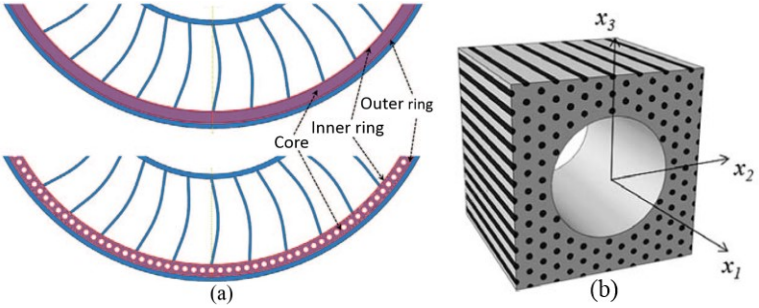

Figure 1.5: (a) Continuous shear band and porous shear band; and (b) reinforced porous shear band [29]

As concluded in [27,28], the hysteretic loss associated with cyclic shear in the shear band is one of the main sources of the rolling resistance. Therefore, a number of studies have focused on replacing the continuous shear band with linear-elastic porous or cellular structures to reduce the rolling resistance [29,30]. Ju et al. [29] proposed a 3D FE model with a porous PU-composite shear band instead of the original continuous-PU shear band, as shown in Fig. 1.5(a). The porous PU was reinforced with carbon fibers to achieve desired vertical stiffness, as illustrated in Fig. 1.5(b). The study showed that the porous shear band could reduce rolling resistance by 25%. The authors also stated manufacturing complexities of the cellular shear band due to high sensitivity of the cell-wall thickness on the effective moduli of metallic cellular shear band.

Honeycomb NPWs

The static and dynamic properties of NPWs with hexagonal honeycomb spokes have been investigated in a number of recent studies using FE methods. Kim et al. [31,32] established 3D FE models of a pneumatic tire and three hexagonal honeycomb NPWs with the same load carrying capacity, and compared the contact pressure distribution and footprint shape of the four models under the static loading condition. The study revealed nearly rectangular footprint of the NPWs due to their high out-of-plane stiffness, and lower contact pressure of NPWs compared to the pneumatic tire. Moreover, unlike the pneumatic tire, the vertical stiffness of the NPWs decreased with increase in the vertical load, which was attributed to initial high resistance of the cell-wall under compression and subsequent easier buckling of the cell-walls. Later, Kim et al. [33] designed four honeycomb NPWs with 2D and 3D hexagonal honeycomb spokes and investigated the contact pressure distribution and local stress distributions in the spokes (Fig. 1.6). The NPWs with 3D honeycomb spokes showed larger local stress due to the small cross section area in the lateral direction, while the NPWs with 2D cross section spokes revealed lower contact pressures than those with 3D spokes. In order to design a NPW with high fatigue resistance, cellular spoke

geometries with regular and auxetic honeycomb structures have been investigated [5]. It has been shown that the ratio of the inclined cell length to the overall cell height is a key factor determining the in-plane flexibility of the hexagonal honeycombs under uni-axial loading conditions. An increase in the cell angle yields higher flexibility of the honeycomb spokes with reduced local stress and thus improved fatigue resistance.

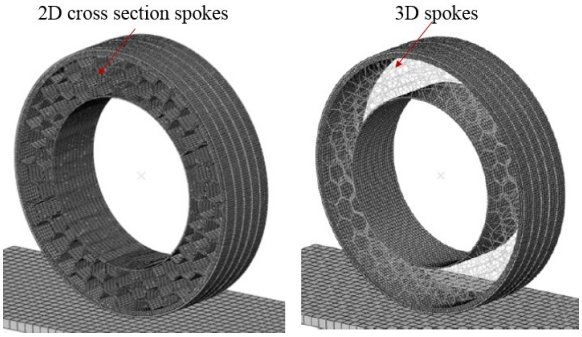

Figure 1.6: Honeycomb NPW with 2D cross section and 3D spokes [33]

Since the rolling resistance of a NPW is mostly attributed to the shear band elastomer, a few studies have applied honeycomb structures to the shear band design in order to reduce the rolling resistance [30,34]. Combining FEM, neural networks, design of experiments, sensitivity analysis, and genetic algorithms, Thyagaraja et al. [30] obtained constitutive metamaterial properties of the shear layer. Shankar et al. [34] conducted a comparative study on the size optimization of four meso-structures, as shown in Fig. 1.7, to meet the design requirements of a shear beam targeting 10% shear flexure with 10 MPa effective shear modulus. It was concluded that optimized S-type, with a wall thickness of 0.411 mm and an amplitude of 0.608, meets the design requirements of the shear beam.

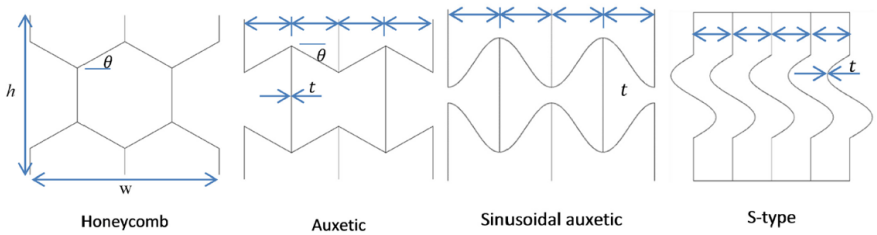

Figure 1.7: Meso-structures for the shear band [34]

A few studies have also investigated dynamic properties of the honeycomb NPWs [6,13,14]. Jin et al. [6] investigated the static and dynamic properties of NPWs with regular hexagonal

honeycombs using FEM and concluded that honeycomb NPWs exhibit higher load carrying capacity and lower maximum stress in spokes and tread than those of the pneumatic tires. Besides, the rolling resistance of a honeycomb NPW with the smallest cell expanding angle is considerable low, which can be attributed to its lower mass and small deformations of the honeycomb spokes. In addition, the stress level in the spokes and tread under dynamic loading are higher than those under static loading. Lee et al. [13,14] studied the dynamic properties of the auxetic and regular hexagonal honeycomb NPWs by modal analysis and steady state vibration analysis under a series of vertical loads and rolling speeds. The study concluded that the low initial modal frequency (23.37 Hz) may not be adequate for the vehicle ride comfort performance. Besides, the non-homogeneous mass distribution induced by the discrete spokes could cause local vibration and affect the vibration associated with reaction forces.

ME-wheel

A schematic representation of the ME-wheel, developed by Zhao et al. [4], for off-road military vehicles, is shown in Fig. 1.8. The ME-wheel mainly consists of an elastic outer wheel, hinges, wheel hub, and pins. The elastic outer wheel is composed of elastic rings, which are linked together by clamps, and a rubber layer with a tread pattern. The hinges, sustaining only the tension, are installed with pins and pin seats located on the elastic ring clamps and the bolt hole of the wheel hub. The elastic outer wheel is connected to the wheel hub by a number of hinge units. During acceleration or deceleration along a straight line, the hub endures vertical and longitudinal forces, and driving or braking moments, which are transmitted to the elastic outer wheel by hinge units. The hinge units, with high tension stiffness, cause the ME-Wheel to incur large deformation in contact area, which is considered desirable for good vehicle handling performance. Moreover, the bending of hinge units together with large deformations of the elastic rings could help reduce the vibration caused by road irregularities [35-36].

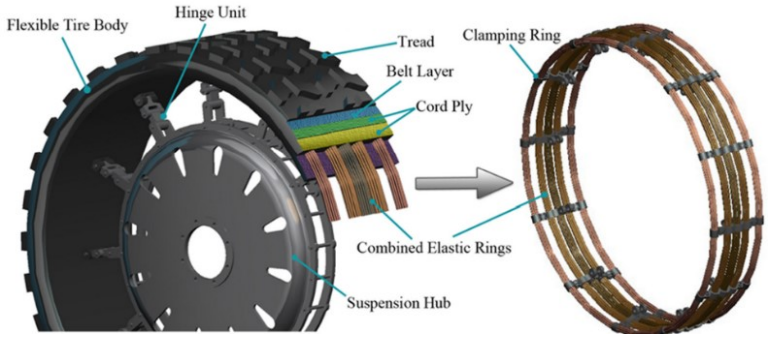

Figure 1.8: ME-Wheel and the connection of elastic rings [4]

Wang et al. [37] performed analysis to study the transmission of forces within the internal structures of a ME-Wheel under driving and braking conditions. It was concluded that the ME-Wheel offers effective mechanical transmission characteristics. The study also developed simplified vehicle models with the ME-Wheel and pneumatic tires in the ADAMS software to perform relative analyses. The simulation results showed good ride comfort of the vehicle model with ME-Wheels in the low speed range, while the pneumatic tire vehicle model showed better ride comfort at higher speeds. Zhao et al. [4] investigated multi-axis stiffness of the ME wheels with different structures (two- or three-link structures) and number of spokes using the FE model. Increasing the number of spoke yielded higher vertical, longitudinal, lateral and torsional stiffness, while three-link spokes induced lower longitudinal, lateral and torsional stiffness. The results also suggested negligible effect of spoke structure on the vertical and lateral stiffness. Fu et al. [38] established a theoretical model for lateral stiffness of a ME-Wheel to determine primary influencing factors. The effects of vertical load, structure parameters of tire bead and shear modulus of rubber layer on the lateral stiffness were subsequently investigated using a FE model. The results showed increase in lateral stiffness with increasing vertical load and shear modulus. The lateral stiffness, however, decreased with increase in the depth to width ratio of the tread-band. Later, Zang et al. [43] studied the effects of wheel structure and operating conditions on the radial stiffness of a ME-Wheel. In the pneumatic tires, the wheel lateral stiffness is generally lower than the longitudinal stiffness [39]. Opposite trend, however, was observed in reported ME wheels [4,35]. The static wheel/road contact pressure distribution was explored via experiments and FE simulations [40,41], and smaller contact pressure and stress concentration in wheel shoulder area were observed in ME wheels, when compared to the pneumatic tires. The influences of camber angle on the static and dynamic wheel/road contact pressure distribution were further investigated in [10,35,42]. The traction/braking properties at various camber angle were studied using

experimental and FE methods [10,42]. The results obtained from steady-state transport analyses suggested that the longitudinal forces peak at slip ratios ranging from 15% to 20%, which is comparable to those of the pneumatic tires. Zhu et al. [11,12] investigated the cornering properties of ME wheels using experimental, analytical, and FE methods. The cornering force saturated at slip angles of about 10° instead of 3° to 5° observed for the passenger car pneumatic tires. A few studies have also investigated modal properties of ME wheels [15,43,44], fatigue life [45] and dynamic interactions with deformable terrains [36,46,47].

1.2.3 Performance measures of the pneumatic tires

The performance characteristics of the pneumatic tires could be reflected by their stiffness and modal properties. For instance, the ride comfort of an on-road or off-road vehicle is closely related to the vertical stiffness of the tires, while its handling characteristics are significantly affected by tires' cornering properties [48]. Moreover, the dynamic responses of a pneumatic tire could be characterized using its modal parameters [49]. A number of widely used performance measures for the pneumatic tires are thus reviewed in order to assess the performance characteristics of the NPWs.

Multi-axis stiffness properties

The static multi-axis stiffness properties are the most fundamental characteristics of the pneumatic tires, which significantly affect their capacities to support the vehicle weight, cushion road irregularities, transmit traction/braking forces and change or maintain the direction of travel [39]. Fig. 1.9 depicts the commonly used tire axis system suggested by the Society of Automotive Engineers [48]. The (equivalent) vertical stiffness is defined as the ratio of the normal load applied to the tire and its overall vertical deflection. On the other hand, the longitudinal, lateral and yaw stiffness, respectively, are evaluated as the rate of change of the external horizontal force applied to the loaded tire in X- or Y-direction (Fig. 1.9) or the moment about Z-direction with respect to the resulting translational or angular displacement near zero deformation.

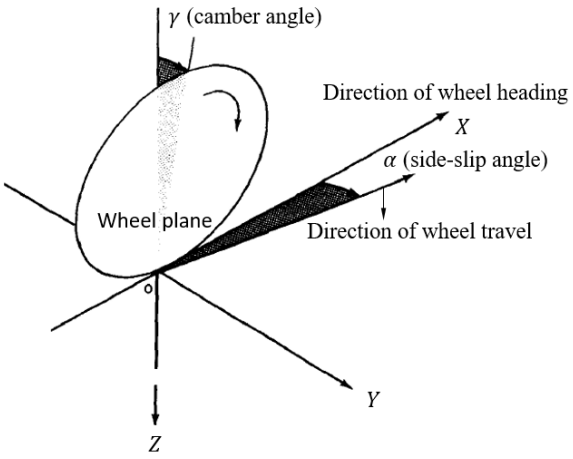

Figure 1.9: Tire axis system [48]

The multi-axis force/moment-deformation relations of the pneumatic tires could be obtained by measurements or alternatively using FE simulations [50-52]. Fig. 1.10 illustrates measured multi-axis stiffness values for the pneumatic tires of various dimensions [39]. The results in the figure invariably show that the pneumatic tires are stiffest in the longitudinal direction and softest in the lateral direction. The influences of the inflation pressure and normal load on multi-axis stiffness of the pneumatic tires have also been investigated in a number of studies using both experimental and simulation methods [50,51,53,54]. The results suggest positive effects of the inflation pressure and normal load on these stiffness characteristics, which are strongly coupled.

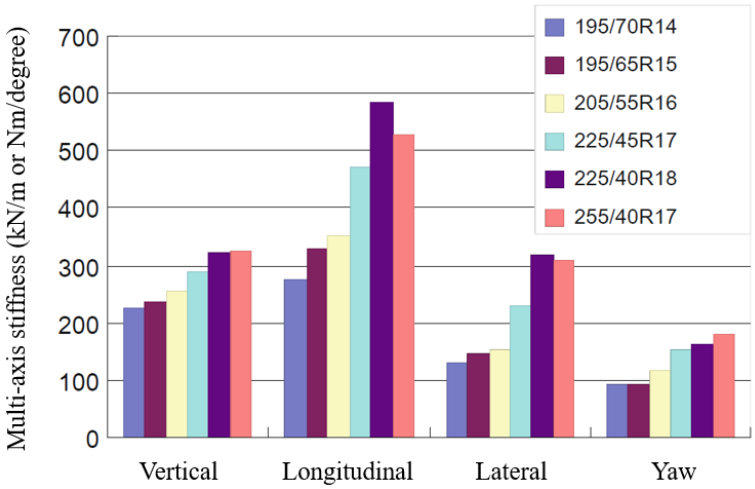

Figure 1.10: Measured multi-axis stiffness values for pneumatic tires of different sizes [39]

Cornering properties

When a straight-line rolling pneumatic tire is subjected to a side force (F_s), it will move along a path at an angle with respect to the wheel plane, as illustrated in Fig. 1.11. This angle is defined as 'side-slip angle (α)' and the lateral force developed in the tire-road contact patch is called the 'cornering force' ($F_{y\alpha}$). The cornering force and side-slip angle relation is of fundamental importance to the directional control and stability of the vehicles [48]. The mechanism of the cornering behavior, and the typical tire cornering force and self-aligning moment (M_Z) variations with side-slip angle are illustrated in Figs. 1.11(a) and 1.11(b), respectively. The self-aligning moment is the product of the pneumatic trail and the cornering force of the tire, and serves as the primary restoring torque, which helps the steered tire return to the original position after negotiating a turn. The offsets in the cornering force and self-aligning moment with respect to the origin, as observed in Fig. 1.11(b), are attributed to the ply steer and conicity effects [55,56]. The cornering force increases linearly with the slip angle at relatively low slip angles caused by elastic deformation of the tire tread [48]. With increase in the slip angle, the cornering force increases at a lower rate due to partial sliding of tire tread (trailing part). The cornering force approaches saturation and the tread begins to slide laterally. Similarly, the self-aligning moment increases with slip angle and approaches its maximum at a particular slip angle. It decreases with further increase in the slip angle due to sliding of the trailing part of tire tread, which directly affect the pneumatic trail. The rate of change of the cornering force with respect to the slip angle near the origin defines the cornering stiffness of the tire, which is a determining parameter for the linear handling and stability behavior of the vehicles. The nonlinear cornering force characteristics at higher side-slip angles governs the handling and stability properties of the vehicles at higher lateral accelerations.

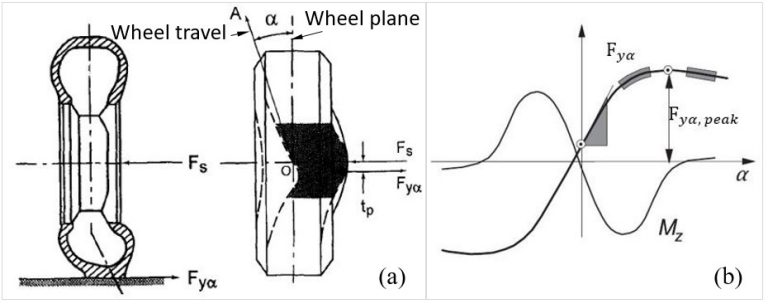

Figure 1.11: (a) Tire cornering mechanism; (b) Cornering force and self-aligning moment characteristics [48]

The cornering force and self-aligning moment responses of a rolling pneumatic tire under different side-slip angles could be derived using expensive test machines [51,52,57,58]. Alternatively, a number of studies have employed FE methods to predict tire cornering force and self-aligning moment characteristics, using either transient or steady-state transport analysis [59-61]. It has been revealed that both analyses methods could offer accurate predictions of tire cornering properties under relatively low side-slip conditions. The steady-state transport analysis, however, provides more accurate predictions of the cornering force and self-aligning moment developed under higher side-slip angles. Moreover, the transient analyses using either implicit or explicit time integration techniques are computationally demanding owing to the limited time increment size in order to yield stable and accurate response predictions [62-64].

A number of studies have investigated the influences of operating conditions on cornering properties of the pneumatic tires using both measurements and FE simulations [51,53-55]. It has been shown that the normal load reveals notably positive effects on the cornering stiffness, which, however, tend to saturate at relatively higher normal loads [54]. Moreover, the cornering force and self-aligning moment characteristics are only slightly influenced by the rolling speed. The inflation pressure, however, shows highly nonlinear influences on the cornering stiffness due to its opposite effects on the stiffness of tire sidewall and the area of tire-road contact patch [53,54].

Some studies have investigated the influences of geometric and material properties of tire components on the cornering force and self-aligning moment responses [53,57,65]. The results suggest positive effects of the belt angle on both cornering and self-aligning stiffness, which are less sensitive to the number of belt cords and nearly independent on the strength of carcass cords. Moreover, the elastic property of the rubber tread is determined as a critical design parameter in view of tire cornering stiffness [53,57]. While the cornering properties of pneumatic tires have been widely investigated using experimental and numerical simulation techniques, such studies on NPWs with honeycomb spokes could not be found.

Modal properties

The dynamic responses of a rolling pneumatic tire are essentially the superposition of many directionally sensitive motions, which are primarily excited by its interaction with the terrain and tire non-uniformities. Each motion, however, could be characterized by its associating modal parameters including natural frequency, mode shape, modal damping and modal mass. Estimation of these parameters, particularly the natural frequencies and vibration modes, could thus help gain

insight into the responses of the pneumatic as well as non-pneumatic wheels when subjected to in-plane and out-of-plane excitations, which determine their ride properties, noise level, traction/braking and handling performances. A number of studies have thus investigated modal properties of the pneumatic tires by experimental, analytical, or FE methods, while considering different operating and boundary conditions [49,66,67].

Many studies conducted modal testing for non-contacting stationary tires with free spindles [68-70]. Their modal parameters were identified using the acceleration responses excited by vibration exciters and measured at multiple locations on tire/rim perimeters using accelerometers. The influences of spindle (free, pined and fixed) and contact patch (free and fixed) constraints of the pneumatic tires on the modal properties were further investigated together with their dependence on the inflation pressure and normal load [69-72]. Alternatively, some studies used holography technique to derive natural frequencies and mode shapes of non-contacting stationary tires with fixed spindle [73,74]. The modal parameters of loaded rotating tires, however, have been addressed in fewer studies. Studies have identified modal parameters of loaded rolling tires with pinned spindle from tread and sidewall vibration velocities, which were excited by cleats and measured by laser Doppler vibrometer [75-77]. Limited number of natural frequencies could also be extracted from spindle displacement or force responses, using Fast Fourier Transformation (FFT) [78-80]. This method, however, could not identify mode shapes suggesting tire local deformations. The reported experimental approaches could only determine a few mode shapes in each direction with relatively low natural frequencies. The mode shapes with complex deformation patterns as well as higher natural frequencies are difficult to identify owing to the damping effects. Moreover, many out-of-plane mode shapes could rarely be triggered [81].

Many studies employed physics-based models, also referred to as analytical models, to predict in-plane vibrations of the pneumatic tires. In order to take advantage of the mathematical simplicity associated with the axis symmetry of tire structure, such models initially viewed the tire with no ground contact as a thin circular shell or a ring on elastic foundations representing pressurized sidewall [49,82]. The ground contact was subsequently added as external displacement or load constraint [83,84]. These models with complex formulations could offer physical insight into vibration characteristics of the pneumatic tires. There are, however, many limitations resulting from the assumptions associated with such models. For instance, the models using the thin shell assumption could not predict tire dynamic responses caused by high frequency road excitations

[49]. Moreover, parameterization of these models necessitates relatively complex measurements [83-85].

Finite element (FE) tire models could easily handle various combinations of spindle and contact constraints together with variations in geometric and material properties of the tire components. Many studies thus employed FE methods to investigate both in-plane and out-of-plane vibration characteristics of the pneumatic tires [86,87]. Early FE studies used limited number of shell or membrane elements to model the tires (cord-rubber composites) and yielded reasonably accurate predictions of their modal properties with high computational efficiency [88-91]. These elements, however, are associated with relatively complex formulations owing to the consideration of the stiffness variations resulting from the inflation pressure and large displacements as well as the complicated properties of the laminated composite materials. Alternatively, many studies employed solid and shell elements with much simpler formulations to explicitly represent the geometric and material properties of tire components, using various commercial software [66,71,81,92]. Reasonably close agreements between measured and FE-predicted natural frequencies were obtained for non-rolling tires with different combinations of spindle and patch constraints [66,93]. A number of studies considered the influences of geometric and material properties of the tires together with the inflation pressure and normal load on natural frequencies of chosen vibration modes [66,72,94]. Less agreements between the natural frequencies obtained from simulations and measurements, however, were observed for the rolling tires. For instance, FE simulations showed notable reductions in natural frequencies of only several vibration modes when tire's rotation was initiated [66,81]. The measured results, however, revealed generally lower natural frequencies for most vibration patterns considered at the onset of rotation [75,76].

In recent years, a few studies have also investigated modal properties of NPWs with honeycomb spokes [13,14] or hinge-unit spokes (ME wheels) [15,43,44] using either simulation or experimental methods, as stated above. Most of these studies, however, only considered modal properties of NPWs with fixed spindle but no ground contact or external normal load. More efforts are thus necessitated for the loaded NPWs. Moreover, there may exit other additional performance measures in the case of NPWs such as spokes' stresses and deformations.

1.3 Research objectives and scope

From the review of reported studies, it became evident that the NPWs with regular honeycomb spokes yield higher load carrying capacity with relatively lower wheel mass and thus the rolling resistance than their auxetic counterparts. The response characteristics of the honeycomb NPW subjected to horizontal force/moment, however, have not yet been explored. These include longitudinal, lateral and yaw stiffness properties of the non-rolling wheel as well as its cornering force and self-aligning moment characteristics under rolling scenarios. These stiffness properties could be obtained using finite element (FE) simulations with satisfactory accuracy. Moreover, only limited knowledge exits for the modal properties of loaded honeycomb NPW for both stationary and rolling conditions. Accurate predictions of modal parameters, however, may only be obtained for stationary wheels or tires when using FE methods. The overall goal of the thesis research is to realize NPW designs that could provide in-plane and out-of-plane properties comparable to those of the pneumatic tires. The specific goals of the dissertation research are summarized below:

i. Develop 3D finite element models for NPWs with regular honeycomb spokes of different configurations for predictions of their static and dynamic responses and validate these wheel models using available results in published studies.
ii. Investigate relative merits of honeycomb NPWs by comparing their in-plane and out-of-plane properties with a reference pneumatic tire (205/55R16) of similar load carrying capacity and dimensions.
iii. Develop efficient parametric sensitivity analyses technique using design of experiments (DOE) to investigate the influences of essential design variables on multi-axis and cornering stiffness characteristics as well as natural frequencies of important vibration modes of the honeycomb NPW.
iv. Propose an alternate honeycomb spoke configuration to achieve more comparable out-of-plane properties to those of the reference pneumatic tire, and evaluate its multi-axis and cornering stiffness characteristics.

1.4 Organization of dissertation (manuscript-based)

This dissertation is prepared according to the manuscript-based format described in “Thesis Preparation, Examination Procedures and Regulations” guidelines of the School of Graduate Studies, Concordia University. The dissertation is organized in seven chapters, which address the

abovementioned research goals and objectives, including the introduction and literature review. The first chapter presents a comprehensive literature review on the studies reporting the spoke designs of NPWs, static and dynamic analyses of NPWs and some critical performance measures of the pneumatic tires. The research objectives and scope of this dissertation research are also presented in this chapter. Chapter 2 presents finite element (FE) modelling of NPWs with honeycomb spokes and comparative analyses of their static and dynamic properties in relative to a reference pneumatic tire (goal (i) and (ii)). Chapters 3 to 5 present parametric studies on multi-axis stiffness, cornering stiffness and modal properties of the honeycomb NPW using Taguchi or response surface methods (goal (iii)). FE modelling of NPWs with novel spoke designs is presented in Chapter 6 for analyses of their in-plane and out-of-plane properties (goal (iv)). Chapters 2 to 6 are compiled from three articles published in peer-reviewed journals and two manuscripts submitted for peer review. These are further summarized below:

Chapter 2 presents the following article, published in the Proceedings of the Institution of Mechanical Engineers, Part D: Journal of Automobile Engineering:

Zheng Z, Rakheja S, Sedaghati R. A comparative study of static and dynamic properties of honeycomb non-pneumatic wheels and a pneumatic wheel. Proc I Mech Eng, Part D, J Auto Eng. 2021;235(14):3631-3646 [108].

This article presents development of three-dimensional finite element (FE) models for the honeycomb NPWs with three different spokes' configurations, realized by varying the cell angle. The validity of the proposed NPW FE models was demonstrated by comparing the predicted wheel responses with the reported data. A FE model of the pneumatic wheel of identical size was also formulated and verified on the basis of the measured vertical force-deflection and cornering properties. The verified NPW models were subsequently employed to study their feasibility through comparisons of in-plane as well as out-of-plane properties with those of the pneumatic wheel. The influences of the cell angle and normal wheel load on the static and dynamic properties of the NPWs were also investigated. The results showed load-dependent longitudinal stiffness of the wheel due to strong coupling between radial and longitudinal deformations of the honeycomb spokes. The lateral stiffness, however, was observed to be load-independent due to negligible coupling between radial and lateral deformations of the spokes. The spokes of the honeycomb NPWs could thus be easily tuned to achieve vertical and longitudinal stiffness comparable to those of the reference pneumatic wheel. The lateral and cornering stiffness of the NPWs with the planar

spokes, however, were substantially higher, irrespective of the spokes' configuration considered. The significantly higher cornering stiffness resulted in rapid saturation of the cornering force of the NPWs at side-slip angles about 1.1°, which is likely to cause lateral sliding of the wheels and potential loss of directional control under higher side slip conditions.

Chapter 3 presents the following article, published in the Composite Structures:

Zheng Z, Rakheja S, Sedaghati R. Multi-axis stiffness and road contact characteristics of honeycomb wheels: A parametric analysis using Taguchi method. Compos Struct. 2021;279:1-14 [115].

This article presents finite element (FE) modelling a non-pneumatic wheel (NPW) with three different honeycomb cell angles together with their verification in order to investigate their multi-axis stiffness and road contact characteristics. The experiment designs based on $L_8(2^7)$ and $L_9(3^4)$ orthogonal arrays are subsequently formulated to identify influential design factors affecting the wheel response measures and their nonlinear effects. The multi-axis stiffness of the NPW are strongly influenced by the spokes design parameters, although the yaw stiffness is mostly affected by the tread parameters. The road contact properties, however, are dominantly affected by the annular beam and tread design parameters. The results from these experiment designs are effectively used to establish guidance for design tuning of the NPW for realizing desirable stiffness and road contact properties. A $L_{16}(2^{15})$ orthogonal array experiment is further formulated to study the interactions among the influential design factors in view of the multi-axis stiffness and road contact responses of the wheel. The results showed negligible contributions due to interactions among the design factors. It is shown that the NPW design parameters can be tuned to achieve multi-axis stiffness properties comparable to those of the pneumatic tires.

Chapter 4 presents the following article, published in the Composite Structures:

Zheng Z, Rakheja S, Sedaghati R. Cornering stiffness characteristics of honeycomb wheels: A parametric analysis using response surface method. Compos Struct. 2022;288:1-15 [118].

This article presents three-dimensional finite element (FE) modelling of a honeycomb wheel with three different cell angles to investigate its cornering stiffness characteristics. The validity of the developed models was demonstrated by comparing predicted wheel responses with the reported data under identical operating conditions. Regression models relating wheel cornering stiffness with the significant design parameters and their two-factor interactions were subsequently formulated using the results derived from the FE models based on the design points obtained using

half fractional factorial and central composite design approaches. The regression models revealed relatively good prediction ability within the design space considered. It is shown that cornering stiffness of the honeycomb wheel is strongly influenced by the geometric and material properties of the annular layer and the tread, while the lateral stiffness is mostly affected by honeycomb spokes and tread design parameters. The regression models could thus serve as an efficient design tool to derive design guidance for honeycomb wheels for realizing desired cornering stiffness.

Chapter 5 presents the following article, submitted to the Composite Structures:

Zheng Z, Rakheja S, Sedaghati R. Modal properties of honeycomb wheels: A parametric analysis using response surface method. Compos Struct.

This paper presents development of finite element (FE) models for a honeycomb non-pneumatic wheel (NPW) with three different spokes configurations of varying cell angles so as to investigate its modal properties under a given normal load. The validity of these wheel models was confirmed through comparisons of predicted wheel responses with available data in published studies for similar wheel material properties and components dimensions. The important vibration modes affecting the wheel responses were initially identified together with the important design factors affecting the modal properties. Response surface models relating the natural frequency of each chosen influential vibration mode with its important design parameters and their two-factor interactions were subsequently formulated using the results of FE simulations corresponding to the design points of screening design and an experimental design based on central composite design (CCD) approach. These regression models showed good fitting accuracy of the natural frequencies obtained in CCDs together with relatively satisfactory prediction ability over the design region considered. The resulting regression models are thus considered to serve as a design guidance for realizing desired wheel modal properties. The results derived from parametric studies showed that natural frequencies of identified in-plane and out-of-plane vibration modes are significantly affected by design parameters of the spokes. These include the thickness and initial elastic modulus of the honeycomb cell-wall and the cell angle. Most of the identified vibration modes are also strongly influenced by the thickness dimensions of the core layer and the tread, while their initial elastic moduli revealed considerable effects only on the wheel Hop and Twist modes.

Chapter 6 presents the following article, submitted to the Composite Structures:

Zheng Z, Rakheja S, Sedaghati R. Multi-axis and cornering stiffness properties of non-pneumatic wheels with symmetric helical honeycomb spokes. Compos Struct.

This paper presents development of three-dimensional finite element (FE) models for a honeycomb non-pneumatic wheel (NPW) with helical spokes configurations of different cell and helix angles in order to fundamentally investigate its multi-axis and cornering stiffness characteristics under 3 kN normal load. The validity of the developed NPW models with 0° helix angle and three different cell angles was verified by comparing predicted wheel responses with results available in published studies, considering both non-rolling and rolling conditions. Simulations were conducted under two design constraints in terms of identical cell-wall thickness and identical load carrying capacity. The results suggest that increasing helix angle results in higher in-plane stiffness of the honeycomb spokes and thus could effectively yield greater vertical and longitudinal stiffness of the wheel. An increase in the helix angle also causes lower lateral stiffness for the wheel designs with 15.8° and 31.5° cell angles resulting from the reductions in the out-of-plane stiffness of their spokes, apart from the notably lower cornering stiffness, particularly when it is increased to 30° and 45°. The cell-wall thickness, however, shows positive influences on multi-axis stiffness of the wheel but negative effects on its cornering stiffness. Owing to the relatively smaller contribution of the spokes to the yaw deformation of the wheel as compared to its lateral deformation, the variations in the spokes configurations revealed relatively lower influences on the yaw stiffness properties.

The major conclusions and contributions of this thesis research are summarized in Chapter 7 together with some thoughts on further works.

Chapter 2

A comparative study of static and dynamic properties of honeycomb non-pneumatic wheels and a pneumatic wheel

2.1 Introduction

Owing to their many desirable features, the pneumatic wheels had substituted the traditional rigid wheels in most rolling transport systems shortly after their invention, which include lower mean contact pressure, lower vertical stiffness, lower energy loss and lower mass per unit load carried [1,4]. Despite their proven superior performances, the pneumatic wheels also exhibit certain deficiencies such as loss of vehicle performance and control in the event of severe leakage or bursting, relatively higher maintenance, complex manufacturing process, and fire hazards and environmental risks associated with the used tires.

In recent years, a number of designs of non-pneumatic wheels (NPWs) have emerged for general vehicular applications. These exhibit very similar design principles, namely, radial flexible spokes [1,4] or honeycomb spokes [6] replacing the air in the pneumatic wheel. It has been shown that the NPWs not only exhibit some of the desired characteristics of the conventional pneumatic wheels but can also overcome their disadvantages such as elimination of potential inflation pressure loss and routine inflation pressure maintenance [1]. The NPWs are also considered to offer enhanced sustainability and reduced environmental risks [2,33].

The reported spoke designs of the NPWs include curved radial flexible spokes as in Tweels [25,27,28], hinge-unit spokes in mechano-elastic (ME) wheels [41,45,46] and polygonal lattice spokes in honeycomb NPWs [6]. The majority of the reported works on the spoke designs, however, have focused on polygonal lattice spokes, with particular focus on the in-plane (vertical-longitudinal plane) properties of the hexagonal honeycomb spokes [19,21,22]. The hexagonal honeycombs can provide target in-plane properties by adjusting the geometric parameters and constituent material properties according to the cellular materials theory (CMT) in the linear elasticity range [24].

The static and dynamic properties of the NPWs with hexagonal honeycomb spokes have been investigated in a number of recent studies using FE methods. The analyses, however, have been mostly limited to load carrying capacity (defined as the vertical deflection under a specific

wheel load) [5,6], tread's stress [6], wheel-road contact pressure distribution [31,33], spokes' deformations and stresses [5,6,31,33], vibration modes [13,14] and rolling resistance [6]. The decrease in the vertical stiffness was observed with an increase in the wheel load, which is attributable to the high initial resistance of the cell-walls to deformations and subsequent easier buckling [31]. For NPW designs of identical cell-wall thickness, decreasing the cell angle resulted in relatively higher load carrying capacity, and lower wheel mass [5]. The peak stress in the tread of a honeycomb NPW was only slightly influenced by the spokes' configuration [6]. Jin et al. [6] investigated the dynamic properties of the NPWs with regular honeycomb spokes in terms of spokes' deformations and stresses, tread stress and rolling resistance. Relatively higher peak stresses in the spokes and the tread were observed under steady-state rolling conditions when compared to the static stresses. Considerably low rolling resistance was observed for the wheel with the spokes with a lower cell angle, which was attributed to its lower mass and spokes' deformations. A few studies have also investigated the NPWs with auxetic spokes with negative cell angles [5,14]. These have shown smaller load carrying capacity than their regular counterparts with identical but positive cell angles. The NPW design with auxetic honeycomb spokes is thus heavier than that with the regular counterpart of identical load carrying capacity, although the spokes' stresses of both designs are comparable [5]. As a result, the NPWs with regular honeycomb spokes could yield relatively higher load carrying capacity with lower wheel mass and thus the rolling resistance when compared to those of their auxetic counterparts. Lee et al. [13,14] investigated the vibration characteristics of NPWs with auxetic and regular honeycomb structures using modal and steady state vibration analyses under different vertical loads and rolling speeds. The study observed fundamental frequency of the NPW for a passenger car in the order of 23 Hz, which was considered inadequate for ride comfort performance. Besides, the non-homogeneous mass distribution attributed to the discrete spokes could cause localized vibration of the spokes and significantly affect the wheels' vibration characteristics.

For general applications of NPWs in ground vehicles, it would be desirable to establish their feasibility in relation to the pneumatic wheels. It is important that the NPWs exhibit properties comparable to those of the pneumatic wheels, especially those relevant to ride, traction/braking and direction control performances of the vehicle. Only limited efforts, however, are evident in establishing the relative static and dynamic properties of NPWs and pneumatic wheels. The aforementioned studies have mostly focused on the static and dynamic properties of honeycomb

NPWs with different spoke's designs in terms of load carrying capacity, spokes' deformations and stresses, tread stress, wheel-terrain contact pressure, rolling resistance, and noise and vibration. The analyses of forces developed by the wheel in the horizontal plane, however, have been attempted in a very few studies limited only to the ME wheels with hinge-unit spokes [10,12,35].

The present study is aimed at (i) evaluating relative in-plane and out-of-plane properties of the honeycomb NPWs with different spokes' configurations and a reference pneumatic wheel; and (ii) investigating the effects of spokes' cell angle and normal wheel load on the static and dynamic properties of NPWs. For these purposes, three-dimensional FE models of the honeycomb NPWs with different spokes' configurations were developed to study their multi-axis stiffness, spokes' forces and deformations, contact pressure distribution, and cornering and self-aligning characteristics. The validity of these models was examined by comparing the predicted peak local stress in the honeycomb spokes and the vertical wheel deflection with the available data from the published studies. An FE model of the pneumatic wheel of comparable size and load carrying capacity was also formulated for relative performance analyses. The static and dynamic properties of the NPWs were evaluated and compared with those of the pneumatic wheel to gain insight into the feasibility and relative merits of the honeycomb NPWs.

2.2 FE modeling of a honeycomb NPW and a pneumatic wheel

A three-dimensional FE model of a honeycomb NPW was developed considering a nominal cell angle of 15.8° in order to evaluate its static and dynamic properties, using ABAQUS/Standard and Explicit, respectively [95]. Owing to the significant effect of the spokes' configuration on the static and dynamic properties, two additional models of the wheel were formulated for two alternate honeycomb spokes with cell angles of 31.5 and 47.1°. The cell angles were chosen to conform to those employed in the reported studies [6], which facilitated verifications of the models. Moreover, these are considered to represent a practical range of cell configurations [5]. The dimensions of the wheel were chosen to be representative of a passenger car pneumatic wheel (205/55R16) [96]. Fig. 2.1 illustrates the model of the honeycomb NPW with 15.8° cell angle, which comprises the rubber tread, outer and inner rings, shear band, honeycomb spokes and the rim. The wheel and rim diameters, and the wheel width, were taken as 632, 406 and 205 mm, respectively, as in the case of the reference pneumatic wheel, while the thickness of the outer and inner rings, shear band, and the tread were fixed as 0.5, 0.5, 9.5 and 5 mm, respectively, as reported in the references [6,31].

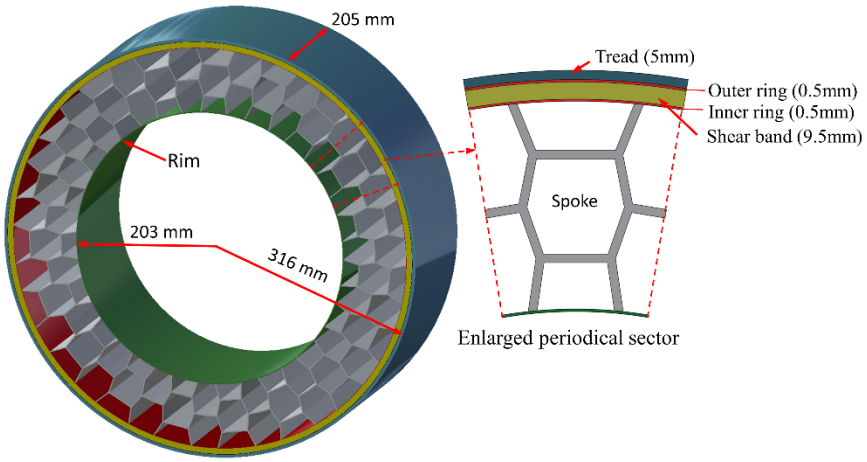

Figure 2.1: Illustrations of the honeycomb NPW (Cell angle: 15.8°)

The rim, and the outer and inner rings, made of aluminum alloy and high strength steel, respectively, were modeled using linear elastic material model. The tread is considered as a synthetic rubber block, while the spokes and shear band are constructed from moldable polyurethane. The synthetic rubber and polyurethane were modeled as hyper-elastic materials using the Ogden material model based on strain energy potential [6]. The material properties of the constituents, including the aluminum, high strength steel, synthetic rubber and polyurethane, were taken as those reported in the references [6,31]. The viscous effects of the synthetic rubber and polyurethane were considered negligible, although a mass-proportional damping was assumed for the transient analysis [56]. The compressibility of the synthetic rubber and polyurethane was introduced so as to achieve relatively greater time increments and to reduce the contribution of the high frequency noise in the transient response [95,97]. The Ogden strain energy potential and the mass proportional damping are given as [6,56]:

$$U = \sum_{i=1}^{N} \frac{2\mu_i}{\alpha_i^2}\left(\bar{\lambda}_1^{\alpha_i} + \bar{\lambda}_2^{\alpha_i} + \bar{\lambda}_3^{\alpha_i} - 3\right) + \sum_{i=1}^{N} \frac{1}{D_i}\left(J^{el} - 1\right)^{2i}, \mu_0 = \sum_{i=1}^{N} \mu_i;\ N{=}3 \tag{2.1}$$

$$\varepsilon_j = \frac{a_R}{2\omega_j} \tag{2.2}$$

where U is the strain energy density and $\bar{\lambda}_i$ are the deviatoric principal stretches; J^{el} is the elastic volume ratio; μ_i, α_i and D_i are the model parameters that are identified from the test data [6,31]; ε_j and ω_j denote the fraction of the critical damping and the natural frequency for a given mode j, respectively, while a_R represents the mass-proportional damping factor. A fundamental mode damping ratio of 5% was assigned for both the rubber and polyurethane, which has been commonly recommended [56].

The compressibility of the tread rubber, and the polyurethane spokes and shear band is related to the Poisson's ratio [97], as:

$$\upsilon = \frac{3(K_0/\mu_0)-2}{6(K_0/\mu_0)-2} \tag{2.3}$$

where K_0 and μ_0 are the initial bulk and shear moduli, respectively, and the ratio K_0/μ_0 was chosen as 50 to obtain a Poisson's ratio (υ) of 0.49. The elastic and hyper-elastic material parameters of aluminum alloy, high strength steel, synthetic rubber, and polyurethane are summarized in Table 2.1.

Table 2.1: Elastic and hyper-elastic material models' parameters

	Density (kg/m^3)	Young's modulus (GPa)	Poisson's ratio
Aluminum alloy	2800	72	0.33
Steel	7800	210	0.29

Synthetic rubber				Polyurethane			
i	μ_i(MPa)	α_i	D_i	i	μ_i(MPa)	α_i	D_i
1	13.36	1.63	5.90E-03	1	13.55	1.51	3.54E-03
2	-6.63	1.90	0	2	-2.34	2.21	0
3	0.06	-2.46	0	3	0.09	-2.47	0

The surface-to-surface contact was defined between the tread elements (slave surface) and the road elements (master surface) to model the wheel contact with the non-deformable road. Hard contact was assigned in the normal direction to minimize possible penetration of the slave surface into the master surface, while road friction in the tangential direction was modelled using isotropic Coulomb formulation [95], considering static and dynamic coefficients of friction as 0.80 and 0.75, respectively, to represent a dry asphalt road [54]. Moreover, the tread, outer and inner rings, shear band, spokes and rim were tied together by surface-based tie constraints. Furthermore, rigid body constraints were assigned to the rim and the road with negligible deformations.

2.2.1 Elements' formulations and mesh convergence study

The one-point integration shell elements S4R were used to describe the rigid elements of the rim and the road. The fully-integrated shell elements S4, employing the Gauss quadrature scheme in the shell plane, were used to discretize the honeycomb spokes, and the outer and inner rings so as to achieve more accurate deformation responses during the transient analysis [95]. The hexahedron fully-integrated solid elements C3D8, when used for nearly-incompressible materials ($0.49 < \upsilon < 0.5$), however, demonstrate undesirable shear locking phenomenon and thus become too stiff

resulting in potential numerical instabilities [54,95]. The reduced-integration solid elements C3D8R were thus used to represent the tread and the shear band, which could yield sufficiently accurate solutions with reasonable computational efficiency even under large-deformations [54,95]. Hourglass control was implemented to suppress the possible zero energy modes of reduced-integration elements.

The 3D wheel mesh, made of equal sectors, was realized through copying and extruding the 2D cross section mesh along the lateral direction (y-axis). The ratio of the height to the length of each solid element was set to be about unity, and the element width was determined by the number of divisions along the y-axis of the wheel, as illustrated in Fig. 2.2. In order to yield convergent numerical solutions with least computational cost, mesh convergence studies were conducted to determine near optimal element sizes for each component. As an example, Fig. 2.3(a) depicts the influence of the relative mesh density of the spokes on the deflection and peak stress response of a spoke of the wheel model with 15.8° cell angle and 3000 N vertical load. This figure also presents the variations in the overall wheel deflection. The peak stress response is presented for the spoke located around the wheel center line in the vicinity of the road contact (Fig. 2.3(a)), while the deflection response describes the peak vertical displacement of the midpoint of a cell within the same spoke. Both the deflection and stress responses obtained are normalized with respect to those obtained from the model considering finest mesh of the spokes (element size = 1 mm; mesh size, n=175050), and the relative mesh density represents the fraction of the finest mesh.

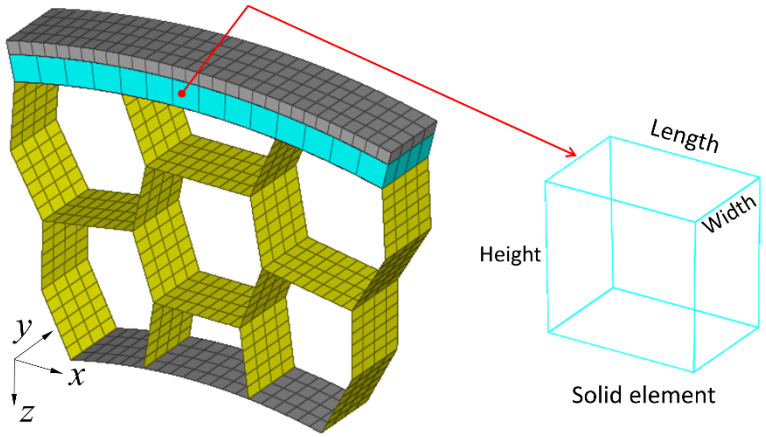

Figure 2.2: Partial 3D FE model of the honeycomb NPW (Cell angle: 15.8°)

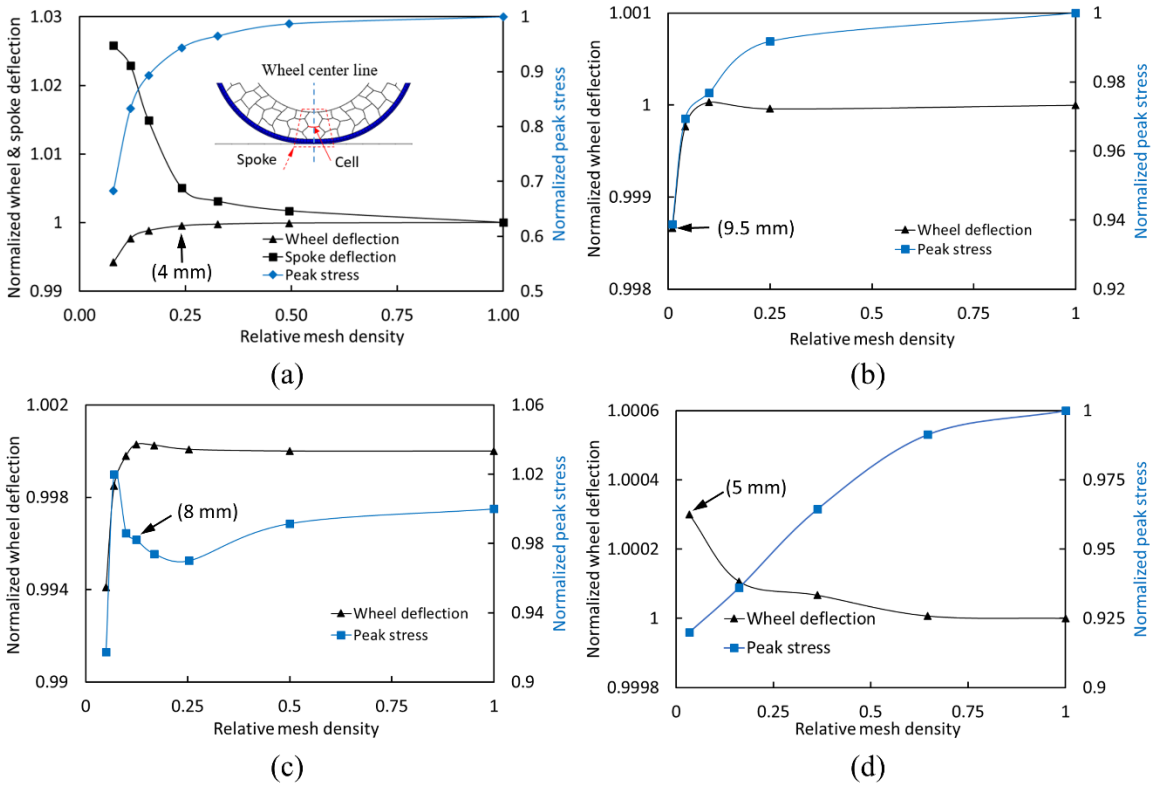

Figure 2.3: Variations in the normalized wheel/spoke deflections and component stress with different relative mesh density of the model components: (a) spokes; (b) shear band; (c) outer and inner rings; and (d) tread (Normal load: 3000 N; Cell angle: 15.8°)

The results suggest that the peak stress response is most significantly affected by the mesh size, while the deformation responses are far less sensitive to the mesh size. The 4 mm element size of the spokes was considered adequate in view of both the accuracy and the computational efficiency. Similar convergence studies were conducted to identify desirable mesh densities for the shear band, outer and inner rings, and the tread, which were identified as 9.5, 8, 8 and 5 mm, respectively, as seen in Figs. 2.3(b), 2.3(c), and 2.3(d). These element sizes were considered to yield sufficiently accurate predictions of the wheel responses, especially the wheel deflection. The desired number of divisions along the *y*-axis was identified in a similar manner through analysis of the cornering force developed by the wheel using explicit time integration technique (ABAQUS/Explicit). Fig. 2.4 illustrates the influence of relative mesh density of the wheel on the cornering force considering forward speed of 10 km/h and side-slip angle of 0.5°. On the basis of the results, a total of 30 divisions were considered adequate, which resulted in the wheel model with total number of 79290 elements and 97249 nodes. Mesh convergence studies were also conducted for the NPW models with cell angles of 31.5 and 47.1°. The results suggested that similar level of convergence could

be achieved using the same sizes of the elements. The three wheel models with cell angles of 15.8, 31.5 and 47.1° are denoted as NPW-I, NPW-II and NPW-III, respectively, hereafter. Variations in the cell angle directly affect the height and length dimensions of the cells used in each model. The cell thickness in each NPW model, however, was tuned in order to achieve identical overall wheel deflection (15.8 mm) under a 3000 N vertical load. The chosen deflection magnitude is similar to that observed for the reference pneumatic wheel, which ensures comparable equivalent vertical mode stiffness of each of the NPW design considered in the study. The cell thickness together with the means of heights and lengths of the honeycomb cells used in each wheel model are summarized in Table 2.2 (Section 2.2.2).

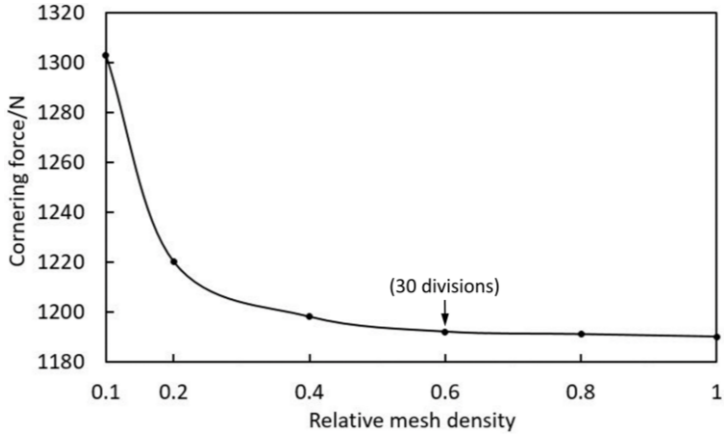

Figure 2.4: Effect of relative mesh density of the wheel model on the cornering force response at forward speed of 10 km/h and side-slip angle of 0.5° (Normal load: 3000 N; Cell angle: 15.8°)

2.2.2 In-plane properties of a honeycomb spoke

The vertical and longitudinal stiffness of a honeycomb NPW are significantly influenced by the in-plane properties of the honeycomb spokes. The mechanical properties of a honeycomb spoke in the linear region can be estimated from the cellular material theory (CMT) [5,24]. The in-plane effective elastic and shear moduli, and the effective density of a honeycomb cell, symmetric about both the axes (Fig. 2.5(a)), are directly related to its geometric and material properties [24], such that:

$$\frac{E_Z}{E} = \left(\frac{t_c}{l}\right)^3 \frac{\cos\theta}{(h/l+\sin\theta)\sin^2\theta}; \frac{E_X}{E} = \left(\frac{t_c}{l}\right)^3 \frac{(h/l+\sin\theta)}{\cos^3\theta} \tag{2.4}$$

$$\frac{G_{ZX}}{E} = \left(\frac{t_c}{l}\right)^3 \frac{(h/l+\sin\theta)}{(h/l)^2\,(1+2h/l)\cos\theta}; \frac{\rho^*}{\rho} = \frac{(t_c/l)(h/l+2)}{2\cos\theta(h/l+\sin\theta)} \tag{2.5}$$

where E_Z and E_X are the effective elastic moduli in the radial and circumferential directions, respectively; G_{ZX} is the effective shear modulus; and ρ^* is the effective density. E and ρ are Young's modulus and density of the constituent material, respectively; The subscripts 'Z' and 'X' denote the axes, as shown in Fig. 2.5(a), and θ, h, l and t_c are the cell angle, height, length and wall thickness, respectively.

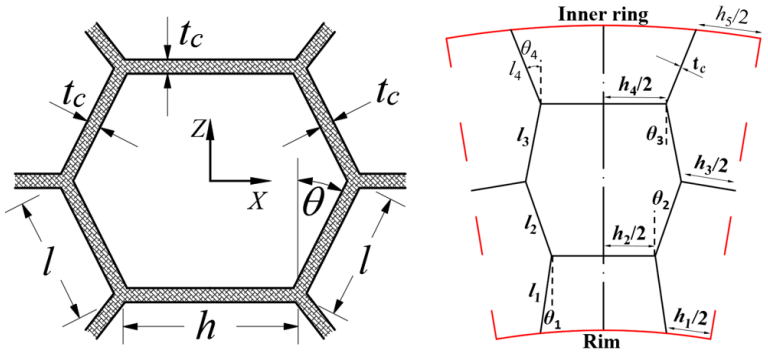

(a) (b)

Figure 2.5: Geometric parameters of a: (a) symmetric honeycomb cell; and (b) honeycomb spoke of a NPW (θ=15.8°)

The honeycomb spoke positioned between the rim and the inner ring in a NPW design (Fig. 2.5(b)) represent a modification of the symmetric honeycomb cells considered in the CMT. The properties of the modified honeycomb cell can also be estimated by considering regular cell dimensions (h, l and θ) as means of h_i, l_i and θ_i, respectively [6,31], as shown in Fig. 2.5(b). Table 2.2 summarizes the mean dimensions together with the wall thickness of the honeycomb cells used in the three models considered in the study. Table 2.2 also presents the in-plane effective elastic and shear moduli, and the effective density of the honeycomb cells normalized with respect to the nominal material properties.

Table 2.2: Dimensions, and in-plane moduli and density of honeycomb cells employed in three NPW models

Model	θ (degree)	l (mm)	h (mm)	t_c (mm)	E_Z/E	E_X/E	G_{ZX}/E	ρ^*/ρ
NPW-I	15.8	24.91	35.23	1.54	0.00198	0.00044	0.00005	0.0652
NPW-II	31.5	28.33	26.79	2.38	0.00123	0.00142	0.00040	0.0989
NPW-III	47.1	35.51	16.13	2.82	0.00053	0.00190	0.00223	0.1208

The results suggest that an increase in the mean cell angle will yield relatively higher effective density, and E_X and G_{ZX} but lower E_Z. The mass and the longitudinal stiffness in the linear elasticity ranges of the NPW-II and NPW-III designs are thus expected to be greater than those of the NPW-I design. The vertical stiffness of the NPW-II and NPW-III designs in the linear region, however, is expected to be relatively lower than that of the NPW-I, although the three designs exhibit identical load carrying capacity.

2.2.3 Modelling of a pneumatic wheel

A three-dimensional FE model of the reference pneumatic wheel (205/55R16), as shown in Fig. 2.6, was also developed and analysed for relative performance analyses of the honeycomb NPWs. The tire model reported in the reference [96] was adapted and its validity was verified on the basis of the reported measured properties in terms of the vertical force-deflection and cornering force characteristics. Briefly, the model comprised the rubber tread, under-tread layer, belts with steel cords, inner-liner, sidewall, apex, abrasion gum, beads and the carcass with high modulus fibre cords. The hyper-elastic rubber components were modelled using strain energy potential associated with the Neo-Hookean material model, while the reinforcements were described by the linear elastic material models. The material model parameters are summarized in Table 2.3, which were identified from the measured stress-strain characteristics. The rubber-cord composites were described as rebars in shell elements (S4R), while the reduced-integration solid elements C3D8R and C3D6 were used to discretize all the other components. Reduced-integration shell elements were also employed to describe the rigid elements of the rim and the road. The model also employed contact model and contact properties identical to those used for the NPW models. Furthermore, the tread mesh was refined so as to accurately model large deformations of the tire within the contact region, as shown in Fig. 2.6.

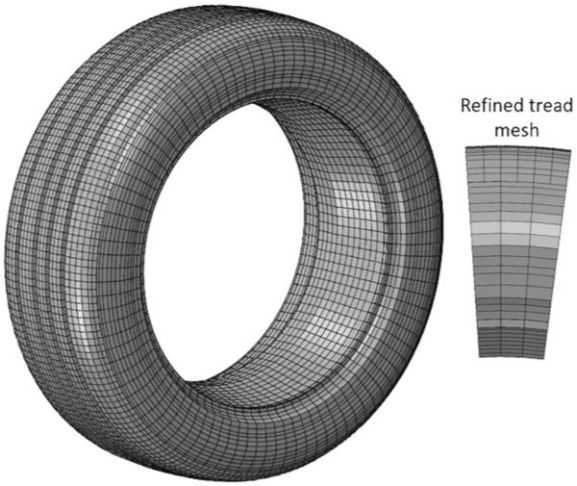

Figure 2.6: FE model of the reference pneumatic wheel

Table 2.3: Elastic and hyper-elastic material models' parameters

Reinforcements			Young's modulus, E (MPa)	Poisson's ratio, υ	
Carcass			3300	0.4	
Belt			84000	0.4	
Rubber components	C_{10} (MPa)	D_1	Rubber components	C_{10} (MPa)	D_1
Tread	0.67	2.98E-02	Apex	0.72	2.77E-02
Inner liner	0.50	3.98E-02	Sidewall	0.34	5.95E-02
Under tread	0.84	2.38E-02	Abrasion gum	1.01	1.99E-02

C_{10} and D_1 describe shear behaviour and compressibility of hyper-elastic materials, respectively

2.2.4 Methods of analyses

Each NPW model was analysed using FE methods to derive the in-plane and out-of-plane properties of the stationary wheel in terms of multi-axis (x-, y- and z-axis, and rotation about z-axis) stiffness, spokes' forces and deformations, and contact pressure distribution, and cornering and self-aligning properties of the rolling wheel. The analysis methods are similar to those reported for the pneumatic wheel, with the exception of the inflation process used for the pneumatic wheel [65]. The multi-axis stiffness was obtained from the iterative solutions using the Newton-Raphson method [4,65]. The contact of the wheel with the road was established by prescribing a small initial displacement of the rim centre, as opposed to a prescribed load, so as to avoid potential convergence difficulties resulting from the possible unbalance force [65]. Subsequently, the rim centre was subjected to a gradually increasing normal load in a ramp-step manner until the resultant contact force approached the desired normal wheel load. The resulting responses were used to obtain the vertical stiffness, spokes' forces and deformations and contact pressure distribution.

Different vertical loads up to 4000 N were considered for relative properties analyses. The road was subsequently displaced in the lateral or longitudinal directions or rotated about the z-axis so as to obtain the horizontal force-deflection and yaw plane moment-deflection characteristics of the wheel.

The cornering and self-aligning characteristics of the NPW models were obtained from the transient dynamic analysis using the explicit time integration technique [95]. The simulations were initiated by imposing a desired vertical load on the wheel center in a ramp-step manner. Following the stabilization of the loaded wheel, a defined level of side-slip was induced by applying the road speed at a predefined angle, with respect to the wheel heading direction, while the rim was permitted to rotate about its axis [54]. The orientation of the road speed was varied to realize side-slip angles up to 5°, while the magnitude of the road forward speed was held as 10 km/h.

2.3 Results and discussions

2.3.1 Model verification

The validity of the FE models of the honeycomb NPW in this study was examined by comparing the predicted vertical wheel deflection and spokes' peak stress responses with those of the wheel models reported in the reference [6] for identical loading conditions, and comparable spokes' configurations and wheel dimensions. The NPW models were analysed to determine their vertical wheel deflection and peak stress developed in the honeycomb spoke located in the vicinity of wheel/road contact, as shown in Fig. 2.3(a), considering different vertical loads in the 2000 to 4000 N range. As an example, Table 2.4 presents comparisons of the resulting responses of the NPW-I model (θ=15.8°) with those reported in the reference [6]. The comparisons show reasonably good agreements between them for the loading conditions considered. The maximum differences between the model-predicted and reported peak stress and wheel deflection responses were in the order of 3.4% and 5.6%, respectively, in the entire load range considered. Comparable levels of peak stresses in the spokes were also found in the reference [31], which further established the validity of the FE NPW models developed in this study.

Table 2.4: Comparisons of wheel deflection and spoke' peak stress responses of the NPW-I model with those reported in the reference [6]

Load (N)	NPW-I (Diameter×width: 632×205 mm)		Jin et al.[6] (Diameter×width: 664×215 mm)	
	Deflection (mm)	Peak stress (MPa)	Deflection (mm)	Peak stress (MPa)
2000	10.41	2.08	10.01	2.09
3000	15.80	2.75	15.06	2.66
4000	21.21	3.36	20.09	3.30

The validity of the FE model formulated for the reference pneumatic wheel was also examined by comparing the model responses with the measured data reported in the reference [96] in terms of vertical load-deflection and cornering force characteristics. The tire model was analyzed under conditions used during the reported measurements in the reference [96], namely, 240 kPa inflation pressure and 4000 N vertical load. The cornering force responses were obtained at 10 km/h forward speed for side-slip angles up to 5°. The model results showed reasonably good agreements with the measured load-deflection and cornering force characteristics, as seen in Fig. 2.7. While the peak deviation in the model-predicted and measured force-deflection responses is in the order of 3.3%, relatively good agreement is also observed in the cornering force for small slip angles up to 2°. Notable deviations, however, are evident under slip angles above 3°. Moreover, the model response revealed saturation of the cornering force at a relatively lower slip angle (≈ 3°) than that observed from the measurements (≈ 4°). Such deviations are likely due to the simplified tread model and underestimated dynamic friction coefficient used in the simulations, although a number of studies using the explicit time integration technique have also reported similar trends [54,55].

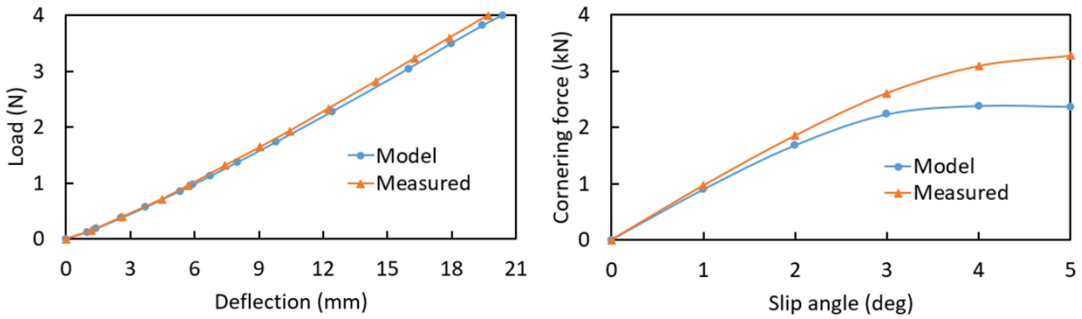

Figure 2.7: Comparisons of: (a) load-deflection; and (b) cornering force responses of the reference pneumatic wheel model with the measured data

The verified FE models of the NPWs were subsequently analyzed to evaluate their multi-axis stiffness and cornering properties in relation to those of the reference pneumatic wheel.

Simulations were also performed to study dependence of NPW's properties on the spokes' cell angle and the normal wheel load. The results are also discussed in view of the spokes' forces and deformations, and the localized contact pressure peaks.

2.3.2 Multi-axis stiffness analyses

Influence of spokes' cell angle on the multi-axis stiffness of NPWs

The NPW models were analysed to determine their multi-axis stiffness characteristics, as shown in Fig. 2.8. The vertical force-deflection characteristics were evaluated considering normal load in the 0 to 3000 N range. The longitudinal and lateral force responses were obtained considering respective deflections up to 8 mm and 6.4 mm. The wheel moment in the yaw-plane was also evaluated under gradually increasing yaw deformation until a saturation of the moment was observed. The three NPW models exhibit comparable and nearly linear vertical force-deflection responses, as seen in Fig. 2.8(a). The results also show some nonlinearity, which is more evident with increasing cell angle as in NPW-II and NPW-III models. This is also partly caused by differences in other cell dimensions, especially the cell thickness. Moreover, all the models showed relatively higher equivalent stiffness under light loads up to about 800 N. The equivalent vertical stiffness decreased slightly with further increase in the load. This is due to the initial high resistance of the spokes to compression and bending deformations, and subsequent easier buckling [31]. Furthermore, the NPW-I model with lower cell angle revealed relatively higher stiffness (238 N/mm) in the vicinity of zero wheel deflection, when compared to those of the NPW-II and NPW-III models (231 and 224 N/mm, respectively). This is consistent with the trend observed in the effective elastic modulus in the radial direction E_Z, predicted by the CMT (Eq. (2.4)), which decreases with increase in the cell angle (Table 2.2). It should be noted that the three NPW models were tuned to yield nearly identical equivalent stiffness under the 3000 N vertical load.

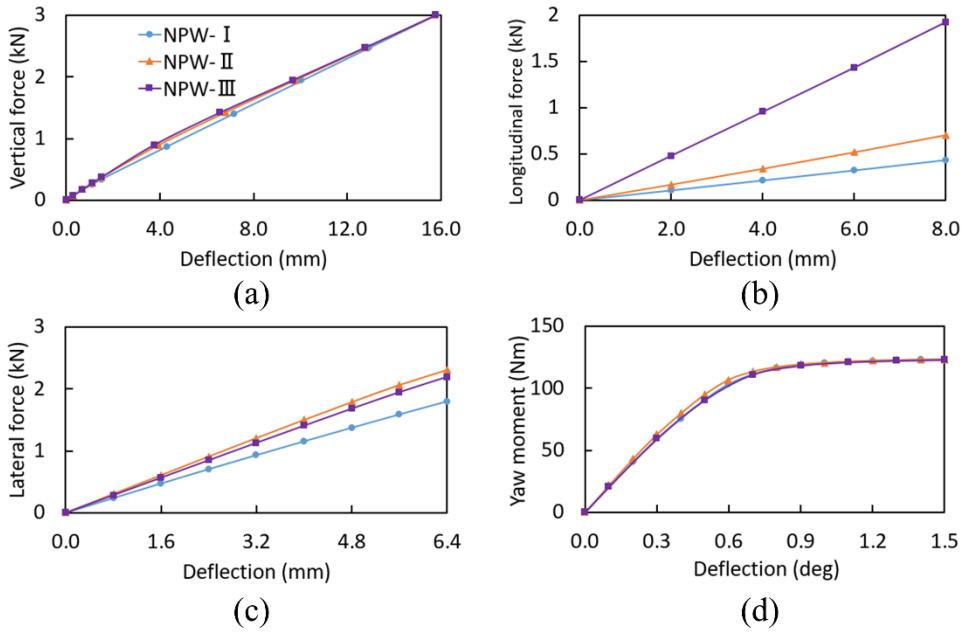

Figure 2.8: Multi-axis force/moment-deflection characteristics of NPW models: (a) vertical; (b) longitudinal; (c) lateral; and (d) yaw

The longitudinal and lateral force responses of the wheels increase nearly linearly with the respective wheel deflection, as seen in Figs. 2.8(b) and 2.8(c). Increasing the cell angle yields substantially higher longitudinal force response and thus the stiffness of the wheel. This is attributable to the increases in G_{ZX} and E_X with increasing cell angle, as observed in Eqs. (2.4) and (2.5), and Table 2.2. The magnitude of the lateral force of the wheel also increases with increase in the cell angle from 15.8 to 31.5°. A further increase in the cell angle to 47.1°, however, resulted in slight reduction in the force in nearly entire range of deflection. This is likely due to nonlinear effect of the cell angle on the out-of-plane shear property of the wheel, considering that the three wheel models differ only in the spokes' configuration (cell angle).

The yaw moment-deflection responses of the NPW models show nearly linear variations up to about 0.3° yaw rotation and yaw moment saturation under deformations exceeding 0.6°. Moreover, the yaw moment of the wheel exhibits negligible influence of the spokes' cell angle. Under yaw deformations, the spokes, outer and inner rings, shear band and the tread undergo longitudinal as well as lateral deformations. The resulting forces along the lateral and longitudinal directions contribute to the yaw moment developed by the wheel. The contribution of the lateral force to the resultant yaw moment, however, is greater than that of the longitudinal force due to higher lateral stiffness and lateral deformation of the wheel, and the higher moment arm. The comparable lateral elasticities of the three NPW designs also lead to negligible effect of the spokes'

configuration on the yaw stiffness. The yaw moment-deflection characteristics also show yaw moment saturation near 120 Nm, irrespective of the cell angle, which is attributed to the road adhesion limit.

Comparisons of multi-axis stiffness of the NPWs and the reference pneumatic wheel

The reference pneumatic wheel model was also analysed to determine its multi-axis force/moment-deflection characteristics considering identical normal loads and wheel deformations. The force-deflection data were used to estimate equivalent linear stiffness of the NPWs and the reference pneumatic wheel along the longitudinal, lateral, vertical and yaw axis. The yaw stiffness values of the NPWs and the pneumatic wheel were obtained from the slope of the moment-deflection curve under a low angular deformation up to 0.2°. The estimated stiffness characteristics of the three NPWs are compared with those of the reference pneumatic wheel model in Fig. 2.9 for a normal wheel load of 3000 N. The vertical stiffness of the NPWs is identical to that of the pneumatic wheel, as it would be expected. The longitudinal stiffness of the nominal NPW (NPW-I) is substantially lower than that of the pneumatic wheel. The results also suggest that NPW design can be modified to achieve longitudinal stiffness comparable to that of the pneumatic wheel. This is clearly evident for the wheel with spokes with higher cell angle (NPW-III). The lateral and yaw stiffness of the NPW designs, however, are substantially higher than those the pneumatic wheel, irrespective of the spokes' configuration considered. The results suggest that the NPW design with planar honeycomb spokes exhibits high out-of-plane stiffness, and is likely to cause lateral slippage under lateral or yaw perturbations. The non-planar honeycomb spokes with relatively lower out-of-plane stiffness may thus be explored to achieve lower lateral and yaw stiffness of the wheel. The shear ring and the tread geometries and properties are also expected to be important design factors affecting the out-of-plane properties of honeycomb NPWs.

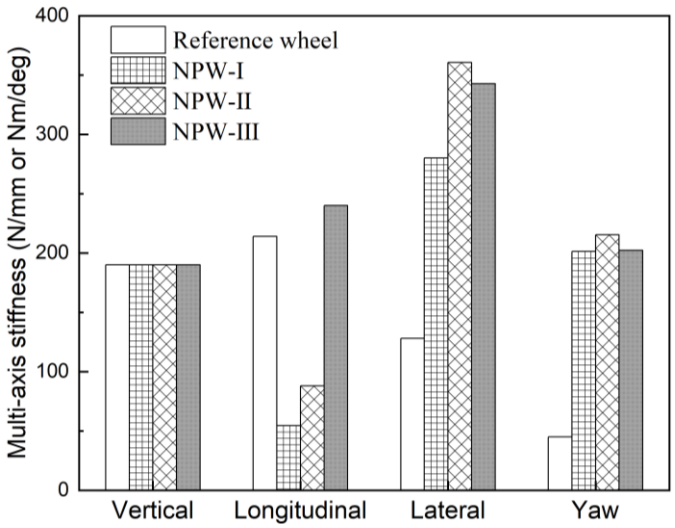

Figure 2.9: Comparisons of linear equivalent multi-axis stiffness characteristics of the NPWs with those of the reference pneumatic wheel

Influence of normal wheel load on multi-axis stiffness of the NPWs

The longitudinal/lateral and yaw stiffness characteristics of the wheel are also dependent on the normal wheel load. The NPW models were thus analyzed to evaluate the influence of the wheel load on the horizontal and yaw plane force/moment-deflection characteristics, by varying the wheel load in the 2000 to 4000 N range. As an example, Fig. 2.10 illustrates the normal load dependence of the force/moment-deflection characteristics of NPW-I under relatively large deformation magnitudes. The results show gradual increase in the longitudinal/lateral force with increasing deflection and force saturation as it approaches the road surface friction limit. The longitudinal stiffness tends to be higher under the higher wheel load, which can be attributed to the hardening tendency of the spokes with increasing deflection, as observed in Fig. 2.10(a). This is also due to strong coupling between the radial and longitudinal deformations of the spokes. The lateral stiffness of the wheel, however, is nearly load-independent suggesting that out-of-plane behavior of the wheel is not affected by the radial load applied to the spokes. This is attributable to negligible coupling between the radial and lateral deformations of the in-plane spokes. Moreover, the lateral force developed by the wheel is dominated by the spokes' deformations compared to those of the tread and the shear ring (shear band and outer and inner rings). Unlike the NPW designs, the pneumatic wheels invariably exhibit higher longitudinal and lateral stiffness under a higher normal load [53].

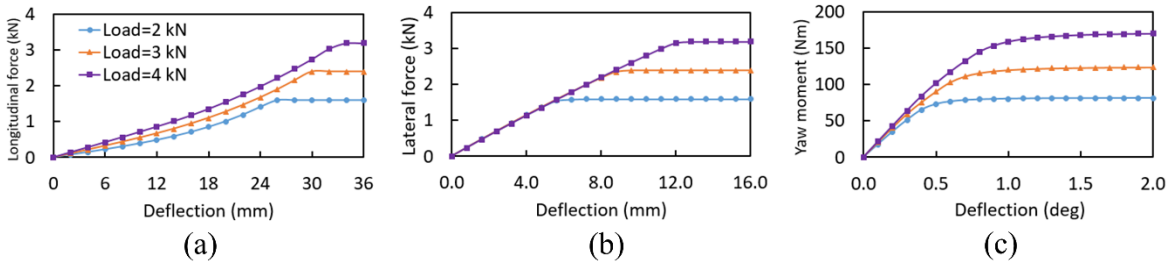

Figure 2.10: Influence of normal wheel load on force/moment-deflection characteristics of NPW-I: (a) longitudinal; (b) lateral; and (c) yaw

An increase in the normal load yields only slightly higher yaw moment in the linear range of deflection (<0.3°). This is due to relatively greater contribution of the wheel lateral force to the yaw moment, which is not affected by the wheel load, as seen in Fig. 2.10(b). The yaw moment developed by the wheel also approaches saturation under higher deformations as it is observed for both the horizontal forces. Saturation moment, however, is strongly dependent on the normal load, which is related to the wheel-road adhesion limit.

2.3.3 Spokes' forces and deformations

The NPW models were analysed to determine spokes' deformations and the resulting force distribution so as to gain an insight into the load-carrying mechanism of the wheel. For this purpose, the ends of the spokes connected to the shear ring were labelled in a sequential manner starting with the end of the spoke located near the wheel center line in the contact region in a counter-clockwise direction, as shown in Fig. 2.11. Owing to the geometric symmetry of the non-rolling wheel, the figure shows ends of the consecutive spokes within one-half of the wheel, which were labeled as '3', '5',…, '37'. The even-numbered labels were used to identify ends of the spokes connected to the shear ring within the other half of the wheel. The nodal forces developed in the elements representing individual spokes of the NPW-I model are extracted and indicated in the figure via the arrowheads in red, considering a vertical load of 3000 N. The results showed that only four of the spokes near the contact region undergo compression loads, while the remaining spokes remain in tension. Moreover, the tension forces are substantially higher than the compression forces, as it is evident from the enlarged illustration of the spokes near the contact region. The normal wheel load applied to the rim center is thus predominantly supported by the honeycomb spokes in tension.

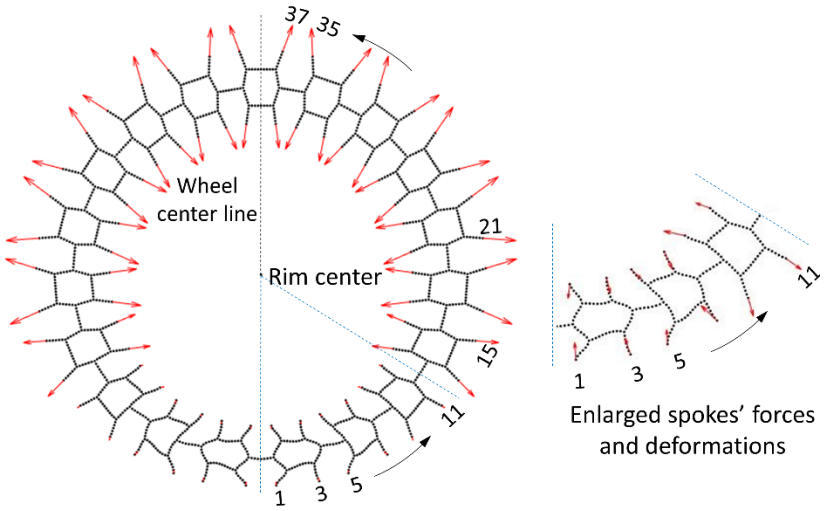

Figure 2.11: The distribution of nodal forces developed by the individual spokes' elements of the NPW-I model subject to 3000 N vertical load (left), and enlarged view of spokes near the contact region

Fig. 2.12(a) illustrates the distribution of the vertical components of the nodal forces (NFORC in ABAQUS) associated with elements representing the spokes along the wheel width. The figure also indicates the labels of the nodes of the spokes' elements. The results show that the nodal forces developed at the spokes' ends, labeled '9', '11', '13', '15', '17' and '21', yield negative vertical force components (downward). The vertical force components of the nodal forces on the ends of the remaining spokes are positive, and responsible for supporting the normal wheel load. The summation of the vertical components of nodal forces within half of the wheel was found to equal exactly 50% of the normal load (1500 N).

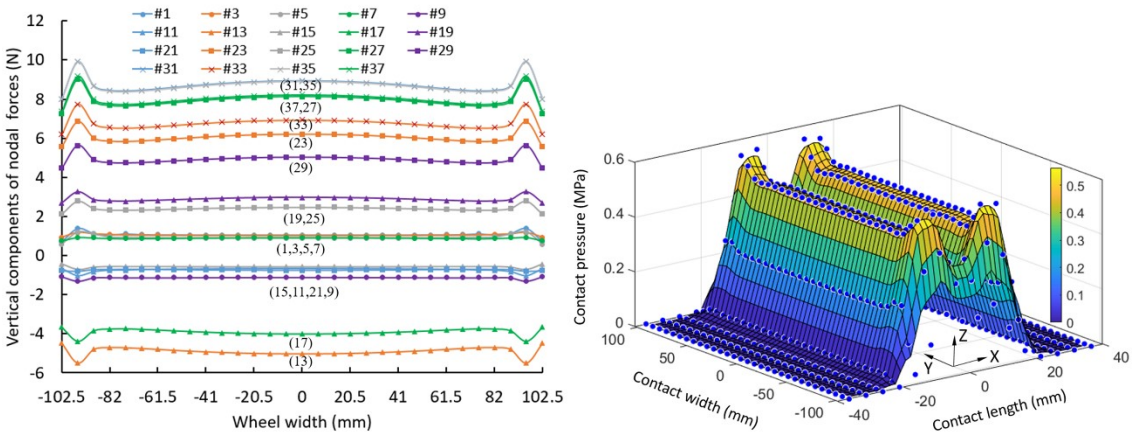

Figure 2.12: Distribution of: (a) vertical components of the nodal forces of the spokes' elements within one-half of the NPW-I; and (b) wheel-road contact pressure (Vertical load = 3000 N)

The results also showed that the peak vertical force components of the nodal forces occurred in the spokes in the shoulders region of the NPW-I. This is evident from the distribution of the wheel-road contact pressure (Fig. 2.12(b)), which is also generally observed for the pneumatic wheels. The results show symmetric contact pressure distribution about the wheel center lines along the contact length (*x*-*z* plane) and width (*y*-*z* plane) directions. The distribution shows localized pressure peaks in the *x*-*z* plane, which is caused by the non-uniformity of the nodal forces shown in Fig. 2.11. Similar distributions of the spokes' forces and deformations, and the contact pressure were also observed for the NPW-II and NPW-III models. Fig. 2.13 illustrates the dimensions of the contact patch of the NPW-I and the reference pneumatic wheel together with the contact pressure distribution in the *x*-*y* plane. The contact characteristics of the NPW-I are notably different from those of the reference pneumatic wheel (Fig. 2.13(b)), especially with regard to the localized pressure peaks in the *x*-*z* plane, which has also been reported in the references [31,33].

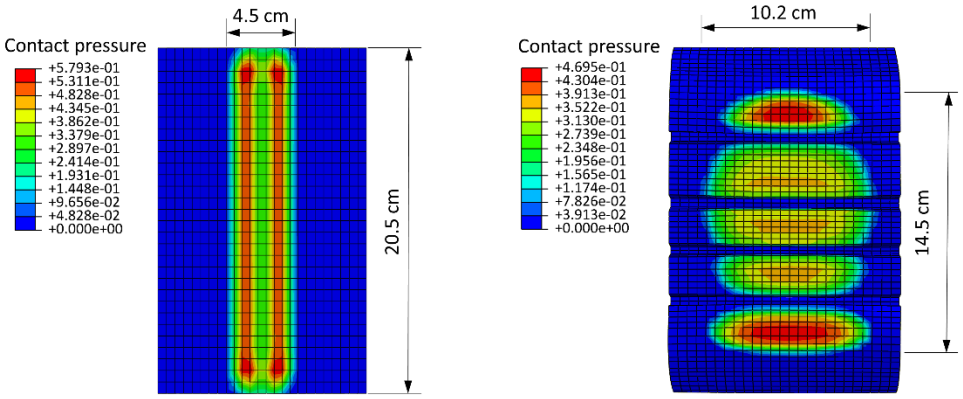

(a) (b)

Figure 2.13: Contact properties of: (a) NPW-I model; and (b) reference pneumatic wheel (Normal load: 3000 N)

2.3.4 Transient analyses of cornering properties

Comparison of cornering properties of the NPWs and the reference pneumatic wheel

The NPW models were further analysed to evaluate their out-of-plane responses in terms of the cornering force and self-aligning moment characteristics using ABAQUS/Explicit. Each wheel model was subjected to a normal load of 3000 N, and permitted to roll by introducing a constant forward velocity of the road. A constant lateral velocity was also applied to the road surface to achieve the desired side-slip angle of the wheel. The simulations were performed to evaluate cornering force and self-aligning moment responses of the NPWs at two different constant forward

speeds (10 and 50 km/h) and side-slip angles up to 5°. The results suggested relatively low sensitivity of the cornering properties of the NPWs on the forward speed, as it has been reported for pneumatic tires [54]. As an example, Fig. 2.14(a) depicts variation in the cornering force and self-aligning moment responses of the NPW-I model under forward speeds of 10 and 50 km/h. The cornering force and self-aligning moment responses of the reference pneumatic wheel were also obtained using the transient analysis considering identical operating conditions, as seen in Fig. 2.14(b). The cornering force developed by the NPW-I increases nearly linearly with the side-slip angle at relatively low slip angles up to about 0.5°, which is mostly attributed to elastic deformation of the tread in the lateral direction. The shear band also undergoes slight lateral deformation, while the out-of-plane deformations of the honeycomb spokes were observed to be very small under such low side-slip angles. A further increase in the slip angle caused bending of the spokes in the lateral plane, although it caused partial sliding of the wheel tread (trailing part) on the rigid road surface. The cornering force thus increases at a lower rate due to relatively lower adhesion of the wheel within the contact region. The cornering force approaches a peak value at a slip angle of about 1.1°. With further increase in the slip angle, the wheel begins to slide laterally.

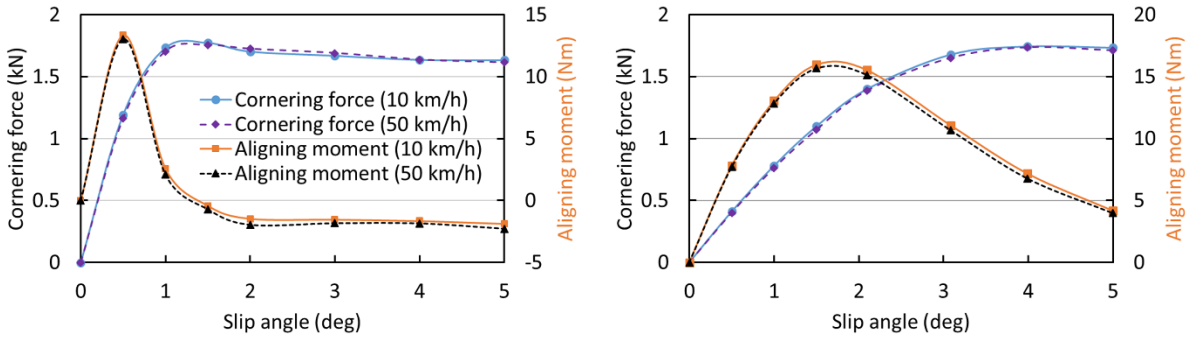

Figure 2.14: Cornering force and self-aligning moment characteristics of: (a) the NPW-I; and (b) the reference pneumatic wheel (Forward speeds = 10 and 50 km/h; Normal load: 3000 N)

The cornering force developed by the reference pneumatic wheel also increased nearly linearly with the slip angle up to about 1.5°. This linear range is substantially higher, when compared to that of NPW-I model (≈0.5°). The cornering force of the pneumatic wheel approached its peak value near 3.5° side-slip angle, which is also considerably higher than that observed for the NPW-I model (≈1.1°). The results thus further confirm that the out-of-plane stiffness of the NPW design with planar honeycomb spokes is substantially higher than that of the pneumatic wheel. High out-

of-plane stiffness of the NPW contributes to considerably higher cornering stiffness of the wheel. The NPW design may thus yield better directional control of vehicles under extremely small slip angles up to about 1.1°, when compared to the pneumatic tyred vehicle. The rapid saturation of the cornering force of the NPW, however, can lead to sliding vehicle and loss of control under medium as well as higher side slip conditions.

The self-aligning moment due to NPW also increases with increasing slip angle and approaches its peak value at a slip angle of about 0.5°. It decreases rapidly with further increase in the slip angle up to about 1.5°. This is due to sliding of the trailing part of the wheel tread, which results in shift in the resultant cornering force towards the wheel center leading to reduced trail of the wheel. The results also show that the self-aligning moment approaches a negative value at slip angles above 1.35°. This suggests that a NPW may resist restoring of the steered wheel after negotiating a turn, when the slip angle exceeds 1.35°. Negative value of the self-aligning moment has also been reported for a passenger car tire at slip angles exceeding 8° [55].

The reference pneumatic wheel, on the other hand, revealed peak aligning moment near 1.5° side-slip angle. The simulation results revealed maximum trail of the NPW-I model of about 1.1 cm, which occurred near 0.5° side-slip angle, while that of the reference pneumatic wheel was about 1.9 cm that also occurred at a slip angle of 0.5°. The lower trail of the NPW is also attributable to its relatively smaller contact patch length, shown in Fig. 2.12(b) and Fig. 2.13(a), compared to that of the pneumatic wheel. The contact patch length of the NPW model under the given load was observed to be about 45% of that of the reference pneumatic wheel (10.2 cm). The NPW, however, yields considerably higher width of the contact patch (20.5 cm), when compared to that of the pneumatic wheel (14.5 cm). The effective contact area of the non-rolling wheel under 3000 N load was thus observed to be nearly 73% of that of the pneumatic wheel, as illustrated in Fig. 2.13. Both the lower contact patch length and area together with high out-of-plane stiffness of the NPW contribute to its higher cornering stiffness, rapid saturation of the cornering force and reduced trail and thus the self-aligning moment at slip angles exceeding 1°.

Influence of wheel load and spokes' cell angle on cornering properties of NPWs

The cornering force and self-aligning moment characteristics of the NPW models are also dependent on the normal wheel load. Furthermore, the variations in the cell angle of the spokes may also influence the cornering properties. The load dependence of the cornering properties was thus investigated for the three spokes' configurations considering wheel load variations in the 2000

to 4000 N range. Fig. 2.15 illustrates variations in the cornering force (left-column) and self-aligning moment (right-column) of the NPWs in the 0 to 5° side-slip angle range considering different wheel loads. Owing to relatively small effect of the speed, the results are limited to the lower forward velocity of 10 km/h. It should be noted that the honeycomb spoke of the rolling NPW-III tends to collapse in the vicinity of the center of the contact patch under the 4000 N wheel load. The excessive deformations of the spokes in the contact region can be observed in Fig. 2.15(c), which is partly attributed to its relatively lower vertical stiffness during rolling. This may cause considerable oscillations in the cornering force and self-aligning moment responses of the honeycomb NPW. The simulations for the NPW-III model were thus limited to only two different normal loads, namely, 2000 and 3000 N.

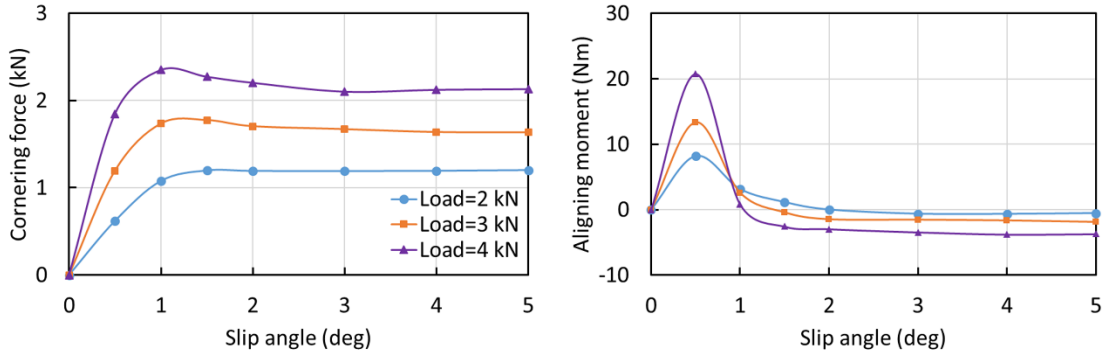

(a)

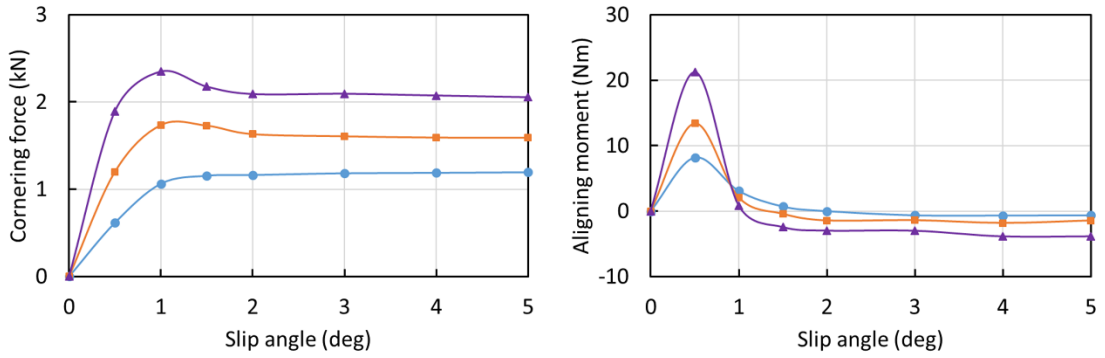

(b)

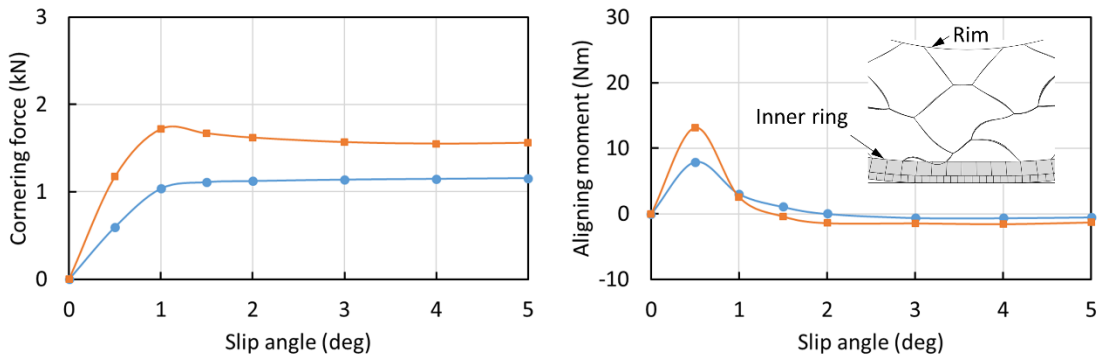

(c)

Figure 2.15: Influence of wheel load on the cornering force (left-column) and self-aligning moment (right-column) characteristics of NPWs: (a) NPW-I; (b) NPW-II; (c) NPW-III (Forward speed = 10 km/h)

The results show comparable cornering and self-aligning characteristics of the three NPW models considering identical normal loads. This suggest minimal effect of the spokes' configuration on the cornering properties of the wheel, and further confirms only minor influence of the spokes' configuration on the out-of-plane properties of the wheels. The cornering stiffness of the wheel, however, increases considerably with increasing normal load, irrespective of the spokes' configuration. The cornering stiffness of the wheels are also summarized in Table 2.5 for different wheel loads considered in the study. Higher cornering stiffness with increasing wheel load is attributable to relatively higher contact area of the wheel and its adhesion with the road, and greater deformations of the spokes in the longitudinal as well lateral planes, which also contribute to higher self-aligning stiffness of the wheel. The wheels under the lower load of 2000 N revealed relatively smoother transition towards saturation in the 1 to 1.5° side-slip range, when compared to that observed for the higher loads. This can be partly attributed to the fact that the cornering force developed is mostly due to deformations of the tread block and the shear ring, when the spokes are lightly loaded. Moreover, the stronger tire-ground adhesion encountered under a higher wheel load can cause non-smooth transition towards sliding. Moreover, increase in the normal load yields cornering force saturation at a higher level, which can be directly related to the road friction limit. The self-aligning moment of the wheels also exhibit similar load dependency, while negative self-aligning moments are evident at slip angles in excess of about 1.5°, irrespective of the normal load.

Table 2.5: Cornering stiffness of NPWs under different normal loads

Load (N)	Cornering stiffness (N/deg)		
	NPW-I	NPW-II	NPW-III
2000	1240	1235	1195
3000	2386	2402	2344
4000	3694	3786	N/A

2.4 Conclusions

1. The distribution of the nodal forces in the spokes showed that the normal wheel load is mainly supported by the spokes in tension. The non-uniform nodal forces of the spokes, however, lead to localized pressure peaks along the contact length direction.
2. The longitudinal stiffness of the baseline honeycomb NPW was considerably lower than that of the pneumatic wheel, while its lateral stiffness was substantially higher. Increasing the cell angle resulted in higher longitudinal stiffness, while the effect on lateral and yaw stiffness was relatively small.
3. It is shown that the spokes design could be easily tuned to achieve longitudinal and vertical stiffness similar to the pneumatic wheel due to strong coupling between them. The lateral stiffness of the in-plane honeycomb spokes, however, was significantly higher, which contributed to substantially higher cornering stiffness and rapid saturation of the cornering force at a low slip angle in the order of 1.1°, irrespective of the spokes' configuration and the normal load. The NPWs are thus likely to yield superior vehicle handling under relatively lower lateral accelerations and low side-slip angles up to 1.1°. The rapid saturation of the cornering force, however, can lead to inferior handling and directional control under slip angles above 1.1°. The laterally stiff wheels also resulted in opposing self-aligning moment of under slip angles above about 1.5 °, which may hinder self-restoration of the steered wheels. It is further concluded that the feasibility of the NPWs may be enhanced by lowering its out-of-plane stiffness through design of non-planar spokes.

Chapter 3

Multi-axis stiffness and road contact characteristics of honeycomb wheels: A parametric analysis using Taguchi method

3.1 Introduction

The dynamic performance of a ground vehicle is predominantly influenced by interactions of the tires with the terrain. The pneumatic tires' designs have evolved to satisfy multiple and conflicting performance demands such as transfer of tractive forces with minimal energy losses, ease of handling and directional control, ride comfort and road holding. The pneumatic tires, however, are known to exhibit many limitations. The road safety risk associated with tire bursting or severe leakage leading to potential loss of vehicle control constitutes the foremost limitation [1]. Other limitations of the pneumatic tires concern the complex manufacturing process and routine inflation pressure maintenance, apart from the considerable environmental risks and fire hazards associated with discarded or stored tires.

The airless wheels, developed for NASA's Lunar Rover, have stimulated concerted efforts in non-pneumatic wheels (NPWs) for general vehicular applications. In the last two decades, a number of NPW designs have evolved, which generally replaced pressurized air in the pneumatic tires by honeycomb spokes [6] or radial flexible spokes [1,4]. Similar to the pneumatic tires, these NPWs exhibit lower vertical stiffness, mean contact pressure and energy dissipation, while ensuring relatively higher load-carrying capacity [1]. These wheels can also eliminate inflation pressure-induced risks and maintenance observed in the pneumatic tires. Moreover, some components of such wheels are made of thermoplastic polyurethane with low hysteresis loss. These components could be manufactured in a simpler process without vulcanization, e.g., moulding, and thus are potentially more environmentally friendly and energy-efficient [7,25].

The majority of the reported studies on NPWs for vehicular applications have focused on Tweels [17,98], mechano-elastic (ME) wheels [10,12], and honeycomb wheels [6]. The analyses on the static and dynamic properties of honeycomb NPWs with hexagonal lattice spokes have been reported in a few studies using the FE methods. When designing honeycomb wheels with same cell-wall thickness, increasing the cell angle resulted in relatively lower vertical stiffness [6]. For

honeycomb NPW designs with same vertical stiffness, increasing the cell angle, however, necessitated greater cell-wall thickness and thus a higher wheel mass [5,6]. Kim and Zhang [18,31,33] investigated the contact pressure distribution of honeycomb NPW designs with reference to that of a pneumatic tire. Nearly rectangular contact patch was observed for honeycomb wheels due to their high out-of-plane stiffness. Jin et al. [6] also studied the dynamic properties of a rolling honeycomb wheel in terms of the rolling resistance, tread stress, and spokes' stresses and deformations. The wheel with a smaller cell angle yielded lower rolling resistance, which was attributed to its relatively lower spokes' deformation and mass. Lee et al. [13] investigated the modal properties of a non-contacting honeycomb NPW and the influence of discrete spokes on wheel's steady state vibration characteristics. The results reported localized vibration resulting from the non-homogeneous mass distribution associated with the discrete spokes. A number of studies also investigated the honeycomb wheels with auxetic spokes (negative cell angle). For a given cell-wall thickness, these wheels showed lower vertical stiffness than their regular counterparts with identical but positive cell angle. For a given target vertical stiffness, these wheels, however, exhibited relatively higher mass and thus the rolling resistance [5]. Yoo et al. [7] investigated the contribution of each component of a honeycomb NPW with auxetic spokes to the hysteresis loss and the wheel's temperature distribution using a thermo-mechanical FE model. The study concluded that the shear band accounts for nearly 72% of the gross energy loss. Lee et al. [13,14] studied the modal properties of a loaded non-rolling honeycomb NPW with auxetic spokes and observed the first vertical vibration mode near 23 Hz, which was considered inadequate in view of ride comfort performance of a road vehicle.

The pneumatic tires in ground vehicles serve as the core element to absorb impacts and road surface irregularities, and produce contact forces and moments to support the vehicle weight, and propulsion and manoeuvring. These functions are significantly influenced by the dynamic viscoelastic properties of the rolling tires. For example, the cornering stiffness is a determining parameter for the handling and direction stability performance of road vehicles, while vehicle ride characteristics are strongly influenced by the tires' rolling dynamic vertical stiffness [99]. The dynamic stiffness characteristics are closely related to the static stiffness properties, which represent the most fundamental characteristics of the pneumatic tires [39]. While considerable data are available on multi-axis stiffness characteristics of pneumatic tires, only limited knowledge exists on such properties of NPWs. It is thus important to investigate the multi-axis stiffness of

NPWs since these could significantly influence multiple performance measures of the vehicle. The aforementioned studies on NPWs with honeycomb spokes have mostly focused on their vertical stiffness apart from the spokes' stresses and deformations, wheel/terrain contact forces, vibration modes, noise and rolling resistance. The multi-axis stiffness of the NPWs have been addressed in only a few studies focusing on the ME wheels with hinge-unit spokes [4,35].

Although the influences of various design parameters on multi-axis stiffness characteristics of pneumatic tires have been studied extensively [52,65], only a few have reported such parametric studies for NPWs. These have considered variations in a single parameter at a time [4] or response surface methods [28] or Taguchi methods [25,26,100]. Taguchi method is a standardized fractional design approach that permits factorial parametric effects for identifying nearly optimal conditions and relative significance of each design factor in a computationally efficient manner [101]. The Taguchi method has been widely used for identifying near optimal product designs or processes involving multiple factors, especially when there are no significant interactions among the design factors [101]. Proddaturi et al. [100] investigated main effects and chosen interactions of the design parameters on vibration characteristics of a Tweel on the basis of two $L_8(2^7)$ orthogonal arrays and explicit FE methods. Another $L_{27}(3^{13})$ orthogonal array together with an outer array were used to incorporate additional control and noise factors so as to minimize the vibration amplitudes using analysis of variance (ANOVA) of the signal to noise (S/N) ratios. Rutherford et al. [25] utilized a $L_8(2^7)$ orthogonal array to study main effects of seven two-level factors and determined four most significant factors affecting the spokes' vibrations of a Tweel using ANOVA. A $L_9(3^4)$ orthogonal array was further employed to investigate nonlinear effects of significant factors and to identify an optimal combination of design parameters for minimizing vibration amplitudes. Certain theoretical limitations of the Taguchi method have been reported in situations involving notable interactions among the design factors, apart from inadequate considerations of the S/N ratios [102,103].

This study is aimed at evaluating the influences of essential design parameters on the multi-axis stiffness and road contact characteristics of the honeycomb NPW together with their dependence on the cell angle. Three-dimensional (3D) FE models of the honeycomb wheel were developed considering three different cell angles to investigate their static properties in terms of contact area, peak contact pressure and multi-axis stiffness. Regular honeycomb spokes were selected for their superior performances in terms of lower hysteresis loss and higher load support capacity than their auxetic counterparts [5,6]. The validity of the models with nominal dimensions

and material properties were established through comparing the responses in terms of overall vertical deflection and spokes' peak local stress with the reported data, considering identical normal load. Numerical experiments were subsequently conducted considering different combinations of design parameters according to Taguchi orthogonal arrays so as to evaluate the main effect of each factor on each of the wheel response measure in an efficient manner. The results are discussed to provide design guidance for the honeycomb NPW.

3.2 FE modelling of the honeycomb NPW and experimental design

Three-dimensional (3D) FE models of a honeycomb NPW were developed in ABAQUS platform considering three different cell angles (15.8, 31.5 and 47.1°) to evaluate their properties in terms of contact area (A_c), peak contact pressure (p_c^{max}) and multi-axis stiffness together with their dependence on the cell angle, θ. The cell angles were chosen to correspond to those for which some results are available for the purpose of models' verifications [6]. Moreover, these are considered to represent a practical range. Fig. 3.1 depicts the honeycomb wheel with 31.5° cell angle, which consists of the rim, honeycomb spokes, circular sandwich beam and the tread. The circular sandwich beam comprises a shear-dominated annular beam sandwiched between two nearly inextensible membrane reinforcements. The nominal dimensions of the honeycomb wheel with different cell angles were chosen to represent the 205/55R16 passenger car pneumatic tire [96]. The rim and wheel radii of the 205-mm-wide wheel were taken as 406 and 632 mm, respectively. The thickness dimensions of the tread, inner and outer reinforcements and the annular beam were taken as 5, 0.5, 0.5 and 9.5 mm, respectively, as reported in [6,31].

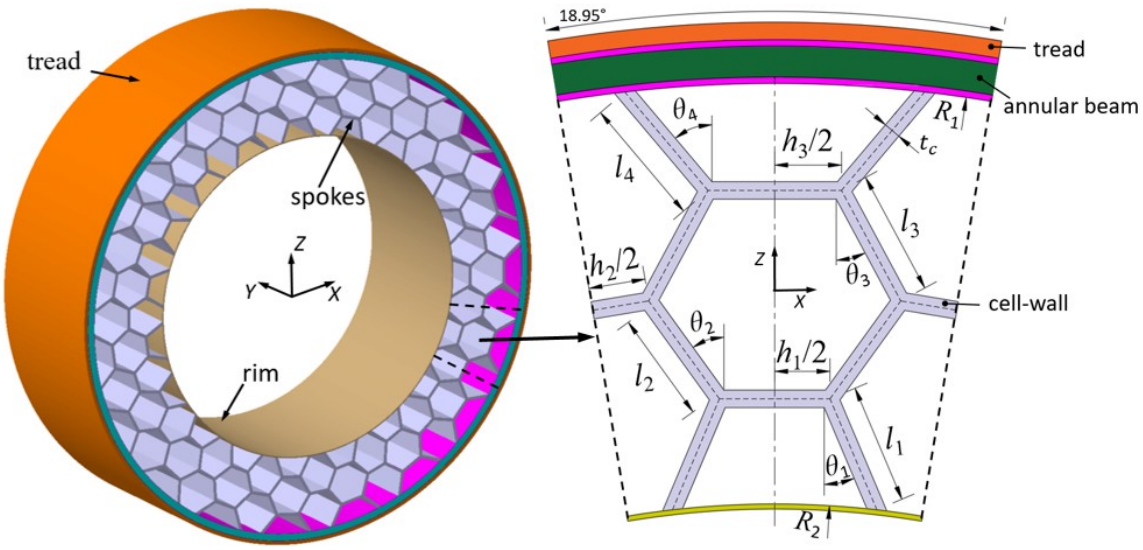

Figure 3.1: Components of the honeycomb NPW with 31.5° cell angle

The mechanical properties of the honeycomb NPW are significantly influenced by the spokes' geometry and properties of the cell-wall material. The in-plane (longitudinal-vertical) effective elastic and shear moduli of a 2D honeycomb spoke in the linear region can be estimated from the following relations [5,24]:

$$E_Z = E(t_c/l)^3 \frac{\cos\theta}{(h/l+\sin\theta)\sin^2\theta} \tag{3.1}$$

$$E_X = E(t_c/l)^3 \frac{(h/l+\sin\theta)}{\cos^3\theta} \tag{3.2}$$

$$G_{ZX} = E(t_c/l)^3 \frac{(h/l+\sin\theta)}{(h/l)^2\,(1+2h/l)\cos\theta} \tag{3.3}$$

where E_Z and E_X are the in-plane effective elastic moduli along Z- and X-axis (Fig. 3.1), respectively, and G_{ZX} denotes the in-plane effective shear modulus. In the above relations, E is the elastic modulus of the cell-wall material, t_c is the cell-wall thickness, and l, h and θ relate to the means of cell-wall lengths (l_i, i=1,..,4), heights (l_j, j=1,..,3) and angles (θ_k, k=1,..,4), respectively, as shown in Fig. 3.1. The effective density of a 2D honeycomb spoke ρ^* can also be estimated from the density of the cell-wall material ρ and the cell dimensions, as [5,24]:

$$\rho^* = \rho \frac{(t_c/l)(h/l+2)}{2\cos\theta(h/l+\sin\theta)} \tag{3.4}$$

Moreover, the lengths and heights of the cell-walls are approximately related to cell angles, rim radius R_2 and inner reinforcement radius R_1 (Fig. 3.1) through following relations:

$$\sum_{i=1}^{4} l_i \cos\theta_i = R_1 - R_2 \tag{3.5}$$

$$h_2 + (h_1 + h_3)/2 + l_2 \sin\theta_2 + l_3 \sin\theta_3 \approx (R_1 + R_2)\pi/N \tag{3.6}$$

In the above relations, N represents the number of spokes, which is taken as 19, as reported in [6,31].

The steel reinforcements and aluminum alloy rim were modelled using the linear elastic material model. The honeycomb spokes and annular beam, and the tread, made of hyper-elastic polyurethane and synthetic rubber, respectively, were modelled using the Ogden material model [95], as:

$$U = \sum_{i=1}^{M} \frac{2\mu_i}{\alpha_i^2}\left(\bar{\lambda}_1^{\alpha_i} + \bar{\lambda}_2^{\alpha_i} + \bar{\lambda}_3^{\alpha_i} - 3\right) + \sum_{i=1}^{M} \frac{1}{D_i}\left(J^{el} - 1\right)^{2i};\ M{=}3 \tag{3.7}$$

where U is the strain energy per unit volume; $\bar{\lambda}_1$, $\bar{\lambda}_2$ and $\bar{\lambda}_3$ are the deviatoric principal stretches; μ_i and α_i are material parameters that are identified from the measured stress-strain data [6]; J^{el} is the elastic volume strain and D_i determines material's compressibility, which can also be related to the Poisson's ratio ν [95,97], such that:

$$\nu = \frac{3(K_0/\mu_0)-2}{6(K_0/\mu_0)-2};\ \mu_0 = \sum_{i=1}^{M} \mu_i;\ K_0 = \frac{2}{D_i} \tag{3.8}$$

where μ_0 and K_0 represent initial shear modulus and bulk modulus, respectively. The ratio, K_0/μ_0, was fixed as 50, which resulted in a Poisson's ratio of 0.49 for both the synthetic rubber and polyurethane. The nominal material parameters for the polyurethane, synthetic rubber, steel and the aluminium alloy, are summarized in Table 3.1 together with the material compressibility D_i [6,31].

Table 3.1: Parameters for the hyper-elastic and elastic materials [6,31]

i	Polyurethane			Rubber		
	μ_i(MPa)	α_i	D_i	μ_i(MPa)	α_i	D_i
1	13.55	1.51	3.5E-03	13.36	1.63	5.9E-03
2	-2.34	2.21	0	-6.63	1.90	0
3	0.09	-2.47	0	0.06	-2.46	0

	Elastic modulus (GPa)	Poisson's ratio, υ	Density (kg/m^3)
Steel	210	0.29	7800
Aluminium alloy	72	0.33	2800

In the developed FE models, the spokes (hyper-elastic), rim, and two reinforcements were discretized by reduced-integration (S4R) elements. The reduced-integration shell element was used to prevent shear locking phenomenon in thin-wall spokes and reinforcements. The fully integrated solid elements with hybrid formulation C3D8H were used to describe nearly incompressible annular beam and tread in order to obtain more accurate predictions of wheel

responses. A mesh convergence study was performed to identify near-optimal element sizes on the basis of the overall wheel deflection and spokes' peak stress responses under a normal load of 3 kN, and the cornering force at a forward velocity of 10 km/h and side-slip angle of 0.5°. The in-plane element size × width (lateral direction) for the spokes, two reinforcements, annular beam and the tread were subsequently determined as 4×7, 8×7, 9.5×9.5×7 and 5×5×7 mm, respectively. The rim was considered as a rigid body assuming its negligible deformation and its mesh size was specified as 5×7 mm. These mesh densities resulted in 75870 elements and 94891 nodes for the wheel model with 31.5° cell angle. Mesh convergence studies were also performed for the wheel models with 15.8 and 47.1° cell angles. The results showed that similar level of convergence could be obtained by using identical elements sizes.

Each wheel component was subsequently assembled using the surface-to-surface tie formulation or shared nodes. Moreover, the wheel contact and interaction with a non-deformable terrain (dry asphalt) were modelled by defining a surface-to-surface contact between the tread elements and the rigid surface (road), assuming static and kinetic coefficients of friction as 0.80 and 0.75, respectively [54].

3.2.1 Method of analyses

The governing nonlinear equilibrium equations of the 3D FE models of the honeycomb NPW were solved iteratively using Newton's method so as to derive its contact area, peak contact pressure and multi-axis stiffness characteristics. The wheel model was translated vertically considering relatively small displacement until the wheel contact with the road was initiated. The normal load was subsequently applied to the rim center in a ramp manner up to 3 kN. The vertical stiffness, K_z, was measured as the quotient of the nominal load (3 kN) and the resulting overall vertical deflection. The road was subsequently revolved about *Z*-axis (Fig. 3.1) or displaced in longitudinal or lateral directions in order to derive wheel's yaw moment-deflection, and longitudinal and lateral force-deflection characteristics. The yaw stiffness of the wheel, K_φ, was obtained under a small yaw deformation, in the vicinity of 0.25°. The longitudinal (K_x) and lateral (K_y) stiffness were evaluated in a similar manner, considering 2-mm deflection of the wheel in either direction.

3.2.2 Model verification

The cell-wall thickness of the three honeycomb spokes used in the wheel models with nominal dimensions and material properties were tuned so as to achieve equivalent vertical stiffness

identical to that of the reference pneumatic tire (205/55R16), which deflected by about 15.8 mm under the normal load of 3 kN. The in-plane moduli and densities of the 2D honeycomb spokes configuration with three different cell angles, normalized with respect to the elastic modulus (E) and density (ρ) of the cell-wall material, respectively, are summarized in Table 3.2 together with their dimensions. The FE models were verified by comparing the overall vertical deflection and peak spokes' stresses with those of the wheels reported in [6], which employed comparable spokes and wheel dimensions together with nearly identical material properties. Each wheel model was loaded to obtain its overall vertical deflection and the peak stress, which was observed in the spoke situated near the center of the wheel/road contact, considering three different normal loads (2, 3 and 4 kN). As an example, Fig. 3.2 illustrates comparisons between the predicted responses of the wheel model with 15.8° cell angle with those reported in [6]. The comparisons suggest reasonably close agreements of the model results with the reported data under the normal loads considered. The maximum differences between the predicted and reported wheel deflection and peak spoke stress are about 5.6 and 3.4%, respectively.

Table 3.2: Dimensions, and normalized moduli and densities of the 2D honeycomb spokes employed in the NPW models with different cell angles (θ)

θ (deg)	l (mm)	h (mm)	t_c (mm)	E_Z/E	E_X/E	G_{ZX}/E	ρ^*/ρ
15.8	24.9	35.2	1.5	0.0020	0.0004	0.00005	0.065
31.5	28.3	26.8	2.4	0.0012	0.0014	0.00040	0.099
47.1	35.5	16.1	2.8	0.0005	0.0019	0.00223	0.121

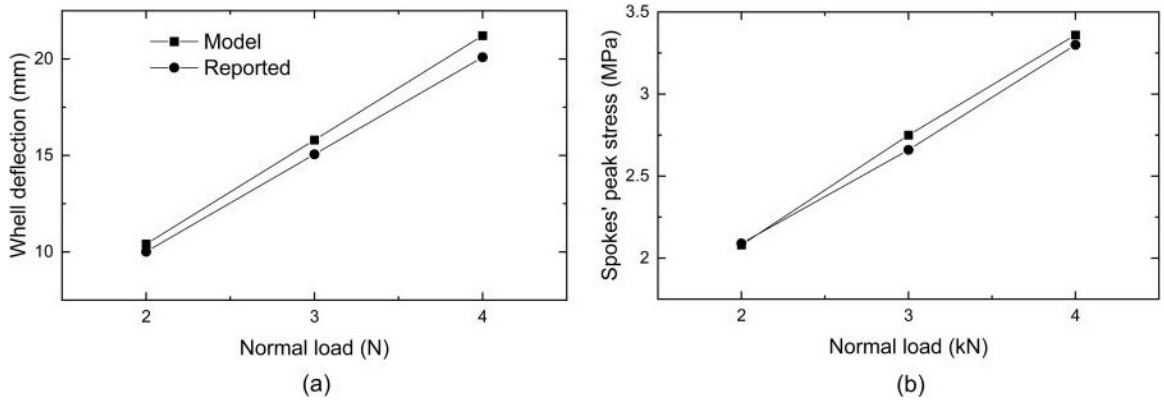

Figure 3.2: Comparisons of (a) wheel deflection and (b) spokes' peak stress responses of the NPW model (θ=15.8°) with those reported in [6]

3.2.3 Design of experiments using Taguchi method

For the NPW with given wheel width, normal load and road friction, the primary design factors that influence the contact area A_c, peak contact pressure p_c^{max} and multi-axis stiffness characteristics of the honeycomb wheel include the thickness (t_t, t_a, t_r, t_c) and initial elastic moduli (E_{0t}, E_{0a}, E_{0r}, E_{0c}) of the tread, annular beam, two reinforcements and the honeycomb cell-wall. The effects of these design parameters are further coupled with the variations in the cell angle θ. In this study, the thickness and elastic moduli of the two reinforcements were fixed as, t_r=0.5 mm and E_{0r}=210 GPa, as reported in [5,6]. This helped reduce to six design factors, namely, (t_t, t_a, t_c) and (E_{0t}, E_{0a}, E_{0c}). A comprehensive analysis of the effects of the six design factors and the resulting 15 two-factor interactions, however, would require huge computational demand. This is more challenging when non-linear effects are influential, which necessitate at least three levels for each design factor. This study was initially conducted considering two levels of each design variable in order to further limit the computational demand. The number of levels, however, was subsequently increased to three for factors showing significant effects.

Taguchi method using orthogonal arrays for efficient experimental designs was employed to determine the main effect representing the average effect of two levels of a design factor, while considering variations in all other design factors. The results obtained from ANOVA of the resulting main effects were used to determine relative significance of each design factor for a chosen performance measure. A $L_8(2^7)$ orthogonal array, shown in Table 3.3, was initially formulated considering the six two-level factors design. The thickness and initial elastic modulus of the cell-wall, denoted as factors *A* and *B*, respectively, were assigned to the first two columns. The third column, however, was left empty so as to evaluate their interaction (*A*×*B*), which was initially considered as influential. The thickness and initial moduli of the annular beam and the tread can be assigned to the remaining columns in any order since these columns are orthogonal. In the table, the thickness of the beam and the tread are denoted by factors *C* and *E*, respectively, while their initial moduli are presented by factors *D* and *F*. The experiment design involving only static analyses does not require repetitive runs or outer arrays since the noise factors are not significant. Table 3.3 also presents two levels of the design variables and their combinations, which were chosen to realize broad variations in vertical stiffness of the wheel. It should be noted that the reported studies on honeycomb NPWs have generally employed relatively high modulus tread (20.3 MPa) [6,14,31], which is substantially higher than that of the pneumatic tire tread. Such

wheel designs may yield substantially higher cornering stiffness, and its saturation at very small side-slip angles. In this study, a relatively softer tread with initial elastic modulus ranging from 4 to 8 MPa, representative of the passenger car pneumatic tires' tread [65,104,105], was employed.

In order to incorporate the nonlinear effects, the analyses were repeated considering three levels of design parameters that were judged to be more significant. For this purpose, another design of experiment based on the $L_9(3^4)$ orthogonal array were conducted. The $L_{16}(2^{15})$ orthogonal array experiments, apart from the L_9 orthogonal array experiment design, were subsequently employed to evaluate the interactions among the significant factors regarding each response measure.

Table 3.3: Experimental design using L_8 orthogonal array

Trial #	*A* (mm)	*B* (MPa)	*A*×*B*	*C* (mm)	*D* (MPa)	*E* (mm)	*F* (MPa)
1	2.5	18.0		10	12.0	5	4.0
2	2.5	18.0		20	18.0	15	8.0
3	2.5	30.0		10	12.0	15	8.0
4	2.5	30.0		20	18.0	5	4.0
5	3.5	18.0		10	18.0	5	8.0
6	3.5	18.0		20	12.0	15	4.0
7	3.5	30.0		10	18.0	15	4.0
8	3.5	30.0		20	12.0	5	8.0

A: cell-wall thickness, t_c; *B*: cell-wall's initial elastic modulus, E_{0c}; *C*: annular beam's thickness, t_a; *D*: annular beam's initial elastic modulus, E_{0a}; *E*: tread thickness, t_t; *F*: tread's initial elastic modulus, E_{0t}; *A*×*B*: interaction of *A* and *B*

3.3 Results and discussion

Simulations were performed to investigate the influences of selected design factors on the wheel responses in terms of contact area A_c, peak contact pressure p_c^{max} and multi-axis stiffness (K_x, K_y, K_z and K_φ) using the design of experiments on the basis of $L_8(2^7)$, $L_9(3^4)$ and $L_{16}(2^{15})$ orthogonal arrays. The results, obtained for the three different cell angles, are discussed in the following sub-sections to emphasize the effects of design parameters and interactions among them.

3.3.1 Influence of cell angle on the wheel responses

The influences of variations in the cell angle θ on the responses in terms of A_c, p_c^{max}, and K_x, K_y, K_z and K_φ are initially investigated using the design of experiments based on the L_8 orthogonal array considering two levels of selected design parameters (Table 3.3). The multi-axis stiffness characteristics obtained under 3 kN normal load are summarized in Table 3.4. The results suggest

that increasing θ generally leads to lower vertical stiffness, K_z, which is more evident when θ is increased from 15.8 to 31.5°. An increase in θ, however, yields higher longitudinal stiffness, K_x, which approaches a substantially higher value for θ=47.1°. These trends are consistent with those observed in the normalized in-plane elastic (E_Z/E) and shear moduli (G_{ZX}/E) of a 2D honeycomb spoke, as illustrated in Table 3.5, which determine K_z and K_x of the wheel, respectively, considering identical sandwich beam and tread for a given trial (Table 3.3). This consistency is evident for both the cell wall thickness considered in the numerical experiments (t_c=2.5 and 3.5 mm). The results show substantial decrease in E_Z/E and increase in G_{ZX}/E with increasing θ, which also lead to higher elastic buckling and lower shear deformations in the spokes located within the contact region. As an example, Fig. 3.3 illustrates deformations of the spokes of the wheel models with three different cell angles corresponding to trial #4 (Table 3.3). The wheels with increasing θ revealed vertical deflections of 10.7, 14.1 and 16.5 mm, respectively, under the normal load of 3 kN. The three wheel models also revealed longitudinal displacements of 6.7, 4.9 and 2 mm, respectively, when subjected to a relatively small longitudinal load of 0.35 kN. Moreover, the spokes of the wheel model with 47.1° cell angle and design parameters corresponding to trials #1 and #3 (Table 3.3) were observed to collapse due to their considerable elastic buckling. This was partly attributed to lower thickness and initial elastic modulus of the annular beam (t_a=10 mm, E_{0a}=12 MPa).

Table 3.4: Variations in multi-axis stiffness of the wheels with different cell angles obtained from L_8 orthogonal array experiments

Cell angle / Trial #	Stiffness											
	Vertical, K_z (kN/m)			Longitudinal, K_x (kN/m)			Lateral, K_y (kN/m)			Yaw, K_φ (Nm/deg)		
	15.8°	31.5°	47.1°	15.8°	31.5°	47.1°	15.8°	31.5°	47.1°	15.8°	31.5°	47.1°
1	113	89	N/A	62	87	N/A	252	213	N/A	139	124	N/A
2	223	170	146	42	57	128	242	207	165	106	101	94
3	152	116	N/A	71	103	N/A	365	305	N/A	120	108	N/A
4	280	213	182	52	72	171	368	318	255	125	120	113
5	191	146	126	67	92	220	356	299	238	182	159	139
6	242	185	160	54	76	182	283	248	204	82	77	74
7	270	202	173	82	117	231	412	360	300	89	85	79
8	318	242	208	78	115	295	518	442	356	210	190	170
overall mean	224	170		64	90		350	299		132	120	

N/A – Not available due to considerable buckling and collapse of the spokes

Table 3.5: Normalized in-plane elastic and shear moduli of the 2D honeycomb spokes

θ (deg)	l (mm)	h (mm)	t_c=2.5 mm		t_c=3.5 mm	
			E_Z/E	G_{ZX}/E	E_Z/E	G_{ZX}/E
15.8	24.9	35.2	0.0068	0.0002	0.019	0.0006
31.5	28.3	26.8	0.0013	0.0004	0.003	0.0011
47.1	35.5	16.1	0.0003	0.0014	0.001	0.0038

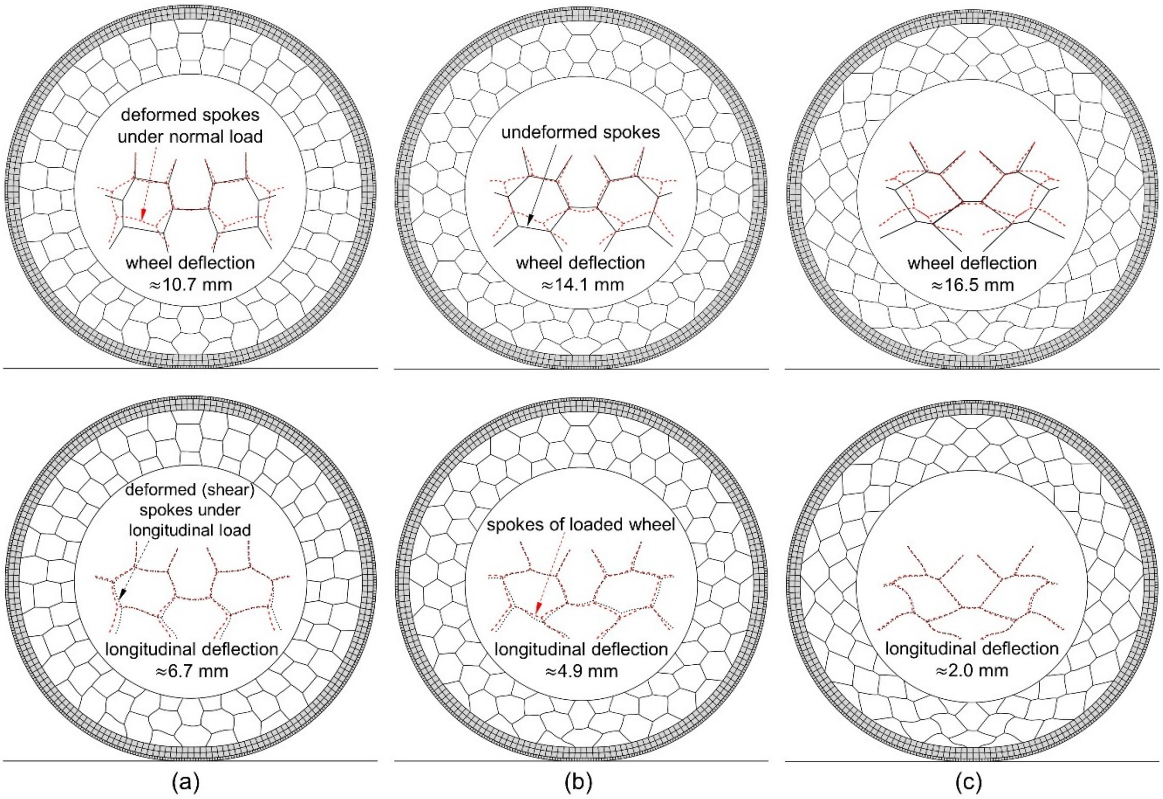

Figure 3.3: Elastic buckling and shear deformations of spokes of the wheel models with different cell angles: (a) 15.8°, (b) 31.5° and (c) 47.1° (normal load = 3 kN, longitudinal load = 350 N)

Increasing θ also resulted in decrease in the lateral stiffness K_y and yaw stiffness K_φ of the wheel models, as it is observed for K_z (Table 3.4). This is likely due to negative influence of θ on the out-of-plane shear stiffness of the honeycomb spokes. As an example, Fig. 3.4(a) illustrates the lateral deformation of the centre planes of the wheel models corresponding to trial #4 (Table 3.3), when the road is displaced laterally by 2 mm. The results presented for the wheel models with different cell angles suggest identical lateral deformations (2 mm) in the contact region where no sliding occurs. The wheel deformation decreases gradually beyond the contact region and approaches negative values in nearly entire top half of each wheel model, as it would be expected. The wheel centre plane exhibits relatively higher lateral deformation near the contact region with

increasing θ, which is attributed to its higher lateral flexibility. The results in Table 3.4 suggest relatively smaller reduction in K_φ with an increase in θ, when compared to that in K_y. As an example, Fig. 3.4(b) depicts the lateral deformations of the centre planes of the three wheel models corresponding to trial #4 considering negligible longitudinal deformations, when the road is rotated by 0.25° about Z-axis. The results show nearly identical lateral deformations of the wheels in the contact region, which are symmetric about the contact centre. The deflected centre planes of the wheels are also sloped in the contact region at an identical angle of 0.25° with respect to the X-axis, where the tread fully adheres to the road surface. Increasing θ results in higher lateral deformation of the wheel, away from the contact region, suggesting lower K_φ.

Owing to relatively higher out-of-plane stiffness of the honeycomb spokes compared to their in-plane stiffness, the honeycomb NPW models generally exhibit considerably higher K_y compared to K_x and K_z, irrespective of the design parameters and the cell angle considered (Table 3.4). The difference between the K_y and K_x, however, decreases significantly with increasing θ. For instance, the results obtained for trial #5 (Table 3.3) show that K_y is nearly 4.3 times K_x for θ=15.8º, and it is only 8% higher than K_x for θ=41.7º. These suggest that a honeycomb wheel with substantially higher cell angle may potentially yield higher longitudinal stiffness than its lateral stiffness, as it is generally observed for the pneumatic tires [39].

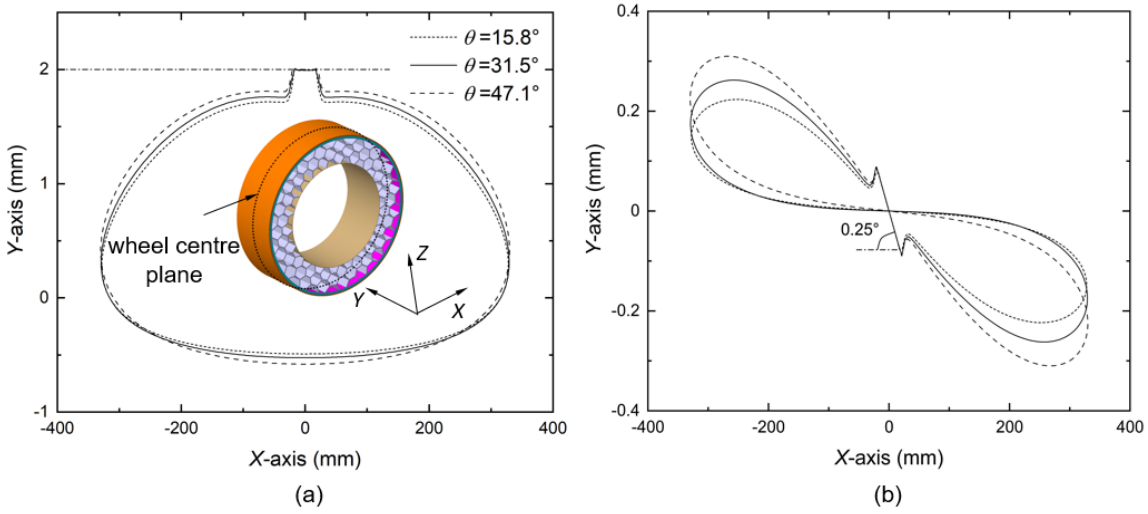

Figure 3.4: Influence of cell angle on the lateral deformation of the centre plane under (a) 2 mm lateral displacement of the road; and (b) 0.25° yaw rotation of the road (Parameters: trial #4 in Table 3.3)

Table 3.6 summarizes the influences of variations in θ on the resulting A_c and p_c^{max} in addition to the mean contact pressure, $\bar{p}$, considering different combinations of the design parameters (Table 3.3). The results presented for the 3 kN normal load suggest only minimal effects of θ on A_c, $\bar{p}$ and p_c^{max}, although it significantly affects K_z of the wheel, as observed in Table 3.4. This suggests relatively higher sensitivity of K_z to θ compared to the contact characteristics. This is partly due to negative deformations (expansion) of the spokes away from the contact region, which generally yields relatively slight reduction in A_c with increasing θ. The maximum differences in the A_c and p_c^{max} were observed to be in the orders of 9.8 and 5.6%, respectively, for the range of cell angles considered. The minimal influences of θ on A_c, $\bar{p}$, and p_c^{max} were also evidenced, for instance, by contact properties of the NPW models with three different cell angles corresponding to trial #2 (Tables 3.3 and 3.6), as shown in Fig. 3.5. The three wheel models showed comparable p_c^{max}, A_c and thus $\bar{p}$ under identical normal load of 3 kN, irrespective of θ considered.

Table 3.6: Influences of cell angle on the wheel contact area, and mean and peak contact pressures obtained from the L_8 orthogonal array experiments

Cell angle / Trial #	Contact area (cm^2), A_c			Mean contact pressure (MPa), $\bar{p}$			Peak contact pressure (MPa), p_c^{max}		
	15.8°	31.5°	47.1°	15.8°	31.5°	47.1°	15.8°	31.5°	47.1°
1	219.2	218.5	N/A	0.1368	0.1373	N/A	0.2378	0.2129	N/A
2	105.1	99.3	94.8	0.2855	0.3020	0.3166	0.4292	0.4248	0.4263
3	167.6	165.0	N/A	0.1790	0.1819	N/A	0.2426	0.2399	N/A
4	100.1	98.0	96.2	0.2998	0.3062	0.3117	0.4553	0.4597	0.4410
5	137.3	136.7	131.5	0.2186	0.2194	0.2281	0.4372	0.4127	0.4168
6	134.7	140.7	133.7	0.2228	0.2133	0.2243	0.3224	0.3234	0.3250
7	137.7	140.1	134.9	0.2179	0.2141	0.2224	0.2774	0.2816	0.2937
8	100.5	98.4	96.7	0.2985	0.3049	0.3103	0.4292	0.4339	0.4122
overall mean	137.8	137.1		0.2324	0.2349		0.3539	0.3486	

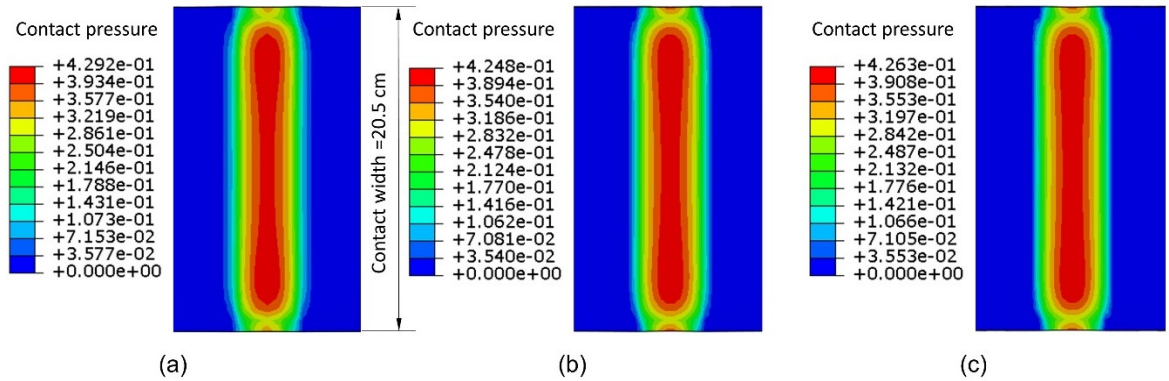

Figure 3.5: Contact pressure distribution of the wheel models with different cell angles: (a) 15.8°, (b) 31.5° and (c) 47.1° (normal load = 3 kN)

3.3.2 Influences of selected design parameters on the wheel responses

The influences of two levels of selected design factors on the static characteristics of the honeycomb NPW are further evaluated considering two different cell angles (15.8 and 31.5°), assuming negligible two-factor interactions when aliased with the main effects. The responses obtained for the wheel models with θ=47.1° were not considered due to excessive buckling of the spokes, as observed for trial #1 and #3 (Tables 3.4 and 3.6). Fig. 3.6 illustrates the main effects of each factor on the response measures normalized to the respective overall mean, summarized in Tables 3.4 and 3.6. The subscripts '$_1$' and '$_2$' denote two levels of the design factors (A,…,F) presented in Table 3.3. The results reveal comparable main effects for the two NPW models with only few exceptions. Opposing effects of factors B (E_{0c}) and C (t_a) on p_c^{max} and K_φ, respectively, are evident in Figs. 3.6(b) and 3.6(f), although the effects are very small.

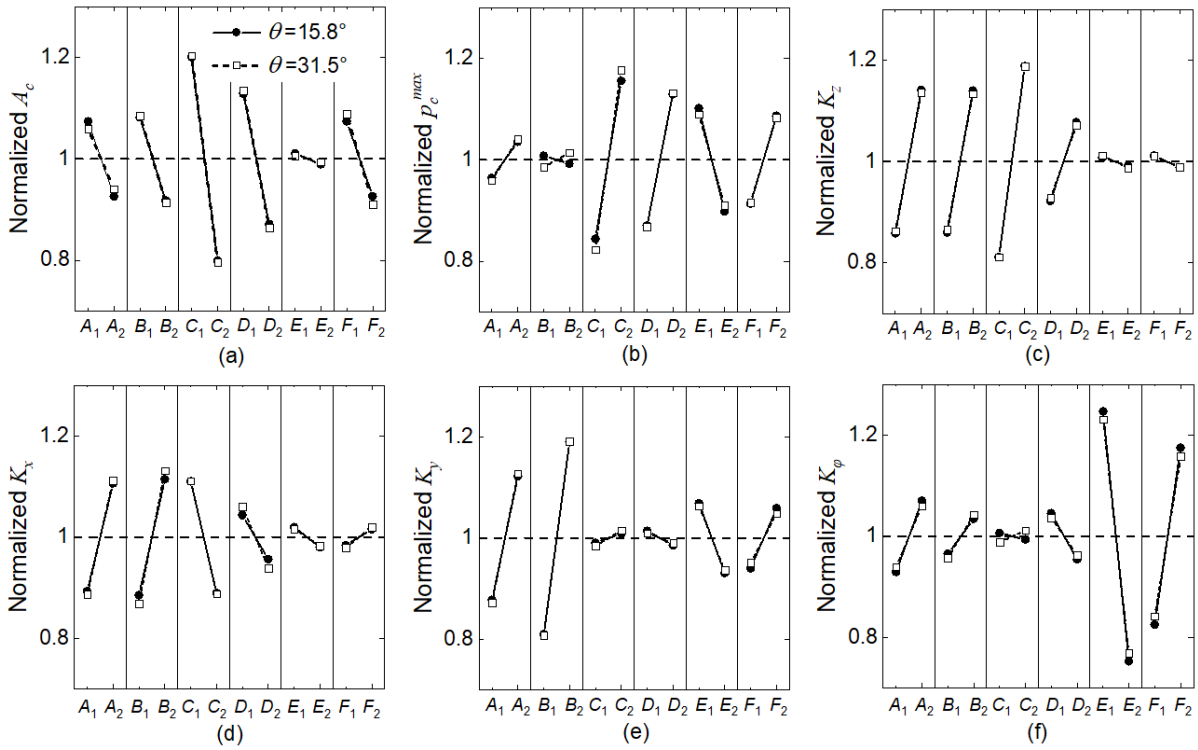

A: cell-wall thickness, t_c; B: cell-wall's initial elastic modulus, E_{0c}; C: annular beam's thickness, t_a;
D: annular beam's initial elastic modulus, E_{0a}; E: tread thickness, t_t; F: tread's initial elastic modulus, E_{0t};
Figure 3.6: Effects of two levels of selected design factors on the normalized responses of the NPW with cell angles of 15.8 and 31.5°: (a) contact area, A_c, (b) peak contact pressure, p_c^{max}, (c) vertical stiffness, K_z, (d) longitudinal stiffness, K_x, (e) lateral stiffness, K_y, and (f) yaw stiffness, K_φ

As expected, the factors *A* (cell-wall thickness, t_c) and *B* (cell-wall's initial elastic modulus, E_{0c}) have positive (increasing) effect on K_z and K_x of each wheel model (Figs. 3.6(c) and 3.6(d)). This is consistent with their influences on the in-plane elastic (E_Z/E) and shear moduli (G_{ZX}/E) of a 2D honeycomb spoke, as seen in Eqs. (3.1) and (3.3), and Table 3.5, which significantly affect K_z and K_x, respectively, of the wheel. The resulting higher K_z leads to lower A_c, apart from the slight influence on p_c^{max}, which is attributable to stress concentration in the discrete honeycomb spokes, and the effects on the stresses in the sandwich beam and the tread, as shown Figs. 3.6(a) and 3.6(b). Increases in factors *A* and *B* also yield relatively higher values of K_y and K_φ, irrespective of the cell angle considered, as seen in Figs. 3.6(e) and 3.6(f). The influences on K_φ, however, are relatively small, when compared to those on K_y and K_x. This is attributable to relatively lower contribution of the honeycomb spokes to the yaw deformation compared to the lateral and longitudinal deformations.

Increasing the factor *C* (annular beam's thickness, t_a) or the factor *D* (annular beam's initial elastic modulus, E_{0a}) causes the bending stiffness of the circular sandwich beam to increase, which yields relatively higher K_z of the wheel, as seen in Fig. 3.6(c). This causes notable reduction in A_c and increase in p_c^{max}, as observed in Figs. 3.6(a) and 3.6(b). These suggest greater sensitivity of A_c and p_c^{max} to annular beam properties compared to those of the spokes. An increase in the factor *C* also yields relatively higher tangential flexibility of the wheel and thereby lower K_x, with only minimal effect on K_y and K_φ. Slightly higher K_y of each wheel model was observed with increasing factor *C*, as depicted in Fig. 3.6(e). The NPW with θ=31.5° also revealed slightly higher K_φ with an increase in the factor *C* (Fig. 3.6(f)), while an opposite effect was observed for the wheel models with θ=15.8°. These are likely attributable to the two-factor interactions in addition to the slight main effects of factor *C* on K_y and K_φ.

In order to further verify the predicted main effects of the factor *C*, additional four numerical experiments were conducted for the wheel models with θ=31.5° considering the higher level of the factor, C_2 (t_a=20 mm). The simulation results were compared with those of the wheel models employing the lower level of the factor, C_1 (t_a=10 mm), (trials #1, 3, 5 and 7 in Table 3.3), as shown in Table 3.7. The results consistently suggest significant influences of the factor *C* on A_c, p_c^{max}, and K_z and K_x. The results also show minimal and opposing effects of factor *C* on K_y and K_φ, which are also consistent with those observed in Figs. 3.6(e) and 3.6(f). For example, an

increase in the factor *C* (trial #1) leads to slight reductions in K_y and K_φ, while opposite effects are evident in results obtained for trial #5. These indicate relatively important interactions between the factor *C* and the other design parameters.

Table 3.7: Influences of annular beam's thickness (factor *C*) and initial elastic modulus (factor *D*) on wheel responses (θ=31.5°)

	Trial 1		Trial 3		Trial 5		Trial 7		Trial 1		Trial 3		Trial 6		Trial 8	
	Factor *C* (t_a, mm)								Factor *D* (E_{0a}, MPa)							
	10	20	10	20	10	20	10	20	12	18	12	18	12	18	12	18
K_z	89	135	116	176	146	228	202	311	89	110	116	143	185	231	242	308
K_x	87	73	103	74	92	77	117	100	87	79	103	84	76	71	115	110
K_y	213	207	305	299	299	302	360	344	213	212	305	308	248	250	442	453
K_φ	124	117	108	111	159	161	85	76	124	117	108	110	77	74	190	180
A_c	219	119	165	117	137	78	140	118	219	157	165	136	141	117	98	78
p_c^{max}	0.21	0.35	0.24	0.36	0.41	0.50	0.28	0.39	0.21	0.33	0.24	0.29	0.32	0.38	0.43	0.50

K_z: vertical stiffness (kN/m); K_x: longitudinal stiffness (kN/m); K_y: lateral stiffness (kN/m); K_φ: yaw stiffness (Nm/deg); A_c: contact area (cm^2); p_c^{max}: peak contact pressure (MPa);

Increasing the factor *D* (E_{0a}) also results in slightly lower K_x, K_y and K_φ, as shown in Figs. 3.6(d), 3.6(e) and 3.6(f). This is partly caused by the lower A_c, as seen in Fig. 3.6(a), and in-part to the negligible influence of factor *D* on the equivalent elastic modulus of the sandwich beam E_{eq}, which can be evaluated, using the 'rule of mixtures' [54], as:

$$E_{eq} = E_{0a}\frac{t_a}{t_a+2t_r} + E_{0r}\frac{2t_r}{t_a+2t_r} \tag{3.9}$$

where E_{0a} and E_{0r} represent the elastic moduli of the annular beam and the two reinforcements, respectively, as stated above. In the above relation, t_a (10 and 20 mm) and t_r (0.5 mm) relate to their respective volume fractions. Owing to the substantially higher elastic modulus of the two reinforcements (E_{0r}=210 GPa), the variations in E_{0a} (12 to 18 MPa) would yield only small effects on E_{eq} and thus the shear stiffness of the wheel.

In order to further verify the predicted main effects of factor *D*, additional four simulations were performed considering design parameters combinations employing higher initial elastic modulus of the annular beam, D_2 (E_{0a}=18 MPa). The results were obtained for the model with 31.5° cell angle, as an example, and compared with those attained for the lower initial elastic modulus, D_1 (E_{0a}=12 MPa), (trials #1, 3, 6 and 8 in Table 3.3). The comparisons, presented in Table 3.7, consistently reveal relatively significant effects of the factor *D* on A_c, p_c^{max}, K_z and K_x. The results attained for trial #1 show only slight reduction in K_y with an increase in the factor *D*,

while those corresponding to trials #3, 6 and 8 suggest slight increases. Similar effects are also observed on K_φ, which are attributable to interactions between the factor *D* and other design parameters. Moreover, the results in Fig. 3.6 show only minimal effects of the annular beam design parameters on K_y and K_φ, when compared to those on K_x. This is due to minimal contribution of the annular beam to the out-of-plane deformation of the wheel.

An increase in the factor *E* (tread thickness, t_t) or the factor *F* (tread's initial elastic modulus, E_{0t}) can cause higher bending stiffness of the tread, which may be expected to cause relatively higher K_z of the wheel. The results presented in Fig. 3.6(c), however, suggest opposing effects, although the effects are very small (≤ 2%). The substantially small effects of factors *E* and *F* on K_z are attributable to extremely low bending stiffness of the tread compared to that of the sandwich beam. This coupled with interactions with the other design factors is thus believed to cause the opposing effects on K_z. Moreover, an increase in factor *F* can lead to lower A_c together with higher p_c^{max}, as seen in Figs. 3.6(a) and 3.6(b). The results also suggest that the contact area is far more sensitive to the elastic modulus of the tread compared to its thickness. Moreover, an increase in the factor *E* or a decrease in factor *F* yields lower shear stiffness of the wheel leading to slight reductions in K_x and K_y with notable reduction in K_φ, as shown in Figs. 3.6(d), 3.6(e) and 3.6(f). The results further suggest that the tread properties can yield more significant influences on K_y and K_φ of the wheel, while K_z and K_x are dominantly affected by the properties of the spokes and the annular beam.

Owing to the important effects of the cell wall thickness (factor *A*) and initial elastic modulus (factor *B*) on the properties of the wheel, the results presented in Tables 3.4 and 3.6 are analysed to assess their interaction effects. Fig. 3.7 presents the effects of two levels of both the factors on the normalized response measures considering two cell angles, 15.8 and 31.5°. The results generally suggest relatively small interactions between the two factors for both the cell angles. Fig. 3.7(b), however, constitutes an exception and suggests notable interaction between the two factors within the ranges studied in view of p_c^{max}, although the effects are very small. The interactions between the two factors on the other wheel responses are relatively small, which is more evident in K_y and K_z considering nearly parallel shifts for the two cell angles.

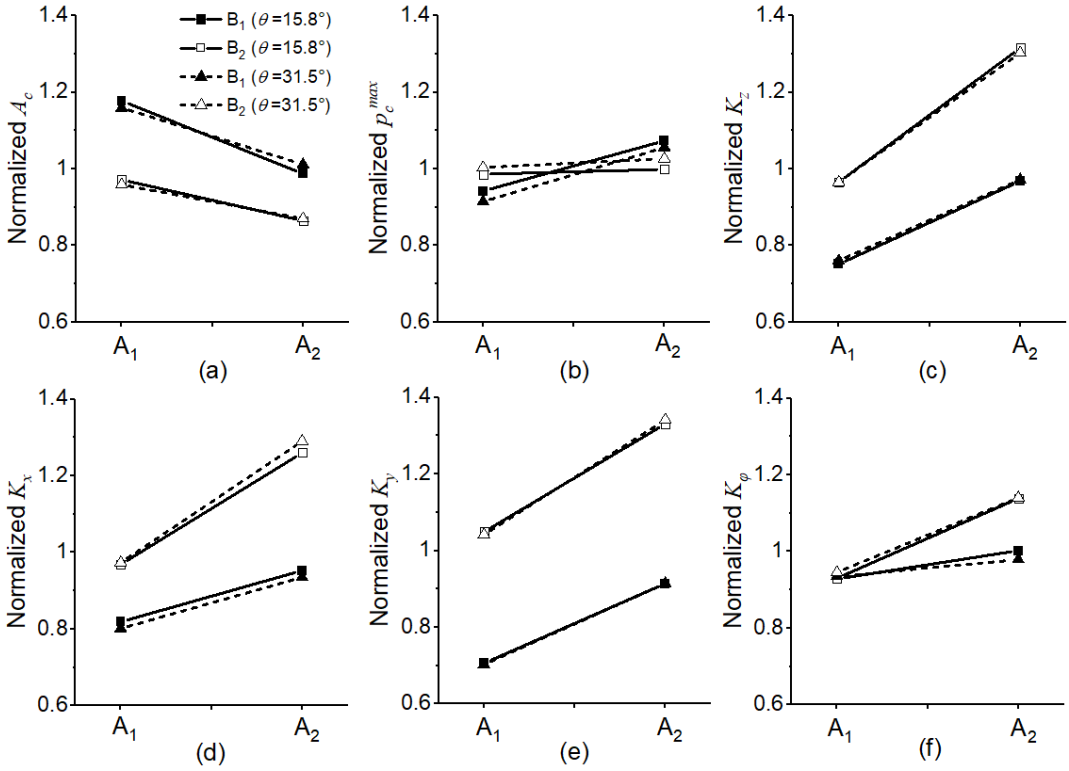

A: cell-wall thickness, t_c; B: cell-wall's initial elastic modulus, E_{0c};

Figure 3.7: Interactions between factors A and B on the responses of the NPW with cell angles of 15.8 and 31.5°: (a) contact area, A_c, (b) peak contact pressure, p_c^{max}, (c) vertical stiffness, K_z, (d) longitudinal stiffness, K_x, (e) lateral stiffness, K_y, and (f) yaw stiffness, K_φ

Significance analysis

The relative significance of the selected design factors is further investigated through analysis of variance (ANOVA). The effect of a design factor is considered significant when p-value is less than 0.05. Owing to the important effects of the cell-wall parameters (factors A and B), the interaction between the factors A and B is also evaluated. The results, summarized in Table 3.8, confirm significant effects of factors A and B on all of the response measures, with exception of p_c^{max} and K_φ. The interaction between them, however, is not significant. The results also suggest significant effects of the tread and annular beam parameters on p_c^{max}, while the tread design parameters show significant effects on K_y and K_φ. Although the results are presented for the wheel models with θ=15.8°, similar trends were also observed for the NPW models with θ=31.5°.

Table 3.8: Summary of significance analyses of the design factors (p-values) for the wheel model with θ=15.8°

P-value	contact area, A_c	peak contact pressure, p_c^{max}	Multi-axis stiffness			
			Vertical, K_z	Longitudinal, K_x	Lateral, K_y	Yaw, K_φ
A	**	-	**	**	***	-
B	**	-	**	**	***	-
A×B	-	-	-	-	-	-
C	**	**	***	**	-	-
D	**	**	**	-	-	-
E	-	**	-	-	**	***
F	**	**	-	-	**	**

***: p-value<0.005; **: p-value<0.05; -: p-value>0.05; A: cell-wall thickness, t_c; B: cell-wall's initial elastic modulus, E_{0c}; C: annular beam's thickness, t_a; D: annular beam's initial elastic modulus, E_{0a}; E: tread thickness, t_t; F: tread's initial elastic modulus, E_{0t}; A×B: interaction of A and B;

3.3.3 Analysis of L_9 orthogonal array experiments and design parameter tuning

In order to study the nonlinear effects of design factors on the wheel responses, an experiment design based on an $L_9(3^4)$ orthogonal array is formulated considering three levels of relatively influential factors. This orthogonal array could incorporate up to four influential design factors, which was considered adequate for this study. The three levels are denoted by '1', '2' and '3', which correspond to 'low', 'medium' and 'high' values, respectively, as shown in Table 3.9. The 'low' and 'high' values correspond to the two factors considered in the L_8 orthogonal array experiments. The results obtained from ANOVA (Table 3.8) are used to identify the most influential factors for each response measure, while other factors are held to respective medium values. In order to reduce the number of experiments, the factors significantly affecting A_c, K_z and K_x could be limited only to A, B, C and D, while the tread-related factors, E and F, are held constant (level '2': E_2=10 mm, F_2=6 MPa). Similarly, factors A, B, E and F are taken as the influential design parameters for K_y, while those for K_φ, are limited only to factors E and F. For the response measure p_c^{max}, factors C, D, E and F constitute the influential factors, as seen in Table 3.8. Table 3.10 summarizes the L_9 orthogonal arrays formulated for analyses of effects considering three levels of the influential parameters, assuming negligible interactions among the factors. The subscripts ('1', '2', '3') used with a factor denote the level of the factor.

Table 3.9: Three levels of factor considered for formulating the L_9 orthogonal arrays

Level	Factor					
	A (mm)	*B* (MPa)	*C* (mm)	*D* (MPa)	*E* (mm)	*F* (MPa)
Low - '1'	2.5	18	10	12	5	4
Medium – '2'	3.0	24	15	15	10	6
High – '3'	3.5	30	20	18	15	8

A: cell-wall thickness, t_c; *B*: cell-wall's initial elastic modulus, E_{0c}; *C*: annular beam's thickness, t_a;
D: annular beam's initial elastic modulus, E_{0a}; *E*: tread thickness, t_t; *F*: tread's initial elastic modulus, E_{0t};

Table 3.10: L_9 orthogonal arrays with three-levels of identified influential factors

Trial #	Response measures			
	A_c, K_z, K_x	K_y	K_φ	p_c^{max}
1	$A_1B_1C_1D_1$	$A_1B_1E_1F_1$	E_1F_1	$C_1D_1E_1F_1$
2	$A_1B_2C_2D_2$	$A_1B_2E_2F_2$	E_1F_2	$C_1D_2E_2F_2$
3	$A_1B_3C_3D_3$	$A_1B_3E_3F_3$	E_1F_3	$C_1D_3E_3F_3$
4	$A_2B_1C_2D_3$	$A_2B_1E_2F_3$	E_2F_1	$C_2D_1E_2F_3$
5	$A_2B_2C_3D_1$	$A_2B_2E_3F_1$	E_2F_2	$C_2D_2E_3F_1$
6	$A_2B_3C_1D_2$	$A_2B_3E_1F_2$	E_2F_3	$C_2D_3E_1F_2$
7	$A_3B_1C_3D_2$	$A_3B_1E_3F_2$	E_3F_1	$C_3D_1E_3F_2$
8	$A_3B_2C_1D_3$	$A_3B_2E_1F_3$	E_3F_2	$C_3D_2E_1F_3$
9	$A_3B_3C_2D_1$	$A_3B_3E_2F_1$	E_3F_3	$C_3D_3E_2F_1$

A: cell-wall thickness, t_c; *B*: cell-wall's initial elastic modulus, E_{0c}; *C*: annular beam's thickness, t_a;
D: annular beam's initial elastic modulus, E_{0a}; *E*: tread thickness, t_t; *F*: tread's initial elastic modulus, E_{0t};
K_z: vertical stiffness (kN/m); K_x: longitudinal stiffness (kN/m); K_y: lateral stiffness (kN/m);
K_φ: yaw stiffness (Nm/deg); A_c: contact area (cm^2); p_c^{max}: peak contact pressure (MPa);

Table 3.11 summarizes the simulation results obtained from the experiment design based on the L_9 orthogonal arrays for the wheel models with two different cell angles (θ=15.8 and 31.5). The results suggest only minimal influence of θ on A_c and p_c^{max}, as it was observed in Table 3.6. An increase in θ, however, causes notable increase in K_x and decrease in K_z, K_y and K_φ. These are also consistent with the trends observed in Table 3.4 and Fig. 3.6, which demonstrate the validity of the predicted effects of θ on the wheel responses in the L_9 orthogonal array experiments.

Table 3.11: Variations in contact area, peak contact pressure and multi-axis stiffness obtained from the L_9 orthogonal array experiments

Trial #	A_c (cm^2)		p_c^{max} (MPa)		K_z (kN/m)		K_x (kN/m)		K_y (kN/m)		K_φ (Nm/deg)	
	15.8°	31.5°	15.8°	31.5°	15.8°	31.5°	15.8°	31.5°	15.8°	31.5°	15.8°	31.5°
1	202	210	0.272	0.238	113	89	63	88	248	211	139	128
2	138	136	0.274	0.269	189	146	57	69	307	261	169	152
3	102	100	0.298	0.298	281	213	52	72	356	304	189	170
4	120	118	0.298	0.299	212	163	53	68	293	249	102	96
5	122	126	0.309	0.310	234	179	59	82	312	273	126	116
6	161	171	0.445	0.449	192	147	80	108	454	385	143	132
7	120	119	0.346	0.341	269	206	55	79	308	266	83	80
8	141	152	0.478	0.480	225	171	78	111	445	377	102	95
9	139	138	0.418	0.420	265	201	85	123	438	382	115	109
overall mean	138	141	0.349	0.345	220	168	65	89	351	301	130	120

A_c: contact area (cm^2); p_c^{max}: peak contact pressure (Mpa); K_z: vertical stiffness (kN/m);
K_x: longitudinal stiffness (kN/m); K_y: lateral stiffness (kN/m); K_φ: yaw stiffness (Nm/deg)

Fig. 3.8 illustrates the effects of the influential factors on each response measure normalized with respect to the corresponding overall mean value (Table 3.11). The results generally suggest mildly nonlinear effects of the design factors on the response measures with only few exceptions. The strongly nonlinear effects of spokes factors (*A* and *B*) on A_c, tread factors (*E* and *F*) on p_c^{max}, and tread's initial elastic modulus (factor *F*) on K_y are evident in Figs. 3.8(a), 3.8(b) and 3.8(e), respectively. A_c decreases with increase in factors *A* and *B*, and exhibits saturation as the two factors exceed their respective medium levels. This is likely due to dominant effects of the annular beam parameters (factors *C* and *D*) on A_c, as seen in Fig. 3.8(a). The main effects on the responses of the wheel with both cell angles revealed consistency with those obtained in the L_8 orthogonal array experiments (Fig. 3.6), which suggests only minimal potential effects of the neglected interactions.

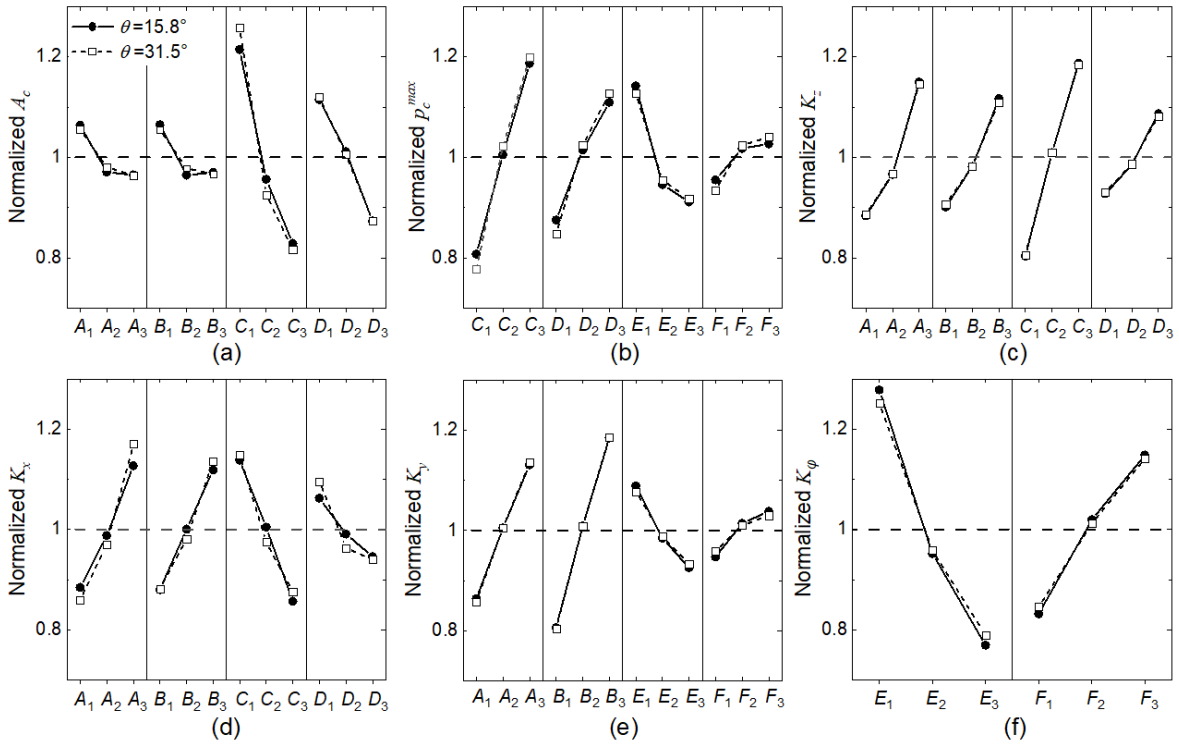

A: cell-wall thickness, t_c; *B*: cell-wall's initial elastic modulus, E_{0c}; *C*: annular beam's thickness, t_a; *D*: annular beam's initial elastic modulus, E_{0a}; *E*: tread thickness, t_t; *F*: tread's initial elastic modulus, E_{0t};

Figure 3.8: Effects of three levels of influential factors on the normalized responses of the wheel with cell angles of 15.8° and 31.5°: (a) contact area, A_c, (b) peak contact pressure, p_c^{max}, (c) vertical stiffness, K_z, (d) longitudinal stiffness, K_x, (e) lateral stiffness, K_y, and (f) yaw stiffness, K_φ.

Considerable parametric analyses and design optimization efforts have been reported in order to realize stiffness properties of NPWs similar to those of the pneumatic tires [106]. In this context, Fig. 3.9 presents comparisons of the overall means of the multi-axis stiffness of the NPW with two cell angles (K_x, K_y, K_z and K_φ) with those of four different pneumatic tires of comparable size, namely 195/70R14, 195/65R15, 225/45R17 and 225/40R18 [39]. It is evident that the NPW yields comparable K_z and K_φ as those of the pneumatic tires, while K_x is substantially lower due to higher in-plane flexibility of the spokes. The lateral stiffness of the NPW designs, however, is substantially higher than those of the pneumatic tires, which is due to higher out-of-plane rigidity of the spokes, and is likely to cause inferior directional control and handling performance of the vehicle. It should be noted that increasing θ could help decrease K_y while considerably increasing K_x (Table 3.4).

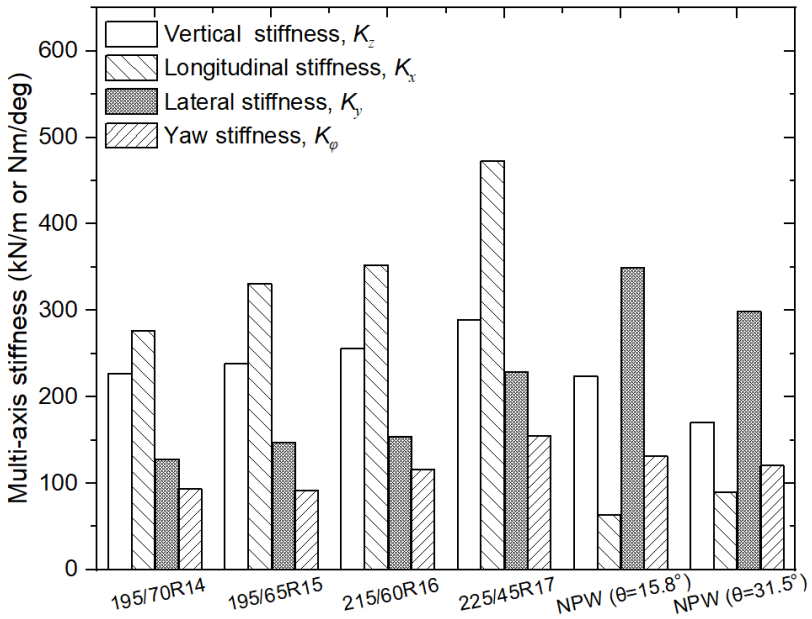

Figure 3.9: Comparisons of multi-axis stiffness of the NPW and pneumatic tires

The results in Fig. 3.8 provide important guidance for design tuning of the NPW to realize desired multi-axis stiffness characteristics. Moreover, the wheel design may be tuned to yield relatively higher A_c but lower p_c^{max} for improved wheel grip and wear performance, respectively. For instance, the combinations of the spokes and annular beam parameters, $A_1B_1C_1D_1$ and $A_3B_3C_1D_1$, may be considered to yield relatively higher A_c and K_x, respectively, of the wheel. Similarly, the combinations $C_1D_1E_3F_1$ and $A_1B_1E_3F_1$ may be considered as desirable design parameters for lower p_c^{max} and K_y, respectively. Additional simulations were performed for parameters combinations perceived to yield relatively higher K_x and A_c, and lower K_y and p_c^{max}. Other combinations may also be considered to tune the stiffness characteristics. For example, the combinations $A_3B_3C_3D_3$ and E_3F_1 may be considered to achieve higher K_z but lower K_φ, respectively. The results attained from these additional simulations are presented in Table 3.12.

Table 3.12: Comparison of predicted wheel responses with those obtained from simulations

	A_c (cm^2)		p_c^{max} (MPa)		K_z (kN/m)		K_x (kN/m)		K_y (kN/m)		K_φ (Nm/deg)	
	15.8°	31.5°	15.8°	31.5°	15.8°	31.5°	15.8°	31.5°	15.8°	31.5°	15.8°	31.5°
Combination	$A_1B_1C_1D_1$		$C_1D_1E_3F_1$		$A_3B_3C_3D_3$		$A_3B_3C_1D_1$		$A_1B_1E_3F_1$		E_3F_1	
Predicted, Eq. (3.10)	202	210	0.192	0.165	340	257	94	138	191	168	78	76
Simulations	202	210	0.213	0.210	414	311	96	133	222	192	83	80
Difference (%)	0	0	10.0	21.4	17.8	17.4	2.1	3.8	14.0	12.5	6.0	5.0

A: cell-wall thickness, t_c; B: cell-wall's initial elastic modulus, E_{0c}; C: annular beam's thickness, t_a; D: annular beam's initial elastic modulus, E_{0a}; E: tread thickness, t_t; F: tread's initial elastic modulus, E_{0t};

Alternatively, the responses corresponding to a given design parameter combination may be predicted using the Taguchi method [101]:

$$Y = \bar{Y} + \sum_{i=1}^{n}(\bar{Y}_i - \bar{Y}) \tag{3.10}$$

where Y is the response measure corresponding to a chosen influential design parameter combination, n is the number of design parameters in the combination, $\bar{Y}$ is the mean value of the response measure obtained across the 9 trials of the experiment design (Table 3.11), and $\bar{Y}_i$ represents the mean of the response measures obtained for desired level of factor i. For example, for predicting the yaw stiffness, $\bar{Y}_1$ corresponds to the mean of K_φ obtained for combinations E_3F_1, E_3F_2 and E_3F_3 (trials #7, #8 and #9 in Tables 3.10 and 3.11), where the factor E at level 3 yields lowest value of K_φ (Fig. 3.8). Similarly, $\bar{Y}_2$ denotes the mean for combinations E_1F_1, E_2F_1 and E_3F_1 (trails #1, #4 and #7) with factor F at level '1' leading to lowest K_φ. The predicted response measures are compared with the simulation results in Table 3.12.

It should be noted that the desirable parameter combinations for higher A_c and lower K_φ correspond to trials #1 and #7 of the experiment design (Table 3.10). These two trials revealed highest A_c and lowest K_φ, respectively, compared to the other trials in the L_9 orthogonal array experiments (Table 3.11). The results of additional simulations presented in Table 3.12, also suggest relatively higher K_z and p_c^{max}, and lower K_y. Moreover, the predicted A_c is identical to that obtained from the additional simulation, which indicates its four influential factors are independent. Only small differences are observed in K_x and K_φ for both the two cell angles (3.8 and 6%), which are suggestive of weak interactions among the associated influential factors. Notable differences, however, are evident in p_c^{max}, K_z and K_y, which range from 10% to 21.4%. These suggest relatively significant interactions among the associated influential factors, which are further investigated in the following section.

3.3.4 Interactions among the influential parameters

In order to further evaluate the influences of two-factor interactions on p_c^{max}, K_z and K_y, an experiment design based on an $L_{16}(2^{15})$ orthogonal array is formulated. Since the influence of essential factors on p_c^{max}, K_z and K_y is monotonic (Fig. 3.8), the experiment design is limited only to two levels ('1' and '3') of the influential factors as identified previously. This helped reduce the

computational demand. From Fig. 3.8, it is evident that factors *CDEF*, *ABCD* and *ABEF* constitute the influential factors in view of p_c^{max}, K_z and K_y, respectively. The L_{16} orthogonal array experiment is designed to consider two-factor interactions of the influential factors, as illustrated in Table 3.13. These are assigned as columns 1, 4, 7 and 8 of the L_{16} orthogonal array according to the triangular table of interactions [101].

Table 3.13: Peak contact pressure, vertical and lateral stiffness of L_{16} orthogonal array experiments

Trial #	p_c^{max} (MPa)			K_z (kN/m)			K_y (kN/m)		
	Combination	15.8°	31.5°	Combination	15.8°	31.5°	Combination	15.8°	31.5°
1	$C_1D_1E_1F_1$	0.272	0.238	$A_1B_1C_1D_1$	115	90	$A_1B_1E_1F_1$	248	211
2	$C_1D_1E_1F_3$	0.293	0.249	$A_1B_1C_1D_3$	143	111	$A_1B_1E_1F_3$	257	217
3	$C_1D_3E_3F_1$	0.261	0.262	$A_1B_3C_3D_1$	225	172	$A_1B_3E_3F_1$	318	277
4	$C_1D_3E_3F_3$	0.298	0.298	$A_1B_3C_3D_3$	283	215	$A_1B_3E_3F_3$	356	304
5	$C_1D_1E_3F_1$	0.213	0.210	$A_1B_1C_3D_1$	176	137	$A_1B_1E_3F_1$	222	192
6	$C_1D_1E_3F_3$	0.249	0.246	$A_1B_1C_3D_3$	220	168	$A_1B_1E_3F_3$	240	205
7	$C_1D_3E_1F_1$	0.384	0.371	$A_1B_3C_1D_1$	146	112	$A_1B_3E_1F_1$	374	318
8	$C_1D_3E_1F_3$	0.426	0.400	$A_1B_3C_1D_3$	182	139	$A_1B_3E_1F_3$	394	332
9	$C_3D_1E_3F_1$	0.321	0.320	$A_3B_1C_3D_1$	239	184	$A_3B_1E_3F_1$	288	252
10	$C_3D_1E_3F_3$	0.364	0.361	$A_3B_1C_3D_3$	303	230	$A_3B_1E_3F_3$	319	275
11	$C_3D_3E_1F_1$	0.458	0.463	$A_3A_3C_1D_1$	211	159	$A_3A_3E_1F_1$	492	422
12	$C_3D_3E_1F_3$	0.480	0.505	$A_3B_3C_1D_3$	264	198	$A_3B_3E_1F_3$	532	451
13	$C_3D_1E_1F_1$	0.381	0.365	$A_3B_1C_1D_1$	156	120	$A_3B_1E_1F_1$	334	286
14	$C_3D_1E_1F_3$	0.417	0.397	$A_3B_1C_1D_3$	194	148	$A_3B_1E_1F_3$	351	298
15	$C_3D_3E_3F_1$	0.385	0.380	$A_3B_3C_3D_1$	324	245	$A_3B_3E_3F_1$	397	351
16	$C_3D_3E_3F_3$	0.436	0.432	$A_3B_3C_3D_3$	414	311	$A_3B_3E_3F_3$	459	399
overall mean		0.352	0.344		225	171		349	299

Table 3.13 summarizes the experiment design and the resulting p_c^{max}, K_z and K_y, which are analyzed to assess the two-factor interactions and the main effects. The results showed only minimal interactions of the influential design factors in view of the response measures p_c^{max}, K_z and K_y. As an example, Fig. 3.10 presents the effects of two levels of the influential factors on the normalized K_y for both the cell angles of the NPW. The results, invariably, show non-intersecting shifts, irrespective of the cell angle. Similar non-intersecting shits were also observed in p_c^{max} and K_z (results not shown). These suggested negligible influences of the two-factor interactions on the perceived parameter combinations leading to desired wheel responses. Moreover, the resulting main effects revealed trends similar to those obtained from the L_9 orthogonal array experiments (Fig. 3.8). The combinations of design parameters for higher K_z, and lower p_c^{max} and K_y are thus determined as $A_3B_3C_3D_3$, $C_1D_1E_3F_1$ and $A_1B_1E_3F_1$, respectively, which are consistent with those identified from the L_9 orthogonal array experiments. These combinations correspond to trial #16,

#5 and #5 of the L_{16} orthogonal array experiments (Table 3.13), respectively. Table 3.14 further summarizes the simulation results obtained for these three parameter combinations.

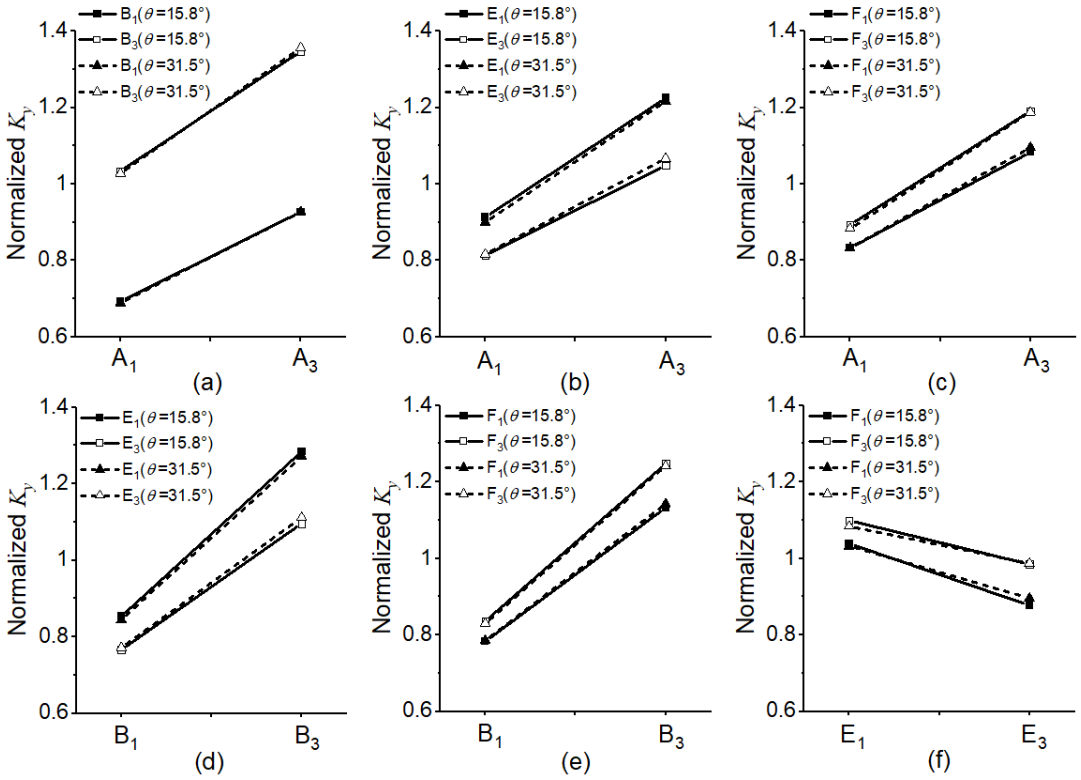

A: cell-wall thickness, t_c; B: cell-wall's initial elastic modulus, E_{0c};
E: tread thickness, t_t; F: tread's initial elastic modulus, E_{0t};

Figure 3.10: Interactions among the four influential factors on the lateral stiffness, K_y, of the NPW with cell angles of 15.8 and 31.5°

Table 3.14: Comparison of wheel responses obtained from the simulations with predicted results considering two-factor interactions

	Peak contact pressure (MPa)		Vertical stiffness (kN/m)		Lateral stiffness (kN/m)	
	15.8°	31.5°	15.8°	31.5°	15.8°	31.5°
Combinations	$C_1D_1E_3F_1$		$A_3B_3C_3D_3$		$A_1B_1E_3F_1$	
Predicted, Eq. (3.10)	0.203	0.207	408	307	224	194
Simulations	0.213	0.210	414	311	222	192
Difference (%)	4.7	1.4	1.4	1.3	0.9	1.0

The response measures of the NPW are also predicted using Eq. (3.10) considering two-factor interactions. The predicted response values are compared with the simulations results in Table 3.14, which correspond to parameter combinations leading to relatively higher K_z, and lower p_c^{max} and K_y of the NPW. The comparisons show only small differences between the simulation and

predicted results, irrespective of the cell angle. The maximum difference in K_z, p_c^{max} and K_y are in the order of 1.4%, 4.7% and 1%, respectively. These slight differences are likely attributable to the higher-order interactions. The results also show that the desirable parameter combinations yield lateral stiffness of the wheel closer to those of the pneumatic tires (Fig. 3.9).

3.4 Conclusions

1. The FE models of the honeycomb NPW with three different cell angles showed reasonably good agreements with the reported responses in terms of the vertical deflection and maximum spokes' stress. The honeycomb wheel with the higher cell angle of 47.1° revealed excessive deformations of the spokes in the proximity of the contact region due to reduction in the elastic modulus of the honeycomb cell in the radial direction.

2. The NPW designs revealed substantially lower longitudinal stiffness compared to those the pneumatic tires of similar sizes, which was attributed to higher in-plane flexibility of the honeycomb spokes. The higher out-of-plane rigidity of the NPW designs, however, resulted in substantially higher lateral stiffness compared to those of the pneumatic tires. Increasing the cell angle resulted in relatively lower lateral stiffness of the wheel with notable increase in the longitudinal stiffness. The parametric analyses involving two- and three-levels of the design factors revealed that the vertical and longitudinal stiffness of the wheel are strongly related to the spokes and annular beam parameters, while the lateral stiffness is strongly affected by the spokes as well as tread design parameters.

3. The results served as important design guidance for the wheel to realize desired multi-axis stiffness together with higher contact area and lower peak contact pressure. While the spokes parameters revealed only minor effects on the peak contact pressure, the annular beam and tread parameters showed considerable influence on the contact area and contact pressure. It is shown that the NPW designs can be tuned to realize in-plane and out-of-plane stiffness characteristics comparable to those of the pneumatic tires.

4. The parametric analyses revealed strongly nonlinear effects of the spokes properties on the contact area, while the nonlinear effects of tread properties were evident on the peak

contact pressure and the lateral stiffness. The results obtained from the experiment designs based on the $L_9(3^4)$ and $L_{16}(2^{15})$ orthogonal arrays confirmed minimal contributions of the interactions among all the influential design factors.

Chapter 4

Cornering stiffness characteristics of honeycomb wheels: A parametric analysis using response surface method

4.1 Introduction

Non-pneumatic wheels (NPWs) generally consist of a circular sandwich beam, also referred to as shear ring, connected to the wheel hub by uniformly and discretely distributed solid spokes. The NPWs offer superior safety performance by eliminating potential pressure-related failures encountered with the pneumatic tires. The removal of air may also reduce the extent of coupling among the multi-axis stiffness properties of the wheel resulting in higher design flexibility [1]. In addition, the NPWs are considered as fuel-efficient designs due to the relatively low hysteresis loss associated with thermoplastic polyurethane, which constitutes the shear ring and spokes [7]. The NPWs may thus be considered meritorious substitutes for the pneumatic tires for ground vehicles.

A number of design concepts in NPWs have been reported during the past two decades, which differ primarily in the spokes design. These mostly include hinge-unit spokes as in mechano-elastic wheels [4,10,12], radially flexible spokes in Tweels[17,25,98], and hexagonal cellular spokes in honeycomb NPWs [5,6]. It has been shown that NPWs with regular hexagonal honeycomb spokes (positive cell angle) could offer relatively good performance in terms of relatively uniform contact pressure distribution [16], high load carrying capacity [16-18], low rolling resistance [16], and good vehicle ride quality [18]. Many studies thus investigated the influences of geometric parameters of hexagonal honeycomb cells on multiple performance measures under different loading and rolling conditions, using finite element (FE) methods. For NPW designs with same cell-wall thickness, an increase in the cell angle yielded lower load carrying capacity of the wheel together with slight influence on the peak stresses in the spokes and the tread [5,6]. For NPW designs with identical load carrying capacity, an increase in the cell angle necessitates higher cell-wall thickness, which would result in lower peak spokes' stress, higher spokes' mass and thus higher rolling resistance of the wheel [5,6,31].

Kim et al. [31,33] reported near-rectangular footprint of NPWs with notable contact pressure peaks in the wheel heading direction, which was partly due to the discrete spokes. The peak contact

pressure, however, was only slightly influenced with variations in the cell angle. Papageorgiou et al. [107] conducted a parametric analysis to investigate the effects of cell-wall length, height, thickness and cell angle on the load carrying capacity, peak stress and mass of the wheel, apart from peak spokes' stress. The results suggested that these mechanical behaviours could be easily modified or improved by tuning the design parameters considered. Ju et al. [5] also investigated NPWs with auxetic honeycomb spokes (negative cell angle). When designing NPWs with same cell-wall thickness, these wheels exhibited lower load carrying capacity than those with regular honeycomb spokes with identical but positive cell angle. For a given load carrying capacity, these wheels, however, showed higher rolling resistance resulting from their higher mass. This study thus focuses on the NPWs with regular honeycomb spokes.

Other studies on honeycomb NPWs have explored selected performance measures for given spokes designs, using the FE methods. These included modal properties of non-rolling NPWs for non-contacting as well as loaded conditions [13,14], vibration characteristics, and hysteresis energy loss and resulting steady-state temperature distribution of the rolling wheel [7,13,14]. These have generally shown localized vibrations due to non-homogeneous mass distribution of the discrete honeycomb spokes. Moreover, the most of the hysteresis loss (≈70%) of a rolling NPW has been attributed to the shear ring [7].

While the reported studies have extensively investigated the response characteristics of honeycomb NPWs in terms of load-deflection relations, wheel-ground contact pressure distribution, vibration modes, rolling resistance, temperature distribution, and stresses in the spokes and the tread, only limited efforts are evident on the out-of-plane properties of NPWs [108]. The cornering properties of the NPWs, in-particular, have not been adequately investigated, which directly influence the vehicle's directional control and stability. A recent study reported the cornering force and self-aligning moment characteristics of honeycomb NPWs with varying cell angles using FE methods [108]. The comparisons of the cornering properties of NPWs with those of a reference pneumatic tire showed considerably higher cornering stiffness (defined as the rate of change of cornering force with respect to side-slip angle in the vicinity of zero side-slip, N/deg) of the honeycomb wheels, irrespective of the cell angle considered, in addition to cornering force saturation at very low slip angles. This was attributed to the substantially high out-of-plane stiffness of NPWs, when compared to the pneumatic tires [108]. Owing to the deformation of the side wall and the adherence to the ground, a rolling pneumatic tire tends to travel along a path at

an angle to its heading direction (denoted as side-slip angle), when subjected to a side force at its rim center. The relation between the cornering force developed in the wheel-ground contact region and the side-slip angle is a determining factor for vehicles' handling and stability performance. High cornering stiffness coupled with cornering force saturation at very low slip angles would yield inferior handing and directional control, and side-slippage of the vehicle under medium to high side slip conditions [108]. Conversely, a wheel with a too low cornering stiffness will undergo extremely large side deformation in order to meet the cornering force demand during a turning manoeuvre. In order for the honeycomb NPWs to be considered as practical substitutes, it is vital to achieve cornering stiffness comparable to those of the pneumatic tires.

In order to achieve cornering properties comparable to those of a pneumatic tire, it is vital to seek NPW designs with relatively lower out-of-plane stiffness, which may be realized through a detailed parametric analysis of wheel design parameters, apart from the cell angle. The parametric sensitivity analyses are widely conducted using sequential approach ('one-parameter-at-a-time' approach). This strategy, however, does not permit the simultaneous contributions due to interactions among the key design parameters, which are frequently observed in the engineering systems [109]. Besides, sensitivity analysis using high-fidelity FE models and one-parameter-at-a-time approach is impractical due to very high computational cost. Alternatively, high-fidelity FE models can be effectively utilized to develop regression models using response surface methods (RSM) which permit both main as well as interaction effects of design parameters, and enable identifications of desirable design parameters combinations for near-optimal performance measures in an efficient and reliable manner [110,111]. Moreover, the RSM methods can facilitate formulations of computationally efficient linear or nonlinear prediction models.

The present study is aimed at a comprehensive parametric analysis of a honeycomb NPW in view of its cornering force characteristics. For this purpose, three-dimensional high-fidelity FE models of the rolling honeycomb NPW with three different cell angles were developed so as to evaluate the wheel's cornering stiffness. Owing to the detrimental effects of negative cell angles on the load carrying capacity and rolling resistance, the study was limited only to (regular) honeycomb spokes with positive cell angle. These models were verified by comparing the predicted responses with the reported data in the literature considering similar design parameters and identical operating conditions. The responses included the overall vertical deflections and peak stresses developed in the spokes of the stationary wheel, and the cornering stiffness of the rolling

wheel. Screening experiments were initially conducted using the developed FE models based on design points identified using one-half two-level fractional factorial design so as to eliminate design factors showing negligible or minimal effects. The numerical experiments were subsequently conducted to study effects of significant design parameters following the central composite designs (CCDs) approach. The RSM technique was finally employed to evaluate the main effects of important design parameters while considering their interaction effects, and to formulate relations between the wheel's cornering stiffness and the chosen design parameters. The results provide essential design guidance for tuning the cornering properties of NPWs.

4.2 Finite element modelling of a honeycomb NPW and design of experiments

A honeycomb NPW design was considered for developing three-dimensional (3D) FE models of the rolling wheel so as to assess its cornering force characteristics. Three different models of the wheel were developed considering three different spokes' cell angle (47.1, 31.5 and 15.8°), which are considered to be more practical, as reported in previous studies [5,6]. Fig. 4.1 depicts the NPW design with three different cell angles, which comprises the rubber tread, annular sandwich beam (shear ring), cellular polyurethane spokes and the aluminium rim. The tread pattern was not considered due to its minimal influence on cornering properties in relatively small side slip angles, as observed for the pneumatic tires [55]. The annular sandwich beam, consisting of a polyurethane core layer sandwiched between two near-inextensible steel rings, and the honeycomb spokes mainly constitute the load supporting elements of the wheel. It should be noted that the cell-wall length (l) and height (h), and the cell angle (θ), relate to the means of l_i, h_i and θ_i (i=1,..,4), respectively, as illustrated in Fig. 4.1(c). These dimensions are further related to the radii of the rim (R_2) and the steel ring (R_1) connected to the cellular cells, apart from the number of spokes (N) in wheel circumferential direction, as:

$$\sum_{i=1}^{4} l_i \cos\theta_i = R_1 - R_2 \tag{4.1}$$

$$(h_1 + h_2 + h_3 + h_4)/2 + l_2 \sin\theta_2 + l_3 \sin\theta_3 \approx (R_1 + R_2)\pi/N \tag{4.2}$$

The number of spokes, in the order of 19, was taken as reported in refs. [6,108].

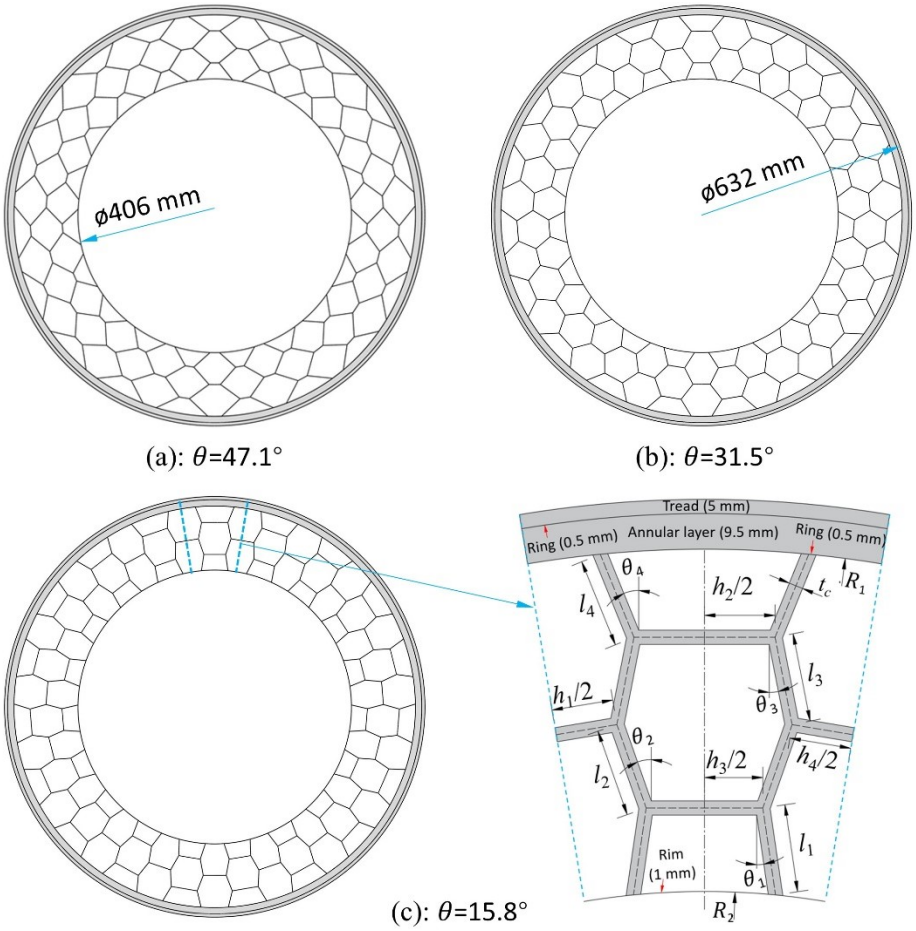

Figure 4.1: Honeycomb wheel with spokes design of different cell angles: (a) 47.1, (b) 31.5 and (c) 15.8°

The elastic (steel and aluminium) and hyper-viscoelastic (polyurethane and rubber) mechanical behaviours of wheel's constituents were modelled by generalized Hooke's law and Ogden strain energy potential combined with Prony series [95], respectively, such that:

$$U = \sum_{i=1}^{Q} \frac{2\mu_i}{\alpha_i^2}\left(\bar{\lambda}_1^{\alpha_i} + \bar{\lambda}_2^{\alpha_i} + \bar{\lambda}_3^{\alpha_i} - 3\right) + \sum_{i=1}^{Q} \frac{1}{D_i}\left(J^{el} - 1\right)^{2i};\ Q{=}3 \tag{4.3}$$

$$\frac{G_R(t)}{G_R(t{=}0)} = 1 - \sum_{p=1}^{M}\{g_i[1 - \exp(-t/\tau_i)]\};\ M{=}3 \tag{4.4}$$

where U and J^{el} represent the strain energy density and the elastic volume ratio, respectively, while $\bar{\lambda}_1$, $\bar{\lambda}_2$ and $\bar{\lambda}_3$ denote the deviatoric principal stretches. μ_i, α_i and D_i are the model parameters of this hyper-elastic material model. $G_R(t)$ is the time-dependent shear relaxation modulus, while g_i and τ_i are i^{th} Prony series parameters. The above-stated material model parameters were identified from measured stress-strain and stress relaxation characteristics [112], which were also employed by previous studies [6,108] and were summarized in Table 4.1 together with the elastic moduli and Poisson's ratios of the steel and aluminium components.

Table 4.1: Model parameters for hyper-viscoelastic and elastic materials [6,108]

i	Polyurethane					Rubber				
	μ_i(MPa)	α_i	D_i (MPa^{-1})	g_i	τ_i (s)	μ_i(MPa)	α_i	D_i (MPa^{-1})	g_i	τ_i (s)
1	13.55	1.51	3.5E-03	0.125	0.002	13.36	1.63	5.9E-03	0.2	0.002
2	-2.34	2.21	0	0.125	0.02	-6.63	1.90	0	0.2	0.02
3	0.09	-2.47	0	0.125	0.2	0.06	-2.46	0	0.2	0.2

Elastic materials	Elastic modulus (GPa)	Poisson's ratio	Density (kg/m^3)
Steel	210	0.29	7800
Aluminium	72	0.33	2800

The dimensions of the wheel and the spokes including the cell angles (47.1, 31.5 and 15.8°) were chosen corresponding to the design reported in ref. [108], which also approximately conform to those of the design reported in ref. [6]. The selected design parameters permitted verifications of the FE models in the present study. Specifically, the wheel and rim diameters together with their width dimensions were taken as 632, 406, 205 and 205 mm, respectively, as partly depicted in Figs. 4.1(a) and 4.1(b). The thickness dimensions of the rim, annular layer, steel rings and the tread were taken as 1, 9.5, 0.5, 0.5 and 5 mm, respectively (Fig. 4.1(c)). The cell dimensions of the three honeycomb spokes configurations in terms of cell-wall length, height and thickness are summarized in Table 4.2 together with the corresponding cell angles. The maximum difference in the wheel and components dimensions (except the cell-wall thickness, t_c) of the current and the reported designs [6] is less than 6.03%. It should be noted that for the fair comparison t_c of each spoke design was tuned to achieve an identical equivalent vertical stiffness, in the order of 190 kN/m, under a given normal load of 3 kN. This chosen stiffness is comparable to that of the designs reported in ref. [6], which is about 202 kN/m.

Table 4.2: Cell dimensions of spokes considering different cell angles

Cell angle (deg) $\theta_1, \theta_2, \theta_3, \theta_4, (\theta)$	Cell-wall		
	Length (mm) $l_1, l_2, l_3, l_4, (l)$	Height (mm) $h_1, h_2, h_3, h_4, (h)$	Thickness t_c, (mm)
38.3, 50.4, 44.0, 55.6, (47.1)	32.8, 34.6, 36.4, 38.1, (35.5)	17.7, 15.9, 13.2, 17.7, (16.1)	2.82
22.6, 35.6, 27.9, 39.9, (31.5)	27.5, 27.6, 28.7, 29.5, (28.3)	25.8, 30.4, 25.1, 25.8, (26.8)	2.38
8.9, 19.9, 11.7, 22.7, (15.8)	24.7, 24.8, 25.0, 25.2, (24.9)	34.4, 39.4, 32.6, 34.4, (35.2)	1.54

The FE models of the honeycomb NPW were developed in ABAQUS/Standard platform using the symmetric model generation capability [95]. As an example, a 3D sector FE model of the honeycomb NPW with (θ=47.1°) was initially generated by extruding the two-dimensional cross-

section mesh of a representative sector of the wheel which includes a single spoke along the wheel revolution axis (y-axis), as illustrated in Figs. 4.2(a) and 4.2(b). The generated 3D sector model was subsequently revolved about y-axis to build the full FE model of the entire wheel (Fig. 4.2(c)). The developed 3D FE models can be effectively used to study the steady-state dynamic interaction between the rolling honeycomb wheel and the non-deformable terrain [96]. More detailed descriptions of model development including element formulations, contact definitions and mesh convergence study have been presented in a recent study [108]. The static and dynamic friction coefficients of 0.80 and 0.75, respectively, were chosen to represent a non-deformable dry asphalt terrain [54,108].

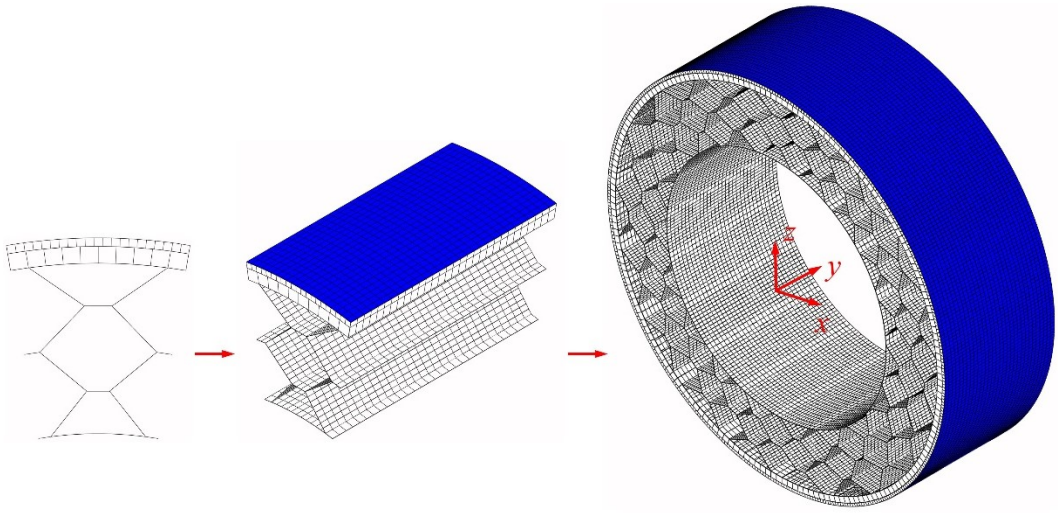

Figure 4.2: FE modelling of the honeycomb wheel (θ=47.1°): (a) two-dimensional cross-section mesh of the representative sector, (b) 3D sector model, (c) full model

4.2.1 Methodology

Between the application of a given side slip angle and the attainment of resulting steady-state motion, the rolling honeycomb wheel is in the transient state. The transient and the desired steady-state dynamic responses of the rolling wheel could be modeled using implicit or explicit time integration techniques [59]. These methods, however, are computationally inefficient due to their limited time increment size in order to yield stable and accurate response predictions, and the relatively large wheel model size [95]. In addition, these techniques necessitate repeated simulations to obtain steady-state responses for each given side slip angle, which pose considerable additional computational demand.

Alternatively, the steady-state motion could be derived directly without modelling its prior transient states (time-dependent). This is achieved by employing a coordinate frame attached to the wheel revolution axis, which could yield translation without spin. In this traveling frame, wheel rotation is described by its constituent material transporting through stationary mesh (Eulerain approach), while wheel deformation is represented in a Lagrangian manner [65,95]. The nonlinear equilibrium equations of the rolling wheel model are subsequently solved iteratively using Newton-Raphson's method. The methodology can be implemented using steady-state transport analysis available in ABAQUS/standard. The default convergence criteria was chosen, which could ensure sufficiently close converged solution to the exact solution at each iteration or increment [95]. The solutions yield steady-state responses corresponding to each incremental side slip angle considered. The cornering force under different side slip angles could thus be obtained in a single simulation. This computationally efficient approach based on steady-state transport analysis also offers notable improvement in predicting wheel cornering properties under relatively higher side slip angles, when compared to the methods using implicit or explicit time integration techniques [59].

The simulation process in the present study included static loading of the wheel followed by the steady-state analyses of the rolling wheel. The wheel model was initially displaced vertically to initiate its contact with the fixed rigid road. This was followed by the application of a linearly increasing normal load (up to 4 kN) to the rim center. This two-step loading strategy could help eliminate potential convergence problems resulting from unbalanced contact forces [95]. Subsequently, the material transport velocity (angular) was defined to represent wheel rotation, while a desired constant forward velocity was assigned to the abovementioned coordinate frame to achieve constant speed forward motion of the rotating wheel. Varying the angular velocity could yield straight line free rolling solution with zero torque about the wheel revolution axis. It should be noted that a friction coefficient of zero was assigned for static loading, which was gradually increased to 0.75 for the rolling analysis. This ensured smooth transition between stationary and rolling frictional stresses, and thus eliminated potential convergence difficulties [59,95]. The vertical force-deflection relations for evaluating wheel's vertical stiffness, however, were obtained from static loading of the wheel with a friction coefficient of 0.80. Following the straight line free rolling, an additional gradually increasing lateral velocity was assigned to the travelling frame so as to model wheel cornering behaviour under different side slip angles. The side slip angle (α) is

defined as the angle formed between wheel heading and travelling directions, and relates to wheel velocity components [54], as:

$$v_y = v_x \tan \alpha \tag{4.5}$$

where v_x and v_y denote wheel forward and lateral velocities, respectively.

4.2.2 Verifications of the honeycomb wheel models

The validity of the three honeycomb wheel models with different cell angles was verified by comparing their static and dynamic (steady-state) responses with the available data, which were obtained from verified FE wheel models [6,108]. Jin et al. [6] demonstrated verification of the FE model of the honeycomb NPW by comparing dynamic deformations of the spokes within the contact region with those observed for a prototype wheel of similar structure [113]. The validity of the models presented in this study is initially examined by comparing the static responses in terms of peak local stress in the spokes and vertical deflections of the wheel with those reported in ref. [6], under three different normal loads (2, 3 and 4 kN). It should be noted that as expected the peak local stress was invariably observed in the spoke in the vicinity of the center of the wheel-ground contact region for all the three models, as shown in Fig. 4.3(a), which was attributed to its relatively higher strain. The cornering force responses of the rolling wheel models were subsequently obtained using steady-state transport analysis, considering a forward speed of 10 km/h and side slip angles up to 5°. The cornering stiffness of the wheel was estimated from the gradient of the cornering force in the 0 to 0.2° side-slip angle range.

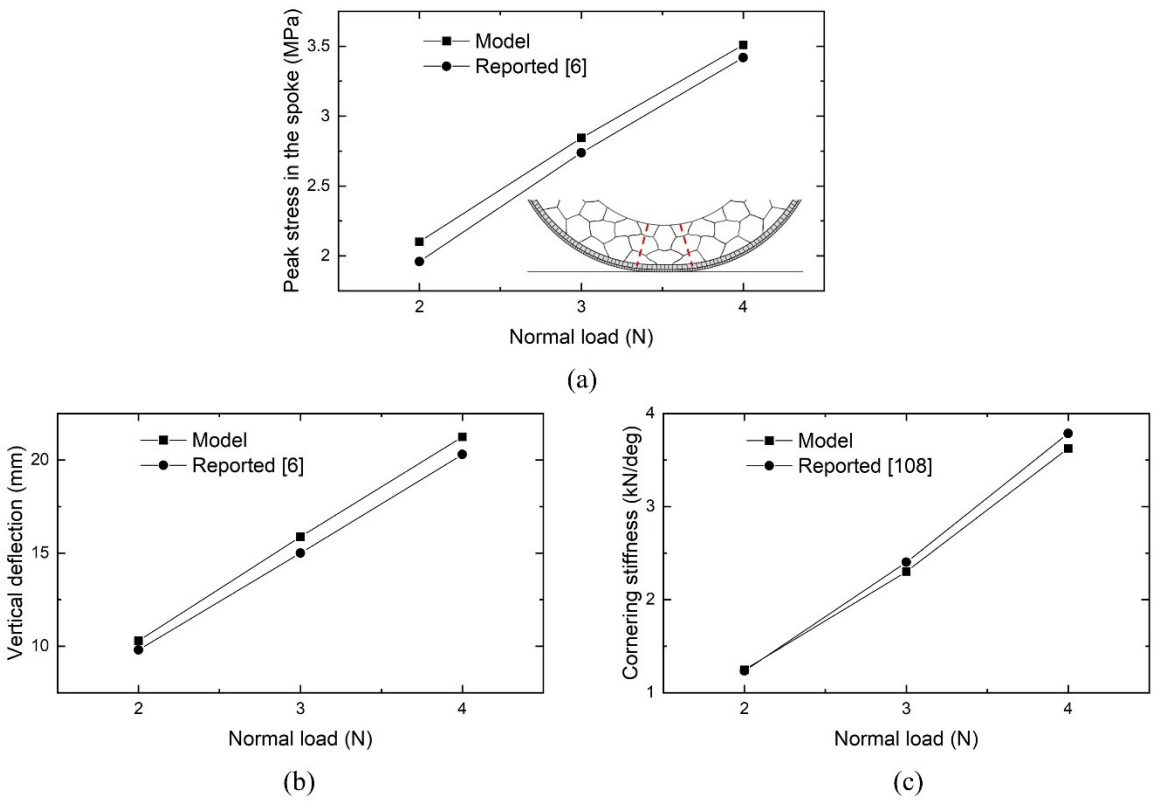

Figure 4.3: Comparisons of (a) spokes' peak local stress, (b) vertical deflection and (c) cornering stiffness of the wheel model (θ=31.5°) with reported data

As an example, Figs. 4.3(a) and 4.3(b) compare the peak spokes' stress and vertical deflection responses of the wheel model with cell angle of 31.5°, respectively, with those of the reported wheel design [6], which employed identical material properties and loading conditions together with similar wheel and spokes dimensions. The comparisons are presented for three different normal loads (2, 3 and 4 kN). The predicted static responses are in reasonably good agreement with the reported data for the wheel loads considered. The maximum deviations between the predicted and reported peak spokes' stress and wheel deflection were 7.2% and 5.8%, respectively, which may be attributable to small differences in the wheel and spokes dimensions. Similarly, Fig. 4.3(c) compares the predicted cornering stiffness of the wheel model for three different normal loads with those reported in [108], which employed identical material properties and dimensions. The results in the reported study, however, were obtained using the explicit time integration technique. The comparison suggests reasonably good agreements between the predicted and reported cornering stiffness for the range of normal loads considered. The results, however, show relatively higher deviation between the two, in the order of 4.1%, under the 4 kN wheel load. The

similar degrees of agreements were also observed between the model and reported results for the other wheel models with 47.1 and 15.8° cell angles.

In order to evaluate the influence of forward speed on the cornering properties of each wheel model, the abovementioned simulations were repeated at two additional speeds (30 and 50 km/h). As an example, Fig. 4.4 illustrates the effect of forward speed on the cornering stiffness of the wheel model with 31.5° cell angle considering three different normal loads (2, 3 and 4 kN). The results suggest only slight reduction in the cornering stiffness with increase in the forward speed, irrespective of the wheel load considered. Similar trend has also been observed for the pneumatic tires [54]. The maximum reduction in cornering stiffness, in the order of 2.4%, was observed for the higher wheel load of 4 kN. Similar influences of forward speed were also evident for the honeycomb wheel models with 47.1 and 15.8° cell angles. The forward speed could thus be limited to 10 km/h for the following parametric analysis without considering the inertia effects, which could cause potential convergence challenges for simulations [95].

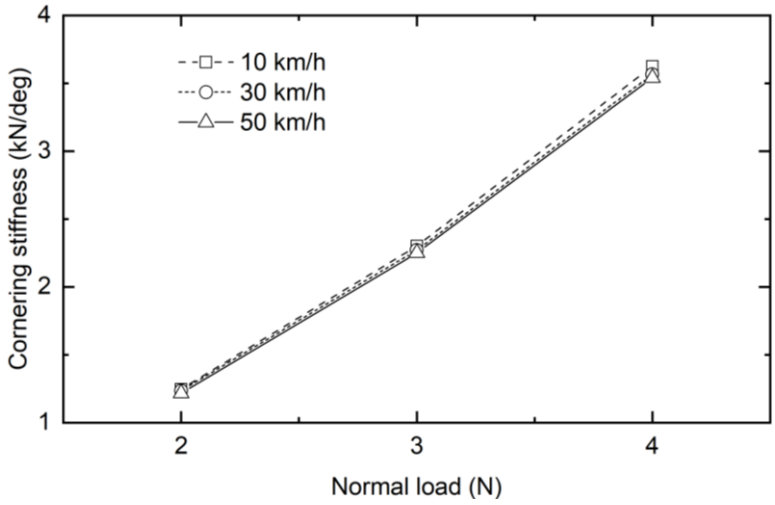

Figure 4.4: Influence of forward speed on cornering stiffness of the wheel model with 31.5° cell angle

4.2.3 Experiment designs

The verified FE models of the wheel are used for the subsequent experiment designs and parametric studies. The design parameters that influence the cornering stiffness (K_α) of a honeycomb wheel include the initial elastic moduli (E_{0c}, E_{0r}, E_{0a}, E_{0t}) and thickness (t_c, t_r, t_a, t_t) of the cell-wall, two steel rings, annular layer and the tread, apart from the cell angle (θ) of the three spokes designs (Fig. 4.1). It should be noted that θ is related to cell-wall heights and lengths,

as seen in Eqs. (4.1) and (4.2). The elastic moduli and thickness of the two steel rings were taken as, E_{0r}=210 GPa and t_r=0.5 mm, respectively, as in the reported wheel designs [6,31,108], which could yield relatively high load carrying capacity. This leads to six design parameters, namely, (E_{0c}, E_{0a}, E_{0t}) and (t_c, t_a, t_t), which are coupled with θ.

An experiment design is initially formulated considering only one-half fraction of the full factorial design (2^{6-1}) involving two levels of each design factor to investigate the influence of the six design parameters on cornering stiffness, K_α, together with its dependence on θ in an efficient manner. The main effects of selected parameters were evaluated in terms of the mean effects corresponding to different levels of each design factor. The resulting fifteen two-factor interactions could be evaluated independent of each other, although these may be confounded by other high-order interactions, which were assumed negligible according to the sparsity-of-effects principle [114]. The screening experiments could thus eliminate insignificant parameters, using the analysis of variance (ANOVA), with adequate consideration of the potentially important two-factor interactions. In the experiment designs, the thickness dimensions of the honeycomb cell-wall, annular layer and the tread (t_c, t_a, t_t) are denoted by factors *A*, *C* and *E*, respectively, while their initial elastic moduli (E_{0c}, E_{0a}, E_{0t}) are denoted as factors *B*, *D* and *F*. The low and high levels of each design factor considered in the 2^{6-1} designs, represented as '-1' and '+1', respectively, are shown in Table 4.3. The designed fractional factorial matrix is an optimum Taguchi array as each level of each parameter appears the same number of times in the array with no repetitions of parameter-level combination. The levels of the design factors were chosen to derive wheel designs with wide-ranging load carrying capacities. Moreover, the chosen levels of tread parameters, E_{0t} and t_t, represent the practical design ranges for the passenger car pneumatic tires [96,104]. Table 4.4 summarizes the factor-level combinations of the 2^{6-1} designs for each three values of θ. The output responses for each experiment run were evaluated using developed 3D FE models. Each simulation including static loading and steady-state rolling analyses of the wheel takes about 2.5 hours on an HP Z8 dual-processor (2×2.10 GHz) workstation.

Table 4.3: Low and high levels of six design factors considered in the 2^{6-1} designs

Level	Factors					
	A: t_c (mm)	*B:* E_{0c} (MPa)	*C:* t_a (mm)	*D:* E_{0a} (MPa)	*E:* t_t (mm)	*F:* E_{0t} (MPa)
Low: '-1'	2.5	18	10	12	5	4
High: '+1'	3.5	30	20	18	15	8

Factors (*A*, *C* and *E*) and (*B*, *D* and *F*) represent thickness dimensions (t_c, t_a, t_t) and initial elastic moduli (E_{0c}, E_{0a}, E_{0t}) of cell-wall, annular layer and tread, respectively

Table 4.4: Matrix of 2^{6-1} designs considering different cell angles

Run#	Factor-level combinations	Run#	Factor-level combinations
1	$A_{-1}B_{-1}C_{-1}D_{-1}E_{-1}F_{-1}$	17	$A_{-1}B_{-1}C_{-1}D_{-1}E_{+1}F_{+1}$
2	$A_{+1}B_{-1}C_{-1}D_{-1}E_{-1}F_{+1}$	18	$A_{+1}B_{-1}C_{-1}D_{-1}E_{+1}F_{-1}$
3	$A_{-1}B_{+1}C_{-1}D_{-1}E_{-1}F_{+1}$	19	$A_{-1}B_{+1}C_{-1}D_{-1}E_{+1}F_{-1}$
4	$A_{+1}B_{+1}C_{-1}D_{-1}E_{-1}F_{-1}$	20	$A_{+1}B_{+1}C_{-1}D_{-1}E_{+1}F_{+1}$
5	$A_{-1}B_{-1}C_{+1}D_{-1}E_{-1}F_{+1}$	21	$A_{-1}B_{-1}C_{+1}D_{-1}E_{+1}F_{-1}$
6	$A_{+1}B_{-1}C_{+1}D_{-1}E_{-1}F_{-1}$	22	$A_{+1}B_{-1}C_{+1}D_{-1}E_{+1}F_{+1}$
7	$A_{-1}B_{+1}C_{+1}D_{-1}E_{-1}F_{-1}$	23	$A_{-1}B_{+1}C_{+1}D_{-1}E_{+1}F_{+1}$
8	$A_{+1}B_{+1}C_{+1}D_{-1}E_{-1}F_{+1}$	24	$A_{+1}B_{+1}C_{+1}D_{-1}E_{+1}F_{-1}$
9	$A_{-1}B_{-1}C_{-1}D_{+1}E_{-1}F_{+1}$	25	$A_{-1}B_{-1}C_{-1}D_{+1}E_{+1}F_{-1}$
10	$A_{+1}B_{-1}C_{-1}D_{+1}E_{-1}F_{-1}$	26	$A_{+1}B_{-1}C_{-1}D_{+1}E_{+1}F_{+1}$
11	$A_{-1}B_{+1}C_{-1}D_{+1}E_{-1}F_{-1}$	27	$A_{-1}B_{+1}C_{-1}D_{+1}E_{+1}F_{+1}$
12	$A_{+1}B_{+1}C_{-1}D_{+1}E_{-1}F_{+1}$	28	$A_{+1}B_{+1}C_{-1}D_{+1}E_{+1}F_{-1}$
13	$A_{-1}B_{-1}C_{+1}D_{+1}E_{-1}F_{-1}$	29	$A_{-1}B_{-1}C_{+1}D_{+1}E_{+1}F_{+1}$
14	$A_{+1}B_{-1}C_{+1}D_{+1}E_{-1}F_{+1}$	30	$A_{+1}B_{-1}C_{+1}D_{+1}E_{+1}F_{-1}$
15	$A_{-1}B_{+1}C_{+1}D_{+1}E_{-1}F_{+1}$	31	$A_{-1}B_{+1}C_{+1}D_{+1}E_{+1}F_{-1}$
16	$A_{+1}B_{+1}C_{+1}D_{+1}E_{-1}F_{-1}$	32	$A_{+1}B_{+1}C_{+1}D_{+1}E_{+1}F_{+1}$

Factors (*A*, *C*, *E*) and (*B*, *D*, *F*) denote thickness dimensions and initial Elastic moduli of cell-wall, annular layer and tread, respectively

The central composite design (CCD) approach was subsequently employed to formulate a response surface quadratic function relating K_α with significant design factors and their two-factor interactions. The quadratic regression model was considered in order to account for potentially nonlinear dependence of K_α on the design factors, and the two-factor interactions. The number of levels for each design factor was, however, increased to three so as to incorporate the potential nonlinear effects. The detailed descriptions of the CCD-based experiment designs used in the study are presented in Section 4.3.2.

4.3 Results and discussion

The simulations were conducted for the NPW designs with different geometric and material properties, apart from the cell angle θ, so as to evaluate the main effects of chosen design factors and their two-factor interactions in view of wheel cornering stiffness K_α. The results obtained from

one-half fractional factorial (2^{6-1} designs) and subsequent central composite designs (CCDs) are discussed in the following subsections.

4.3.1 One-half fractional factorial designs (2^{6-1})

The cornering force responses of each wheel design were obtained using the developed 3D FE models for all 2^{6-1} design points (Table 4.4) considering forward speed of 10 km/h, side slip angles (α) up to 5°, and 3 kN normal load. The cornering stiffness K_α was subsequently evaluated over a small range of side-slip angle (up to 0.2°). The equivalent vertical stiffness (K_z) was also evaluated for each design factors combination from the resulting force-deflection response in the 0 to 3 kN normal load range. Table 4.5 summarizes values of K_α and K_z. It should be noted that the results were not evaluated for some of parameter combinations for the wheel designs with 47.1° cell angle due to excessive deformations of the spokes which could lead to undesired oscillations in wheel/road contact force/moment responses [108]. The results obtained from three 2^{6-1} designs considering three different cell angles are initially examined to study the influence of θ on K_α of the honeycomb wheel.

Table 4.5: Cornering and vertical stiffness of 2^{6-1} designs with different cell angles

Run #	Cornering stiffness, K_α (N/deg)			Vertical stiffness, K_z (N/mm)			Run #	Cornering stiffness, K_α (N/deg)			Vertical stiffness, K_z (N/mm)		
	47.1°	31.5°	15.8°	47.1°	31.5°	15.8°		47.1°	31.5°	15.8°	47.1°	31.5°	15.8°
1	N/A	2529	2545	N/A	89	113	17	N/A	2108	2038	N/A	92	117
2	N/A	2928	2785	N/A	118	152	18	N/A	1468	1462	N/A	121	156
3	N/A	3124	3034	N/A	111	143	19	N/A	1556	1515	N/A	113	146
4	2259	2329	1990	133	155	204	20	1768	1822	1830	139	163	216
5	N/A	2095	2264	N/A	135	174	21	981	970	998	120	152	177
6	1483	1493	1603	157	181	235	22	1246	1286	1304	160	186	243
7	1551	1537	1618	147	169	220	23	1276	1309	1321	150	174	228
8	1991	1971	2110	207	241	316	24	891	980	908	211	246	325
9	2503	2518	2344	98	109	140	25	1157	1148	1177	99	111	143
10	1825	1748	1785	125	145	190	26	1451	1469	1546	129	150	198
11	N/A	1880	1797	N/A	137	179	27	1501	1520	1568	122	141	186
12	2248	2175	2224	167	194	257	28	1070	1052	1086	171	199	265
13	1184	1134	1229	143	167	217	29	1104	1190	1138	146	169	222
14	1602	1598	1677	194	228	298	30	916	855	929	196	230	302
15	1661	1601	1711	181	213	279	31	911	871	935	183	215	283
16	1120	1117	1150	259	307	406	32	1060	1221	1106	265	315	420
Grand mean of 32 runs								N/A	1644	1648	N/A	171	223

N/A: Not available owing to excessive deformations of the spokes in the contact region

The results in Table 4.5 invariably show decreasing K_z with an increase in θ, irrespective of variations in the six design factors considered. This is attributable to the negative influence of θ on the effective elastic modulus of a 2D honeycomb spoke in the radial direction of the wheel (E_Z), which relates to cell dimensions (Fig. 4.1) [24,115] as:

$$E_Z = (t_c/l)^3 \frac{\cos\theta}{(h/l+\sin\theta)\sin^2\theta} E_{0c} \tag{4.6}$$

The effective elastic modulus of a two-dimensional honeycomb cell, normalized with respect to the initial elastic modulus of the cell-wall material (polyurethane), E_Z/E_{0c}, decreases substantially with increase in θ, as shown in Fig. 4.5, for both levels of the cell-wall thickness (t_c=2.5 and 3.5 mm, as in Table 4.3). This is attributable to the increasing cell-wall length for the spokes configurations with higher θ (Table 4.2). The reduction in E_Z/E_{0c} yields relatively greater deformation of the spokes within the contact region and lower K_z of the wheel design with a higher cell angle. The deformations of the spokes of the wheel designs with θ=47.1° were excessive, especially for lower levels of the thickness and initial elastic modulus of the annular layer (factors *C* and *D*), which correspond to runs #1-3 and #17-19 in Tables 4.4 and 4.5. As an example, Fig. 4.6 illustrates relative deformations of the spokes of the NPW models with three cell angles and lower levels of all the design factors (run #1). The excessive deformations of the spokes within the contact region is clearly evident in the figure for the NPW design with θ=47.1°. This may potentially impact the annular beam during rolling with adverse effects on vehicle ride quality and noise performance. The saturation trend in E_Z/E_{0c} may indicate minimal increase in spokes deformation and wheel deflection with further increase in θ.

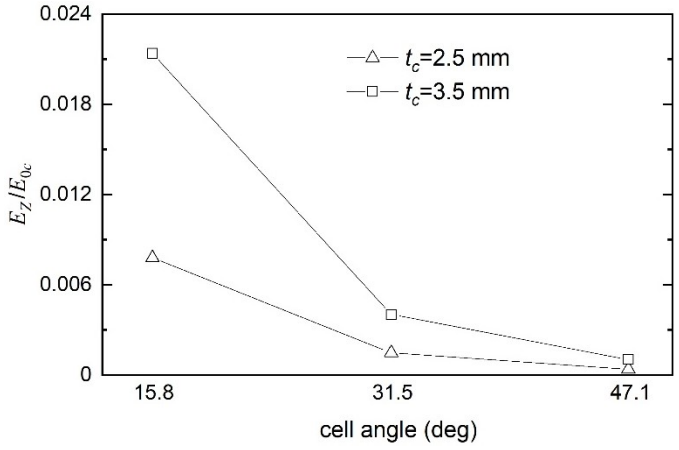

Figure 4.5: Influence of cell angle on normalized effective elastic modulus (E_Z/E_{0c}) of a 2D spoke with different cell-wall thickness

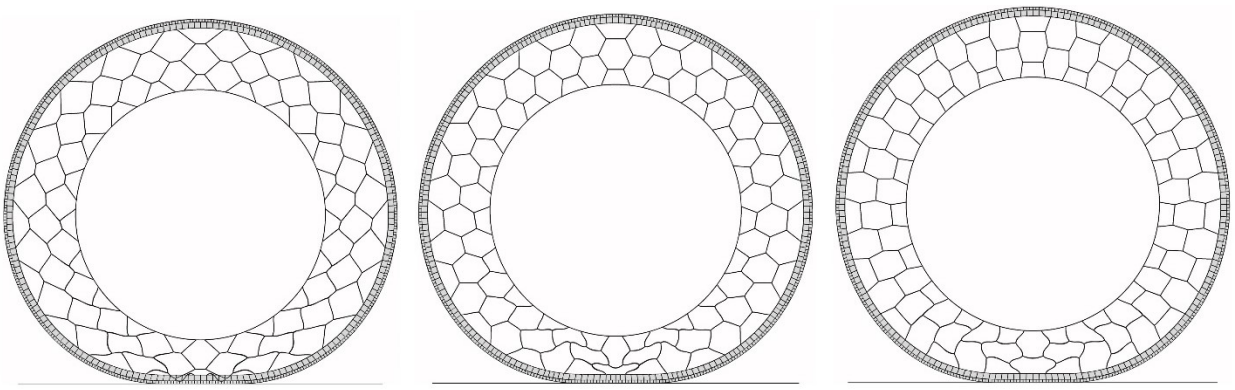

(a) (b) (c)

Figure 4.6: Deformations of spokes of wheel designs with different cell angles: (a) 47.1, (b) 31.5 and (c) 15.8° coupled with lower levels of other design factors (run #1)

Table 4.6 summarizes the mean cornering stiffness ($\overline{K_\alpha}$) obtained from two-level experiment designs considering θ=31.5 and 15.8°. The mean outcomes represent the average of K_α obtained for low and high levels of each factor. For instance, $\overline{K_\alpha}$ of the wheel designs with θ=31.5° at low and high levels of factor *A* are calculated by averaging K_α of odd- and even-numbered runs listed in Tables 4.4 and 4.5, which correspond to lower and higher levels of factor *A*, respectively. The results show $\overline{K_\alpha}$ values of 1693 and 1594 N/deg for the two levels of factor *A*, as provided in Table 4.6. The results in Table 4.6 generally suggest relatively slight influence of θ on $\overline{K_\alpha}$. The peak effect of variations in θ is limited to only -3.64%, which is evident for higher level of annular layer thickness (C_{+1}). The results in Table 4.5, however, show considerable effects of θ on K_α for the runs #4 and #30, which correspond to experiments with $A_{+1}B_{+1}C_{-1}D_{-1}E_{-1}F_{-1}$ and $A_{+1}B_{-1}C_{+1}D_{+1}E_{+1}F_{-1}$, respectively. These exhibit nearly 17% increase and 8% reduction in K_α, respectively, when θ is increased from 15.8° to 31.5°. These are suggestive of notable interactions between the cell angle and the other the design factors [114]. The effect of θ, however, is relatively small, when increased to 47.1°, although the mean effects could not be evaluated due to excessive deformations observed for some of the runs.

Table 4.6: Mean cornering stiffness ($\overline{K_\alpha}$) of wheel designs at low and high levels of each design factor considering different cell angle

Level of factors	$\overline{K_\alpha}$ (N/deg)		Deviation	Level of factors	$\overline{K_\alpha}$ (N/deg)		Deviation
	θ=31.5°	θ=15.8°	(%)		θ=31.5°	θ=15.8°	(%)
A_{-1}	1693	1702	-0.53	D-1	1844	1833	0.60
A_{+1}	1594	1593	0.06	D+1	1444	1463	-1.31
B_{-1}	1659	1676	-1.08	E-1	1986	1992	-0.29
B_{+1}	1629	1619	0.61	E+1	1302	1304	-0.17
C_{-1}	1961	1920	2.06	F-1	1417	1420	-0.27
C_{+1}	1327	1375	-3.64	F+1	1871	1875	-0.22

Factors (A, C, E) and (B, D, F) denote thickness and initial elastic moduli of cell-wall, annular layer and tread, respectively

Significance analysis

Analysis of variance (ANOVA) was performed for each 2^{6-1} design with different cell angles using Minitab 19 software to identify design factors with relatively small main effects. The eliminations of insignificant factors together with the two-factor interactions can subsequently permit the implementation of CCD approach in an efficient manner. The design factors and two-factor interactions with p-value less than 0.05 were considered as significant effects. The results of ANOVA, summarized in Table 4.7, confirmed minimal effects of factor B (E_{0c}) and its related two-factor interactions with annular layer and tread parameters (BC, BD, BE and BF) on the variations observed in K_α over the design space considered. Although, the results suggest insignificant two-factor AB (t_c, E_{0c}), AF (t_c, E_{0t}) and DE (E_{0a}, t_t) interactions for each 2^{6-1} design with different cell angles, the subsequent experiments were designed on the basis of all the two-factor interactions of remaining main effects.

Table 4.7: Results of ANOVA obtained for the 2^{6-1} designs with 31.5 and 15.8° cell angles

Factor/interaction	p-value		Factor/interaction	p-value	
	31.5°	15.8°		31.5°	15.8°
A	*<0.001*	*0.002*	*BC*	0.063	0.417
B	0.051	0.053	*BD*	0.907	0.334
C	*<0.001*	*<0.001*	*BE*	0.509	0.525
D	*<0.001*	*<0.001*	*BF*	0.073	0.227
E	*<0.001*	*<0.001*	*CD*	*<0.001*	*0.007*
F	*<0.001*	*<0.001*	*CE*	*<0.001*	*0.004*
AB	0.605	0.303	*CF*	*0.013*	0.103
AC	*<0.001*	0.061	*DE*	*<0.001*	*<0.001*
AD	0.159	*0.047*	*DE*	0.195	0.077
AE	*0.029*	0.125	*EF*	*<0.001*	*0.003*
AF	0.082	0.883			

Factors (A, C, E) and (B, D, F) denote thickness and initial elastic moduli of cell-wall, annular layer and tread, respectively; *AB* refers to interaction between factors *A* and *B*

4.3.2 Central composite designs

Additional experiments, designed according to CCD approach [109], were conducted for wheel designs with θ=31.5 and 15.8°, in order to develop regression models relating wheel's cornering stiffness to the five significant design factors (*A*, *C*, *D*, *E* and *F*) and interactions among them, as:

$$K_\alpha^* = \beta_0 + \sum_{j=1}^{5} \beta_j x_j + \sum_{j=1}^{5} \beta_{jj} x_j^2 + \sum_{1 \le i < j}^{5} \beta_{ij} x_i x_j \quad (4.7)$$

where K_α^* is model-predicted cornering stiffness, x_j (j=1,..,5) is design factor, and β_0, β_j, β_{jj} and β_{ij} are unknown model coefficients. Each factor is normalized and permitted to vary in the -1 to +1 range, where the 0 value corresponds to the medium level of the factor. The model coefficients are identified by fitting each regression model to the corresponding experimental results, using least squares error minimization technique.

The experiments were designed considering three levels of the significant design factors (*A*, *C*, *D*, *E*, *F*) so as to investigate their nonlinear influences on K_α. Table 4.8 summarizes the three levels (low, medium and high) of design factors, which are denoted as '-1', '0' and '+1', respectively. The experiment design, summarized in Table 4.9, comprised a two-level half fractional factorial design (2^{5-1} design, runs #1-16) together with ten axial (runs #17-26) and one center (runs #27) runs. The 2^{5-1} designs in CCD approach allow for assessments of two-factor interactions and main effects, while the results of axial and center runs combined with 2^{5-1} designs are used to identify the regression model coefficients (β_{jj}) of quadratic terms [114]. It should be noted that the center run does not need to be replicated for FE simulations, since it corresponds only to medium levels of all factors. The K_α and K_z, obtained for each run in the CCD, are presented in Table 4.10 for the two cell angles. The results suggest relatively small influence of θ on K_α of the wheel, as it was observed for K_α in the 2^{6-1} design (Tables 4.5 and 4.6). Moreover, negative influence of θ on K_z is also evident, as it was observed in Table 4.5.

Table 4.8: Low, medium and high levels of important design factors used for the central composite designs

Level	*A*: t_c (mm)	*C*: t_a (mm)	*D*: E_{0a} (MPa)	*E*: t_t (mm)	*F*: E_{0t} (MPa)
Low: '-1'	2.5	10	12	5	4
Medium: '0'	3.0	15	15	10	6
High: '+1'	3.5	20	18	15	8

(E_{0c}, E_{0a}, E_{0t}) and (t_c, t_a, t_t) are initial elastic moduli and thickness of cell-wall, annular layer and tread

Table 4.9: Matrix of central composite designs for the wheel with a given cell angle

Run#	Factor-level combinations	Run#	Factor-level combinations
1	$A_{-1}C_{-1}D_{-1}E_{-1}F_{+1}$	15	$A_{-1}C_{+1}D_{+1}E_{+1}F_{-1}$
2	$A_{+1}C_{-1}D_{-1}E_{-1}F_{-1}$	16	$A_{+1}C_{+1}D_{+1}E_{+1}F_{+1}$
3	$A_{-1}C_{+1}D_{-1}E_{-1}F_{-1}$	17	$A_{-1}C_0D_0E_0F_0$
4	$A_{+1}C_{+1}D_{-1}E_{-1}F_{+1}$	18	$A_{+1}C_0D_0E_0F_0$
5	$A_{-1}C_{-1}D_{+1}E_{-1}F_{-1}$	19	$A_0C_{-1}D_0E_0F_0$
6	$A_{+1}C_{-1}D_{+1}E_{-1}F_{+1}$	20	$A_0C_{+1}D_0E_0F_0$
7	$A_{-1}C_{+1}D_{+1}E_{-1}F_{+1}$	21	$A_0C_0D_{-1}E_0F_0$
8	$A_{+1}C_{+1}D_{+1}E_{-1}F_{-1}$	22	$A_0C_0D_{+1}E_0F_0$
9	$A_{-1}C_{-1}D_{-1}E_{+1}F_{-1}$	23	$A_0C_0D_0E_{-1}F_0$
10	$A_{+1}C_{-1}D_{-1}E_{+1}F_{+1}$	24	$A_0C_0D_0E_{+1}F_0$
11	$A_{-1}C_{+1}D_{-1}E_{+1}F_{+1}$	25	$A_0C_0D_0E_0F_{-1}$
12	$A_{+1}C_{+1}D_{-1}E_{+1}F_{-1}$	26	$A_0C_0D_0E_0F_{+1}$
13	$A_{-1}C_{-1}D_{+1}E_{+1}F_{+1}$	27	$A_0C_0D_0E_0F_0$
14	$A_{+1}C_{-1}D_{+1}E_{+1}F_{-1}$		

Factors (A, C, E) and (B, D, F) denote thickness and initial elastic moduli of honeycomb cell-wall, annular layer and tread, respectively

Table 4.10: Cornering and vertical stiffness of the central composite designs with different cell angles

Run #	Cornering stiffness, K_α (N/deg)		Vertical stiffness, K_z (N/mm)		Run #	Cornering stiffness, K_α (N/deg)		Vertical stiffness, K_z (N/mm)	
	31.5°	15.8°	31.5°	15.8°		31.5°	15.8°	31.5°	15.8°
1	3137	3068	101	129	15	880	938	193	253
2	2397	2153	137	178	16	1222	1111	276	365
3	1532	1605	153	198	17	1382	1412	147	191
4	1998	2155	212	277	18	1316	1339	204	267
5	1924	1787	124	161	19	1853	1839	132	172
6	2204	2255	171	224	20	1148	1190	205	267
7	1593	1716	191	250	21	1596	1637	151	197
8	1108	1156	269	354	22	1199	1218	190	249
9	1582	1550	103	132	23	1869	1901	170	221
10	1859	1885	143	188	24	1172	1173	174	229
11	1309	1328	157	204	25	1097	1116	171	223
12	962	937	216	283	26	1562	1593	172	225
13	1519	1558	127	166	27	1355	1390	171	224
14	1072	1091	175	230					

N/A: Not available owing to excessive deformations of the spokes in the contact region

Owing to the large deformations of the spokes of the NPW designs with θ=47.1° (runs #1, 5, 9, 13 and 19), the coefficients of the regression model, Eq. (4.7), were identified only for the designs with θ=31.5 and 15.8°. The coefficients of the significant main factors and their interactions (total 21 for quadratic response function considering interactions) are summarized in Table 4.11. Table 4.12 presents results of ANOVA demonstrating significance levels of the design factors and their

two-factor interactions for the two cell angles. The results in Table 4.12 suggest that all the design factors considered in the model are significant (p-value<0.05), while the quadratic terms of factors A, D and F (AA, DD and FF) and two-factor (AD, AF) interactions are not significant for both the cell angles. Moreover, the two-factor interactions AE and CF are also not significant for the designs with θ=15.8° and θ=31.5°, respectively. The accuracy of the regression models to predict output responses (cornering and vertical stiffness) were evaluated using coefficient of determination (R^2>0.999) between the cornering stiffness obtained from the FE and regression models. The regression models showed good prediction abilities with $R^2_{predicted}$ of 0.954 and 0.905 for θ=31.5 and 15.8°, respectively.

Table 4.11: Coefficients of the regression model relating cornering stiffness to the significant design factors of the wheel design with different cell angles

Coefficient	Factor/ Interaction	Cell angle		Coefficient	Factor/ Interaction	Cell angle	
		31.5°	15.8°			31.5°	15.8°
β_0		1362.22	1391.50	β_{12}	*AC*	37.95	21.95
β_1	*A*	-39.94	-48.86	β_{13}	*AD*	2.12	2.15
β_2	*C*	-321.86	-280.58	β_{14}	*AE*	18.99	6.77
β_3	*D*	-202.71	-193.80	β_{15}	*AF*	6.49	17.37
β_4	*E*	-343.52	-345.89	β_{23}	*CD*	78.60	53.76
β_5	*F*	213.81	240.84	β_{24}	*CE*	110.69	53.81
β_{11}	*AA*	-14.30	-16.40	β_{25}	*CF*	-6.56	-31.77
β_{22}	*CC*	137.40	123.00	β_{34}	*DE*	75.96	66.71
β_{33}	*DD*	34.50	36.30	β_{35}	*DF*	-17.18	-32.62
β_{44}	*EE*	157.60	145.60	β_{45}	*EF*	-34.97	-70.42
β_{55}	*FF*	-33.60	-36.70				

Table 4.12: Results of ANOVA for quadratic models with 31.5 and 15.8° cell angle

Terms	p-value		Terms	p-value	
	31.5°	15.8°		31.5°	15.8°
Model	*<0.001*	*<0.001*	*AC*	*0.001*	*0.032*
A	*<0.001*	*0.001*	*AD*	0.726	0.795
C	*<0.001*	*<0.001*	*AE*	*0.017*	0.424
D	*<0.001*	*<0.001*	*AF*	0.304	0.070
E	*<0.001*	*<0.001*	*CD*	*<0.001*	*<0.001*
F	*<0.001*	*<0.001*	*CE*	*<0.001*	*<0.001*
AA	0.369	0.447	*CF*	0.299	*0.007*
CC	*<0.001*	*0.001*	*DE*	*<0.001*	*<0.001*
DD	0.058	0.122	*DF*	*0.025*	*0.006*
EE	*<0.001*	*<0.001*	*EF*	*0.001*	*<0.001*
FF	0.063	0.119			

Factors (A, C, E) and (B, D, F) denote thickness and initial elastic moduli of cell-wall, annular layer and tread, respectively; AB refers interaction between A and B

4.3.3 Influences of design factors on cornering stiffness

The regression models are subsequently used to investigate the main effect of each significant design factor (*A*, *C*, *D*, *E* and *F*) on the cornering stiffness, K_α, while considering their two-factor interactions. It should be mentioned that the main effects represent level average corresponding to different levels of each significant design factor. The main effects predicted from the regression models were observed to be comparable for both the cell angles (θ=31.5 and 15.8°). As an example, Fig. 4.7 illustrates variations in K_α with varying levels of each design factor for θ=15.8°. The results generally suggest weakly nonlinear effects of the factors over the design space considered.

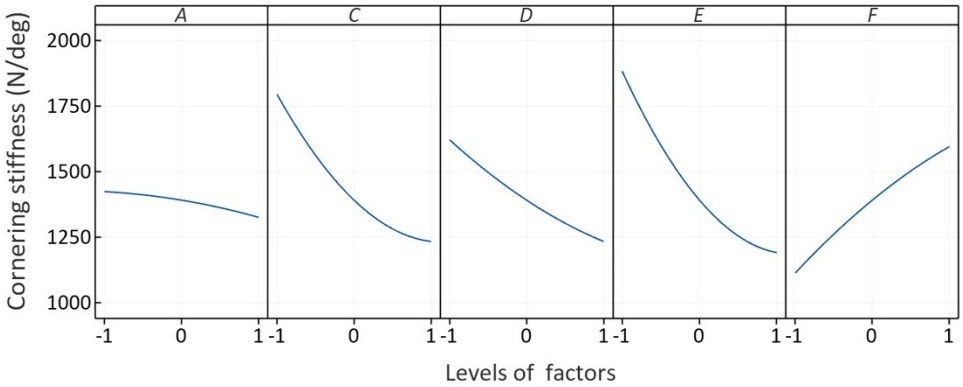

Factors (*A*, *C*, *E*) and (*B*, *D*, *F*) denote thickness and initial elastic moduli of cell-wall, annular layer and tread, respectively

Figure 4.7: Variations in cornering stiffness predicted by the regression model with varying levels of each design factor (θ=15.8°)

An increase in factor *A* (cell-wall thickness, t_c) yields only slight reduction in K_α, as shown in Fig. 4.7, although it was identified as a statistically influential factor. The honeycomb cells with lower t_c undergo higher lateral deformations and yield relatively higher cornering force under lower side slip before the sliding occurs. This can be evidenced from the cornering force-slip and lateral force-deflection characteristics of the wheel, presented in Fig. 4.8 considering two different cell wall thickness, t_c=2.5 and 3.5 mm, while the other design factors are held at their respective medium level. These correspond to runs #17 and 18 in Table 4.9, under 3 kN normal load, 0.75 friction coefficient and 10 km/h forward speed. The lateral force-deflection characteristics were obtained from the static FE analysis by displacing the road laterally up to 10 mm. The wheel model with t_c=2.5 mm yields slightly higher cornering force under low side-slip angles and thereby higher K_α,

when compared to that of the wheel with t_c=3.5 mm, as seen in Fig. 4.8(a). The relatively higher lateral deformation of the wheel with t_c=2.5 mm is also evident in Fig. 4.8(b).

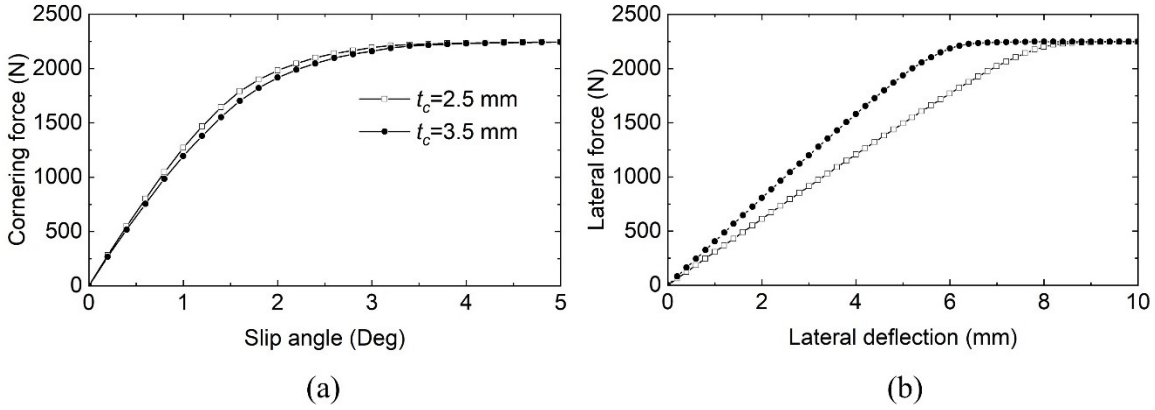

Figure 4.8: (a) Cornering force-slip and (b) lateral force-deflection characteristics of the wheel models with different cell-wall thickness, t_c (Friction coefficient: 0.75; Normal load: 3 kN)

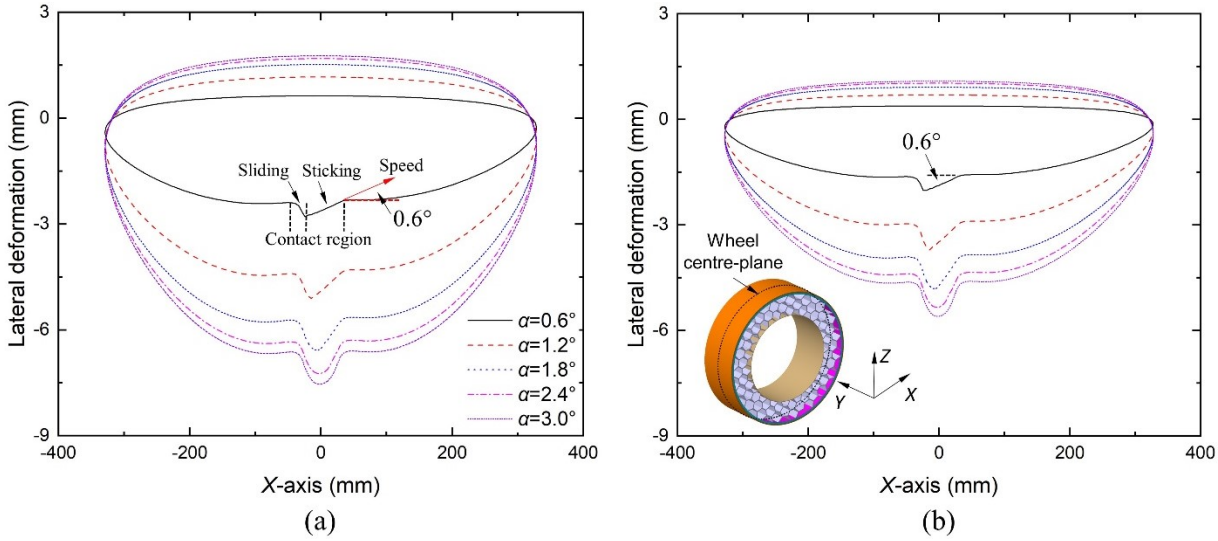

Figure 4.9: Lateral deformations of the centre-plane of the wheel models with different cell-wall thickness, t_c: (a) 2.5 mm and (b) 3.5 mm, under different side slip angles (α) up to 3°

Fig. 4.9 further illustrates the lateral deformation of the wheel at its centre plane at different side-slip angles, ranging from 0.6 to 3° for t_c=2.5 mm and t_c=3.5 mm. The wheel model with t_c=2.5 mm invariably exhibits notably higher lateral deformations in the contact region when compared to those of the wheel with t_c=3.5 mm, irrespective of the side slip angle considered. For example, for α=0.6°, the mean lateral deformations of the wheel with 2.5mm and 3.5 mm thick cell-wall are 2.58 and 1.83 mm, respectively. The considerably higher lateral deformation of the wheel with t_c=2.5 mm contributes to slightly higher cornering force under side-slip angles up to about 3.2°,

as seen in Fig. 4.8(a), although its lateral stiffness (K_y) is noticeably smaller compared to that of the wheel with t_c=3.5 mm, as seen in Fig. 4.8(b). Under low side-slip angles, where the tread adheres to the road surface with negligible sliding, the cornering force can be estimated from the product of the mean lateral deformation in the contact region with the lateral stiffness K_y. For example, the estimated cornering force of the wheel with t_c=2.5 mm at α=0.2° is 279 N, which is slightly higher than 264 N estimated for the wheel with t_c=3.5 mm. These estimated forces are in reasonable good agreements with those obtained from the simulations (282 N for the wheel with t_c=2.5 mm and 268 N for t_c=3.5 mm). Moreover, the results in Fig. 4.9 show opposing deformations of the upper and lower halves of each wheel model, as it would be expected. Results also show relatively higher magnitudes of lateral deformations with increasing α, irrespective of t_c. The relative increase in deformation magnitude (mean lateral deformations in the contact region), however, diminishes with increase in α, as seen in Fig. 4.10, which is attributed to lateral sliding of the tread with respect to the ground. The results suggest that the wheel model with t_c=2.5 mm would yield considerable higher lateral deformation compared to that of the wheel with t_c=3.5 mm, when sliding becomes dominant (α>3°), which can also be attributed to its relatively lower K_y.

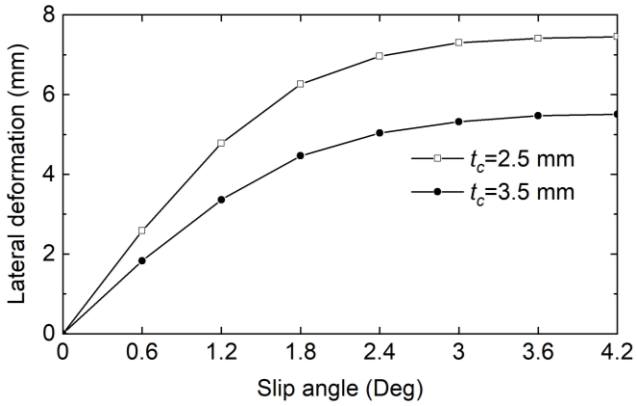

Figure 4.10: Mean lateral deformation of wheel models with different cell-wall thickness (t_c) at different side slip angles

An increase in factor *C* (annular layer thickness, t_a) results in considerable reduction in K_α, as seen in Fig. 4.7, which is attributable to decrease in the lateral deformation. Fig. 4.11 illustrates variations in the cornering force and lateral deformation responses of the wheel models with t_a=10 and 20 mm (runs #19 and 20 in Table 4.9), as a function of the slip angle, together with the lateral

force-deflection characteristics. The (mean) lateral deformation of the wheel model with t_a=10 mm is notably higher than that of the wheel with t_a=20 mm, especially under lower side slip angles up to 3°, as seen in Fig. 4.11(b). An increase in t_a, however, yields only slight reduction in K_y, as seen in Fig. 4.11(c). This is partly due to the relatively small contribution of the annular beam's deflection to the wheel lateral deformation, and in-part to the negative effects of factor *C* on the equivalent elastic modulus (E_{eq}) of the composite beam, which relates to the thickness and elastic modulus of its constituents as [54]:

$$E_{eq}=E_{0a}\frac{t_a}{t_a+2t_r}+E_{0r}\frac{2t_r}{t_a+2t_r} \tag{4.8}$$

In the analyses, E_{0r} and t_r were taken as 210 GPa and 0.5 mm, respectively. Initial elastic modulus, E_{0a}, was varied within a small range (12 to 18 MPa, as seen in Table 4.8), which resulted in minimal influence on E_{eq}. Increasing t_a from 10 to 20 mm thus leads to significantly lower E_{eq} but only slight reduction in K_y. This is also evidenced from the comparable lateral deformation magnitudes observed at relatively large side slip angles (α≈4.2°). The higher lateral deformation of the wheel with t_a=10 mm thus contributes to notably greater cornering force and K_α under low side-slip angles, as illustrated in Fig. 4.11(a).

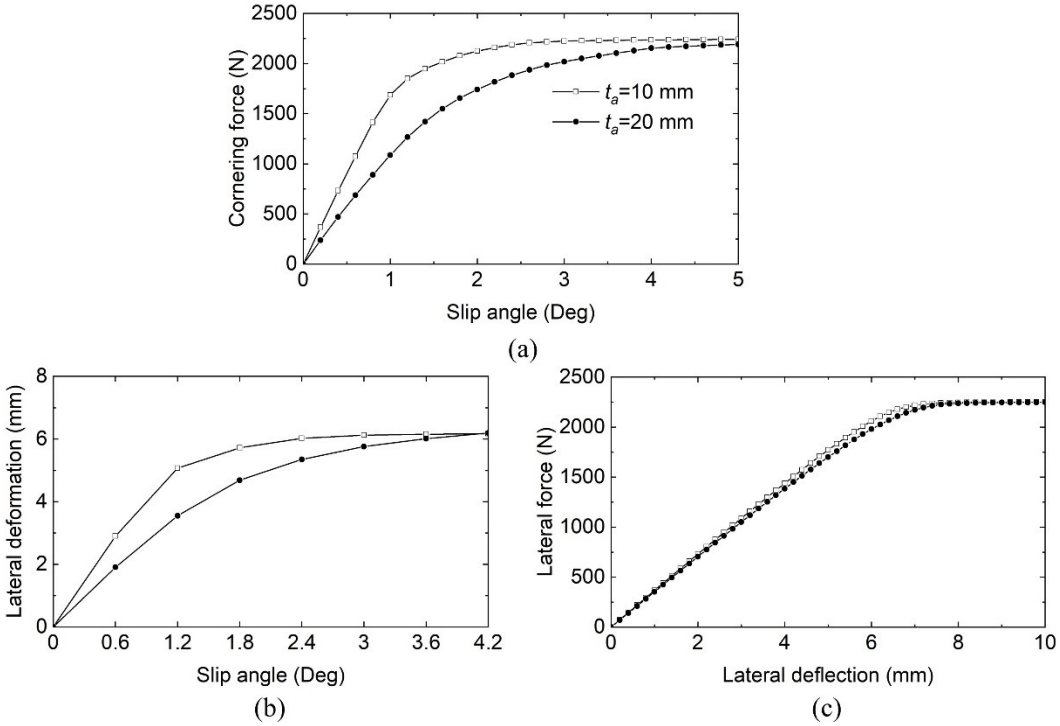

Figure 4.11: Influence of variations in the annular layer thickness (t_a) on (a) cornering force-slip, (b) lateral deformation-slip, and (c) lateral force-deflection characteristics of the wheel model

Lower K_α was also observed with an increase in factor *D* (initial elastic modulus of annular layer, E_{0a}), as illustrated in Fig. 4.7. Fig. 4.12 illustrates the cornering force-slip and lateral deformation-slip responses of the wheel for runs #21 and 22 (Table 4.9), which employ different values of E_{0a}, 12 and 18 MPa, respectively. This figure also presents the influence of E_{0a} on the lateral force-deflection characteristics of the wheel. Similar to the influence of factor *C* (t_a), the wheel with lower E_{0a} (12 MPa) undergoes considerably higher lateral deformation under small α (Fig. 4.12(b)), while the effect of E_{0a} on K_y is negligible (Fig. 4.12(c)), which contributes to higher cornering force and thus K_α than the wheel with E_{0a}=12 MPa. The influence of E_{0a} on K_α, however, is relatively small, when compared to that of factor *C*. This is partly attributable to its minimal influence of E_{eq} of the composite beam, as seen in Eq. (4.8), and thus on K_y of the wheel.

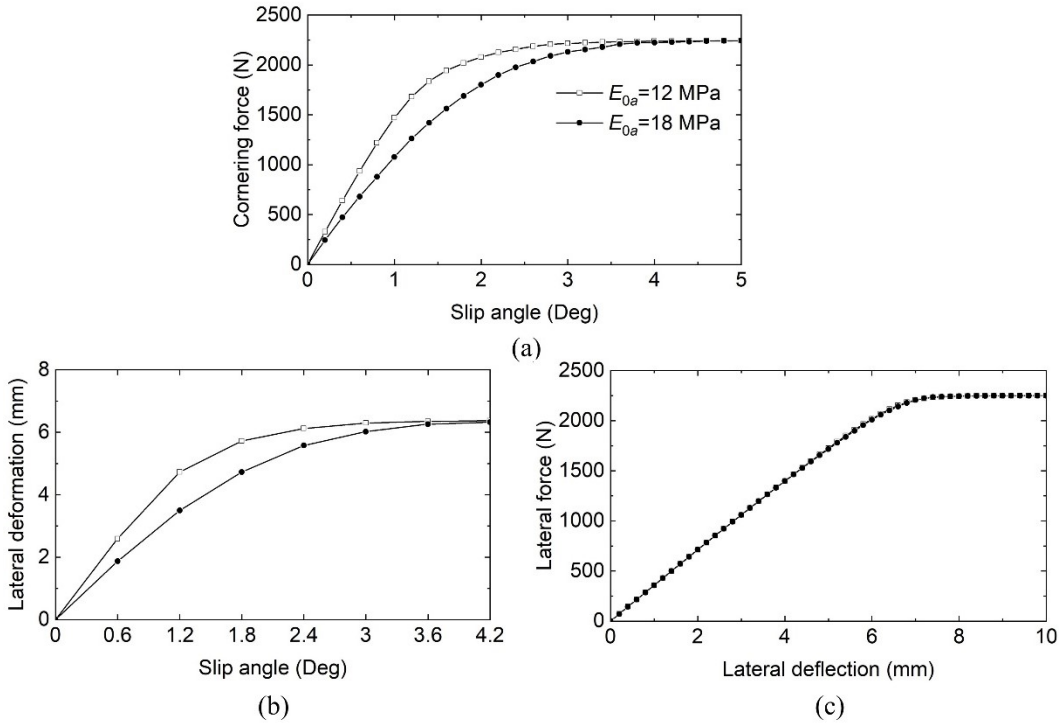

Figure 4.12: Influence of initial elastic moduli of the annular layer, E_{0a}, on: (a) cornering force-slip, (b) lateral deformation-slip, and (c) lateral force-deflection responses of the wheel

An increase in factor *E* (tread thickness, t_t) also results in lower K_α, as it was observed for factors *C* and *D*, as seen in Fig. 4.7. Varying the tread thickness affects its flexibility in the shear mode and thus the lateral deformation, which leads to more significant influence on K_α of the wheel. This is evidenced in the cornering and lateral deformation characteristics of the wheel as a function of the slip angle in Figs. 4.13(a) and 4.13(b), respectively. The results correspond to runs #23 and 24 in Table 4.9, which employ different t_t (5 and 15 mm), and show that higher tread thickness yields lower lateral deformation and K_y, and thus considerable lower K_α.

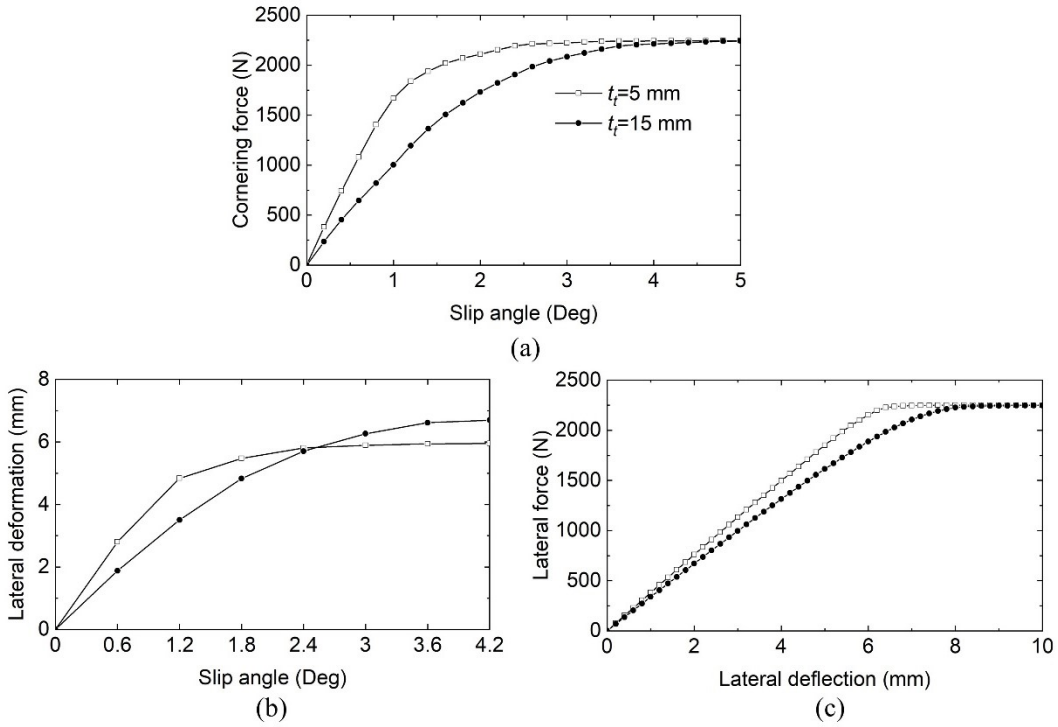

Figure 4.13: Influence of tread thickness, t_t, on: (a) cornering force-slip, (b) lateral deformation-slip, and (c) lateral force-defection responses of the wheel

Unlike the tread thickness, an increase in factor *F* (initial elastic moduli of tread, E_{0t}) results in higher K_α, as depicted in Fig. 4.7. Fig. 4.14 further illustrates the influence of E_{0t} on the cornering force-slip, lateral deformation-slip and lateral force-deformation responses of the wheel. These correspond to runs #25 and 26 in Table 4.9, which involve two different values of E_{0t} (4 and 8 MPa). Results suggest that an increase in E_{0t} yields higher lateral deformation and cornering force under small side slip conditions and thereby higher K_α. This tendency is opposite to that observed for increasing E_{0a}, shown in Fig. 4.12, which is attributable to the sandwiched structure of the annular layer. Relative higher K_y of the wheel with E_{0t}=8 MPa further contributes to higher cornering force and thus K_α.

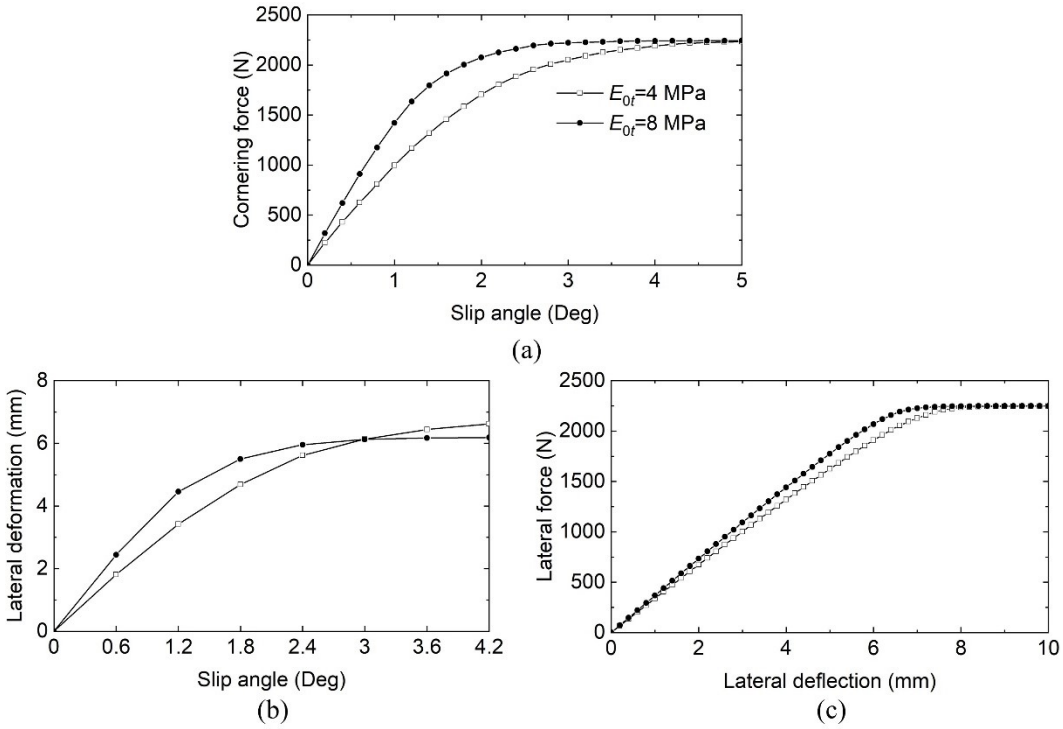

Figure 4.14: Influence of initial elastic moduli of the tread, E_{0t}, on: (a) cornering force-slip, (b) lateral deformation-slip, and (c) lateral force-defection responses of the wheel

The results from the parametric study suggest that the design factors related to the annular layer and the tread strongly influence the cornering stiffness of the NPW. The effects of design factors related to the honeycomb cell-wall (factors *A* and *B*) on K_α are relatively smaller when compared to those related to annular layer and the tread. The tuning of the tread and annular layer parameters can thus help achieve desired cornering characteristics of the honeycomb NPW. Increasing annular layer design factors (*C* and *D*) could help reduce K_α of the wheel with only slight effect on its K_y. A thicker or softer tread, on the other hand, would yield lower K_α and K_y of the wheel.

4.4 Conclusions

1. The FE models for the honeycomb wheel with different spokes' designs (cell angle) revealed satisfactory agreements with the reported studies in terms of peak spokes' stress, vertical deflection and cornering stiffness. The NPW designs with 47.1° cell angle coupled with thin and soft annular layer revealed excessive deformations and collapse of the spokes in the vicinity of the wheel-ground contact region.
2. The regression models derived for 31.5 and 15.8° cell angles could yield good approximations of cornering stiffness of the wheel, and permit parametric analyses in an

efficient manner, while considering important two-factor interactions. The models could provide essential design guidance for realizing desired cornering stiffness of the NPW designs.

3. The results obtained from screening experiments and parametric studies showed that the cornering stiffness of the honeycomb NPW is dominantly affected by the annular layer and tread design parameters. This is due to their significant effects on the out-of-plane compliance of the wheel. The initial elastic modulus of cell-wall material, however, showed only slight influence on wheel cornering stiffness, which was attributable to its negative effect on lateral deformation and positive effect on the lateral stiffness.

Chapter 5

Modal properties of honeycomb wheels: A parametric analysis using response surface method

5.1 Introduction

5.1.1 Modal properties of pneumatic tires

Vibration of a rolling wheel is primarily caused by its dynamic interactions with the terrain and the surrounding air, apart from possible non-uniformities of the wheel [81]. Such vibration can propagate to the vehicle body leading to ride discomfort and compartment noise, and contribute to community noise, although the structure- and air-borne ride disturbances are generally coupled [66,81]. The noise and vibration characteristics of pneumatic wheels have been widely investigated using analytical, experimental and numerical methods, while only limited knowledge exists on vibration properties of the evolving non-pneumatic wheels. The reported studies on pneumatic wheels have shown that the noise caused by tire's interactions becomes predominant over that caused by the drivetrain and engine at vehicle speeds over 40 km/h [75]. In addition, vibration-induced fluctuations in wheel-road contact force and moment responses may affect the steering ability, road-holding capacity, and thus the handling as well as traction/braking performance of the vehicle. The knowledge of wheel vibration characteristics is thus important for predicting and interpreting vehicle ride quality and tire noise generation.

Wheel vibration in an essence is a combination of various directionally sensitive motions, each of which could be characterized by its modal parameters in terms of natural frequencies, mode shapes, modal mass and modal damping. These parameters are influenced by the geometric and material properties of their constituents, apart from the operating and boundary conditions [68,94]. Many studies have thus investigated vibration characteristics of pneumatic tires under different conditions using experimental, analytical or finite element (FE) methods [81,94].

Numerous experimental investigations have been reported on the modal properties of tire-rim assemblies under different constraints and operating conditions, particularly for the non-rotating scenarios [68-71]. In these measurements, tire-rim assemblies are generally excited by an instrumented impact hammer or vibration exciter along radial and tangential directions, and the resulting responses are measured at multiple locations on tire/rim perimeters using accelerometers.

Curve-fitting of the frequency response functions derived using measured inputs and outputs could identify natural frequencies and modal damping of corresponding mode shapes [69]. Yam et al. [68] conducted modal testing of a free non-contacting tire suspended by bungie cords with natural frequency less than 1 Hz, which is far less than the first natural frequency of the tire. This could yield intrinsic modal properties of the tire-rim assembly with minimal contaminations from constraints. Moreover, a number of studies compared modal properties of tire-rim assemblies under various combinations of spindle (free, pined and fixed) and contact patch (free and fixed) constraints [70,71]. The results showed significant influences of boundary conditions on the lower vibration modes in each direction. The influences, however, diminished rapidly due to the progressively decreasing rim motion with increasing frequency. In addition, positive influences of inflation pressure and wheel load on natural frequencies were reported as expected, although with few exceptions [68,70,72].

The modal parameters of loaded rotating tires (pinned spindle) have also been investigated in a few studies, which were identified from tread and sidewall vibration velocities excited by cleats and measured by laser Doppler vibrometer [75,76]. The results reported significant decrease in natural frequencies when a stationary tire undergoes rotation, while the effect of rotating velocity was relatively small. It should be noted that limited number of natural frequencies could also be determined from spindle displacement and force variations trigged by drop- and cleat-test, respectively. The mode shapes suggesting tire local deformation, however, could not be identified from these tests.

The reported experimental methods could determine a number of mode shapes with relatively low natural frequencies. The high natural frequencies, however, are difficult to identify due to the superposition of mode shapes caused by tire damping effects [81], apart from the higher density and complexity of vibration modes. In addition, many vibration patterns involving out-of-plane deformations could rarely be triggered.

Many studies developed analytical models, also referred to as physics-based models, to predict tire in-plane (vertical-longitudinal) vibration characteristics. These generally approximate the tire with no contact as a thin circular shell or as a ring belt supported by distributed springs representing the sidewall and pressurized air [49,82], while taking advantages of the axisymmetric structure and the associated mathematical simplicity. Ground contact is induced either as an external load or displacement constraints. Soedel [49] investigated dynamic responses of a rolling

tire, using modal expansion method, as functions of its non-contact modes and natural frequencies (stationary or rotating). This model, however, failed to deal with high frequency road excitations due to the thin shell assumption. Moreover, accurate predictions of tire vibration responses necessitate sufficient modal information of non-contacting tires, which is still challenging for present industrial practice, particularly for the rotating scenarios. Soedel and Prasad [85] derived natural frequencies and mode shapes of a stationary tire with ground contact from its non-contact modal information using the receptance and the modal expansion methods. This analytical model, however, only considered vibration modes excited by pure radial displacements. Huang and Su [83] developed a ring on elastic foundation model for a rolling tire and determined natural frequencies corresponding to its symmetric and anti-symmetric modes, arising from the radial and tangential contact constraints or forces, respectively. The results showed bifurcation of natural frequencies of flexible modes due to Coriolis acceleration associated with tire rotation. The model, however, was verified only for a stationary tire with ground contact, and showed limited accuracy for higher-order modes.

While the above-stated physics-based models could provide valuable insights into the tire dynamic characteristics, the formulations of these models, however, are relatively complex and necessitate measurements for model parameterization. Finite element (FE) methods have been widely used to study three-dimensional (3D) vibration characteristics of tires due to their capacities in handling various spindle and contact constraints, apart from variations in material and geometric properties of the constituents [81]. Studies have reported different element formulations to study modal properties of tires. A geometrically non-linear, doubly curved, axisymmetric shell element was developed to predict natural frequencies of a steel belted radial tire, considering pined or fixed spindle and non-contact conditions [88,89]. The element formulation considered the orthotropic properties of laminated composite materials and the stiffness variations resulting from inflation pressure and large displacements. Similarly, Saigal et al. [90] developed a membrane element to conduct qualitative evaluations of free vibration characteristics of tires. This element, however, could only model certain tires with relatively low inflation pressure. Chang et al. [91] investigated dynamic responses of a radial tire subjected to different road excitations using the shell element developed in [88,89] and the modal expansion method. It is noted that the abovementioned FE analyses employed only a few elements and yielded reasonably accurate predictions of tire modal parameters with limited computational cost. These elements, however, involved relatively

complex formulations. Alternatively, many studies have used elements with relatively simple formulations available in commercial software [66,81,94]. This allowed for explicit representation of tire components and their material properties, although a large number of elements were generally needed.

The modal properties of stationary tires with various spindle and patch constraints have been widely studies using different commercial software [71,81,92,94]. For instances, Zhang et al. [94] developed a comprehensive nonlinear FE model of a non-contacting tire with fixed spindle considering isotropic rubber tread block and multiple anisotropic cord-reinforced belt and carcass layers. The results reported notably negative influence of the cord angle on natural frequencies over 60 Hz. Some studies considered modal properties of loaded tires with free [66,71], pined [71], fixed [71,92] and vertically movable spindle [81]. The results showed the bifurcation in natural frequencies of repeated roots corresponding to non-contacting scenarios at the onset of loading. Higher natural frequencies were also reported with increasing inflation pressure or wheel load. Satisfactory agreements between FE-predicted and measured natural frequencies were observed for stationary tires, irrespective of spindle and patch constraints [66,93]. Relatively fewer studies [66,81], however, have investigated natural frequencies and mode shapes of loaded rotating tires. Only limited verifications of FE tire models under such conditions could be found due to difficulties in obtaining modal parameters from operational modal analysis. The results showed considerable reduction in natural frequencies of some of the vibration modes (e.g., torsion mode involving rotation about the wheel axis) at the onset of rotation. This is mainly due to the fact that the rotational motion relieved the contact stress developed under the static loading condition, leading to reduction in the tire stiffness [66,81]. The measured natural frequencies in [75,76], however, showed significant reductions for most vibration patterns considered, when tire's rotation was initiated. The FE methods are thus considered to provide accurate predictions of tire modal properties under stationary conditions with or without loading, while those under rolling conditions would be of concern.

5.1.2 Honeycomb non-pneumatic wheels

Honeycomb non-pneumatic wheels (NPWs) in general use hexagonal cellular spokes, also referred to as honeycomb spokes, replacing the pressurized air and continuous sidewalls of the pneumatic tires. The other components include the rim, an annular sandwich beam and the tread block. This

airless design could eliminate inflation pressure-induced maintenances and failures, and reduce couplings among the wheel's multi-axis stiffness and thus broader wheel design space [1,108]. Moreover, the honeycomb spokes and the core layer of the sandwich beam could be constructed using thermoplastic polyurethane of relatively low hysteresis loss [7]. These wheels could thus be considered as potential substitutes of the pneumatic tires with improved safety, and rolling resistance and environment performance.

Studies on honeycomb NPWs for vehicular applications have primarily focused on the influences of variations in wheel geometrical and material parameters on multiple performance measures under stationary and rolling conditions, using the FE methods. These include multi-axis stiffness [108,115], spokes' stresses and deformations [5,6,107], cornering force and self-aligning moment [108], wheel/road contact pressure distribution [115] and rolling resistance [6]. Detailed reviews of studies on different properties of NPWs have been reported in [108,115]. It has been shown that for a given target load carrying capacity, NPWs with regular honeycomb spokes (positive cell angle) exhibit lower mass and could thus offer lower rolling resistance, when compared to their auxetic counterparts of identical but negative cell angle. Moreover, the cell angle of honeycomb spokes showed notable influences on multi-axis stiffness properties of the wheel [115]. The regular honeycomb spokes of varying cell angles were thus chosen for the present study to investigate modal properties of the honeycomb NPWs.

While considerable data are available for above-mentioned wheel properties, only limited efforts are evident on vibration properties of the honeycomb NPWs. Lee et al. [13-14] investigated vibration characteristics of two NPWs with regular and auxetic honeycomb spokes under steady-state rolling conditions, respectively, using the FE methods. The response spectra of the wheels invariably showed additional excessive amplitude peaks under excitation frequencies related to the number of discrete spokes as well as the rolling speed. The study also reported modal properties of NPWs under stationary conditions. The unloaded wheel with regular spokes revealed lowest natural frequency of 33.2 Hz corresponding to the torsion mode, while the first mode of the pneumatic tires in general occurs in the lateral mode [66,81,92]. Moreover, the loaded wheel with auxetic spokes revealed hop mode of 23 Hz, which is comparable to those of passenger car pneumatic tires that occur in the 10 to 20 Hz range [116]. These studies obtained modal parameters of specific NPW designs, while the influences of variations in wheel design parameters were not

considered, which are vital for establishing the essential design guidance regarding vibration properties of these promising design concepts.

The influences of design parameters on natural frequencies of selected vibration modes of stationary pneumatic tires with fixed spindle and no ground contact have been investigated using FE methods, while considering variations in one-parameter-at-a-time approach [92,94]. This sequential approach, however, fails to consider the effects caused by interactions among the design parameters, which are commonly seen in engineering systems [109]. Besides, it is impractical to conduct a parametric analysis using this approach due to the large number of parameters combinations and the resulting high computational cost of FE simulations, particularly for multiple design variables. An alternative approach is the response surface method (RSM), which allows for development of response surface models considering both main and interaction effects of the design parameters in a systematic, reliable and efficient manner [109,110]. The parametric effects on vibration properties of NPWs, however, have been attempted in a very few studies limited only to a mechano-elastic NPW design with hinge-unit spokes [44,117].

This study aims at evaluating the effects of chosen wheel design parameters on natural frequencies corresponding to the influential vibration modes of a stationary honeycomb NPW with different spokes configurations, considering a given normal load of 3 kN. To achieve this, three-dimensional (3D) FE models of the NPW with three different (positive) cell angles were initially developed. The validity of these models was demonstrated through comparisons of FE-predicted wheel responses with available data in the published studies, considering identical material properties as well as similar wheel and components dimensions. The responses include spokes' peak stress and wheel overall vertical deflections under various normal loads, apart from natural frequencies of a honeycomb wheel with fixed spindle and no ground contact. FE simulations were subsequently conducted according to the design points determined from the one-half fractional factorial design, considering two levels for each factor, so as to exclude design parameters of minor influences. The effects of the remaining significant design factors and their two-factor interactions were further investigated using FE simulations for the design points developed using the central composite design (CCD) approach. Regression models relating natural frequencies of influential vibration modes with corresponding significant design factors were finally formulated considering both main as well as interaction effects, using the RSM technique. The results could offer important design guidance for honeycomb NPWs in view of their vibration characteristics.

5.2 FE modelling of the honeycomb NPW and experimental design

Comprehensive three-dimensional FE models were developed for a honeycomb NPW of varying cell angles (θ) so as to investigate wheel's modal properties together with their dependence on θ. The models were formulated considering three different cell angles (15.8, 31.5 and 47.1°), which are considered as practical designs [5,6]. Moreover, some data have been reported for the wheel designs with identical θ values in [6,13,108], which facilitated verifications of the developed FE wheel models in the present study.

Fig. 5.1 illustrates the honeycomb NPW comprising the aluminium rim, a number of polyurethane spokes (θ=31.5°), annular composite beam and the rubber tread. The three-layer annular composite beam, also referred to as shear ring, consists of a shear-dominated core layer (polyurethane) sandwiched between two nearly inextensible steel rings. The FE modelling of the honeycomb wheel design has been described in recent studies [108,115]. Briefly, the mechanical behaviours of the elastic rim and rings are modelled using the linear elasticity theory, while those of the hyper-elastic tread, spokes and the core layer are described using Ogden strain energy potential, which relates to the deviatoric principal stretches ($\bar{\lambda}_1$, $\bar{\lambda}_2$ and $\bar{\lambda}_3$) and the elastic volume ratio (J^{el}) as:

$$U = \sum_{i=1}^{Q} \frac{2\mu_i}{\alpha_i^2}\left(\bar{\lambda}_1^{\alpha_i} + \bar{\lambda}_2^{\alpha_i} + \bar{\lambda}_3^{\alpha_i} - 3\right) + \sum_{i=1}^{Q} \frac{1}{D_i}\left(J^{el} - 1\right)^{2i};\ Q{=}3 \tag{5.1}$$

where U is the strain energy per unit volume, while μ_i, α_i and D_i (i=1, 2, 3) represent the material model parameters. These model parameters were taken as those reported in [6,13,108], which were identified using measured stress-strain relations, as summarized in Table 5.1, together with those of the elastic materials. It should be pointed out that the studies on pneumatic tires have reported only minimal differences between the damped and un-damped natural frequencies [48]. The viscous effects associated with polyurethane and rubber components could thus be considered negligible when studying wheel's modal properties with particular focus on natural frequencies.

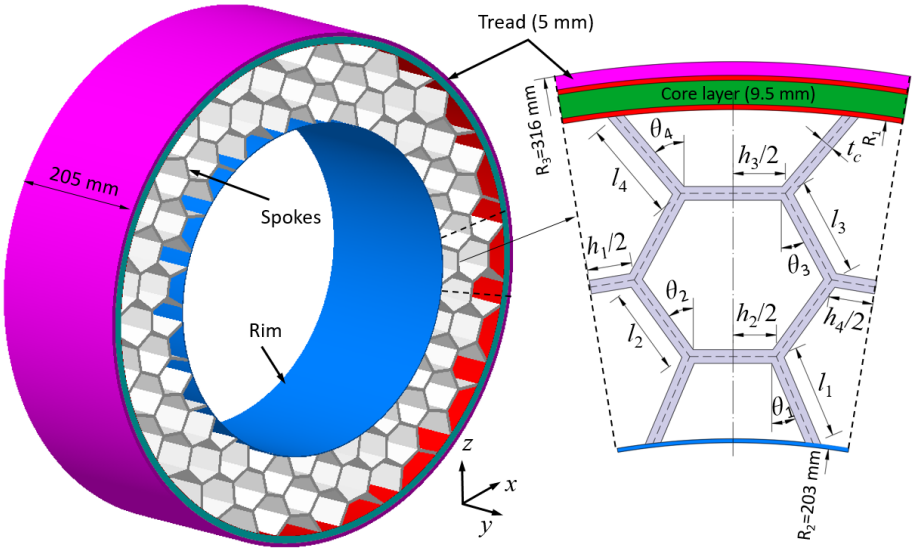

Figure 5.1: Components and dimensions of honeycomb NPW with 31.5° cell angle

Table 5.1: Material model parameters for polyurethane, rubber, steel and aluminium [6,108]

i	Polyurethane			Rubber		
	μ_i(MPa)	α_i	D_i (MPa^{-1})	μ_i(MPa)	α_i	D_i (MPa^{-1})
1	13.55	1.51	3.5E-03	13.36	1.63	5.9E-03
2	-2.34	2.21	0	-6.63	1.90	0
3	0.09	-2.47	0	0.06	-2.46	0
	Elastic modulus, E (GPa)		Poisson's ratio, ν		Density (kg/m^3)	
Steel	210		0.29		7800	
Aluminium	72		0.33		2800	

The nominal dimensions of the honeycomb NPW considering different θ were chosen to conform to a radial-ply car tire (205/55R16) [96]. These dimensions in terms of rim and wheel width together with their radii are thus taken as 205, 203 and 316 mm, respectively (Fig. 5.1). Moreover, the thickness of the rim, which was considered as a rigid body in the wheel models owing to its negligible deformations, was fixed as 1 mm, while those of the core layer, two steel rings and the tread were taken as 9.5, 0.5 and 5 mm, respectively, similar to those reported in [6]. In addition, the cell-wall dimensions in terms of the cell angle (θ) and the cell-wall height (h) and length (l) are considered as the means of θ_j, h_j and l_j (j=1,..,4), respectively, as shown in Fig. 5.1. These dimensions of the three spoke designs considering different θ are summarized in Table 5.2 together with corresponding cell-wall thickness (t_c). It should be mentioned that t_c of the three spoke deigns were tuned so as to yield wheel vertical deflection close to that of the reference pneumatic tire (15.8 mm) when supporting 3 kN normal load [96].

Table 5.2: Cell-wall dimensions of honeycomb NPWs considering different cell angles

Cell angle, θ (deg)	Cell-wall		
	Height, h (mm)	Length, l (mm)	Thickness, t_c (mm)
15.8	35.2	24.9	1.54
31.5	26.8	28.3	2.38
47.1	16.1	35.5	2.82

The details concerning the material models and properties, wheel/road contact and interactions, and element formulations have been presented in [108,115] in addition to the mesh convergence study and model verifications. Briefly, the static coefficient of friction was taken as 0.80 so as to represent the interaction of the wheel with a dry asphalt road under the quasi-static loading condition [54]. The rim, spokes and two steel rings in the wheel model were represented by reduced-integration shell elements (S4R) available in ABAQUS software, while the core layer and tread were discretized by C3D8RH solid elements with reduced integration and hybrid formulation. The mesh convergence study was conducted to determine near-optimal element sizes for each component, which could ensure convergence of the results with minimal computation cost. The responses considered are the peak stress in the spokes and overall vertical deflection of the wheel under 3 kN normal load, apart from its cornering force at 10 km/h forward speed and 0.5° side-slip angle. The in-plane (*x*-*z* plane, as in Fig. 5.1) element dimensions × width in *y*-direction for the tread, core layer, rim, spokes and the two steel rings were determined as 5×5×7, 9.5×9.5×7, 5×7, 4×7 and 8×7, respectively. It should be noted that the validity of the developed FE wheel models with different θ was demonstrated by comparing predicted vertical deflections of the wheel and peak stresses in the spokes with those reported in [6], which employed identical material properties and loading condition, as well as comparable wheel and components dimensions. Comparisons of predicted and reported wheel responses showed relatively good agreements under different normal loads, ranging from 2 to 4 kN. The peak error between the two was observed to be less than 5.6% [108,115]. Additional model verifications in view of wheel's modal properties are conducted in the present study, as described in the following subsection.

5.2.1 Method of analyses and additional model verifications

In order to investigate modal properties of the loaded wheel, the static loading simulation was initially conducted. This was achieved by applying a 3 kN normal load to the center of the wheel

rim in a ramp manner. The other degrees-of-freedom (DoF) of the rim center as well as those of the road were constrained as described in [81]. The nonlinearities resulting from material constitutive relations, large-displacement effects and wheel/road contact were considered, although subsequent modal analysis of the loaded wheel was performed based on linear theory. The contact of the loaded wheel model with the road constrains zero normal motions for the contact nodes, while their tangential displacements depend on the corresponding interaction state [81]. In the adhesion region of the contact patch, the tangential motion remains zero, which is also unconstrained within the slipping region. The modal properties of the wheel models were evaluated via solutions of the eigenvalue problem:

$$\left(-\omega_\eta^2[M] + [K]\right)\phi_\eta = 0 \tag{5.2}$$

where $[M]$ is the symmetric and positive definite mass matrix of the wheel model, and $[K]$ denotes its stiffness matrix; ω_η and ϕ_η represent the natural frequency and mode shape, respectively, corresponding to vibration mode η. It should be mentioned that $[K]$ is influenced by the stress state of the wheel model under given operating and boundary conditions, apart from the stress-strain relations for the wheel constituent materials.

The validity of the developed FE wheel model was examined considering θ=31.5° by comparing the natural frequencies of selected vibration modes with the available data reported in [13]. The material properties and dimensions of this wheel model, however, were tuned to approximately conform to those of the reported NPW design (not shown) [13]. Fig. 5.2 shows the comparison of model-predicted natural frequencies with the reported results, considering fixed spindle and non-contact conditions. In this figure, the selected three vibration modes correspond to Torsion, Yaw and Twist modes, respectively, the deformations of which are discussed in Section 5.2.2. The results suggest reasonably good agreements with the reported natural frequencies, while the peak difference between reported and predicted natural frequencies is less than 2.4%. The developed FE wheel models could thus be considered valid in view of the available information in [6,13], and be used for subsequent parametric study on the natural frequencies of chosen vibration modes.

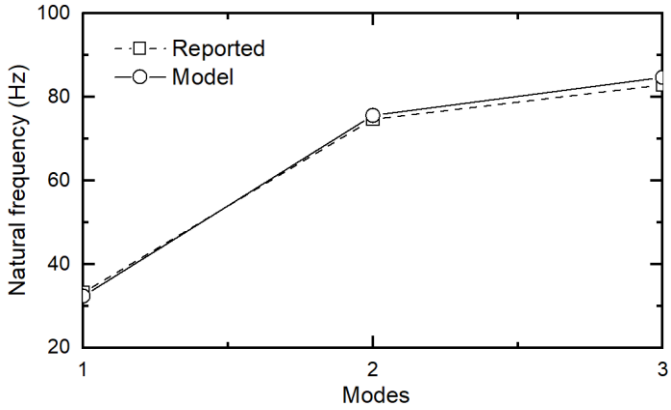

Figure 5.2: Comparison of model-predicted and reported natural frequencies [13] for the honeycomb wheel model with 31.5° cell angle

5.2.2 Chosen vibration modes

A honeycomb NPW exhibits a large number of in-plane (*x*-*z* plane, as in Fig. 5.1) and out-of-plane vibration modes. The dynamic responses of the wheel, however, are expected to be predominantly influenced only by limited number of modes of vibration, as in the case of pneumatic tires [91]. The significance of a vibration mode may be judged on the basis of the modal participation factor or modal effective mass, given as [95]:

$$\gamma_{\eta i} = \frac{1}{\phi_\eta^{\mathrm{T}}[M]\phi_\eta}\phi_\eta^{\mathrm{T}}[M]T_i \tag{5.3}$$

$$m_{\eta i}^{\mathrm{eff}} = \left(\gamma_{\eta i}\right)^2\left\{\phi_\eta^{\mathrm{T}}[M]\phi_\eta\right\} \tag{5.4}$$

where $\gamma_{\eta i}$ and $m_{\eta i}^{\mathrm{eff}}$ are the modal participation factor and modal effective mass corresponding to vibration mode η in direction i (i=x, y, z, θ_x, θ_y, θ_z), respectively. θ_x, θ_y, and θ_z represent rotations about *x*-, *y*-, and *z*-directions, respectively. ϕ_η^{T} denotes the transpose of the eigenvector ϕ_η, and T_i represents the rigid body responses resulting from imposed rigid body excitations along direction i [95].

The vibration modes showing high magnitude of $\gamma_{\eta i}$ or $m_{\eta i}^{\mathrm{eff}}$ could be readily excited by road excitations along direction i. Moreover, $\gamma_{\eta i}$ and $m_{\eta i}^{\mathrm{eff}}$ may vary considerably under different operating and boundary conditions. This study, however, focuses only on the dominant vibration modes of the wheels in contact with the ground while subjected to a given normal load (3 kN). Moreover, the vibration modes with natural frequencies (f) higher than 100 Hz are not considered due to their relatively small influences on vehicle ride and handling performances [92]. As an example, Fig. 5.3 illustrates the modal effective mass fraction (MEMF), defined as the ratio of the

modal effective mass and the total mass, associated with the vibration modes of the wheel model with θ=31.5°, and nominal dimensions and material properties in Table 5.1. The figure shows the variations for all the 137 vibration modes with $f \leq 300$ Hz.

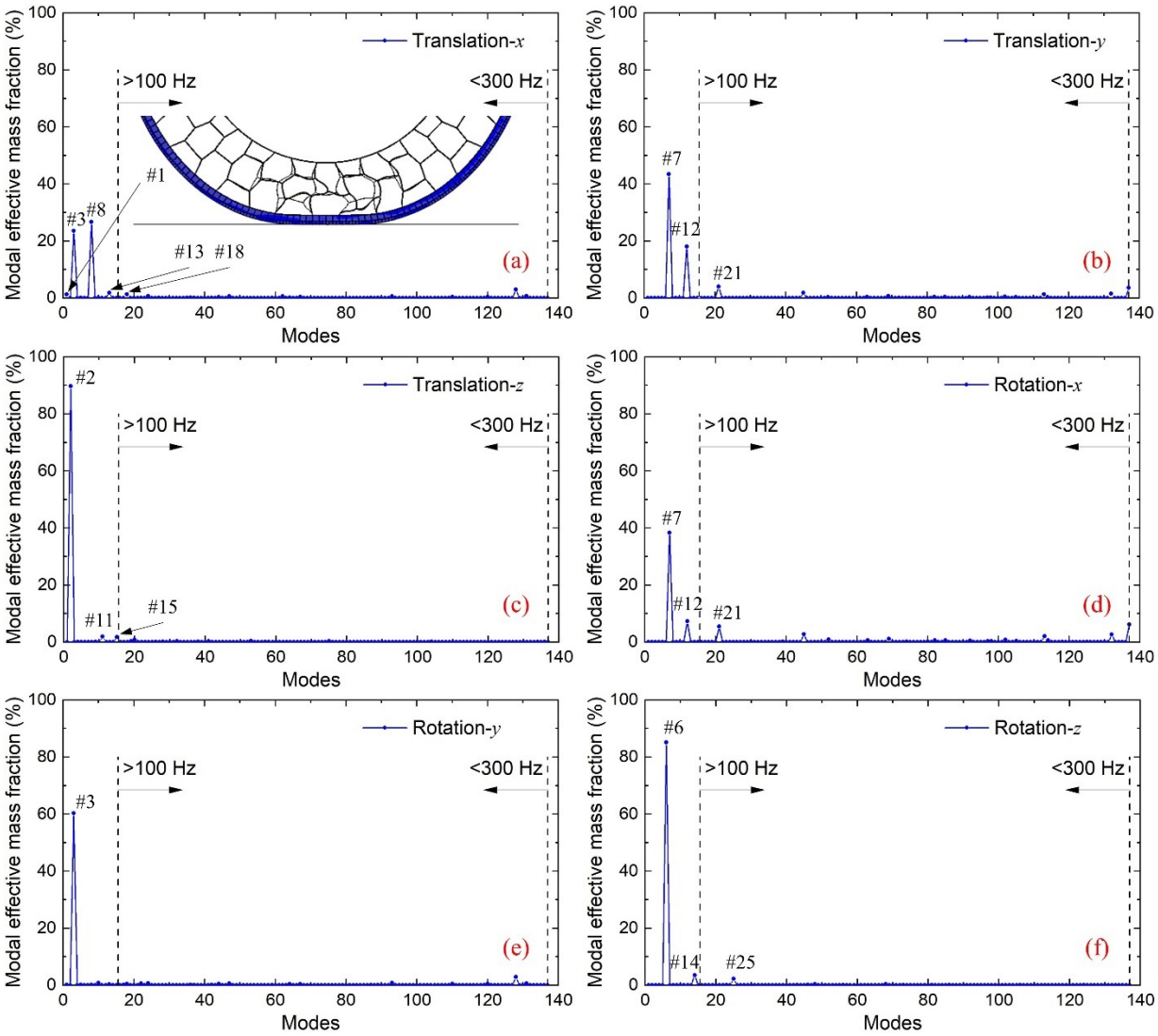

Figure 5.3: Modal effective mass fraction (MEMF) of vibration modes (natural frequencies ≤ 300 Hz) in different directions: (a) x; (b) y; (c) z; (d) Rotation θ_x; (e) Rotation θ_y; (f) Rotation θ_z

The results suggest that only a few modes of vibration exhibit notably high MEMF in each direction, as it would be expected. The highest MEMF (≈ 89.7%) was observed for the first vertical mode (#2, f=22.15 Hz), symmetric about y-z plane and denoted as Hop, as seen in Fig. 5.3(c). This mode revealed local deformations near the wheel/road contact region together with wheel translation along the z-direction, as seen in Fig. 5.4. The frequency of this critical mode is comparable with those of the passenger car tires [54,71], which further suggests the validity of the

developed FE wheel model. It should be mentioned that a relatively lower Hop mode frequency would be expected when a heavier rim is used, which is due to its mass dynamics in the *z*-direction. The vibration isolation characteristics of the suspension system and therefore vehicle ride quality is significantly influenced by wheel hop resonance. The other two symmetric modes in *z*-direction with f<100 Hz (#11 and #15), shown in Fig. 5.4 and designated as Oval and Tri, respectively, exhibit much smaller MEMF (<1.9%), as seen in Fig. 5.3(c). These two modes are thus not considered as important in-plane modes.

The first torsion mode (#3, f=33.29 Hz), designated as Torsion, shows relatively high MEMF for rotational motion about the *y*-axis and the translational motion along *x*-direction, in the order of 60.4 and 23.6%, respectively, as seen in Figs. 5.3(a) and 5.3(e). This is attributable to the coupling between the rotational motion and the tangential deformations of the wheel, resulting from the contact constraint, as depicted in Fig. 5.4. The mode #8 (f=62.95 Hz), denoted as Oval-Diag, is viewed as another important in-plane vibration pattern considering its relatively high MEMF (26.2%) in the *x*-direction, as depicted in Figs. 5.3(a) and 5.4. Significant influences of these important tangential modes (Torsion and Oval-Diag) are expected in view of vehicle braking/traction performances. Insignificant MEMF, however, are observed for mode #13 (Tri-Diag) and mode #18 (Quad-Diag), as partly seen in the figures. In addition, the mode #1 (f=17.68 Hz) exhibits considerably low MEMF of 1.36 % along the *x*-direction, as seen in Fig. 5.3(a). Unlike the above-stated important in-plane vibration modes which reveal global motions or deformations, this mode only exhibits local (shear) deformations in the spokes near the wheel/road contact region. This mode is thus viewed as an insignificant vibration pattern, although its frequency may lie in the vicinity of natural frequency of the unsprung mass.

Contact-induced coupling is also observed between the translational motion of the loaded wheel along the *y*-axis and its rotational motion about the *x*-axis, as seen in Fig. 5.5. The out-of-plane vibration modes #7, #12 and #21, symmetric about the *y*-*z* plane, thus show relatively higher MEMF in both the directions, as seen in Figs. 5.3(b) and 5.3(d). The modes #7 and #12 with f<100 Hz, denoted as (first) Lateral and Twist, respectively, are thus chosen as influential out-of-plane vibration patterns. The mode #6, denoted as Yaw, shows nearly 85% MEMF in the rotational direction about the *z*-axis, while the other two modes (#14 and #25) are associated with relatively minor contributions, as illustrated in Fig. 5.3(f). This mode is thus considered as an additional important out-of-plane vibration pattern. These chosen important out-of-plane vibration modes in

terms of Lateral, Twist and Yaw, shown in Fig. 5.5, may dominate wheel responses when subjected to side or steering excitations.

It should be noted that the Hop, Torsion, Lateral and Yaw modes of the wheel loaded against the road are transformations of the rigid body modes corresponding to the non-contacting wheel with free spindle [70]. Moreover, same important in-plane as well as out-of-plane vibration modes were also observed for the wheel models with 15.8 and 47.1° cell angles, although their frequencies and the corresponding MEMF differed.

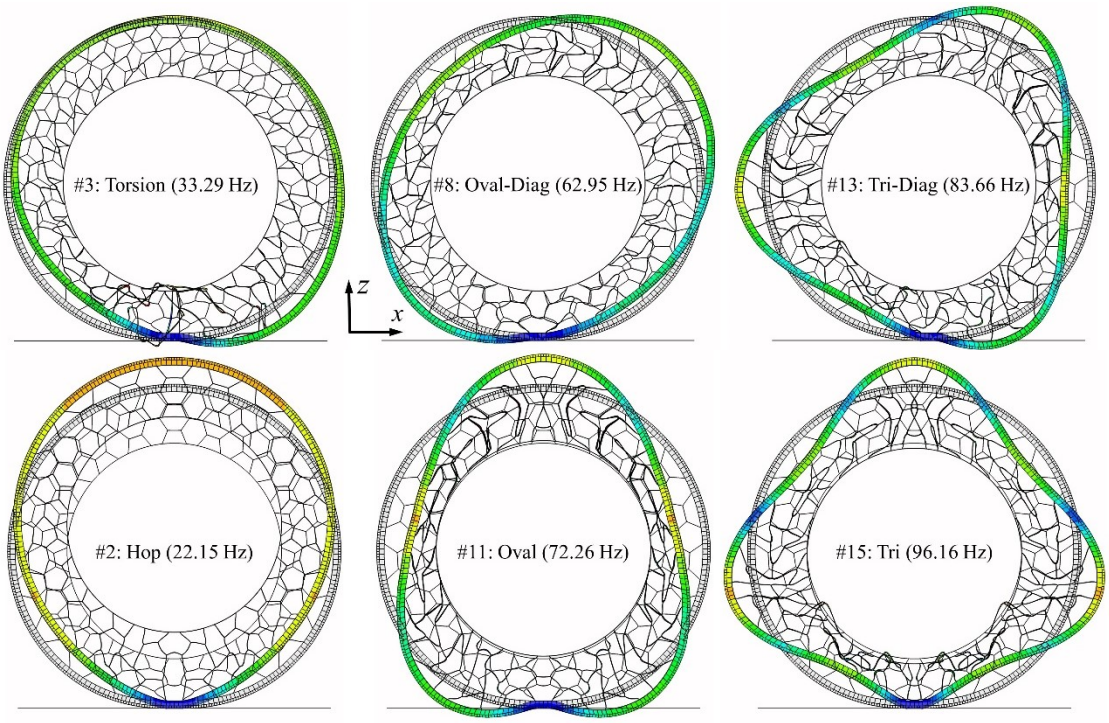

Figure 5.4: In-plane mode shapes of the wheel model with 31.5° cell angle (deformation scaling factor = 63.9)

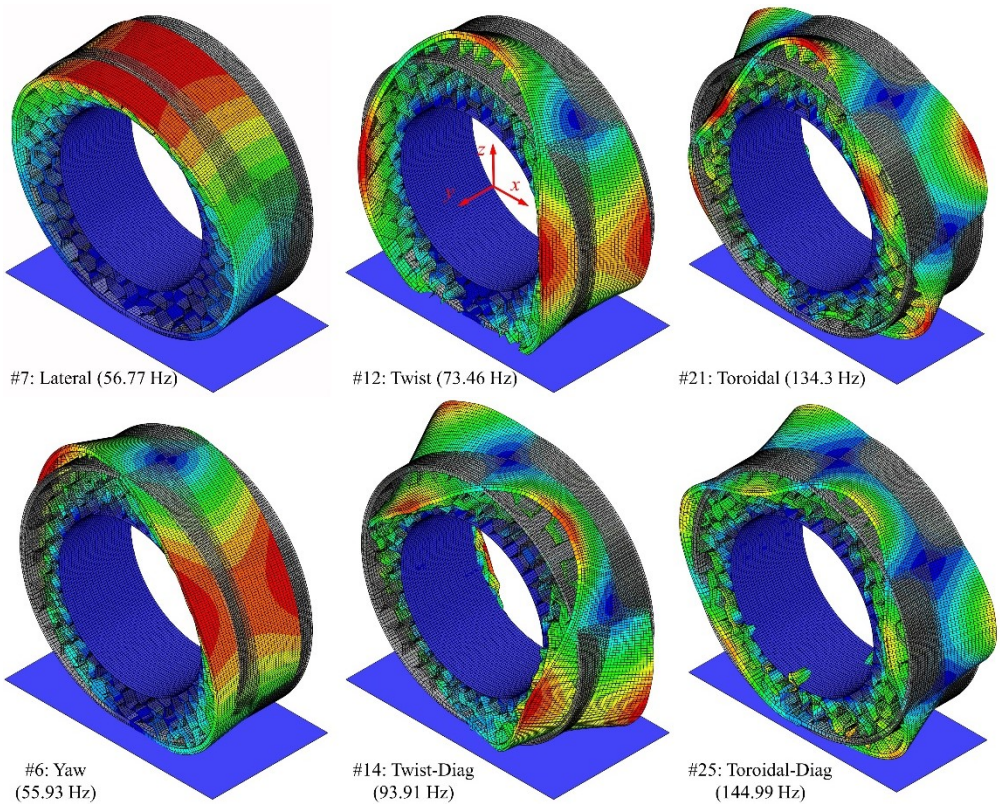

Figure 5.5: Out-of-plane modes of the wheel model with 31.5° cell angle (deformation scaling factor = 63.9)

5.2.3 Design of experiments

The natural frequencies (f) of the chosen important vibration modes are influenced by a number of wheel design parameters. These include the thickness dimensions (t_c, t_a, t_t) and initial elastic moduli (E_{0c}, E_{0a}, E_{0t}) of the honeycomb cell-wall, core layer (annular layer) and the tread, apart from the cell angle (θ), considering given rim dimensions and wheel width. The thickness and elastic moduli of the two steel rings, however, are taken as 0.5 mm and 210 GPa, respectively, as reported in [5,6,115]. This could ensure relatively high load bearing ability for the honeycomb wheels. Moreover, θ is related to cell-wall lengths (l_i) and heights (h_i) due to the design constraints in wheel circumferential and radial directions (Fig. 5.1), as:

$$(h_1 + h_2 + h_3 + h_4)/2 + l_2 \sin\theta_2 + l_3 \sin\theta_3 \approx (R_1 + R_2)\pi/N \tag{5.5}$$

$$\sum_{i=1}^{4} l_i \cos\theta_i = R_1 - R_2 \tag{5.6}$$

where R_1=302 mm and R_2=205 mm are radii of the rim and the steel ring connected to the spokes (Fig. 5.1), respectively, while N represents the number of spokes along the wheel perimeter, which is fixed as 19, as in reported wheel designs [5,6,115].

In order to conduct efficient parametric analyses, screening experiments were initially developed to eliminate relatively less important design parameters corresponding to each chosen influential vibration mode. To achieve this, only one-half fraction of a two-level factorial design involving above-stated six design factors, denoted as 2^{6-1} design, was developed for each of the three θ, as summarized in Table 5.3. In this table, factors (A, B), (C, D) and (E, F) represent the thickness and initial elastic modulus of the honeycomb cell-wall, core layer and the tread, respectively. Moreover, the low and high levels of each design factor are denoted as '-' and '+', respectively, and their corresponding values are presented in Table 5.4. It should be mentioned that the levels of factors E (t_t) and F (E_{0t}) were chosen corresponding to the practical design range of the tread parameters used in the passenger car pneumatic tires [48,115]. The responses of wheel designs considering these factor-level combinations (Tables 5.3 and 5.4) were obtained using developed FE wheel models which could ensure relatively broad variations in wheels' multi-axis stiffness properties and thus frequency (f) of each chosen vibration mode. Each simulation involving loading of the wheel model and natural frequency extraction required about 1 hour on an HP Z8 dual-processor (2×2.10 GHz) workstation.

The main effect of a design factor is defined as the difference between its average effect considering different levels of the factor, while the interaction between two factors (two-factor interaction) is calculated as half of the difference between the average effects of one design factor at different levels of the other factor [109,110]. The developed 2^{6-1} design with 32 runs (Table 5.3) could evaluate the six main effects as well as the resulting fifteen two-factor interactions independent of each other, although these may be confounded by higher-order interactions, which in-general are negligible [109,110]. The relative significance of these main effects associated with the six design factors were confirmed via analysis of variance (ANOVA), with sufficient consideration of the potentially influential two-factor interactions. This could help eliminate design factors with minor influences.

Table 5.3: Design matrix of screening experiments considering different cell angles

Run#	Factor-level combinations	Run#	Factor-level combinations
1	$A_- B_- C_- D_- E_- F_-$	17	$A_- B_- C_- D_- E_+ F_+$
2	$A_+ B_- C_- D_- E_- F_+$	18	$A_+ B_- C_- D_- E_+ F_-$
3	$A_- B_+ C_- D_- E_- F_+$	19	$A_- B_+ C_- D_- E_+ F_-$
4	$A_+ B_+ C_- D_- E_- F_-$	20	$A_+ B_+ C_- D_- E_+ F_+$
5	$A_- B_- C_+ D_- E_- F_+$	21	$A_- B_- C_+ D_- E_+ F_-$
6	$A_+ B_- C_+ D_- E_- F_-$	22	$A_+ B_- C_+ D_- E_+ F_+$
7	$A_- B_+ C_+ D_- E_- F_-$	23	$A_- B_+ C_+ D_- E_+ F_+$
8	$A_+ B_+ C_+ D_- E_- F_+$	24	$A_+ B_+ C_+ D_- E_+ F_-$
9	$A_- B_- C_- D_+ E_- F_+$	25	$A_- B_- C_- D_+ E_+ F_-$
10	$A_+ B_- C_- D_+ E_- F_-$	26	$A_+ B_- C_- D_+ E_+ F_+$
11	$A_- B_+ C_- D_+ E_- F_-$	27	$A_- B_+ C_- D_+ E_+ F_+$
12	$A_+ B_+ C_- D_+ E_- F_+$	28	$A_+ B_+ C_- D_+ E_+ F_-$
13	$A_- B_- C_+ D_+ E_- F_-$	29	$A_- B_- C_+ D_+ E_+ F_+$
14	$A_+ B_- C_+ D_+ E_- F_+$	30	$A_+ B_- C_+ D_+ E_+ F_-$
15	$A_- B_+ C_+ D_+ E_- F_+$	31	$A_- B_+ C_+ D_+ E_+ F_-$
16	$A_+ B_+ C_+ D_+ E_- F_-$	32	$A_+ B_+ C_+ D_+ E_+ F_+$

Factors (A, B), (C, D) and (E, F) represent the thickness and initial elastic modulus of honeycomb cell-wall, core layer and tread, respectively

Table 5.4: Two levels of each design factor considered in screening experiments (2^{6-1} designs)

Level	Design factors					
	A: t_c (mm)	B: E_{0c} (MPa)	C: t_a (mm)	D: E_{0a} (MPa)	E: t_t (mm)	F: E_{0t} (MPa)
Low: '-'	2.5	18	10	12	5	4
High: '+'	3.5	30	20	18	15	8

Factors (A, C and E) and (B, D and F) denote thickness dimensions (t_c, t_a, t_t) and initial elastic moduli (E_{0c}, E_{0a}, E_{0t}) of honeycomb cell-wall, core layer and tread, respectively

Central composite designs (CCDs) involving only significant design factors were subsequently developed in order to formulate second-order response surface models, which relate frequency of each chosen vibration mode with corresponding important design factors together with their two-factor interactions. Three levels, however, were considered for these important design factors in order to investigate their nonlinear influences. The detailed descriptions of these CCDs are presented in the following subsections.

5.3 Results and discussion

FE simulations were conducted for the design points of the screening and subsequent central composite designs (CCDs). The simulation results obtained for different cell angles (θ) are discussed in the following subsections with particular focus on the influences of the design factors and their two-factor interactions on the natural frequencies (f) of chosen vibration modes.

5.3.1 Screening designs (2^{6-1})

The natural frequencies of chosen influential vibration modes corresponding to the wheel designs with different factor-level combinations (Table 5.3) were obtained using the developed FE wheel models, considering a normal load of 3 kN. The results for these wheel designs with different θ are summarized in Tables 5.5 and 5.6 together with their equivalent vertical stiffness (K_z), which is evaluated as the ratio of the wheel load and the resulting vertical deflection.

Table 5.5: Hop mode natural frequencies and vertical stiffness of screening designs with different cell angles

Run #	Hop mode natural frequency (Hz)			Vertical stiffness, K_z (N/mm)			Run #	Hop mode natural frequency (Hz)			Vertical stiffness, K_z (N/mm)		
	15.8°	31.5°	47.1°	15.8°	31.5°	47.1°		15.8°	31.5°	47.1°	15.8°	31.5°	47.1°
1	16.8	14.8	N/A	113	89	N/A	*17*	14.5	13.5	N/A	117	92	N/A
2	17.2	15.9	N/A	152	118	N/A	*18*	15.5	14.1	N/A	156	121	N/A
3	18.1	17.0	N/A	143	111	N/A	*19*	15.9	14.6	N/A	146	113	N/A
4	18.7	17.4	14.7	204	155	133	*20*	16.5	15.0	13.6	216	163	139
5	18.4	17.1	N/A	174	135	N/A	*21*	16.7	15.6	14.9	177	137	120
6	18.9	17.2	16.4	235	181	157	*22*	17.2	15.9	14.9	243	186	160
7	19.7	18.0	17.1	220	169	147	*23*	17.9	16.5	15.4	228	174	150
8	20.2	18.5	17.6	316	241	207	*24*	18.9	16.9	16.2	325	246	211
9	18.4	17.4	16.6	140	109	98	*25*	16.6	15.4	14.7	143	111	99
10	19.0	17.2	15.7	190	145	125	*26*	17.3	15.7	14.3	198	150	129
11	19.9	18.5	N/A	179	137	N/A	*27*	18.0	16.4	15.0	186	141	122
12	20.5	18.6	17.5	257	194	167	*28*	18.5	16.8	15.7	265	199	171
13	21.1	19.6	18.7	217	167	143	*29*	19.3	17.7	17.1	222	169	146
14	21.3	19.6	18.8	298	228	194	*30*	19.6	18.0	17.1	302	230	196
15	22.4	20.5	19.7	279	213	181	*31*	20.3	18.7	17.8	283	215	183
16	23.5	21.3	20.1	406	307	259	*32*	21.7	19.5	18.5	420	315	265
Mean								18.7	17.2	N/A	223	171	N/A

N/A: Not available due to excessive deflections of the spokes in wheel/road contact region

Table 5.6: Natural frequencies corresponding to Torsion, Yaw, Lateral, Twist and Oval-Diag vibration modes considered in screening designs with different cell angles

Run	Torsion (Hz)			Yaw (Hz)			Lateral (Hz)			Twist (Hz)			Oval-Diag (Hz)		
#	15.8°	31.5°	47.1°	15.8°	31.5°	47.1°	15.8°	31.5°	47.1°	15.8°	31.5°	47.1°	15.8°	31.5°	47.1°
1	32.5	26.2	N/A	45.9	41.1	N/A	46.5	42.5	N/A	60.6	53.4	N/A	64.8	50.9	N/A
2	39.5	31.5	N/A	52.8	46.8	N/A	53.8	48.9	N/A	66.5	57.7	N/A	68.3	54.0	N/A
3	40.2	32.3	N/A	58.1	51.3	N/A	59.8	54.3	N/A	71.9	61.9	N/A	76.0	59.2	N/A
4	50.3	37.8	39.3	66.4	58.8	50.7	69.1	62.2	53.7	80.2	68.1	59.1	83.6	64.5	55.8
5	28.1	22.1	N/A	39.7	36.3	N/A	38.7	35.5	N/A	58.9	54.0	N/A	57.3	45.8	N/A
6	33.6	27.5	26.6	43.9	40.0	35.4	44.9	41.1	35.9	62.8	56.6	52.4	61.2	48.2	43.5
7	33.8	27.1	26.1	48.0	43.6	38.3	49.5	45.3	39.5	66.5	59.4	54.3	67.1	52.3	45.3
8	44.4	33.9	34.0	55.8	50.3	44.2	57.6	52.6	45.8	73.1	64.1	57.8	73.1	58.0	50.5
9	32.7	26.4	26.0	46.9	42.4	37.2	46.6	42.6	37.1	63.8	57.5	52.5	65.1	51.8	44.7
10	38.7	31.4	31.7	52.7	47.4	41.5	53.9	49.1	42.6	69.2	60.8	55.0	67.8	55.6	48.5
11	38.6	32.0	N/A	58.1	52.2	N/A	59.9	54.5	N/A	74.4	65.1	N/A	75.8	59.8	N/A
12	51.2	38.6	40.1	67.2	59.6	51.8	69.3	62.7	54.4	82.8	70.7	62.3	82.8	65.1	57.1
13	27.9	22.1	21.2	38.7	35.4	31.2	38.8	35.7	31.1	63.2	58.9	55.2	58.8	48.6	43.7
14	34.5	28.6	26.4	45.0	41.2	36.8	45.1	41.4	36.1	67.4	61.9	58.2	62.0	51.5	46.7
15	35.0	27.6	26.0	49.2	44.7	39.6	49.8	45.6	39.8	71.3	64.5	59.9	68.3	54.5	48.2
16	43.3	33.9	34.0	55.1	50.0	44.0	57.8	52.8	46.0	76.9	68.5	62.5	73.9	60.0	53.2
17	27.2	22.0	N/A	37.6	33.8	N/A	38.6	35.2	N/A	49.4	43.9	N/A	55.0	42.9	N/A
18	32.8	26.4	N/A	43.0	38.5	N/A	44.8	40.7	N/A	54.7	47.5	N/A	61.1	47.0	N/A
19	33.1	26.5	N/A	47.1	42.1	N/A	49.5	44.8	N/A	58.5	50.5	N/A	66.5	50.0	N/A
20	42.5	32.7	33.3	54.8	48.7	42.1	57.6	51.7	44.8	66.3	56.5	49.3	73.2	56.2	47.8
21	24.1	19.4	18.7	32.1	29.4	25.8	33.5	30.8	26.9	49.0	45.4	42.1	50.7	40.8	35.6
22	30.0	25.0	23.3	37.7	34.4	30.3	39.1	35.8	31.3	53.9	48.9	44.9	55.8	44.0	38.6
23	30.2	24.2	22.7	41.1	37.4	32.7	42.9	39.3	34.3	56.8	51.1	46.3	59.8	46.5	39.9
24	35.4	28.8	29.6	46.7	42.4	37.2	49.9	45.4	39.7	62.1	54.7	49.4	67.5	52.8	44.9
25	27.4	22.1	21.7	37.5	34.1	29.8	38.6	35.3	30.8	51.8	46.6	42.5	57.2	44.4	37.8
26	33.8	27.2	26.7	43.7	39.4	34.5	45.0	41.0	35.7	57.5	50.6	45.5	61.1	47.8	41.4
27	34.0	27.3	26.3	47.8	42.9	37.4	49.7	45.1	39.3	61.2	53.5	47.6	67.0	51.1	43.3
28	39.6	32.5	33.6	54.4	49.1	42.7	57.5	52.0	45.2	67.9	58.6	51.5	73.4	57.0	48.8
29	25.0	19.4	18.6	33.2	30.2	26.8	33.7	31.0	27.1	54.0	49.8	47.5	52.0	43.1	38.9
30	28.8	23.2	23.1	36.9	33.8	29.6	39.2	35.9	31.4	55.6	51.5	47.6	56.8	46.5	41.3
31	29.1	24.0	22.6	40.3	36.8	32.0	43.0	39.4	34.5	58.5	53.8	49.1	60.8	48.6	42.5
32	38.9	30.3	30.1	47.4	43.1	38.1	50.3	45.9	40.1	65.9	58.8	54.0	68.4	53.6	47.5
Mean	34.9	27.8	N/A	47.0	42.4	N/A	48.6	44.3	N/A	63.5	56.4	N/A	65.4	51.6	N/A

N/A: Not available due to excessive deflections of the spokes in wheel/road contact region

The results in Table 5.5 show broad variation in K_z of the wheel model with θ=15.8°, ranging from 113 N/mm (run #1) to 420 N/mm (run #32). Increasing θ from 15.8 to 31.5° resulted in nearly 23% reduction in K_z, irrespective of the variations in factors A to F (Table 5.3). The further increase in θ to 47.1°, however, resulted in only about 14% reduction. This negative and nonlinear trend is consistent with the influence of θ on the radial effective elastic modulus of the 2D spoke normalized to the initial elastic modulus of its constituent material (E_{0c}), which significantly affects K_z of the wheel, as illustrated in Fig. 5.6(a). The normalized radial (E_Z/E_{0c}) as well as circumferential or shear (G_{ZX}/E_{0c}) effective elastic moduli of the 2D spoke are related to mean dimensions of the honeycomb cell [5,6], as:

$$\frac{E_Z}{E_{0c}} = \frac{\cos\theta}{(h/l+\sin\theta)\sin^2\theta}(t_c/l)^3 \tag{5.7}$$

$$\frac{G_{ZX}}{E_{0c}} = \frac{(h/l+\sin\theta)}{(h/l)^2\,(1+2h/l)\cos\theta}(t_c/l)^3 \tag{5.8}$$

E_z/E_{0c} and G_{ZX}/E_{0c} in Fig. 5.6(a) were calculated for three spokes configurations employed in this study, considering both low and high levels of the cell-wall thickness (t_c=2.5 and 3.5 mm as in Table 5.4). The mean height (h) and length (l) corresponding to each spokes' configuration of different θ have been summarized in Table 5.2. It should be noted that an increase in θ may lead to relatively lower K_z for some wheel designs with 47.1° cell angle and thereby cause excessive deflections in the spokes near the wheel/road contact region, which will impact the shear ring and cause adverse influences on wheel ride and noise performance, particularly under high rolling speeds. As an example, Fig. 5.6(b) depicts the deformations of the spokes observed in the #17 wheel design (Tables 5.3 and 5.5). These excessive deformations are mostly observed in the wheel designs with lower levels of thickness and initial elastic modulus of the core layer (factor *C*: t_a=10 mm and factor *D*: E_{0a}=12 MPa), as seen for the runs #1-3 and #17-19 in Tables 5.3 and 5.5, suggesting significant influence of factors *C* and *D* on K_z, apart from θ.

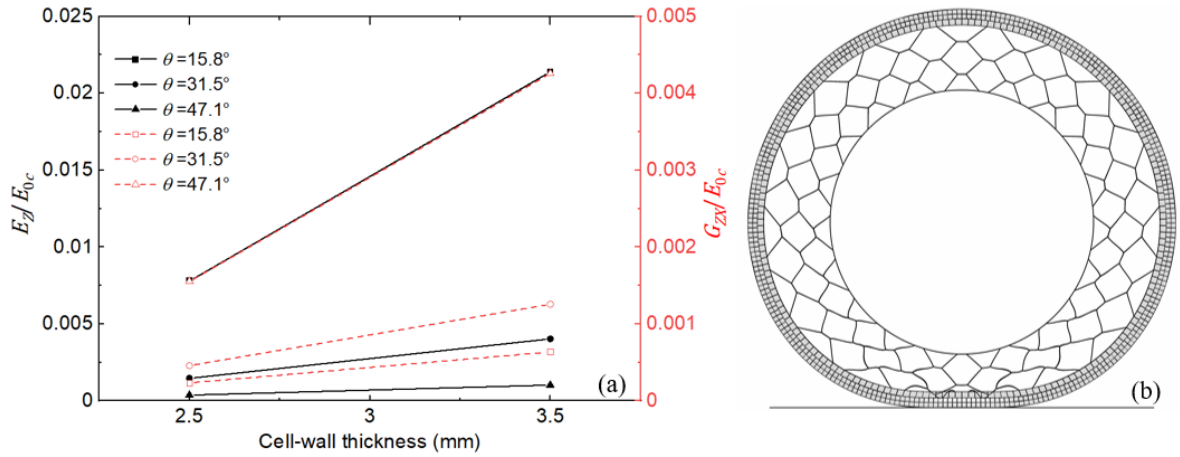

Figure 5.6: (a) Influence of cell angle θ on normalized radial (E_Z/E_{0c}) and circumferential (G_{ZX}/E_{0c}) effective elastic moduli of a 2D honeycomb spoke with different cell-wall thickness; and (b) excessive deflections in the spokes near the contact region of the #17 wheel design (Tables 5.3 and 5.5)

The Hop mode natural frequency (f) is predominantly influenced by K_z of the wheel, apart from its mass properties. Therefore, the results in Table 5.5 also reveal negative effect of θ on the Hop mode frequency for each wheel design considered (Table 5.3), although this influence is relatively small when compared to that observed on K_z. It should be noted that the Hop mode frequencies obtained for wheel designs without excessive deflections of the spokes occur in the 13.5 to 23.5

Hz range, and are comparable to those of most passenger car pneumatic tires, which range from 10 to 20 Hz [116].

Unlike the negative influence on E_Z/E_{0c} of the 2D spoke and K_z of the wheel, an increase in θ shows positive effect on G_{ZX}/E_{0c}, particularly when θ increases from 31.5 to 47.1°, as depicted in Fig. 5.6(a). This positive and nonlinear influence of θ is also expected on the Torsion mode frequencies of the non-contacting wheels, in which the in-plane shear deformations of the spokes dominate the vibration motion. This is evidenced from the observed variations in f associated with the Torsion modes of the #7 wheel design (Tables 5.3 and 5.6), as an example, considering different θ and fixed spindle constraint, as illustrated in Fig. 5.7. In this figure, the three wheel models with 15.8, 31.5 and 47.1° cell angles show increasing f of 6.4, 8.6 and 16.2 Hz, respectively. Introducing the contact constraint, however, causes additional torsion deformations of the shear ring and the tread (Fig. 5.4), and thus much higher Torsion mode frequencies of the wheels with ground contact, in the order of 33.8, 27.1 and 26.1 Hz, respectively, as seen for the run #7 in Table 5.6. Therefore, the wheel design with θ=15.8° shows 27.4 Hz increase in f when loaded against the ground, which is substantially higher than those observed for wheel models with 31.5 and 47.1° cell angles, in the order of 18.5 and 9.9 Hz, respectively. This is likely attributable to radial deflections of the spokes observed in Torsion modes of the grounded wheels, as seen in Fig. 5.4. The wheel designs with higher θ show lower E_Z/E_{0c} and thus smaller increase in f for the Torsion modes, when loaded. Similar trends were also observed for the other wheel models (Table 5.6).

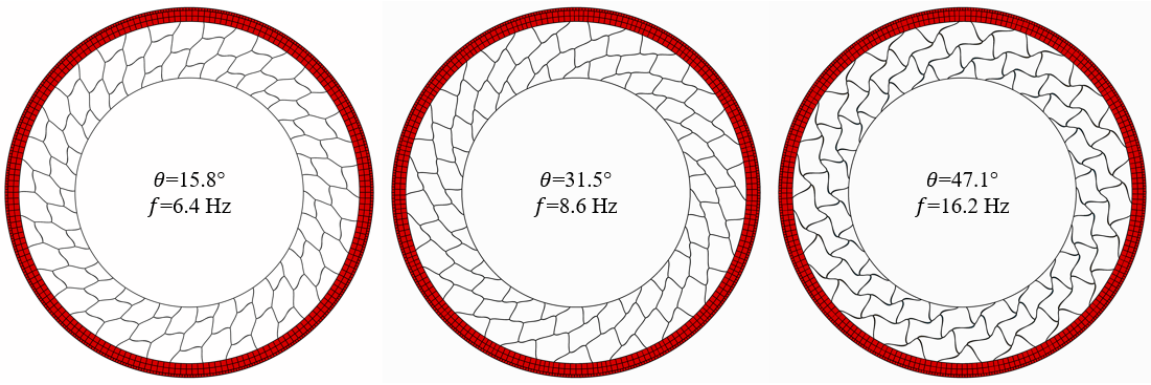

Figure 5.7: Torsion mode frequencies and deformation patterns of non-contacting and fixed spindle wheels (run #7) with different cell angles (θ)

The Oval-Diag mode exhibits extension and compression motions of the shear ring and tread along two mutually perpendicular axis crossing the rim center, which are, however, radially constrained by the spokes, as in the case of the pneumatic tires [94]. As an example, Fig. 5.8 illustrates Oval-Diag modes of the #7 wheel designs (Tables 5.3 and 5.6) with different θ, considering fixed spindle and non-contact conditions. In this figure, the three wheel designs with θ=15.8, 31.5 and 47.1° show decreasing f, in the order of 51.2, 44.6 and 42.5 Hz, respectively. This nonlinear and negative influence of θ is consistent with that on E_Z/E_{0c}, as seen in Fig. 5.6(a). Moreover, with the addition of the contact constraint, higher f, in the order of 67.1, 52.3 and 45.3 Hz, are observed in the wheel designs with increasing θ, as seen in Table 5.6. The Oval-Diag mode of the wheel design with lower θ thus reveal higher increase in f, owing to the higher E_Z/E_{0c} of its spokes.

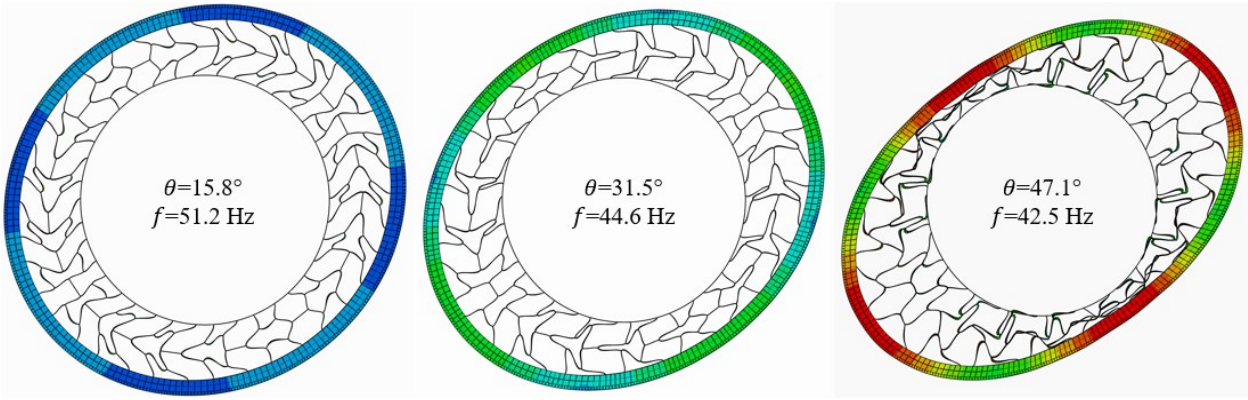

Figure 5.8: Oval-Diag mode frequencies and deformation patterns for non-contacting and fixed spindle wheels (run #7) considering different cell angles (θ)

Reductions in the wheel's Yaw and Lateral mode frequencies are also observed with an increase in θ, irrespective of the factor-level combinations considered, as seen in Tables 5.3 and 5.6. This is owing to the negative effect of θ on out-of-plane stiffness properties of the spokes and thus yaw and lateral stiffness of the wheel [115]. The results in Table 5.6 invariably show lower Twist mode frequencies of the wheel with higher θ, in which complex out-of-plane deformations of the spokes also occur.

Significance analysis

The simulation results obtained from the screening designs (Tables 5.5 and 5.6) are used to assess relative significance of chosen design factors, *A* to *F*, and their two-factor interactions with respect to frequencies of the influential vibration modes using the analysis of variance (ANOVA). The analyses were performed using Minitab 20 software. The factors and two-factor interactions with

p-value higher than 0.05 are considered as insignificant effects. The elimination of these factors together with their two-factor interactions could help formulate efficient central composite designs (CCDs), as discussed in the subsequent sub-section.

As an example, Table 5.7 summarizes the results obtained from ANOVA for the Hop mode frequencies of the wheel designs with θ=15.8 and 31.5°. The wheel designs with θ=47.1° were not considered in the significance analysis and subsequent CCDs due to excessive deflections of the spokes observed in some of experiment runs (Tables 5.5 and 5.6). For the wheel designs with θ=15.8 and 31.5°, the results showed insignificant effects of factor F (E_{0t}) and its interactions with all other factors (*AF*, *BF*, *CF*, *DF* and *EF*) for both the θ values considered. The results in Table 5.7 show significant effects (p<0.05) of all the remaining factors (A to E). These factors are thus included in the subsequent CCDs, apart from their two-factor interactions, although only the interaction *CD* was observed significant. The statistical significance of design factors with regard to other chosen vibration modes for the wheel designs with θ=15.8 and 31.5° were also evaluated in a similar manner, and the results are summarized in Table 5.8. The results suggested important statistical significance of the same design factors (p<0.05; indicated by '✓') for the wheel designs with different θ. For instance, factors A to E are considered as important design factors for the Hop mode of both wheel designs with different θ.The results in this table also suggested relatively slight interactions between the chosen factors (A to F) with θ.

Table 5.7: Results of ANOVA for Hop mode frequencies of wheel designs with 15.8 and 31.5° cell angles

Factor or interaction	p-value		Factor or interaction	p-value	
	15.8°	31.5°		15.8°	31.5°
A	*<0.001*	*0.004*	*BC*	0.328	0.561
B	*<0.001*	*<0.001*	*BD*	0.231	0.987
C	*<0.001*	*<0.001*	*BE*	0.485	0.160
D	*<0.001*	*<0.001*	*BF*	0.846	0.533
E	*<0.001*	*<0.001*	*CD*	*0.001*	*0.008*
F	0.669	0.722	*CE*	0.133	0.194
AB	0.098	0.555	*CF*	0.942	0.481
AC	0.637	0.968	*DE*	0.976	0.650
AD	0.824	0.442	*DF*	0.287	0.525
AE	0.269	0.644	*EF*	0.263	0.760
AF	0.651	0.476			

Factors (*A*, *B*), (*C*, *D*) and (*E*, *F*) represent the thickness and initial elastic modulus of honeycomb cell-wall, core layer and tread, respectively

Table 5.8: Summary of ANOVA results obtained for vibration modes of wheel designs with 15.8 and 31.5° cell angles showing high statistical significance (p<0.05; indicated by ✓)

Factor	Chosen vibration modes					
	Hop	Oval-Diag	Torsion	Lateral	Yaw	Twist
A	✓	✓	✓	✓	✓	✓
B	✓	✓	✓	✓	✓	✓
C	✓	✓	✓	✓	✓	
D	✓	✓				✓
E	✓	✓	✓	✓	✓	✓
F						

Factors (*A*, *B*), (*C*, *D*) and (*E*, *F*) represent the thickness and initial elastic modulus of honeycomb cell-wall, core layer and tread, respectively

5.3.2 Central composite designs (CCDs)

From the screening and ANOVA results presented in Tables 5.7 and 5.8, it is evident that some design factors yield significant influences on the modal properties of the wheel designs with different θ. These factors are thus considered for further experiments in accordance with the CCD approach. The FE simulations were subsequently obtained, considering variations only in the significant design factors, for each chosen vibration mode. As an example, Table 5.9 summarizes the CCDs formulated to study the effects of variations in important factors (*A*-*E*) on the Hop and Oval-Diag modes of the wheel designs with θ=15.8 and 31.5°. Three levels representing low, medium and high levels, denoted as '-', '0' and '+', respectively, were considered for each important design factor so as to investigate their nonlinear influences on modal frequencies. The three levels considered for each design factor are summarized in Table 5.10. The value of factor *F* (E_{0t}), however, was held at its medium level for every design point. The CCDs comprised one-half fraction of a two-level factorial design involving five important factors (2^{5-1} design, runs #1-16) as well as ten axial (runs #17-26) and one center (run #27) points, as seen in Table 5.9. It should be noted that the five main and thus ten two-factor interaction effects are not confounded in the 2^{5-1} designs. Moreover, the axial runs consider variations in each factor from its low to high level, while holding the other factors at their respective medium levels. In addition, FE simulation is not replicated for the center design point, where all factors are at their respective medium levels.

Table 5.9: Central composite designs for Hop and Oval-Diag modes considering different cell angles

Run#	Factor-level combinations	Run#	Factor-level combinations
1	$A_- B_- C_- D_- E_+$	15	$A_- B_+ C_+ D_+ E_-$
2	$A_+ B_- C_- D_- E_-$	16	$A_+ B_+ C_+ D_+ E_+$
3	$A_- B_+ C_- D_- E_-$	17	$A_- B_0 C_0 D_0 E_0$
4	$A_+ B_+ C_- D_- E_+$	18	$A_+ B_0 C_0 D_0 E_0$
5	$A_- B_- C_+ D_- E_-$	19	$A_0 B_- C_0 D_0 E_0$
6	$A_+ B_- C_+ D_- E_+$	20	$A_0 B_+ C_0 D_0 E_0$
7	$A_- B_+ C_+ D_- E_+$	21	$A_0 B_0 C_- D_0 E_0$
8	$A_+ B_+ C_+ D_- E_-$	22	$A_0 B_0 C_+ D_0 E_0$
9	$A_- B_- C_- D_+ E_-$	23	$A_0 B_0 C_0 D_- E_0$
10	$A_+ B_- C_- D_+ E_+$	24	$A_0 B_0 C_0 D_+ E_0$
11	$A_- B_+ C_- D_+ E_+$	25	$A_0 B_0 C_0 D_0 E_-$
12	$A_+ B_+ C_- D_+ E_-$	26	$A_0 B_0 C_0 D_0 E_+$
13	$A_- B_- C_+ D_+ E_+$	27	$A_0 B_0 C_0 D_0 E_0$
14	$A_+ B_- C_+ D_+ E_-$		

Factors (A, B), (C, D) and (E, F) represent thickness and initial elastic modulus of honeycomb cell-wall, core layer and tread, respectively

Table 5.10: Low, medium and high levels of design factors considered in central composite designs

Level	Design factors					
	A: t_c (mm)	B: E_{0c} (MPa)	C: t_a (mm)	D: E_{0a} (MPa)	E: t_t (mm)	F: E_{0t} (MPa)
Low: '-'	2.5	18	10	12	5	4
Medium: '0'	3.0	24	15	15	10	6
High: '+'	3.5	30	20	18	15	8

Factors (A, C and E) and (B, D and F) denote thickness dimensions (t_c, t_a, t_t) and initial elastic moduli (E_{0c}, E_{0a}, E_{0t}) of honeycomb cell-wall, core layer and tread, respectively

Table 5.11 summarizes the resulting frequencies from the CCDs developed for each chosen wheel vibration mode considering different θ. The CCDs for Torsion, Yaw, Lateral and Twist modes (not shown) comprised a two-level full factorial design (2^4 design) involving four important factors together with eight axial and one center points. It should be mentioned that the 2^4 designs could permit separate evaluations of the four main effects and the resulting six two-factor interactions. Moreover, the results in Table 5.11 invariably show reductions in frequencies of the chosen vibration modes with an increase in θ, each of which is consistent with that observed in the screening designs (Tables 5.5 and 5.6).

Table 5.11: Natural frequencies of vibration modes obtained in central composite designs considering different cell angles

Run	Hop (Hz)		Torsion (Hz)		Yaw (Hz)		Lateral (Hz)		Oval-Diag (Hz)		Twist (Hz)	
#	15.8°	31.5°	15.8°	31.5°	15.8°	31.5°	15.8°	31.5°	15.8°	31.5°	15.8°	31.5°
1	14.8	13.6	32.8	26.3	46.5	41.8	46.6	42.6	55.2	42.9	59.5	53.9
2	17.4	15.9	39.2	31.4	52.9	47.2	53.8	49.1	68.4	53.9	64.3	57.0
3	18.0	17.0	38.9	32.1	58.2	51.9	59.9	54.4	75.9	59.2	69.0	60.4
4	16.9	15.3	50.6	38.4	66.8	59.2	69.2	62.5	73.6	56.3	76.2	65.7
5	18.4	17.0	28.0	22.0	39.4	36.1	38.8	35.6	57.3	45.8	63.9	58.7
6	17.5	15.8	34.3	28.1	44.6	40.7	45.0	41.3	55.9	43.9	68.5	61.5
7	18.1	16.3	34.6	27.5	48.7	44.3	49.7	45.5	60.0	46.5	72.8	64.6
8	20.6	18.4	44.3	34.2	55.6	50.4	57.7	52.7	73.3	58.0	79.3	69.6
9	18.4	17.4	27.6	22.1	37.8	34.1	38.6	35.3	65.1	51.8	49.5	45.0
10	17.1	15.6	33.5	26.8	43.3	39.0	44.9	40.9	61.0	47.7	54.2	48.3
11	17.7	16.2	33.6	27.1	47.5	42.5	49.6	45.0	66.8	51.0	57.5	50.8
12	20.5	18.6	41.7	32.9	54.7	49.0	57.6	51.9	82.8	65.1	64.2	55.8
13	19.2	17.9	24.5	19.5	32.6	29.9	33.6	30.9	51.9	43.3	53.0	48.6
14	21.6	19.5	29.7	23.1	37.4	34.2	39.2	35.9	62.1	51.4	56.9	51.7
15	22.6	20.8	30.0	24.3	40.8	37.2	43.0	39.4	68.4	54.6	60.1	54.2
16	21.5	19.7	37.2	30.0	47.0	42.9	50.1	45.7	68.3	53.5	66.5	58.8
17	18.6	17.1	31.0	24.6	43.3	39.3	44.4	40.6	62.6	48.9	60.2	54.2
18	19.4	17.5	38.7	30.0	49.6	44.9	51.7	47.1	69.1	53.3	66.2	58.2
19	18.1	16.6	30.3	24.2	41.1	37.4	41.9	38.4	58.6	47.1	58.3	52.6
20	19.7	17.7	38.5	32.2	51.5	46.6	53.8	49.0	69.9	54.2	67.9	59.6
21	17.4	16.0	36.7	29.4	50.8	45.5	52.6	47.8	67.8	52.8	61.6	54.2
22	19.8	18.0	32.5	26.5	43.1	39.3	44.9	41.1	61.9	49.5	64.7	58.2
23	17.8	16.1	37.2	30.0	51.5	46.6	52.5	48.0	64.3	49.8	69.4	61.7
24	20.0	18.4	32.3	25.9	42.8	38.8	44.8	40.8	64.7	51.9	58.4	51.8
25	19.9	18.3	34.5	27.7	46.6	42.3	48.2	44.0	67.5	54.7	63.3	56.2
26	18.3	16.4							61.4	47.6		
27	19.0	17.2							64.5	51.4		
Mean	18.8	17.2	34.9	27.9	47.0	42.4	48.5	44.2	65.1	51.3	63.4	56.5

The results obtained for the CCDs (Table 5.11) are subsequently employed to formulate response surface models for wheel designs with θ=15.8 and 31.5° so as to relate f of each influential mode with corresponding important factors as well as their two-factor interactions. The quadratic regression models are formulated as [109,110]:

$$f^* = \alpha_0 + \sum_{j=1}^{n} \alpha_j x_j + \sum_{j=1}^{n} \alpha_{jj} x_j^2 + \sum_{1 \le i < j}^{n} \alpha_{ij} x_i x_j \tag{5.9}$$

where f^* denotes the natural frequency predicted by the regression model, while $x_1, x_2, \ldots, x_n$ represent n coded factors, each of which varies between -1 and +1, corresponding to low and high levels, respectively. α_0, α_j, α_{jj} and α_{ij} are the coefficients of each regression model, which are identified by least squares fitting of the FE simulation data (Table 5.11) for minimized error. These coefficients are summarized in Tables 5.12 and 5.13 for different cell angles and vibration modes considered in the study.

Table 5.12: Regression coefficients for Hop and Oval-Diag modes considering different cell angles

	Terms	Hop mode		Oval-Diag mode			Terms	Hop mode		Oval-Diag mode	
		15.8°	31.5°	15.8°	31.5°			15.8°	31.5°	15.8°	31.5°
α_0		18.94	17.21	64.60	50.90						
α_1	*A*	0.38	0.17	2.86	2.18	α_{12}	*AB*	*0.00*	0.05	0.56	0.52
α_2	*B*	0.75	0.60	5.74	3.91	α_{13}	*AC*	*0.00*	*0.02*	-0.04	*-0.08*
α_3	*C*	1.17	1.00	-3.20	-1.90	α_{14}	*AD*	*-0.03*	*-0.02*	-0.05	*-0.04*
α_4	*D*	1.06	1.04	0.41	0.78	α_{15}	*AE*	*0.03*	0.13	*0.31*	*0.04*
α_5	*E*	-0.91	-0.89	-3.70	-3.43	α_{23}	*BC*	*0.05*	*0.02*	-0.43	-0.44
α_{11}	*AA*	*0.07*	*0.07*	1.23	*0.27*	α_{24}	*BD*	*0.02*	*0.00*	*0.01*	*-0.21*
α_{22}	*BB*	*-0.02*	*-0.04*	*-0.39*	*-0.18*	α_{25}	*BE*	*0.00*	*-0.01*	*-0.18*	-0.27
α_{33}	*CC*	-0.34	-0.21	*0.22*	*0.29*	α_{34}	*CD*	0.24	0.27	*0.09*	0.34
α_{44}	*DD*	*-0.04*	0.02	*-0.12*	*0.01*	α_{35}	*CE*	0.05	0.13	0.67	0.59
α_{55}	*EE*	0.16	0.12	*-0.16*	*0.27*	α_{45}	*DE*	*-0.03*	*0.03*	-0.01	*0.00*

Table 5.13: Regression coefficients for wheel Torsion, Yaw, Lateral and Twist modes considering different cell angles

	Terms	Torsion mode		Yaw mode		Lateral mode		Terms	Twist mode	
		15.8°	31.5°	15.8°	31.5°	15.8°	31.5°		15.8°	31.5°
α_0		34.52	27.83	46.60	42.24	48.23	44.04		63.30	56.22
α_1	*A*	3.79	2.76	3.18	2.80	3.61	3.22	*A*	2.81	2.01
α_2	*B*	3.86	3.07	5.29	4.65	6.00	5.35	*B*	4.75	3.46
α_3	*C*	-2.19	-1.73	-3.86	-3.07	-3.94	-3.41	*D*	1.66	1.93
α_4	*E*	-2.76	-2.14	-4.46	-3.92	-3.99	-3.65	*E*	-5.70	-4.89
α_{11}	*AA*	*0.35*	*-0.53*	*-0.15*	*-0.10*	*-0.18*	*-0.17*	*AA*	*-0.09*	*-0.02*
α_{22}	*BB*	*-0.17*	*0.37*	-0.29	-0.25	-0.38	-0.36	*BB*	*-0.20*	*-0.13*
α_{33}	*CC*	*0.11*	*0.10*	0.37	*0.15*	0.52	0.41	*DD*	*-0.13*	*-0.03*
α_{44}	*EE*	*0.21*	*0.10*	0.57	0.48	0.40	0.36	*EE*	0.57	0.52
α_{12}	*AB*	0.81	0.32	0.43	0.40	0.44	0.36	*AB*	0.56	0.46
α_{13}	*AC*	*-0.23*	*0.02*	-0.29	-0.21	-0.24	-0.18	*AD*	-0.13	-0.08
α_{14}	*AE*	-0.48	*-0.28*	-0.21	-0.15	-0.25	-0.23	*AE*	-0.09	*-0.01*
α_{23}	*BC*	*-0.14*	*-0.05*	-0.53	-0.41	-0.52	-0.40	*BD*	-0.18	-0.12
α_{24}	*BE*	-0.43	*-0.11*	-0.43	-0.35	-0.52	-0.48	*BE*	-0.39	-0.21
α_{34}	*CE*	0.35	*0.28*	0.67	0.52	0.84	0.77	*DE*	-0.26	-0.23

The significance levels of the design factors and two-factor interactions corresponding to each chosen wheel vibration mode are further evaluated using ANOVA of the simulation data obtained for CCDs (Table 5.11). The ANOVA results obtained for wheel designs with different θ revealed insignificant effects of some of the higher order terms (p>0.05), which are indicated by italicized values of their regression coefficients, in Tables 5.12 and 5.13. As an example, factors (*A*, *B*, *C* and *E*) and their two-factor interactions are considered as significant effects in view of the wheel Lateral mode, while the quadratic term *AA* (α_{11}) is insignificant, irrespectively of the θ considered,

as seen in Table 5.13. The accuracy of each regression model is evaluated by its coefficient of determination (R^2), which is calculated using the difference between f predicted by the FE wheel models and f^* obtained from the regression model. The regression models for different vibration modes revealed R^2 in excess of 0.99. Moreover, satisfactory prediction ability ($R^2_{predicted}$>0.945) was observed for the regression models corresponding to the Hop, Torsion, Yaw, Lateral and Twist modes. The regression models for Oval-Diag mode of the wheel with θ=15.8 and 31.5°, however, showed relatively smaller $R^2_{predicted}$ values, in the order 0.894 and 0.905, respectively. This is attributable to the inclusion of factor D (E_{0a}) in the models, which showed relatively slight effects when compared to the other significant factors (A, B, C, E), as seen in Table 5.12.

5.3.3 Influences of important design factors on natural frequencies of loaded wheels

The response surface models (Tables 5.12 and 5.13) developed for the wheel designs with θ=15.8 and 31.5° were used to investigate the influences of significant design factors on the frequencies (f) of the chosen influential vibration modes, while considering the two-factor interactions. As an example, Figs. 5.9 and 5.10 illustrate variations in f of each influential vibration mode with varying levels of corresponding important design factors for the loaded wheel with θ=15.8°. It should be mentioned that similar influences of these important design factors were also observed for the wheel with θ=31.5°, suggesting their relatively slight interactions with the cell angle.

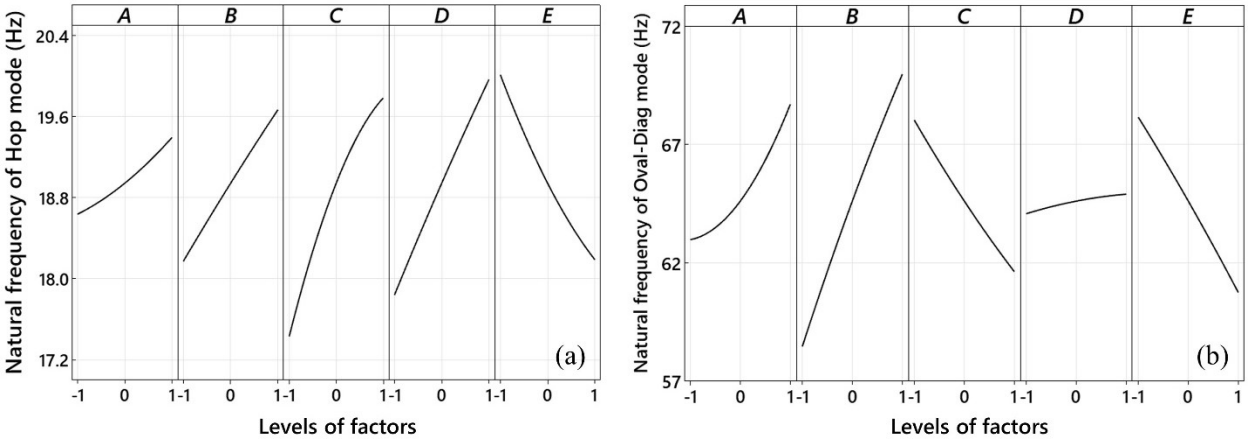

Factors (A, C and E) and (B, D and F) denote thickness dimensions (t_c, t_a, t_t) and initial elastic moduli (E_{0c}, E_{0a}, E_{0t}) of honeycomb cell-wall, core layer and tread, respectively

Figure 5.9: Influences of important design factors on frequencies of (a) Hop and (b) Oval-Diag modes, considering 15.8° cell angle

Hop mode of the loaded wheel with θ=15.8° shows f ranging from 17.3 to 20.2 Hz, within the design space considered, as seen in Fig. 5.9(a). The range of Hop mode frequency of the wheel is comparable with those of many passenger car and truck pneumatic tires with various sizes and load-bearing capacities [54]. Moreover, higher Hop mode frequency is observed with increases in factors *A* (cell-wall thickness, t_c) and *B* (initial elastic modulus of cell-wall material, E_{0c}). This is owing to their positive effects on the radial effective elastic modulus (E_Z) of the honeycomb spoke, which strongly affects the vertical stiffness (K_z) of the wheel, as seen in Eq. (5.7). Furthermore, higher increase in bending stiffness of the annular composite beam (shear ring) and thus K_z of the wheel is expected with increasing levels of factor *C* (core layer thickness, t_a), when compared to factor *D* (initial elastic modulus of core layer material, E_{0a}). The increase in factor *C*, however, causes additional increase in wheel mass. Therefore, factors *C* and *D* may show comparable effects on f corresponding to the wheel Hop mode. Similar to the effect of factor *C*, an increase in factor *E* (tread thickness, t_t) leads to higher mass of the wheel as well as bending stiffness of the tread, which is, however, negligible when compared to that of the shear ring. The higher mass of the wheel together with the slight increase in its K_z thus results in lower f of Hop mode.

The Oval-Diag mode of the wheel involves extensional and compressive deformations of the shear ring and the tread, which are constrained in the radial direction of the wheel by the honeycomb spokes, as illustrated in Figs. 5.4 and 5.8. The increases in factors *A* (t_c) and *B* (E_{0c}) cause higher E_Z/E_{0c} (Eq. (5.7)) and thus increasing Oval-Diag mode frequency, as seen in Fig. 5.9(b). Moreover, the circumferential stiffness of the shear ring is related to its overall thickness (t_a+2t_r) and equivalent elastic modulus (E_{eq}), considering given wheel width (205 mm), which could be estimated from the rule of mixtures, as [54]:

$$E_{eq} = \frac{t_a}{t_a+2t_r}E_{0a} + \frac{2t_r}{t_a+2t_r}E_{0r} \tag{5.10}$$

where t_r=0.5 mm and E_{0r}=210 GPa denote the thickness and elastic moduli of the two steel rings, as stated in Section 5.2.3. Owing to the much smaller E_{0a} (12-18 MPa) as compared to E_{0r}, increasing factor *D* (E_{0a}) results in only slight increase in E_{eq} and thus f of wheel Oval-Diag mode, although it is identified as a statistically significant factor, as seen in Fig. 5.9(b) and Table 5.12. The E_{eq} and (t_a+2t_r) values at the low level of factor *C* (t_a=10 mm) are about 0.5 and 2 times, respectively, those at its high level (t_a=20 mm). Lower f is thus observed owing to the slight influence of factor *C* (t_a) on circumferential stiffness of the shear ring together with its positive

effect on the mass of the wheel. In addition, an increase in factor E (t_t) leads to lower f of the Oval-Diag mode. This is partly due to the increasing mass at higher levels of factor E, and in-part to the relatively small circumferential stiffness of the tread, when compared to the shear ring.

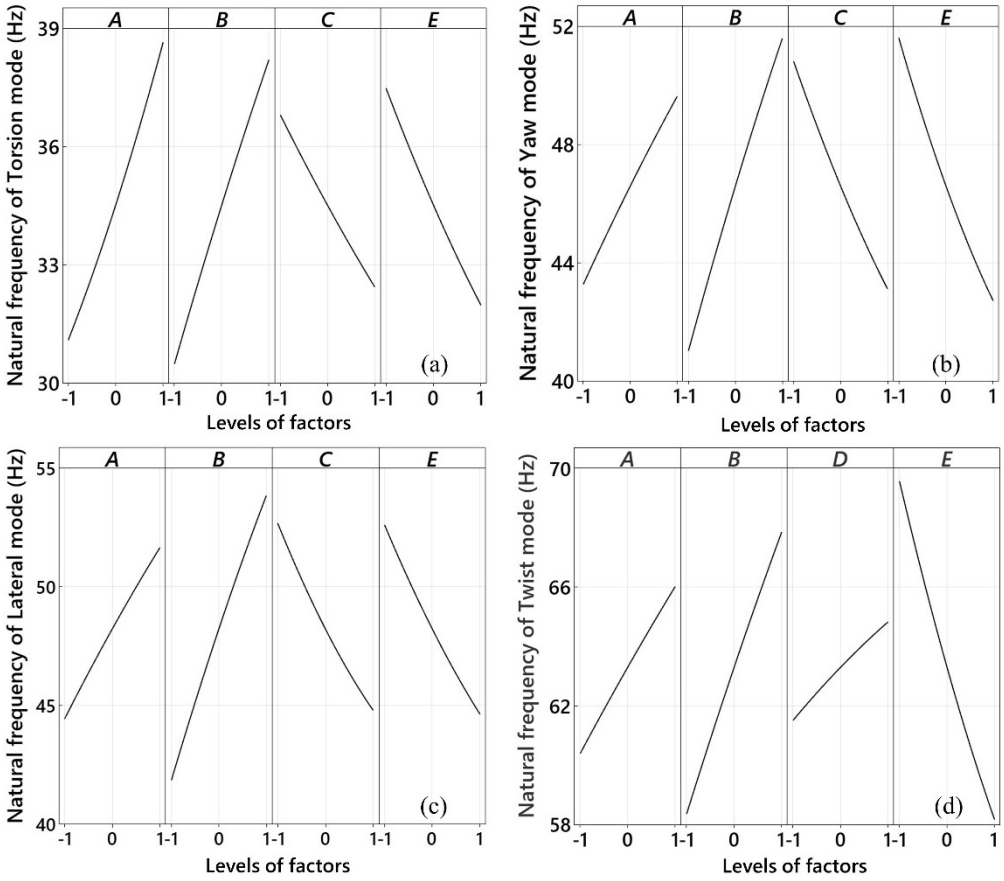

Factors (A, C and E) and (B, D and F) denote thickness dimensions (t_c, t_a, t_t) and initial elastic moduli (E_{0c}, E_{0a}, E_{0t}) of honeycomb cell-wall, core layer and tread, respectively

Figure 5.10: Influences of important design factors on natural frequencies of (a) Torsion, (b) Yaw, (c) Lateral and (d) Twist modes, considering 15.8° cell angle

Fig. 5.10 illustrates the effects of important design factors on frequencies corresponding to Torsion, Yaw, Lateral and Twist modes. The increases in factors A (t_c) and B (E_{0c}) yield higher f of Torsion, Yaw, Lateral and Twist modes. This is due to fact that increases in factors A and B lead to higher G_{ZX}/E_{0c}, apart from higher out-of-plane stiffness of the spokes [115]. Moreover, lower f of the Torsion, Yaw and Lateral modes are observed at higher levels of factors C (t_a) and E (t_t), as illustrated in Figs. 5.10(a), 5.10(b) and 5.10(c), respectively. This is attributable to the greater mass of the wheel and the higher tangential flexibility of the shear ring or the tread, resulting from the increasing thickness dimensions. Similar to the influence on the frequencies of the Torsion,

Yaw and Lateral modes, an increase in factor E (t_t) also yields lower f of the Twist mode. This is due to the higher wheel mass, apart from the relatively smaller out-plane-stiffness of the tread as compared to the spokes and shear ring. Unlike factor C (t_a), an increase in factor D (E_{0a}) only causes higher out-of-plane stiffness of the shear ring without increasing its mass. The positive influence of factor D (E_{0a}) is thus observed, as seen in Fig. 5.10(d). It should be mentioned that most important design factors show mildly nonlinear influences on f of the chosen vibration modes, with the exception of factor A in view of Oval-Diag mode, as seen in Fig. 5.9(b).

The results obtained from the parametric analyses suggest that f of chosen in-plane and out-of-plane vibration modes are strongly coupled via the spokes. Increases in spokes parameters (factors A and B) could help achieve higher f for every vibration mode considered. Increasing thickness dimensions (factors C and E) of the core layer and the tread, however, in general shows opposite effects. The initial elastic modulus of the core layer (factor D) reveals relatively significant effects on only on the Hop and Twist mode frequencies, while that of the tread (factor F) affects the wheel modal properties only slightly.

5.4 Conclusions

1. The FE models developed for the honeycomb NPWs with varying cell angles showed close agreements with the published data in terms of the peak stress of the spokes and the overall vertical deflection and natural frequencies of the wheel. The wheel designs with 47.1° cell angle as well as thin and soft core layer may show excessive deflections in the spokes located within the wheel/road contact region.
2. Parametric studies are conducted for the chosen vibration modes with high magnitudes of modal participation factor or modal effective mass and frequencies below 100 Hz, which are likely to affect wheel dynamic responses and thus the vehicle ride and handling characteristics. The identified in-plane and out-of-plane modes of vibration with frequencies below 100 Hz included Hop, Torsion, Yaw, Lateral, Twist and Oval-Diag modes.
3. Response surface models developed for the wheel designs with 15.8 and 31.5° cell angles showed satisfactory approximations of the frequencies associated with the chosen influential vibration modes, within the design space considered. These models allowed for efficient parametric analyses with sufficient considerations of the interactions among the

important design factors. These models can also be effectively utilized for the development of an efficient design optimization formulation. The results could provide essential guideline for tuning of wheel design parameters to achieve desired modal properties.

4. The results obtained from parametric analyses as well as screening experiments revealed that the natural frequencies of the chosen in-plane and out-of-plane vibration modes are invariably affected by the spokes' design parameters. This is attributable to the coupling between wheel multi-axis stiffness properties. The thickness dimensions of the core layer and the tread, in-general, were found to be more influential with respect to wheel modal properties than their initial elastic moduli.

Chapter 6

Multi-axis and cornering stiffness properties of non-pneumatic wheels with symmetric helical honeycomb spokes

6.1 Introduction

A pneumatic tire is a toroid cord-rubber composite structure filled with pressurized air. This design has shown to satisfy multiple performance demands of the ground vehicles such as comfortable ride, adequate traction for braking and driving manoeuvres, and sufficient steering control and directional stability [54]. The vehicles, however, could loss directional control in case of tire bursting or rapid air leakage, leading to potentially severe body injuries and property losses, particularly under high speeds scenarios. Therefore, a number of design concepts centring about airless or non-pneumatic wheels (NPWs) have been proposed in order to eliminate the safety risks related to the inflation pressure as well as routine maintenances encountered with the pneumatic tires.

The reported NPW design concepts in general consist of a circular composite beam connected to the wheel rim via a number of solid spokes, which are discretely and uniformly distributed along the wheel perimeter, apart from the rubber tread [1,4,5]. These NPW designs differ primarily in their spokes structures, the majority of which include the cellular spokes as in the honeycomb NPWs [5], the radial flexible spokes used in Tweels [1] and the hinge-unit spokes employed in mechano-elastic (ME) wheels [4]. In these NPW designs, the load applied on the rim is mostly suspended to the circular composite beam by the spokes away from the wheel/road contact region [1,108]. This load carrying mechanism is analogous to that of the pneumatic tires, in which the load is primarily supported by the tensioned carcass cords anchored around the beads. Therefore, these designs are also expected to exhibit relatively lower vertical stiffness, lower mean contact pressure and lower wheel mass per unit load carried, when compared to the traditional rigid wheels [1]. Moreover, the spokes and the core layer of the composite beam used in the honeycomb NPWs and Tweels could be constructed from mouldable thermoplastic polyurethane, which shows relatively low hysteresis loss under cyclic loading and thereby lower rolling resistance [7,108]. These NPWs could thus be considered as environmentally friendly designs with improved fuel economy.

A number of recent studies have demonstrated that NPWs with hexagonal honeycomb spokes of positive cell angles could offer sufficient load carrying capacity [16-18], low wheel/road contact pressure with relatively uniform distribution [18], good ride quality [18], and low rolling resistance [16]. Therefore, many studies have investigated the influences of variations in geometric parameters of the (hexagonal) honeycomb spokes on multiple performance measures of the wheel, using finite element (FE) methods. The cell angle revealed negative influences on the load carrying capacity or (equivalent) vertical stiffness of the wheel together with minimal effects on the peak stresses observed in the tread and the spokes [5,6,115]. The NPW designs with increasing cell angle thus necessitate higher cell-wall thickness so as to obtain identical load carrying capacity, resulting in higher masses of the spokes and thus increased rolling resistance of the wheel, apart from lower stresses in the spokes [5,6]. Moreover, the cell angle showed only slight influences on the contact area and peak contact pressure [31,33,115]. Papageorgiou et al. [107] performed a parametric analysis to evaluate the influences of cell-wall thickness, height and length on the vertical stiffness, mass and peak contact pressure of the wheel together with the peak stresses in the spokes and the outer ring. The results showed that tuning of these geometric parameters could yield improved performance measures of the wheel.

On the other hand, some studies evaluated chosen performance measures of honeycomb NPWs with given spokes configurations, using the FE methods. These include modal properties of the fully constrained NPWs with and without ground contact as well as vibrational characteristics and temperature distribution of the steady-state rolling wheels [7,13,14]. The non-contacting NPW with fixed spindle revealed lowest natural frequency of 33.2 Hz corresponding to the torsion mode (rotational deformations about the wheel axis), while the pneumatic tires in general exhibit this in the lateral mode [66,81]. Moreover, excessive amplitude peaks were observed in the response spectra of the rolling wheel, which occurred under excitation frequencies related to its forward speed and number of the discrete spokes. In addition, the core layer of the composite beam contributed about 70% to the total energy loss of the rolling wheel.

The response characteristics of the non-rolling and rolling honeycomb NPWs, when subjected to the normal loads, have been extensively investigated in the abovementioned studies, while only limited knowledge exists on those resulting from horizontal forces and moments excitations, which significantly affect braking/traction and steering performances of the vehicles. A recent study reported multi-axis and cornering stiffness properties of three honeycomb NPWs

with varying cell angles but identical load carrying capacity, which was realized by tuning their corresponding cell-wall thickness, using the FE methods [108]. The results suggested that longitudinal stiffness of the NPWs with relatively low cell angles are considerably lower than that of the chosen reference pneumatic tire with identical load carrying capacity and similar dimensions. The lateral and cornering stiffness of the NPWs, however, were substantially higher than that of the reference pneumatic tire, which was attributed to higher out-of-plane stiffness of the NPWs. An increase in the cell angle, however, could help yield longitudinal stiffness comparable to the reference pneumatic tire, while its effects on lateral and cornering stiffness were relatively small. When a rolling pneumatic tire is subjected to a side force, it deforms and follows a straight path at an angle with respect to its heading direction, which is defined as side slip angle. The cornering stiffness, defined as the slope of the cornering force versus the side slip angle curve near zero side slip, is a determining parameter for directional control and stability performance of vehicles. The NPWs have shown higher cornering stiffness causing rapid saturation of cornering force at very low side slip angles, in the order of about 1.5°, which can cause side slippage of the vehicle under manoeuvres involving higher cornering force demand. This would also lead to adverse effect on handling and directional performance of the vehicle. Conversely, too low a cornering stiffness would lead to excessive side deformations of the wheel in order to reach the cornering force required for negotiating a turn. Similarly, the too low a longitudinal stiffness of the NPWs with relatively small cell angles can lead to extremely large in-plane (vertical-longitudinal) shear deformations. These could cause higher stresses in the wheel resulting in reduced service life. Therefore, it is vital to seek proper combinations of design parameters for the honeycomb NPWs, which could yield multi-axis and cornering stiffness properties comparable to those of the pneumatic tires.

Efficient parametric analyses using Taguchi and response surface methods have been conducted to evaluate the influences of multiple design factors on multi-axis and cornering stiffness characteristics of honeycomb NPWs to establish design guidance [115,118]. These considered spokes of different cell angles and the two-factor interactions of important design parameters, namely, the thickness dimensions and initial elastic moduli of the cell-wall, core layer and the tread. The results suggested that NPWs necessitated a higher cell angle in order to achieve similar longitudinal stiffness as the pneumatic tires of comparable sizes, irrespective of the other design factors considered. Moreover, variations in the design factors related to honeycomb cell

and the tread could help achieve lower lateral stiffness of the wheel, although the lateral stiffness was still notably higher than those of their pneumatic counterparts. This was attributed to the substantially higher out-of-plane stiffness of the in-plane configuration of the honeycomb structures. In addition, tuning of the design factors, particularly those corresponding to the core layer and the tread, could help obtain cornering stiffness comparable to that of the pneumatic tires. These designs in general are coupled with thicker core layer and tread, which tends to lower the longitudinal stiffness.

This study proposes a novel design concept for the honeycomb spokes, called "symmetric helical honeycomb spokes", which could offer higher longitudinal stiffness for the NPWs, particularly those with the lower cell angles, together with additional reductions in their cornering stiffness. The effects of the proposed symmetric helical spokes on the stiffness properties of a honeycomb NPW are evaluated considering spokes configurations of different cell and helix angles. These include multi-axis stiffness of the stationary wheel as well as the cornering stiffness under 10 km/h rolling speed, when subjected a given normal load of 3 kN. For this purpose, comprehensive three-dimensional FE models were developed for the honeycomb NPW with different helical spokes configurations so as to obtain their multi-axis force/moment-deformation and cornering force-side slip angle relations. The validity of the developed FE NPW models with 0° helix angle and different cell angles was then established through comparing the models' responses in terms of overall vertical deflections and cornering stiffness of the wheel as well as the peak stresses in the spokes with the reported results. The influences of cell and helix angles on the stiffness properties of the wheel were subsequently analyzed under two design constraints: (i) identical cell-wall thickness and (ii) identical load carrying capacity, so as to evaluate the relative merits of the symmetric helical spokes.

6.2 FE modelling of the honeycomb NPW

High-fidelity three-dimensional (3D) FE wheel models were developed for a honeycomb NPW, considering three different spokes configurations of varying cell angles (θ), in the order of 15.8°, 31.5° and 47.1°, respectively. These θ values were chosen to conform to those reported in refs. [6,108], where some results are available for the verifications of the developed FE wheel models. The helix angle (β) associated with the spokes configurations of these three wheel models were subsequently increased from 0° to 45° in increments of 15°. This permitted analyses of the

influences of β on multi-axis and cornering stiffness properties of the wheel, while considering different θ.

Fig. 6.1 illustrates the honeycomb wheel with three spokes configurations (β=0°) of different θ. Each wheel design consists of the aluminium rim, cellular polyurethane spokes, sandwich beam and the rubber tread. The sandwich beam, also referred to as the shear ring, comprises a polyurethane core layer sandwiched between two high strength steel rings. The dimensions of the wheel as well as its components including the spokes were taken as those of the designs reported in ref. [108], which also approximately conform to those reported in ref. [6]. The wheel and rim radii together with the wheel width were taken as 316, 203 and 205 mm, respectively, as partly seen in Figs. 6.1(a) and 6.1(c). Moreover, the thickness dimensions of the tread, two steel rings, core layer and the rim were fixed as 5, 0.5, 9.5 and 1 mm, respectively. It should be noted that the rim with negligible deformations was considered as a rigid body in the wheel FE model. Furthermore, the dimensions corresponding to the spokes of different θ in terms of cell-wall heights (h_i), lengths (l_i) and thickness (t_c) are summarized in Table 6.1. In this table, θ, h and l represent the means of θ_i, h_i and l_i (i=1,..,4), respectively, which relate to the radii of the inner steel ring (R_1=302 mm) and rim (R_2=203 mm) as well as the number of spokes (N) along the wheel perimeter, as:

$$(h_1 + h_2 + h_3 + h_4)/2 + l_2 \sin\theta_2 + l_3 \sin\theta_3 \approx (R_1 + R_2)\pi/N \tag{6.1}$$

$$\sum_{i=1}^{4} l_i \cos\theta_i = R_1 - R_2 \tag{6.2}$$

It should be mentioned that N=19 was also taken as reported in refs. [6,108].

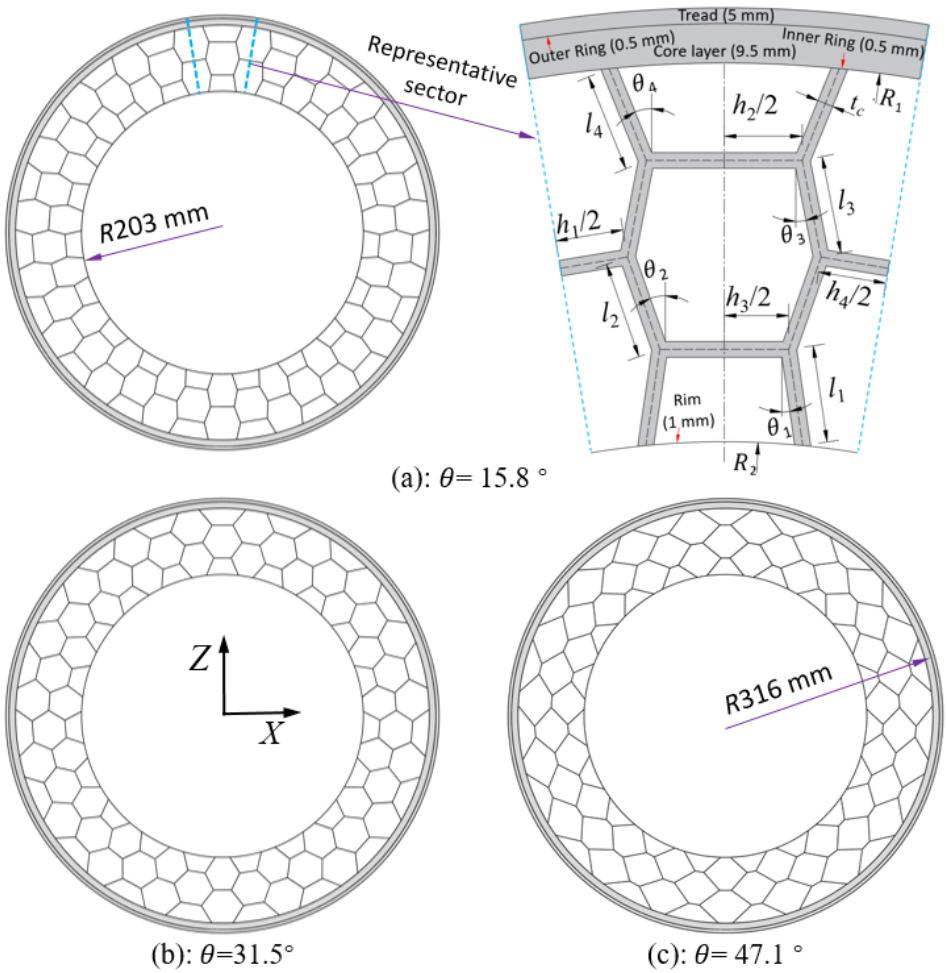

(a): θ= 15.8 °

(b): θ=31.5°

(c): θ= 47.1 °

Figure 6.1: Honeycomb wheel with three spokes configurations of different cell angles (θ)

Table 6.1: Dimensions of three spokes configurations of different cell angles

Cell angle (deg) $\theta_1, \theta_2, \theta_3, \theta_4$, ($\boldsymbol{\theta}$)	Cell-wall		
	Height (mm) h_1, h_2, h_3, h_4, ($\boldsymbol{h}$)	Length (mm) l_1, l_2, l_3, l_4, ($\boldsymbol{l}$)	Thickness t_c, (mm)
8.9, 19.9, 11.7, 22.7, (**15.8**)	34.4, 39.4, 32.6, 34.4, (**35.2**)	24.7, 24.8, 25.0, 25.2, (**24.9**)	1.54
22.6, 35.6, 27.9, 39.9, (**31.5**)	25.8, 30.4, 25.1, 25.8, (**26.8**)	27.5, 27.6, 28.7, 29.5, (**28.3**)	2.38
38.3, 50.4, 44.0, 55.6, (**47.1**)	17.7, 15.9, 13.2, 17.7, (**16.1**)	32.8, 34.6, 36.4, 38.1, (**35.5**)	2.82

The mechanical behaviours of the elastic steel and aluminium were modelled using linear elasticity theory, while those corresponding to the hyper-viscoelastic polyurethane and rubber were described using Ogden strain energy potential combined with Prony series [95], as:

$$U = \sum_{i=1}^{Q} \frac{2\mu_i}{\alpha_i^2}\left(\bar{\lambda}_1^{\alpha_i} + \bar{\lambda}_2^{\alpha_i} + \bar{\lambda}_3^{\alpha_i} - 3\right) + \sum_{i=1}^{Q} \frac{1}{D_i}\left(J^{el} - 1\right)^{2i}; Q{=}3 \quad (6.3)$$

$$\frac{G_R(t)}{G_R(t=0)} = 1 - \sum_{i=1}^{M}\{g_i[1-\exp(-t/\tau_i)]\};\ M=3 \tag{6.4}$$

where U and J^{el} denote the strain energy density and the elastic volume ratio, respectively, while μ_i, α_i and D_i are model parameters that affect the initial shear and bulk moduli of the materials. $G_R(t)$ represents the time varying shear relaxation modulus, while g_i and τ_i (i=1,..,M) are i^{th} Prony series parameters. These material model parameters were taken as those reported in [6,108], which were identified from measured stress-strain and strain- or stress-time relations [112], as summarized in Table 6.2 together with Young's moduli and Poisson's ratios for the elastic materials.

Table 6.2: Model parameters identified from test data for hyper-viscoelastic and elastic materials [6,108]

i	Polyurethane					Rubber				
	μ_i(MPa)	α_i	D_i (MPa^{-1})	g_i	τ_i (s)	μ_i(MPa)	α_i	D_i (MPa^{-1})	g_i	τ_i (s)
1	13.55	1.51	3.5E-03	0.125	0.002	13.36	1.63	5.9E-03	0.2	0.002
2	-2.34	2.21	0	0.125	0.02	-6.63	1.90	0	0.2	0.02
3	0.09	-2.47	0	0.125	0.2	0.06	-2.46	0	0.2	0.2

Elastic materials	Elastic modulus, GPa	Poisson's ratio, v	Density (kg/m^3)
Steel	210	0.29	7800
Aluminium	72	0.33	2800

In the linear region, the in-plane (x-z plane in Fig. 6.1) effective shear and elastic moduli of a 2D honeycomb cell, which relate to its mean dimensions (θ, l, h and t_c) as well as the initial elastic modulus (E_{0c}) of its constituent material (polyurethane), could be approximately evaluated using the following relations [5,24]:

$$\frac{G_{ZX}}{E_{0c}} = \frac{(h/l+\sin\theta)}{(h/l)^2\,(1+2h/l)\cos\theta}(t_c/l)^3 \tag{6.5}$$

$$\frac{E_X}{E_{0c}} = \frac{(h/l+\sin\theta)}{\cos^3\theta}(t_c/l)^3 \tag{6.6}$$

$$\frac{E_Z}{E_{0c}} = \frac{\cos\theta}{(h/l+\sin\theta)\sin^2\theta}(t_c/l)^3 \tag{6.7}$$

where G_{ZX} denotes the effective shear modulus of the 2D spoke, while E_X and E_Z are its effective elastic moduli in x- and z- directions, respectively. These effective moduli significantly influence the in-plane stiffness properties of the wheel.

The high-fidelity FE models of the honeycomb wheel with spokes configurations of different θ and β were developed. As an example, Fig. 6.2 depicts one periodic or full wheel model with 15° helix angle together with four sector models with varying β, considering θ=15.8°. The 2D cross-sectional elements of the tread, outer ring and the core layer of a representative sector (Fig. 6.1(a)) were initially copied and dragged along the y-direction from the side plane of the wheel to its center plane, while those of the inner ring, spokes and the rim were duplicated and extruded along the helixes of varying β, as seen in Figs. 6.2 and 6.3. This could ensure that the elements of the inner ring are connected to those of the rim by the spoke elements via shared nodes. The other components, however, were assembled together and adhered to the inner ring using surface-to-surface tie constraint. These elements were subsequently duplicated and reflected with respect to the wheel center plane to build the sector or partial models. Each of these sector models was copied and revolved about the wheel axis so as to generate corresponding full model of the entire wheel, using the symmetric model generation feature incorporated in ABAQUS software [95]. This approach allowed for efficient modelling of the dynamic interactions between a steady-state rolling wheel and the non-deformable terrain [59,65,96].

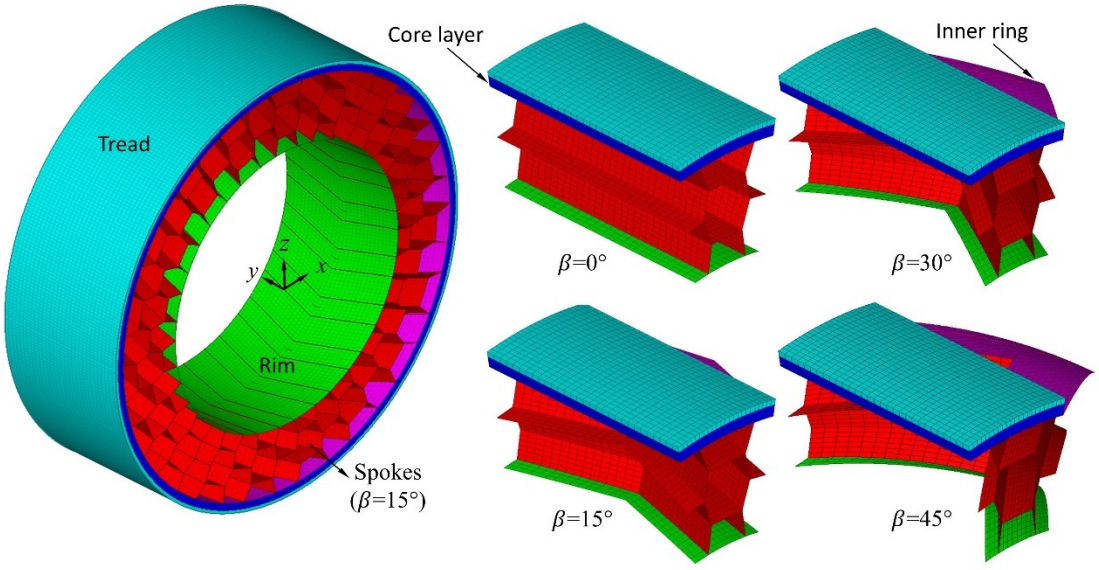

Figure 6.2: Full wheel model with 15° helix angle (β) and four partial models with different β, considering 15.8° cell angle

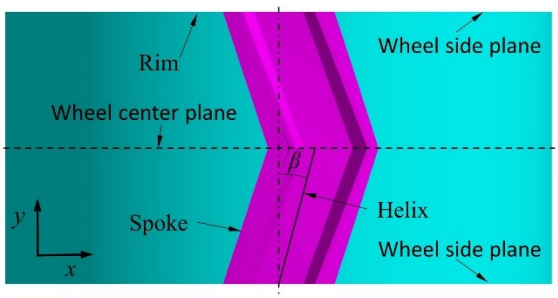

Figure 6.3: Spoke developed on wheel rim considering θ=15.8° and β=15°

More detailed information about the development of the three FE wheel models for non-helical cell configuration (β=0°, θ=15.8°, 31.5° and 47.1°) in terms of element selections, wheel/ground contact and interactions as well as grid convergence study have been presented in recent studies [108,115]. The static and dynamic friction of coefficients were taken as 0.80 and 0.75, respectively, to represent the sticking and sliding interactions of the wheel with the dry asphalt road [54]. It should be noted that the nearly optimal element sizes, which were determined from the grid convergence study, could ensure converged wheel responses with minimized computational cost. The in-plane and out-of-plane wheel responses considered in the convergence study included the peak stresses in the spokes and the overall wheel vertical deflections under various normal loads, apart from the cornering force at 10 km/h forward speed and 0.5° side slip angle. Similar element sizes were also applied to the wheel models with other spokes configurations of β=15°, 30° and 45°.

6.2.1 Method of analyses

The stiffness properties considered in this study include the multi-axis stiffness and the cornering stiffness of the honeycomb wheel under stationary and rolling conditions, respectively. To derive these stiffness values, each wheel model was first displaced vertically to initiate its contact with the fully constrained rigid road. A gradually increasing vertical force was subsequently applied to the rim center until the desired normal load level (3 kN) was achieved. Unbalanced contact forces and thus potential convergence difficulties could be avoided using this two-step loading approach [95]. The vertical stiffness (K_z) is evaluated as the ratio of the normal load (3 kN) and the resulting overall vertical deformation of the wheel. Subsequently, the road was translated along *x*- or *y*-axis or revolved about *z*-axis (Fig. 6.2) so as to yield longitudinal and lateral force-deformation as well as yaw moment-deformation properties. The static coefficient of friction was taken as 0.80, as stated above. The longitudinal (K_x) and lateral (K_y) stiffness of the wheel were assessed within

relatively small deflection ranges, in the vicinity of 0 to 1 mm for both the directions. In a similar manner, the yaw stiffness (K_{φ}) was estimated within 0 to 0.2° yaw rotation range.

When a straight-line rolling honeycomb wheel is subjected to a side slip angle, it deforms and rapidly reaches the steady-state motion. The governing equations of motion of this rolling wheel FE model could be solved using implicit or explicit time integration techniques so as to derive its transient (time-dependent) responses [95]. These direct-integration methods, however, in general necessitate a large number of iterations or limited time increment size in order to obtain accurate predictions of wheel's cornering force responses [59,104]. These could thus cause excessive computational demands, particularly for the large size FE models. Moreover, these methods need repeated simulations for each side slip angle to obtain corresponding steady-state cornering force, resulting in considerable additional computational cost.

In this study, an alternate approach is adopted to derive steady-state responses of the rolling wheel model under side slip conditions directly without consideration of its prior transient states. This was realized using the steady-state transport analysis feature available in ABAQUS/standard [95]. Unlike the above-stated transient analyses, this approach uses a frame of reference fixed to its axis of revolution (y-axis) and travelling with the wheel. This allowed for representation of the wheel rotation, in a Eulerain manner, by its constituent materials transporting through the stationary mesh, while the wheel deformation could be described in a Lagrangian manner. Moreover, the cornering force response of the wheel model at each incremental side slip angle corresponds to a steady-state solution. Therefore, the cornering forces at different side slip angles could be derived using only a single steady-state transport simulation. In addition, this efficient approach could offer improved accuracy when predicting cornering properties under relatively high side slip conditions [59].

Following the static loading of the honeycomb wheel model, a constant forward velocity was specified for the above-stated travelling frame of reference, while an angular velocity was assigned to the transporting materials. This represents the constant forward speed motion of the wheel with braking/driving torque around its revolution axis. Tuning this angular velocity could yield zero torque, which corresponds to the straight-line free rolling solution. Subsequently, an additional lateral velocity, which gradually increases during the analysis, was specified for the travelling frame of reference in order to obtain cornering force responses at different side slip conditions.

The side slip angle (α) represents the angle between the directions of travel and the wheel heading, which relates to forward (v_x) and lateral (v_y) velocity components of the wheel, as:

$$\alpha = \tan^{-1}\frac{v_y}{v_x} \tag{6.8}$$

It should be noted that owing to the considerable difference between stationary and rolling frictional stresses, the abovementioned static load simulation was repeated, however, with zero friction coefficient, which was subsequently increased to 0.75 for the steady-state transport analyses. These could ensure smooth transition of frictional stresses and therefore eliminate potential convergence problems [59,95]. Moreover, the nonlinear equilibrium equations of both stationary and rolling wheel models were solved iteratively using Newton-Raphson's method. Furthermore, the default convergence criteria which could offer relatively accurate solutions at each iteration or increment was used in this study [95].

6.2.2 Model verifications

The validity of the three wheel models with honeycomb spokes of three different cell angles (θ=15.8°, 31.5° and 47.1°) but without the helix (β=0°) was initially verified by comparing the static responses with those reported in [6], which employed similar wheel and components dimensions together with identical material properties. These static responses included the peak stresses developed in the honeycomb spokes and the overall vertical deflections of the wheel, considering three different normal loads (2, 3 and 4 kN). It should be noted that the components dimensions of the wheel model developed in the study (Table 6.1) differed slightly from those of the wheel reported in [6], with the exception of the cell-wall thickness. The peak difference in the dimensions of the two wheels is about 6%. Moreover, the cell-wall thickness of each design was tuned to yield about 190 kN/m vertical stiffness (K_z) to conform to that of a reference pneumatic tire (205/55R16). The vertical stiffness of the reported wheel design (K_z≈202 kN/m), however, was slightly higher. Additional models' verifications were also conducted by comparing their cornering force responses obtained under rolling conditions with those reported in [108], which employed identical material properties and wheel dimensions. The dynamic responses of each wheel model with different θ and normal loads (2, 3 and 4 kN) were derived using the abovementioned steady-state transport analysis feature, considering 10 km/h forward velocity and

side slip angles up to 5°. The cornering stiffness (K_α) of the wheel was evaluated as the cornering force gradient within relatively small range of side slip angles (0 to 0.2°).

As an example, Figs. 6.4(a) and 6.4(b) depict comparisons of model-predicted and reported static responses, considering 31.5° cell angle. Reasonably close agreements are observed between the predicted and reported peak stresses in the spokes and vertical deflections of the wheel, with maximum differences of 7.2% and 5.8%, respectively, for the range of normal loads considered. These deviations may be due to small differences in components dimensions of the wheels, as stated above. Moreover, the peak stresses in Fig. 6.4(a) invariably occurred in the spoke near the center of the wheel/road contact patch, irrespective of θ considered. This is primarily owing to their considerably higher strain resulting from compression deformations, as compared to the spokes away from the contact patch, which undergo tension deformations along the radial direction of the wheel. The results in Fig. 6.4(c) suggest close agreements between the predicted and reported cornering stiffness (K_α) for all three normal loads considered, with less than 4.1% difference, which occurs for the 4 kN wheel load. The differences may be attributable to the fact that the cornering force responses of the reported designs were obtained using verified FE models with explicit time integration technique. Similar levels of agreements were also observed for the wheel models with θ=15.8° and 47.1°. Therefore, these wheel models could be viewed as valid with regard to the reported data, and be employed to investigate the dependences of wheel's stiffness properties on the proposed symmetric helical spokes by varying its helix angle.

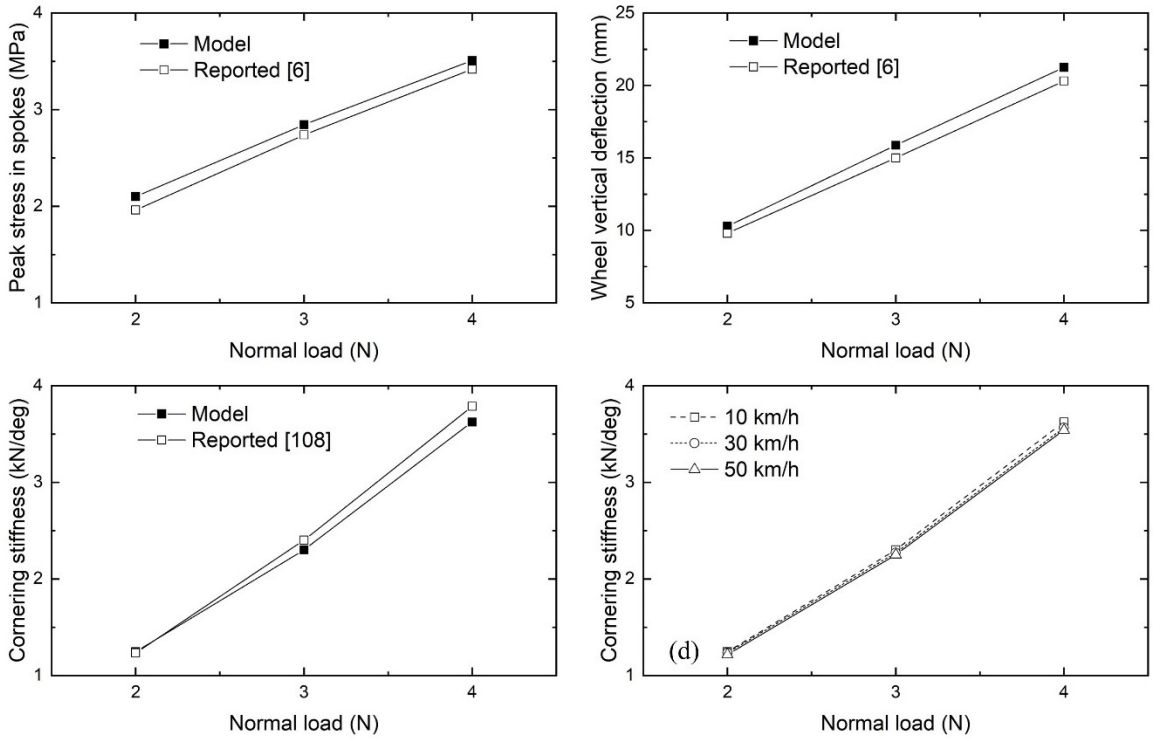

Figure 6.4: Comparisons of model-predicted (a) peak stress in the spokes, (b) vertical deflection and (c) cornering stiffness of the wheel with reported data; (d) Influences of forward velocity on cornering stiffness of the wheel (cell angle: 31.5°; normal loads: 2, 3 and 4 kN)

In order to investigate the effects of forward velocity on the cornering properties of the honeycomb wheel, steady-state transport simulations were conducted for these three wheel models, considering additional two forward speeds (30 and 50 km/h). For instance, Fig. 6.4(d) depicts variations in K_α of the wheel model (θ=31.5°) with varying forward velocities, under different normal loads. Less than 2.4% decrease in K_α, which occurred at higher wheel normal load of 4 kN, was observed with increasing forward velocity, as in the case of the pneumatic tires [54]. The results for the wheel models with θ=15.8° and 47.1° also revealed similar trends. Therefore, the forward velocity was limited to only 10 km/h for subsequent studies on cornering stiffness properties of the rolling wheels.

6.3 Results and discussion

FE simulations were conducted for the wheel models with symmetric helical spokes of different cell (θ) and helix (β) angles so as to investigate their influences on multi-axis and cornering stiffness characteristics of the wheel, under a given normal load of 3 kN. These wheel designs with different spokes configurations were initially assigned with identical cell-wall thickness (t_c). It

should be noted that in the absence of helix angle (β=0°), the reported material properties for the polyurethane and the rubber (Table 6.2) resulted in extremely high cornering stiffness of about 2300 N/deg for the three wheel models (θ=15.8°, 31.5° and 47.1°) under 3 kN normal load and 10-50 km/h forward speeds, as partly seen in Fig. 6.4(d). This could lead to rapid saturation of the cornering force under relatively small side slip conditions, and lateral slippage of the wheel and thus potential loss of vehicle directional control under higher side slip angles [108]. The material model parameters of the polyurethane and the rubber (Table 6.2) were thus tuned, without varying the dimensions of the wheel and its components (expect t_c), which are summarized in Table 6.3. It should be mentioned that the tuned initial elastic modulus of the tread (6 MPa) falls in the practical design range for passenger car tires [96,104]. Moreover, these modified parameters could yield the target vertical stiffness of 190 kN/m for the wheel design with θ=15.8° and β=0°, which conforms to that of the reference pneumatic tire [96].

Table 6.3: Components dimensions and tuned material properties of the wheel models with different spokes configurations of identical cell-wall thickness

Parameters	Values		
Cell angle (°)	15.8	31.5	47.1
Thickness of cell-wall, t_c (mm)	3.5	3.5	3.5
Initial elastic modulus of cell-wall, E_{0c} (MPa)	18	18	18
Thickness of core layer, t_a (mm)	10	10	10
Initial elastic modulus of core layer,E_{0a} (MPa)	18	18	18
Thickness of tread, t_t (mm)	5	5	5
Initial elastic modulus of tread, E_{0t} (MPa)	6	6	6

FE simulations were subsequently repeated for the wheel models with identical load carrying capacity or (equivalent) vertical stiffness, which was achieved by tuning t_c of corresponding spokes. This design constraint has been used in refs. [5,6], which represents the coupling effects of t_c together with θ on the stiffness properties of the wheel. The simulation results obtained for the wheel models with identical cell-wall thickness and identical load carrying capacity are discussed below.

6.3.1 Honeycomb wheel designs considering identical cell-wall thickness

The multi-axis stiffness and cornering stiffness characteristics of the wheel models with identical t_c were initially obtained so as to evaluate their dependence on θ and β associated with the symmetric helical honeycomb spokes, as discussed in the subsequent subsections.

Multi-axis stiffness characteristics

The honeycomb wheel with twelve different spokes configurations of varying cell (θ=15.8°, 31.5° and 47.1°) and helix (β=0°, 15°, 30° and 45°) angles were initially assigned with constant cell-wall thickness (t_c) of 3.5 mm, as stated above. The vertical, longitudinal, lateral and yaw stiffness of the wheel models were evaluated using the methods described in Section 6.2.1. The vertical stiffness (K_z) of these wheel designs under a given normal load of 3 kN are summarized in Table 6.4 together with the mass of each spoke configuration and the length of its associated helix (Fig. 6.3), which relates to β and the width of the rim (205 mm) as:

$$\text{Helix length} = \frac{205}{\cos\beta} \tag{6.9}$$

Table 6.4: Lengths of helices, masses of spokes and vertical stiffness of wheel designs, considering different cell (θ) and helix (β) angles

β (°)	Helix length (mm)	Spokes' mass (kg)			Vertical stiffness, K_z (kN/m)		
		θ=15.8°	θ=31.5°	θ=47.1°	θ=15.8°	θ=31.5°	θ=47.1°
0	205.0	5.01	5.05	5.4	190.0	145.7	125.6
15	212.2	5.17	5.23	5.57	225.6	167.9	138.5
30	236.7	5.71	5.79	6.16	324.7	243.5	186.1
45	289.9	6.83	6.89	7.32	470.9	379.8	302.9

As it would be expected, increasing the helix angle yields notable increases in the length of the helix (Eq. (6.9)), total mass of the spokes and K_z of the wheel, irrespective of the θ value considered. More evident increases are observed corresponding to higher β, particularly when it is increased from 30° to 45°. Moreover, the relative increases in K_z are considerably higher, when compared to those corresponding to masses of the spokes and thus the wheel. For instance, increasing β from 0° to 45° results in 147.1% increase in K_z of the wheel model with θ=15.8°, while the corresponding increases in the spokes mass is 36.3%. It should be noted that the mass of the other components of the honeycomb wheel is about 10 kg.

An increase in cell angle θ from 15.8° to 31.5°, on the other hand, results in 23.5% reduction in K_z of the wheel model with β=0°, as seen in Table 6.4. A further increase to 47.1°, however, leads to relatively smaller reduction in K_z (13.8%). This negative and nonlinear effect of θ on K_z is consistent with its influence on the radial effective elastic modulus (E_Z), as seen in Eq. (6.7), for the 2D spoke normalized to the initial elastic modulus of the constituent material (E_{0c}), which

significantly affects K_z of the wheel, as depicted in Fig. 6.5. Figure also shows variations in the normalized shear modulus (G_{ZX}/E_{0c}) as a function of θ. Both the normalized radial elastic (E_Z/E_{0c}) as well as shear (G_{ZX}/E_{0c}) moduli were calculated using Eqs. (6.5) and (6.7), considering t_c=3.5 mm and mean dimensions (θ, h and l) of the 2D spoke presented in Table 6.1. Similar variations in K_z with varying θ are also observed for the wheel with spokes configurations of β=15°, 30° and 45°. This is attributable to the fact that the normal load acting on the rim center is suspended to the shear ring by the spokes away from the vicinity of wheel/road contact region [108], which invariably show negligible out-of-plane deformations for all β values considered, as depicted in Fig. 6.6. Moreover, increasing θ from 15.8° to 31.5° yields only slightly higher mass of the spokes' , irrespective of β value considered, while a relatively higher increase (≈6.5%) in the mass is observed when θ is increased to 47.1°. This is consistent with the influence of θ on the summation of cell-wall lengths and heights of a sector or partial 2D honeycomb spoke (Fig. 6.1(a)), considering identical t_c for each spokes configuration and the constant wheel width, as partly seen in Table 6.1.

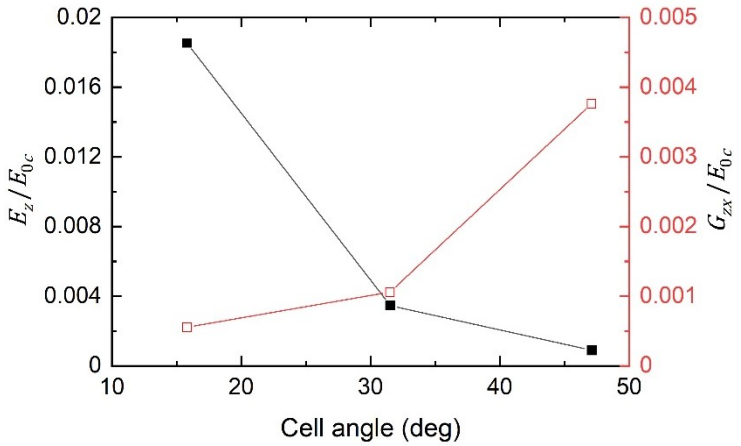

Figure 6.5: Influences of cell angle on the normalized radial (E_Z/E_{0c}) and shear (G_{ZX}/E_{0c}) effective moduli of the 2D honeycomb spoke with β=0°

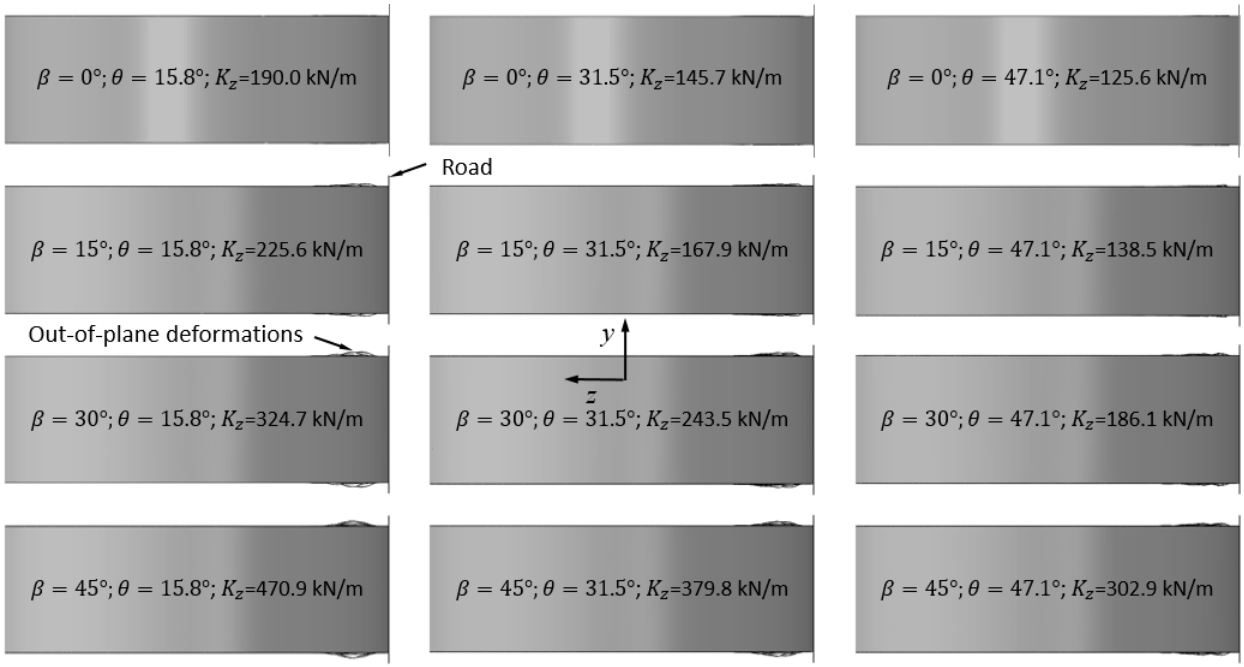

Figure 6.6: Deformations of the honeycomb wheel with spokes configurations of different helix (β) and cell (θ) angles (normal load=3 kN)

Parametric studies of the wheel designs with β=0°, reported in [115], suggested that increasing the thickness dimensions or initial elastic moduli of the honeycomb cell-wall, core layer and the tread, from 40% to 200%, yielded less than 40% increase in K_z of the wheel. It can thus be concluded that β is a more dominant design parameter concerning K_z, when compared to the design parameters considered in ref. [115], including θ. This is of particular importance for designing wheels with high load-carrying capacity for applications in heavy-duty vehicles. It should also be mentioned that increasing β causes relatively small increase (≤12.5%) in mass of the wheel and may thus exhibit only slightly higher rolling resistance.

The horizontal stiffness values of the honeycomb wheel in terms of longitudinal, lateral and yaw stiffness are summarized in Table 6.5, considering twelve spokes configurations of different θ and β together with 3 kN normal load. The simulation results for each of the three stiffness properties were subsequently normalized with respect to those of the wheel design with spokes configurations of β=0° or θ=15.8° so as to clearly reveal their dependence on helix or cell angles, as illustrated in Fig. 6.7.

Table 6.5: Longitudinal, lateral and yaw stiffness of the honeycomb wheel with spokes configurations of different cell (θ) and helix (β) angles

β	Longitudinal stiffness, K_x (kN/m)			Lateral stiffness, K_y (kN/m)			Yaw stiffness, K_φ (Nm/deg)		
(°)	θ=15.8°	θ=31.5°	θ=47.1°	θ=15.8°	θ=31.5°	θ=47.1°	θ=15.8°	θ=31.5°	θ=47.1°
0	66.5	91.5	216.0	342.6	289.1	233.3	143.6	127.1	117.6
15	122.6	133.9	222.3	333.0	286.8	239.8	145.4	130.6	120.5
30	282.9	256.9	296.2	309.1	275.2	247.0	137.8	125.9	121.4
45	530.3	490.2	488.4	281.3	265.0	269.8	131.0	124.0	124.9

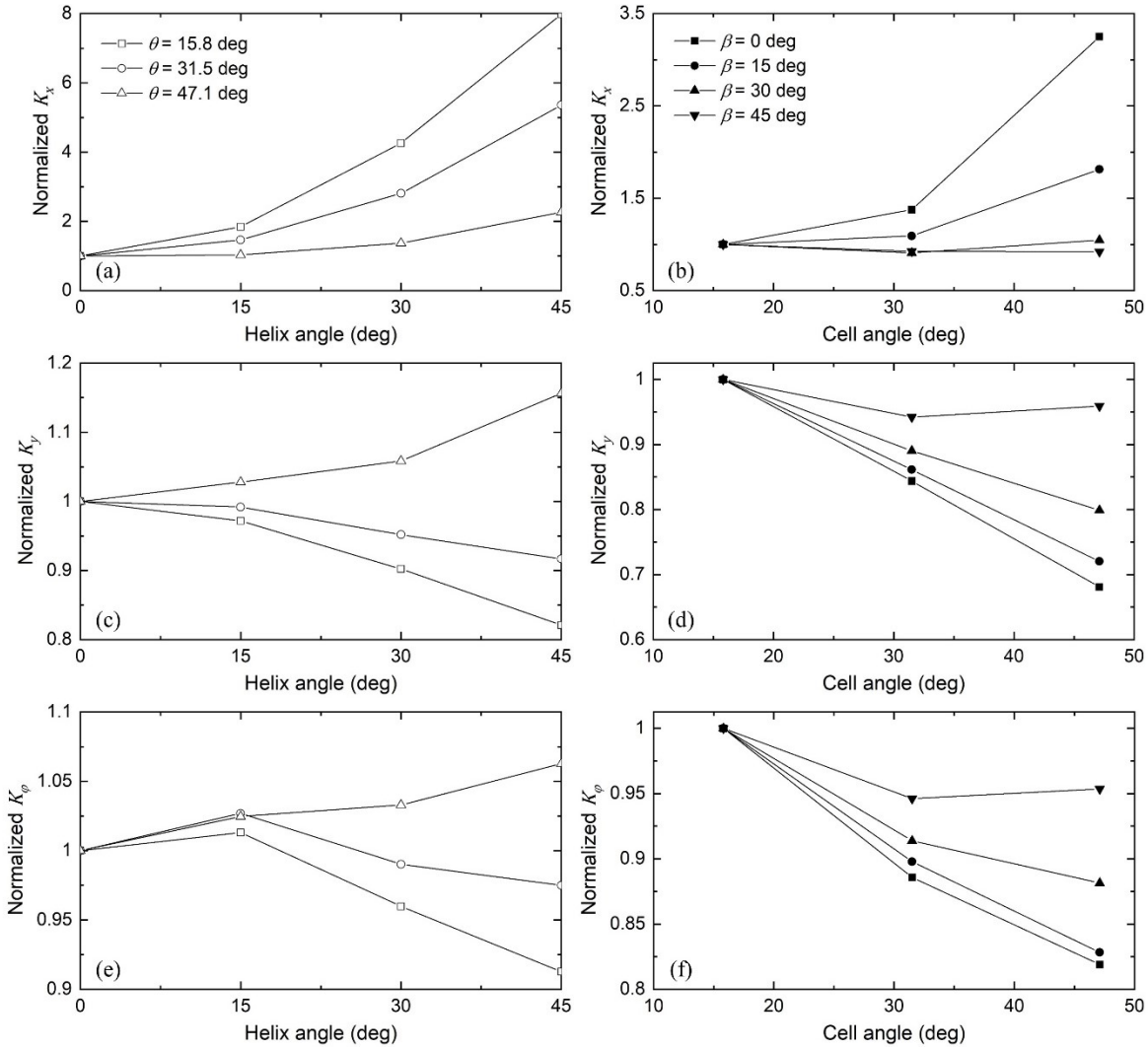

Figure 6.7: Influences of helix and cell angles, β and θ, on the normalized wheel stiffness: (a) and (b) longitudinal, K_x; (c) and (d) lateral, K_y; (e) and (f) yaw, K_φ

The wheel designs with 15.8° and 31.5° cell angles show too low K_x under 3 kN normal load, in the 66.5-91.5 kN/m range, when β=0°, as seen in Table 6.5. These stiffness values are much smaller than those of most passenger car pneumatic tires, which generally exceed 200 kN/m [39,115]. Too low K_x may cause large wheel deformations under relatively high longitudinal slip

conditions, resulting in potentially undesired sensation of discomfort under driving/braking manoeuvres. Increasing β, however, could help achieve notable increase in K_x, which is particularly evident when for lower θ, as shown in Fig. 6.7(a). This is partly attributable to the higher helix length, and in-part to the fact that the spokes of the loaded honeycomb wheel show higher out-of-plane deformations in the vicinity of wheel/road contact region at lower θ, which may generate more resistances to subsequent in-plane shear deformations, as seen in Fig. 6.6. An increase in θ could also yield higher K_x for the wheel models with β=0°, as seen in Fig. 7(b). Moreover, more considerable increase is observed when θ is increased from 31.5° to 47.1°. This nonlinear and positive trend is consistent with the influence of θ on the normalized (in-plane) shear elastic modulus (G_{ZX}/E_{0c}) of the 2D spoke, which significantly affects K_x of the wheel, as seen in Fig. 6.5. Furthermore, the cell angle also shows positive influence on K_x when β is increased to 15°, although with less increase as compared to the case of β=0°. A further increase in β to 30° and 45° causes only slight variations in K_x of the wheel, when increasing θ. These indicate that θ becomes insignificant with respect to K_x when high out-of-plane deformations occur in the spokes. In addition, the spokes configurations with β=15° and 30° or θ=47.1° and β<30° could be considered as proper designs with regards to K_x of the wheel. It should be noted that K_x could also be tuned by varying the thickness dimensions and initial elastic moduli of the honeycomb cell-wall and the core layer [115], although their corresponding influences are generally smaller than those of β and θ.

Lower K_y is obtained with an increase in β for the wheel models with θ=15.8°, as depicted in Fig. 6.7(c). This is due to the fact the spokes of higher β exhibit more out-of-plane deformations under 3 kN normal load (Fig. 6.6), and therefore are considered less resistant to additional lateral deformations resulting from shear loads in the *y*-direction. As expected, relatively less decrease in K_y was observed when increasing θ to 31.5°, owing to the decreasing out-of-plane deformations in the spokes (Fig. 6.6). This negative influence of β, however, switches to positive with a further increase, within the cell angles range considered. This is likely due to the different deformation patterns observed in the spokes of the wheel with different θ, when subjected to shear loading along the *y*-axis. As an example, Fig. 6.8 depicts the deformations of the spokes for the wheel models with β=0° and θ=15.8°, 31.5° and 47.1°, respectively, considering 3 kN normal load and 5 mm lateral displacement. In this figure, the spokes with θ=15.8° and 31.5° reveal bending deformations near the contact region, while those with θ=47.1° show both bending and out-of-

plane shear deformations, which could be attributed to their relatively higher mean cell-length (Table 6.1).

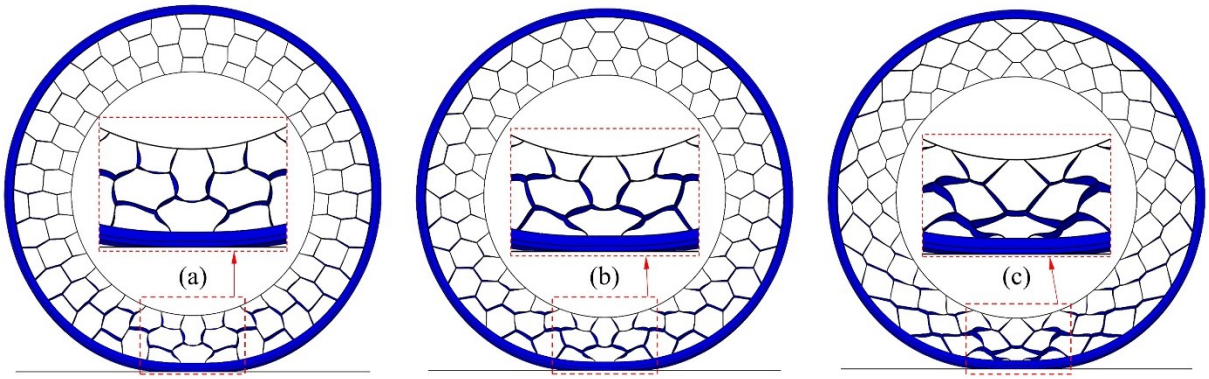

Figure 6.8: Deformation patterns of the spokes of the loaded wheel models with 0° helix angle and (a) 15.8° cell angle, (b) 31.5° cell angle and (c) 47.1° cell angle (normal load=3 kN, lateral displacement=5 mm)

Similar but smaller influences of β were observed with regards to the yaw stiffness K_φ, when compared to those on K_y of the wheel, as illustrated in Figs. 6.7(c) and 6.7(e). This indicates that the yaw moment responses of the wheel models with different spokes configurations are primarily determined by their lateral stiffness properties. Moreover, the comparatively smaller influences (≤9%) of β on K_φ are attributed to relatively lower contribution of spokes to the yaw deformation of the honeycomb wheel as compared to its lateral deformation. This is evidenced from the out-of-plane deformations of the wheel models under yaw and lateral motions, presented in Fig. 6.9, considering β=0° and θ=15.8°, 31.5° and 47.1°, respectively. It should be noted that the both the yaw moments and lateral forces of these wheel models approach the road friction limit. In addition, increasing β from 0° to 15° causes slightly higher K_φ for the wheel models with θ=15.8° and 31.5°. This is likely due to the positive influence of β on K_x (Fig. 6.7(a)), although its contribution to yaw stiffness property is relatively small.

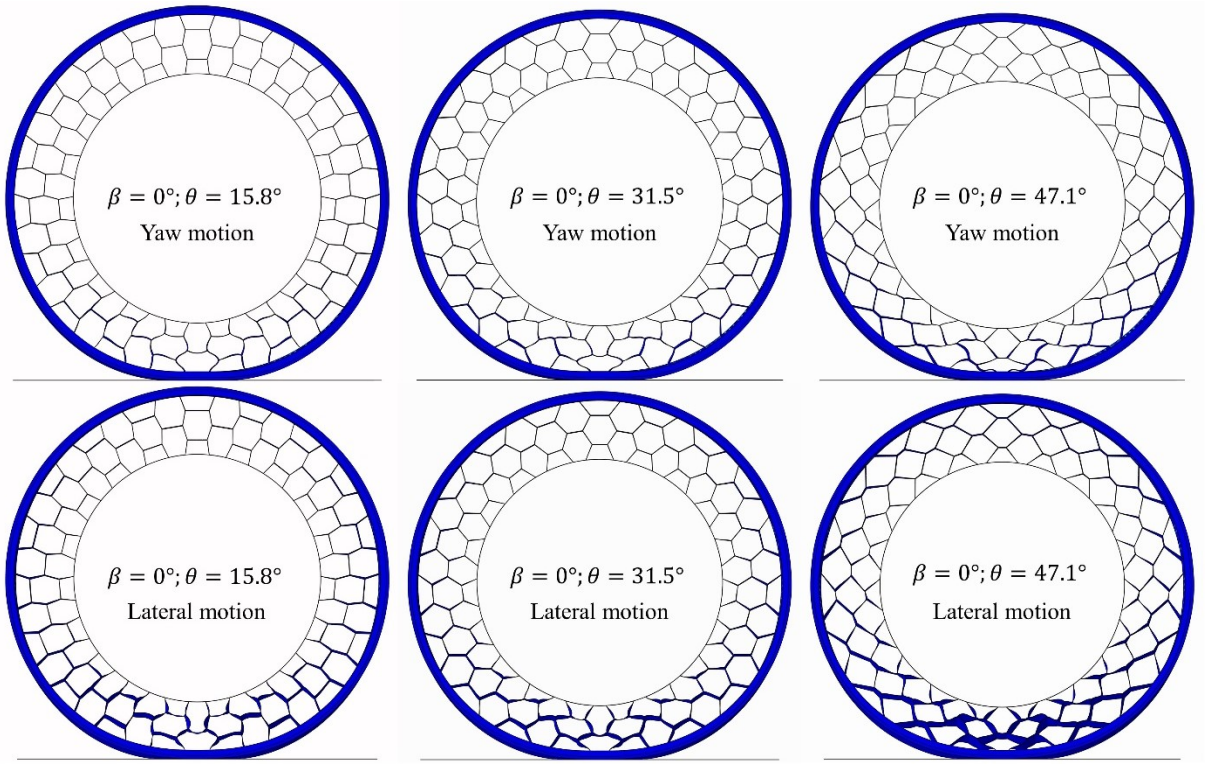

Figure 6.9: Out-of-plane deformations of the spokes of the loaded wheel models under yaw and lateral motions, considering 0° helix angle and 15.8°, 31.5° and 47.1° cell angles (normal load=3 kN, yaw rotation angle=5°, lateral displacement=10 mm)

Increasing θ from 15.8° to 47.1° causes 32% and 18% reductions in K_y and K_φ of the wheel models with β=0°, respectively, as shown in Figs. 6.7(d) and 6.7(f). These reductions are due to the negative influence of θ on the out-of-plane stiffness properties of the honeycomb spokes [115]. Moreover, the comparatively smaller influence of θ on K_φ is owing to the relatively lower contribution of the spokes to the yaw deformations as compared to the lateral deformations of the wheel. Furthermore, these negative influences tend to diminish for the design with higher β and tend to saturate when β is increased to 45°. These suggest that θ becomes less important in view of K_y and K_φ, when the honeycomb spokes undergo higher out-of-plane deformations, as seen in Fig. 6.6. This saturation tendency is consistent with its influence on K_x, as illustrated in Fig. 6.7(b).

Cornering stiffness characteristics

Table 6.6 summarizes cornering stiffness (K_α) of the wheel models with twelve different spokes configurations, considering 3 kN normal load and 10 km/h forward speed, together with their mean lateral deformations at 0.2° side slip angle (α). It should be mentioned that K_α was evaluated within relatively small side slip angle range (0-0.2°), as stated above. Moreover, a lower speed was selected for simulations since the effect of speed on the cornering stiffness is known to be

small, as stated in Section 6.2.2. This permitted simulations in a more computationally effective manner. In order to clearly show the influences of cell and helix angles on K_α, the stiffness results in this table were subsequently normalized to those of the wheel models with β=0° or θ=15.8°, as shown in Figs. 6.10(a) and 6.10(b).

Table 6.6: Cornering stiffness of the honeycomb wheel and its mean lateral deformations at 0.2° side slip angle, considering spokes configurations of different (θ) and helix (β) angles

β (°)	Cornering stiffness, K_α (N/deg)			Mean lateral deformations (mm)		
	θ=15.8°	θ=31.5°	θ=47.1°	θ=15.8°	θ=31.5°	θ=47.1°
0	1785.2	1748.2	1825.0	1.03	1.19	1.55
15	1868.7	1838.3	1833.8	1.10	1.27	1.52
30	1634.4	1574.7	1714.4	1.04	1.13	1.37
45	1349.8	1339.8	1521.6	0.94	0.99	1.11

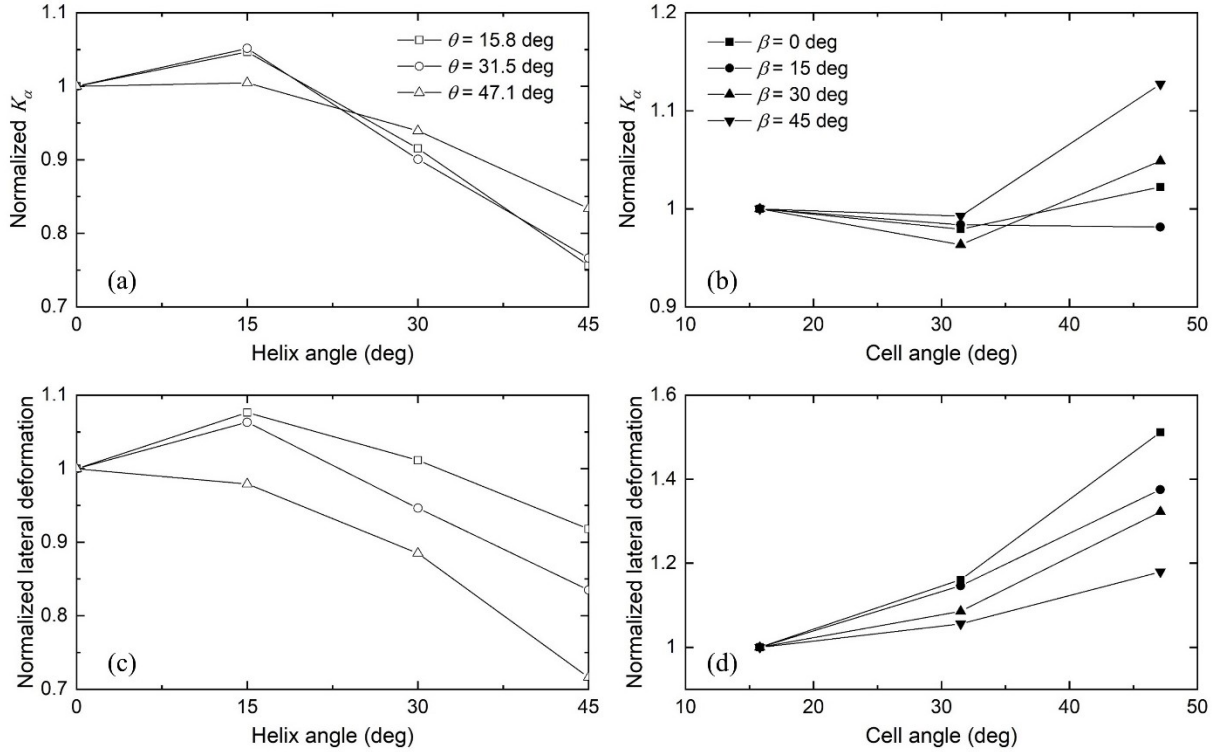

Figure 6.10: Influences of helix and cell angles, β and θ, on normalized: (a) and (b) cornering stiffness, K_α; (c) and (d) mean lateral deformation

It should be noted that K_α of a rolling wheel is related to its mean lateral deformation in the contact region as well as the lateral stiffness, which is obtained under stationary conditions (Table 6.5). This is due to the fact that the cornering force at a sufficiently small side slip angle, where the rubber tread adheres to the ground with negligible slippage, could be approximately estimated as the product of its mean lateral deformation and K_y [48]. For instance, the cornering force estimated

for the wheel model with θ=15.8° and β=0° is 351.3 N at 0.2° side slip angle, which is slightly smaller but in reasonable close agreement with the simulation result, in the order of 357.1 N. Therefore, Figs. 6.10(c) and 6.10(d) present the influences of β and θ on mean lateral deformation of the rolling wheel (Table 6.6) normalized with respect to those with β=0° or θ=15.8° so as to reach a better understanding of their effects on K_α.

Opposing influences of β are observed with regards to K_y and mean lateral deformation of the wheel, when β is increased from 0° to 15°, for each θ value considered, as seen in Figs. 6.7(c) and 6.10(c). For instance, the wheel model with θ=15.8° revealed 7.6% increase in its mean lateral deformation but only 2.8% decrease in K_y. This causes only slight increases in K_α of the wheel models with different θ, ranging from 0.5% to 5%, as shown in Fig. 6.10(a). A further increase in β from 15° to 45° causes notably lower mean lateral deformation and K_y for the wheel models with θ=15.8° and 31.5°. The wheel model with θ=47.1°, however, keeps showing opposite variations in these two performance measures. These lead to relatively smaller influences of β on K_α of the wheel model with θ=47.1°, when compared to those with 15.8° and 31.5° cell angles, as observed in Fig. 6.10(a). It should be stressed that increasing β from 0° to 45° could yield 24%, 23% and 17% reductions in K_α of the wheel models with θ=15.8°, 31.5° and 47.1°, respectively.

An increase in θ invariably causes higher mean lateral deformation for the wheel models with different β, as seen in Fig. 6.10(d). This positive influence diminishes with increasing helix angle. Opposite trends, however, are observed in the influences of θ on K_y of the wheel, as shown in Fig. 6.7(d). Therefore, varying θ in general results in only slight variations in K_α, as depicted in Fig. 6.10(b), although the wheel model with β=45° exhibits about 13% increase in its cornering stiffness.

It is clearly seen that in the absence of β, the wheel designs show very high cornering stiffness, K_α, in the range of 1748.2-1825.0 N/deg (Table 6.6), when compared to that of the reference pneumatic tire (≈830 N/deg). Moreover, these designs need to be coupled with higher θ in order to achieve proper K_x (Table 6.5 and Fig. 6.7), resulting in reduced design space. Introducing "symmetric helical honeycomb spokes" could thus effectively lower cornering stiffness, ranging from 1339.8-1521.6 N/deg, as well as substantially higher longitudinal stiffness, K_x, which could be easily tuned comparable to those of the pneumatic tires. It should be mentioned

that cornering stiffness could be further reduced by tuning the cell-wall thickness and the design parameters related to the core layer and the tread [118].

6.3.2 Honeycomb wheel designs considering identical load carrying capacity

The abovementioned static and dynamic simulations were repeated for the twelve honeycomb wheel models with identical load carrying capacity, which was achieved by tuning their corresponding cell-wall thickness (t_c) in order to yield same vertical deflection under the 3 kN normal load. It should be mentioned that 15.80 mm vertical deflection was initially chosen, which could yield 190 kN/m vertical stiffness (K_z) as that of the above-stated reference pneumatic tire [96]. This vertical deflection, however, caused convergence difficulties for the wheel model with θ=15.8° and β=45° in static loading simulations, resulting from its much higher out-of-plane deformations in the spokes near the contact region. This could be evidenced from the out-of-plane deformations presented in Fig. 6.6, although the wheel model with θ=15.8° and β=45° shows highest K_z and least vertical deflection. Therefore, a relatively smaller vertical deflection, in the order of 11.54 mm, was chosen which could ensure converged solutions for each wheel model and thus the study of wheel stiffness properties over a broad helix angle range. It should be noted that the chosen vertical deflection and the 3 kN normal load resulted in K_z=260 kN/m for each wheel model.

Table 6.7 summarizes the longitudinal (K_x), lateral (K_y) and yaw (K_φ) stiffness of the wheel models with different spokes configurations, together with their corresponding t_c. In this table, the wheel model with higher β or lower θ invariably necessitated smaller t_c so as to yield the chosen load carrying capacity or vertical stiffness (260 kN/m). These indicate positive and negative influences of β and θ on K_z of the wheel, respectively, which are consistent with those observed in Table 6.4. The longitudinal, lateral and yaw stiffness results were subsequently normalized with respect to those of the wheel models with β=0° or θ=15.8°, which are presented in Fig. 6.11.

Table 6.7: Multi-axis stiffness and cell-wall thickness dimensions of the wheel models with spokes configurations of different cell (θ) and helix (β) angles, considering identical load carrying capacity

β (°)	θ=15.8°				θ=31.5°				θ=47.1°			
	t_c	K_x	K_y	K_φ	t_c	K_x	K_y	K_φ	t_c	K_x	K_y	K_φ
0	4.40	86.1	417.7	151.4	5.40	187.3	416.2	135.6	6.35	447.6	386.3	126.8
15	3.86	135.2	365.7	149.1	4.86	210.8	382.6	137.2	5.82	436.7	375.1	131.5
30	3.01	242.2	259.8	134.5	3.68	273.6	289.4	127.1	4.46	404.7	315.4	127.1
45	2.30	364.8	180.6	122.8	2.67	374.9	193.5	117.3	3.16	434.9	240.1	122.5

t_c: cell-wall thickness, mm; K_x and K_y: longitudinal and lateral stiffness, kN/m; K_φ: yaw stiffness, Nm/deg

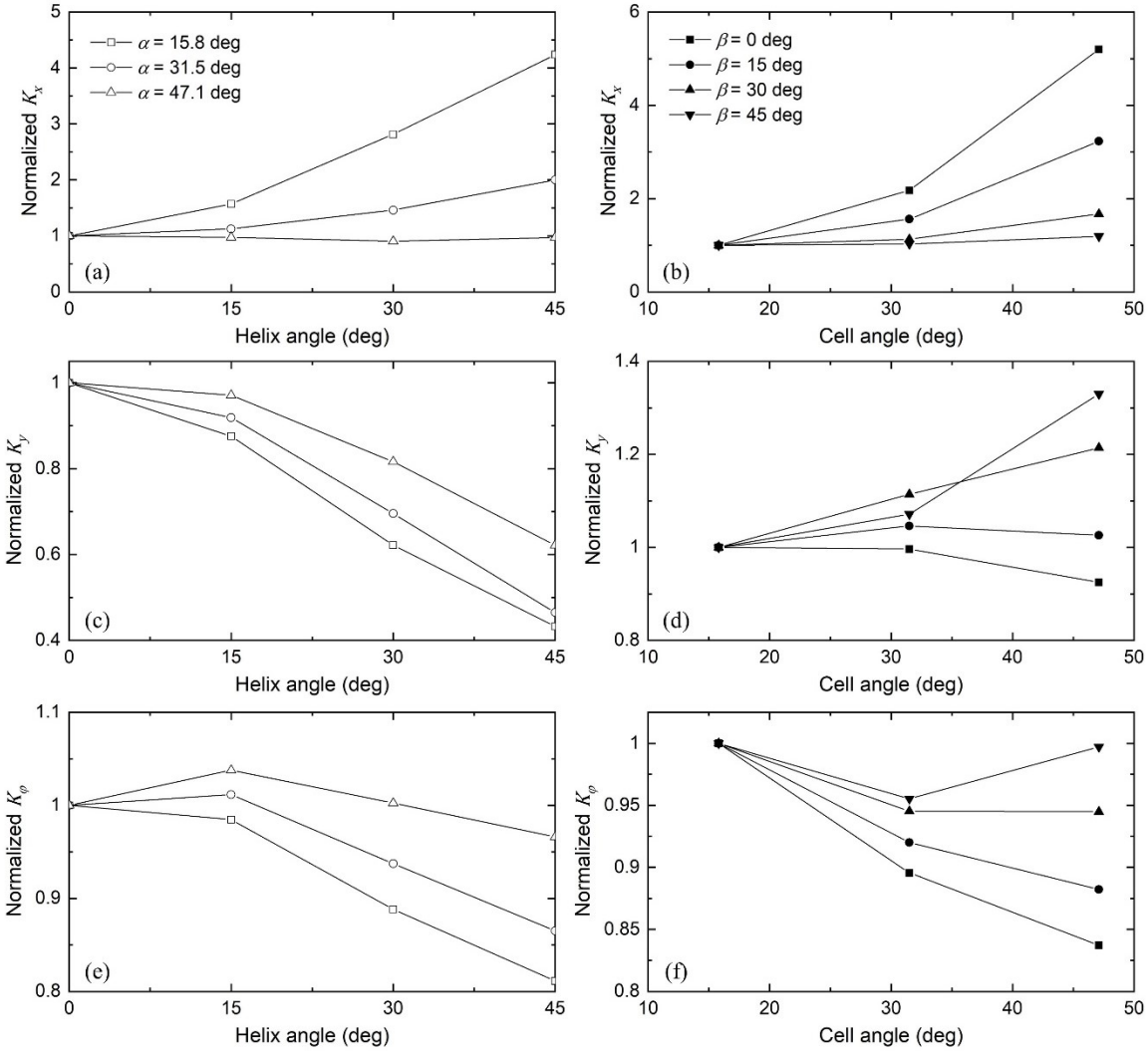

Figure 6.11: Variations in normalized stiffness with varying helix and cell angles (β and θ) considering same load carrying capacity: (a) and (b) longitudinal, K_x; (c) and (d) lateral, K_y; (e) and (f) yaw K_φ

Considerably smaller variations in K_x, in the range of -10% to 324%, were observed with varying β when compared to those (0-698%) of the wheel models with identical t_c=3.5 mm, for the θ values range considered, as seen in Figs. 6.11(a) and 6.7(a). This is attributable to lower value of t_c (Table 6.7) associated with the wheel models with higher β in order to achieve identical load carrying capacity, which causes lower normalized shear effective modulus (G_{ZX}/E_{0c}, Eq. (6.5)) of the honeycomb spokes and thus reductions in K_x of the wheel. Similarly, increasing θ results in more evident variations in K_x (Fig. 6.11(b)), as compared to the results shown in Fig. 6.7(b). This

is owing to the increase in t_c for the wheel models with spokes configurations of higher θ (Table 6.7), which results in additional increase in K_x.

Lower K_y with 54-57% reductions were obtained for the wheel models with θ=15.8° and 31.5°, when increasing β from 0° to 45°, as seen in Fig. 6.11(c). These substantial decreases are partly due to the negative influences of β on K_y (Fig. 6.7(c)), and in-part to the lower t_c of the wheel models with higher helix angle (Table 6.7). Unlike the positive influences of β on K_y observed in the wheel designs with θ=47.1° and t_c=3.5 mm (Fig. 6.7(c)), lower lateral stiffness with 3-38% decreases could be achieved by tuning the helix angle, as seen in Fig. 11(c). The cell-wall thickness could thus be viewed as a more dominating parameter on K_y as compared to the helix angle, within t_c and β values range considered. Moreover, up to 32% reductions in K_y were obtained with an increase in θ of the wheel models with three different β (Fig. 6.7(d)). These reductions, however, are coupled with the increases in K_y resulting from the higher t_c associated with the wheel models with higher θ (Table 6.7), irrespective of β value considered. Therefore, the negative effects of θ on K_y of the wheel, shown in Fig. 6.7(d), tend to diminish and switch to positive effects with an increase in β, as depicted in Fig. 6.11(d).

Similar influences of the decreasing t_c (Table 6.7) were also observed on variations in K_φ corresponding to the wheel models with varying β (Figs. 6.7(e) and 6.11(e)), when comparing its effects on K_y, shown in Figs. 6.7(c) and 6.11(c). The influences of t_c on K_φ, however, are much smaller than those observed on K_y. For example, a decrease in t_c causes about 10% additional reduction in K_φ for the wheel model with θ=15.8° and β=45° (Figs. 6.7(e) and 6.11(e)), while corresponding reduction in its K_y is around 39%, as seen in Figs. 6.7(c) and 6.11(c). This is owing to the relatively smaller contributions of the spokes to the yaw deformations as compared to the lateral deformations, as mentioned above. Therefore, only limited differences were observed in variations in K_φ with varying θ, when comparing the results presented in Figs. 6.7(f) and 6.11(f).

Table 6.8 summarized cornering stiffness, K_α, of the twelve wheel models with different θ and β, apart from their mean lateral deformations at 0.2° side slip angle (α). The results were also normalized with respect to those corresponding to the wheel models with β=0° or θ=15.8°, as shown in Figs. 6.12(a) and 6.12(b).

Table 6.8: Cornering stiffness and mean lateral deformations of the wheel models with spokes configurations of different cell (θ) and helix (β) angles, considering identical load carrying capacity

β (°)	Cornering stiffness, K_α, (N/deg)			Mean lateral deformations (mm)		
	θ=15.8°	θ=31.5°	θ=47.1°	θ=15.8°	θ=31.5°	θ=47.1°
0	1579.6	1466.0	1445.2	0.74	0.69	0.73
15	1771.4	1574.2	1556.3	0.95	0.81	0.81
30	1728.7	1547.0	1543.9	1.31	1.05	0.96
45	1750.0	1582.3	1589.3	1.89	1.62	1.31

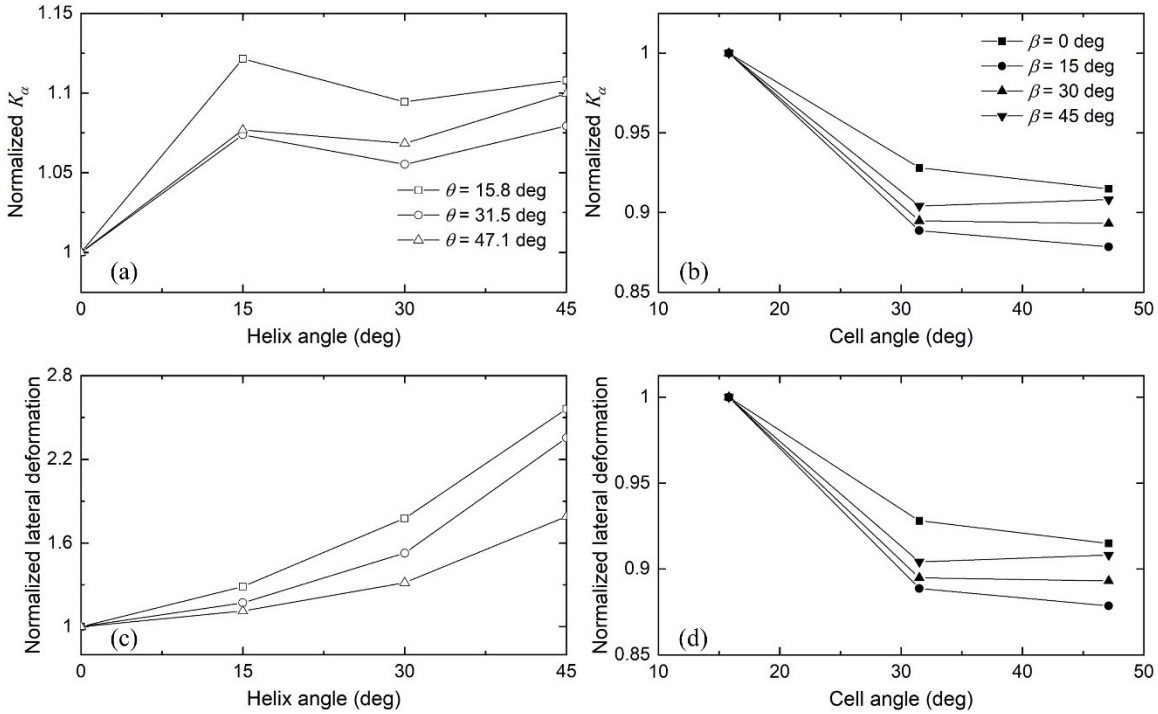

Figure 6.12: Influences of helix and cell angles, β and θ, on normalized: (a) and (b) cornering stiffness, K_α; (c) and (d) mean lateral deformation

The results presented in Figs. 6.12(a) and 6.12(b) suggest positive and negative effects of β and θ, respectively, on K_α of the wheel models designed with identical loading carrying capacity. The observed effects are nearly opposite to those seen for the designs with identical cell-wall thickness (Figs. 6.10(a) and 6.10(b)). These suggest that a decrease in t_c results in higher K_α, which could be evidenced by its influence on K_y and mean lateral deformation of the wheel. In order to gain a better understanding of the cornering behaviour, additional simulations were performed so as to obtain variations in the lateral force, mean lateral deformation and the cornering force corresponding to the wheel with different t_c. As an example, Fig. 6.13 illustrates the lateral force-deflection characteristics of the wheel, and variations in the mean lateral deformation and cornering force responses with varying side slip angle for two different cell-wall thickness

(t_c=2.40 and 4.40 mm). The results were obtained for the wheel model with spokes configuration of θ=15.8° and absence of helix (β=0°). It should be mentioned that the multi-axis and cornering stiffness values of the wheel model with θ=15.8°, β=0° and t_c=4.40 mm were summarized Tables 6.7 and 6.8. As it would be expected, an increase in t_c leads to about 71% higher K_y, from 243.5 kN/m to 416.3 kN/m, together with 48.7% lower mean lateral deformation corresponding to 0.6° side slip angle. Therefore, increasing t_c from 2.4 mm to 4.4 mm causes about 12.2% reduction in K_α. The negative effects of t_c on K_y could also be reflected by comparing the results presented in Figs. 6.7(c) and 6.11(c) as well as those in Figs. 6.10(c) and 6.12(c).

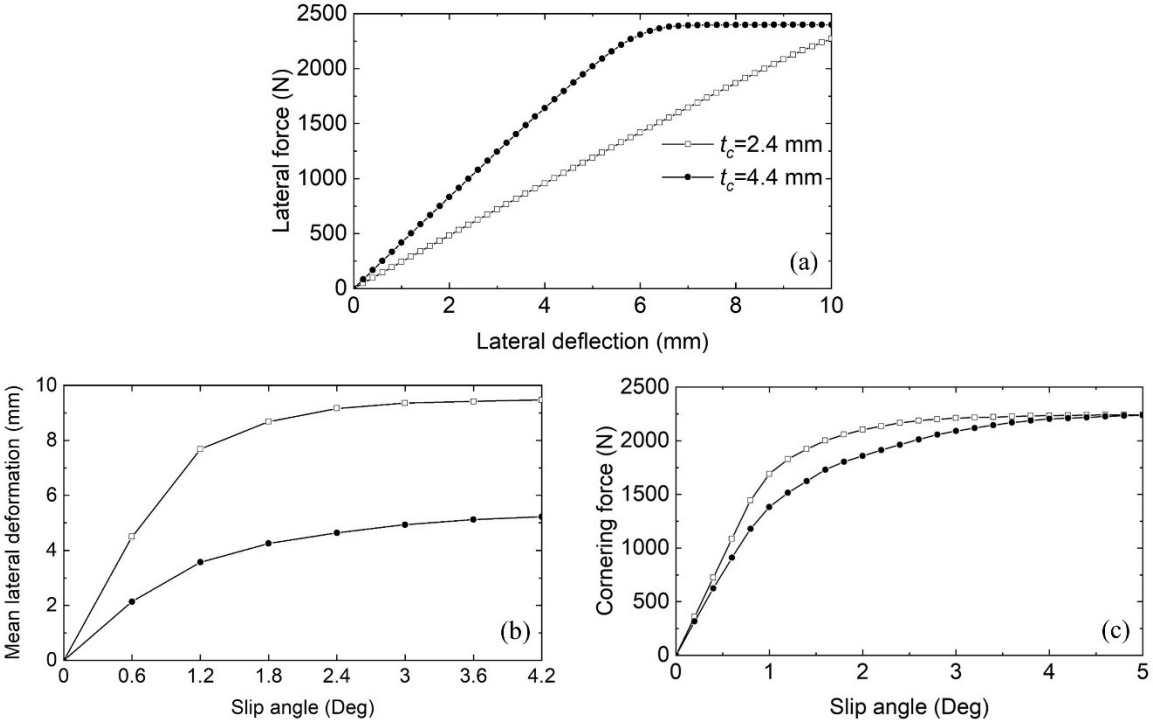

Figure 6.13: Comparisons of (a) lateral force-deflection, (b) mean lateral deformation-slip, and (c) cornering force-slip characteristics of the wheel model with two different cell-wall thickness (t_c)

6.4 Conclusions

1. The FE models developed for the honeycomb NPW with spokes configurations of 0° helix angle and varying cell angles revealed reasonably good agreements with the reported results. These included the peak stresses in the spokes and the overall vertical deflections of the stationary wheel, apart from the cornering stiffness of the rolling wheel, considering 2-4 kN normal load and 10 km/h forward velocity.

2. The NPW designs with spokes configurations of low cell angles and 0° helix angle showed considerably small longitudinal stiffness compared to those of comparable pneumatic tires. This was attributed to the relatively high in-plane shear flexibility associated with the spokes. On the other hand, the high out-of-plane stiffness of the honeycomb spokes caused significantly higher lateral and cornering stiffness for the NPW as compared those of the pneumatic tires of similar dimensions. An increase in the cell angle could help yield longitudinal stiffness comparable to the pneumatic tires together with the lower lateral stiffness. This, however, resulted in notable reduction in vertical stiffness of the NPW, apart from limited variation in its cornering stiffness.
3. Increasing the helix angle could yield higher in-plane stiffness of the spokes and thus greater vertical and longitudinal stiffness of the NPW, apart from lower lateral and yaw stiffness, particularly for the lower cell angle considered. This could also lead to notably lower cornering stiffness, particularly the helix angle is higher than 15°. The cell-wall thickness also showed negative influences on cornering stiffness of the wheel.
4. The NPWs with symmetric helical spokes of 45° helix angle could be used in heavy duty vehicles owing to its extremely high load carrying capacity with relatively low wheel mass.

Chapter 7

Conclusions and Recommendations

7.1 Highlights and contributions

This dissertation research presents systematic studies for non-pneumatic wheels (NPWs) with honeycomb spokes so as to achieve comparable performance characteristics as those of the pneumatic tires, particularly the static multi-axis and dynamic cornering stiffness properties. Alternate novel spokes design concept is proposed to help overcome the limitations of the current spoke designs. The static and dynamic properties of NPWs with current spokes design concept are initially investigated and their merits and limitations are evaluated in relative to a chosen reference pneumatic tire with similar sizes and identical load carrying capacity. Parametric studies involving variations in multiple design parameters are subsequently conducted so as to determine their influences on road contact characteristics, modal properties, and static and dynamic stiffness properties of the honeycomb NPWs. The performance analyses of NPWs with novel spoke designs are finally studied considering their multi-axis and cornering stiffness properties. The following summarizes major highlights and contributions of this dissertation research:

1. 3D finite element (FE) models of NPWs with different spokes configurations are developed and verified, and their static and dynamic responses are investigated when operating under different normal loads and rolling speeds.
2. The multi-axis stiffness properties of stationary honeycomb NPWs as well as their cornering force and self-aligning moment characteristics under rolling conditions are evaluated in relation to a reference pneumatic tire.
3. Efficient parametric analyses using Taguchi method and FE simulations are conducted, and the influences of multiple design parameters and their two-factor interactions on multi-axis stiffness and road contact characteristics of a honeycomb NPW are investigated.
4. Influential design parameters in view of the cornering stiffness of honeycomb NPWs are determined using significance analysis of the results obtained from design of experiments.
5. Design guidance involving influential design variables as well as their two-factor interactions are proposed for the cornering stiffness of honeycomb NPWs using the simulation results of the design points used by central composite designs.

6. Important vibration modes are determined for the stationary honeycomb NPW subjected to 3 kN normal load by comparing corresponding modal effective mass fraction.
7. Influential design parameters for each important in-plane and out-of-plane vibration mode are determined, and corresponding explicit design guidelines are formulated.
8. A novel spokes design concept is proposed, and its relative merits over the current spoke designs are identified.

7.2 Major conclusions

The major conclusions drawn from the study are summarized below:

1. The static and dynamic response characteristics of the developed FE NPW models showed reasonably close agreements with available data in the published studies in terms of the overall wheel deflections, spokes' peak stresses and the natural frequencies, considering similar wheel dimensions and material properties as well as identical operating and boundary conditions.
2. The simulation results showed considerable increase in longitudinal stiffness of honeycomb NPWs with an increase in the normal load, while the lateral stiffness of the wheels were nearly load-independent.
3. An increase in the normal load resulted in higher cornering stiffness, which was only slightly affected by the rolling speed of the wheel.
4. The NPWs with current spoke designs could be easily tuned to achieve vertical and longitudinal stiffness comparable to those of the pneumatic tires, while their lateral and cornering stiffness are considerably higher.
5. Vertical, longitudinal and lateral stiffness of NPWs are strongly coupled via the spokes design parameters including thickness and initial elastic modulus of the cell-wall as well as the cell angle, while the yaw stiffness are mostly affected by the tread design parameters.
6. The vertical and longitudinal stiffness of honeycomb NPWs are also significantly affected by the annular beam design parameters, while the lateral stiffness are additionally influenced by the geometric and material properties of the tread.
7. The honeycomb NPWs with relatively high cell angle could cause excessive deformations and collapse of the spokes near the wheel-ground contact region, particularly when coupled with thin and soft annular layer.

8. The road contact characteristics in terms of mean and peak contact pressure as well as contact area are dominantly affected by the design parameters of the annular beam and the tread.
9. The design parameters related to the annular layer and the tread also strongly affect the cornering stiffness of the honeycomb NPWs, while those corresponding to the spokes show relatively small effects.
10. The influential in-plane and out-of-plane vibration modes of the stationary honeycomb NPW with ground contact were identified as the Hop, Torsion, Yaw, Lateral, Twist and Oval-Diag modes due to their relatively high modal effective mass.
11. The natural frequencies corresponding to each influential vibration modes were considerably affected by the spokes design parameters. The geometric dimensions of the annular layer and the tread in general showed higher influences on modal properties of the honeycomb NPWs than their material properties.
12. The proposed design of spokes with helix could effectively improve braking/traction performances of the NPWs when compared to the current spokes designs, especially for those with relatively low cell angles.
13. The novel spokes design could help yield notable reductions in lateral and cornering stiffness of the honeycomb NPWs, which were more comparable to the pneumatic counterparts.
14. The NPWs with novel spokes design of 45° helix angle showed extremely high load carrying capacity with relatively low mass and thus could be very useful for heavy-duty vehicles.

7.3 Recommendations for future studies

The FE models established for NPWs with honeycomb spokes could be employed for simulations of various manoeuvres so as to investigate the stresses and deformations responses of the wheels and the forces and moments developed in wheel-road contact region, apart from the modal parameters. These models have been verified in view of the information available in published studies including the peak stresses of the spokes and the overall vertical deflections and natural frequencies of the wheel. The verifications could be further extended to enhance their reliability when predicting other performance characteristics, especially under high speed rolling conditions.

Moreover, more efforts are desired for developing more comprehensive design guidance concerning additional performance measures. Furthermore, the proposed spokes design concept necessitates further analyses in order to build its own design guideline. Some possible directions for future studies may include the following:

1. Due to the limited access to the measured data for NPWs with honeycomb spokes, development of a prototype wheel and experimental studies on its tractive (braking) effort versus longitudinal slip (skid) relations as well as cornering force and self-aligning moment versus side slip relations are suggested, particularly under high speed scenarios.
2. The variations in geometric and material properties of two steel rings or reinforcements as well as wheel width dimension would also affect the stiffness and modal properties of honeycomb NPWs. Parametric studies involving these design variables are thus desirable.
3. The influences of multiple design parameters on dynamic longitudinal stiffness, camber stiffness and rolling resistance of the honeycomb NPW need to be investigated.
4. Parametric studies for NPWs with novel spokes design concept are recommended so as to establish design guidance for realizing desired performance characteristics.
5. The noise performance of NPWs with current as well as novel spokes designs need to be investigated in order to be considered as feasible candidates for high-speed vehicles.
6. Modal analysis of rolling NPWs with honeycomb spokes should be investigated using both experimental and simulations methods.
7. The contact and interaction characteristics of honeycomb NPWs with deformable terrains need to be investigated to promote their applications in off-road vehicles.
8. Analytical or phenomenological modelling of honeycomb NPWs are suggested for implementations in vehicle models.
9. Another design concept involving the combination of helical and conventional (current) spokes could be explored.

References

[1] Rhyne TB, Cron SM. Development of a non-pneumatic wheel. Tire Sci Technol. 2006;34(3):150-169.
[2] Manga KK. Computational method for solving spoke dynamics on high speed rolling Tweel™ [master's thesis]. Clemson (SC): Clemson University; 2008.
[3] Ramachandran M. Nonlinear finite element analysis of Tweel geometric parameter modifications on spoke dynamics during high speed rolling. [master's thesis]. Clemson (SC): Clemson University; 2008.
[4] Zhao Y, Du X, Lin F, et al. Static stiffness characteristics of a new non-pneumatic tire with different hinge structure and distribution. J Mech Sci Technol. 2018;32(7):3057-3064.
[5] Ju J, Kim D, Kim K. Flexible cellular solid spokes of a non-pneumatic tire. Compos Struct. 2012;94(8):2285-2295.
[6] Jin X, Hou C, Fan X, et al. Investigation on the static and dynamic behaviors of non-pneumatic tires with honeycomb spokes. Compos Struct. 2017;187:27-35.
[7] Yoo S, Uddin MS, Heo H, et al. Thermoviscoelastic modeling of a nonpneumatic tire with a lattice spoke. P I Mech Eng D-J Aut. 2017;231(2):241-252.
[8] Gasmi A, Joseph PF, Rhyne TB, et al. Closed-form solution of a shear deformable, extensional ring in contact between two rigid surfaces. Int J Solids Struct. 2011;48(5):843-853.
[9] Gasmi A, Joseph PF, Rhyne TB, et al. Development of a two-dimensional model of a compliant non-pneumatic tire. Int J Solids Struct. 2012;49(13):1723-1740.
[10] Deng Y, Zhao Y, Lin F, et al. Simulation of steady-state rolling non-pneumatic mechanical elastic wheel using finite element method. Simul Model Pract Th. 2018;85:60-79.
[11] Zhu M, Zhao Y, Lin F, et al. Thermodynamics modeling of a novel nonpneumatic mechanical elastic wheel for predicting its mechanical-thermal behavior. Numer Heat Transfer A-Appl. 2019;75(7):435-455.
[12] Zhu M, Zhao Y, Lin F, et al. Thermo-mechanical coupled modeling for numerical analyzing the influence of thermal and frictional factors on the cornering behaviors of non-pneumatic mechanical elastic wheel. Simul Model Pract Th. 2019;91:13-27.
[13] Lee C, Ju J, Kim D. Vibration analysis of non-pneumatic tires with hexagonal lattice spokes. Proceedings of the ASME 2012 International Design Engineering Technical Conferences & Computers & Information in Engineering Conference; 2012 Aug 12-15; Chicago (IL).
[14] Lee C, Ju J, Kim D. The dynamic properties of a non-pneumatic tire with flexible auxetic honeycomb spokes. Proceedings of the ASME 2012 International Mechanical Engineering Congress & Exposition; 2012 Nov 9-15; Houston (TX).
[15] Zhao Y, Zhu M, Lin F, et al. Thermal modal analysis of novel non-pneumatic mechanical elastic wheel based on FEM and EMA. Aip Adv. 2018;8(1):1-17.
[16] Aboulyazid AM, Eman MA, Shaaban S, et al. Effect of spokes structures on characteristics performance of non-pneumatic tires. Int J Automot Eng. 2015;11:2212-2223.
[17] Rugsaj R, Suvanjumrat C. Study of geometric effects on nonpneumatic tire spoke structures using finite element method. Mech Based Des Struc. 2020. Advance online publication. DOI: 10.1080/15397734.2020.1777875.
[18] Zhang Z, Fu H, Liang X, et al. Comparative analysis of static and dynamic performance of nonpneumatic tire with flexible spoke structure. Stroj Vestn-J Mech E. 2020;66(7-8):458-466.
[19] Ju J, Summers JD, Ziegert J, et al. Design of honeycomb meta-materials for high shear flexure. Proceedings of the ASME 2009 International Design Engineering Technical Conferences & Computers & Information in Engineering Conference; 2009 Aug 30-Sept 2; San Diego (CA).
[20] Ju J, Summers JD, Ziegert J, et al. Compliant hexagonal meso-structures having both high shear strength and high shear strain. Proceedings of the ASME 2010 International Design Engineering Technical Conferences & Computers & Information in Engineering Conference; 2010 Aug 15-18; Montreal (QC).
[21] Ju J, Summers JD. Compliant hexagonal periodic lattice structures having both high shear strength and high shear strain. Mater Des. 2011;32(2):512-524.

[22] Berglind L, Ju J, Summers JD. Method to design honeycombs for a shear flexible structure. SAE Int J Passenger Cars Mech Syst. 2010;3(1):588-597.
[23] Ju J, Summers JD, Ziegert J, et al. Cyclic energy loss of honeycombs under in-plane shear loading. Proceedings of the ASME 2009 International Mechanical Engineering Congress & Exposition; 2009 Nov 13-19; San Diego (CA).
[24] Gibson LJ, Ashby MF, Schajer G, et al. The mechanics of two-dimensional cellular materials. P Roy Soc Lond A Mat. 1982;382(1782):25-42.
[25] Rutherford W, Bezgam S, Proddaturi A, et al. Use of orthogonal arrays for efficient evaluation of geometric designs for reducing vibration of a non-pneumatic wheel during high-speed rolling. Tire Sci Technol. 2010;38(4):246-275.
[26] Bezgam S. Design and analysis of alternating spoke pair concepts for a non-pneumatic tire with reduced vibration at high speed rolling [master's thesis]. Clemson (SC): Clemson University; 2009.
[27] Veeramurthy M, Ju J, Thompson LL, et al. Optimization of a non-pneumatic tire for reduced rolling resistance. Proceedings of the ASME 2011 International Design Engineering Technical Conferences & Computers & Information in Engineering Conference; 2010 Aug 18-31; Washington (DC).
[28] Veeramurthy M, Ju J, Thompson LL, et al. Optimisation of geometry and material properties of a non-pneumatic tyre for reducing rolling resistance. Int J Veh Des. 2014;66(2); 193-216.
[29] Ju J, Veeramurthy M, Summers JD, et al. Rolling resistance of a non-pneumatic tire having a porous elastomer composite shear band. Tire Sci Technol. 2013;41(3):154-173.
[30] Thyagaraja N, Shankar P, Fadel G, et al. Optimizing the shear beam of a non-pneumatic wheel for low rolling resistance. Proceedings of the ASME 2011 International Design Engineering Technical Conferences & Computers & Information in Engineering Conference; 2011 Aug 28-31; Washington (DC).
[31] Kim K, Kim D. Contact pressure of non-pneumatic tires with hexagonal lattice spokes. SAE Technical Paper 2011-01-0099. 2011.
[32] Kim K, Ju J, Kim D. Static contact behaviors of a non-pneumatic tire with hexagonal lattice spokes. SAE Int J Passenger Cars Mech Syst. 2013;6(3):1518-1527.
[33] Kim K, Kim S, Ju J, et al. Contact pressure of a non-pneumatic tire with three-dimensional cellular spokes. Proceedings of the ASME 2011 International Mechanical Engineering Congress & Exposition; 2011 Nov 11-17; Denver (CO).
[34] Shankar P, Fazelpour M, Summers JD. Comparative study of optimization techniques in sizing mesostructures for use in NonPneumatic tires. J Comput Inf Sci Eng. 2015;15(4):1-6.
[35] Du X, Zhao Y, Wang Q, et al. Grounding characteristics of a non-pneumatic mechanical elastic tire in a rolling state with a camber angle. Stroj Vestn-J Mech E. 2019;65(5):287-296.
[36] Du X, Zhao Y, Wang Q, et al. Numerical analysis of the dynamic interaction between a non-pneumatic mechanical elastic wheel and soil containing an obstacle. P I Mech Eng D-J Aut. 2017;231(6):731-742.
[37] Wang W, Zhao Y, Jian W, et al. Structure analysis and ride comfort of vehicle on new mechanical elastic tire. Proceedings of the FISITA 2012 World Automotive Congress. Berlin/Heidelberg: Springer; 2012. p. 199-209.
[38] Fu H, Zhao Y, Du X, et al. Analysis on influencing factors of lateral stiffness of mechanical elastic wheel. J Shanghai Jiaotong Univ Sci. 2017;51(7):863-869.
[39] Nakajima Y. Advanced tire mechanics. Singapore: Springer; 2019. p. 449-453.
[40] Zang L, Zhao Y, Li B, et al. An experimental study on the ground contact characteristics of non-pneumatic mechanical elastic wheel. Automot Eng. 2016;38(3):350-355.
[41] Du X, Zhao Y, Lin F, et al. Numerical and experimental investigation on the camber performance of a non-pneumatic mechanical elastic wheel. J Braz Soc Mech Sci. 2019;39(9):3315-3327.
[42] Zang L, Zhao Y, Li B, et al. Mechanical elastic wheel improving road holding and wear resistance of tire. Trans Chin Soc Agric Eng. 2014;30(12):56-63.
[43] Zang L, Zhao Y, Jiang C, et al. Mechanical elastic wheel's radial stiffness characteristics and their influencing factors. J Vib Shock. 2015;34(8):181-186.

[44] Zhao Y, Zang L, Chen Y, et al. Non-pneumatic mechanical elastic wheel natural dynamic characteristics and influencing factors. J Cent South Univ. 2015;22(5):1707-1715.
[45] Xiao Z, Zhao YQ, Lin F, et al. Studying the fatigue life of a non-pneumatic wheel by using finite-life design for life prediction. Stroj Vestn-J Mech E. 2018;64(1):56-67.
[46] Zhao Y, Deng Y, Lin F, et al. Transient dynamic characteristics of a non-pneumatic mechanical elastic wheel rolling over a ditch. Int J of Automot Tech. 2018;19(3):499-508.
[47] Deng Y, Zhao Y, Xu H, et al. Finite element modeling of interaction between non-pneumatic mechanical elastic wheel and soil. P I Mech Eng D-J Aut. 2019;233(13):3293-3304.
[48] Wong JY. Theory of ground vehicles. 3rd ed. New York (NY): Wiley; 2001. p. 440-442.
[49] Soedel W. On the dynamic response of rolling tires according to thin shell approximations. J Sound Vib. 1975;41(2):233-246.
[50] Ramji K, Goel VK, Saran VH. Stiffness properties of small-sized pneumatic tyres. P I Mech Eng D-J Aut. 2002;216(2):107-114.
[51] Loeb J, Guenther D, Chen H, et al. Lateral stiffness, cornering stiffness and relaxation length of the pneumatic tire. SAE Technical Paper 900129. 1990.
[52] Yang X. Finite element analysis and experimental investigation of tyre characteristics for developing strain-based intelligent tyre system [Doctoral Thesis]. Birmingham: University of Birmingham; 2011.
[53] Wei C. A finite element based approach to characterising flexible ring tire (Ftire) model for extended range of operating conditions. [Doctoral Thesis]. Birmingham: University of Birmingham; 2014.
[54] Shokouhfar S, Rakheja S, El-Gindy M. Development of a rolling truck tyre model using an automatic model regeneration algorithm. Int J Veh Syst Model Test. 2016;11(1):68-95.
[55] Rao K, Kumar R, Bohara P. Transient finite element analysis of tire dynamic behavior. Tire Sci Technol. 2003;31(2):104-127.
[56] Kamoulakos A, Kao B. Transient dynamics of a tire rolling over small obstacles-a finite element approach with PAM-SHOCK. Tire Sci Technol. 1998;26(2):84-108.
[57] Wei Y, Oertel C, Shen X. Tyre rolling kinematics and prediction of tyre forces and moments: part II-simulation and experiment. Vehicle Syst Dyn. 2012;50(11):1689-1706.
[58] Baffet G, Charara A, Lechner D. Estimation of vehicle sideslip, tire force and wheel cornering stiffness. Control Eng Pract. 2009;17(11):1255-1264.
[59] Rao K, Kumar R. Simulation of tire dynamic behavior using various finite element techniques. Int J Comput Meth Eng Sci Mech. 2007;8:363-372.
[60] Kabe K, Koishi M. Tire cornering simulation using finite element analysis. J Appl Polym Sci. 2000;78(8);1566-1572.
[61] Tönük E, Ünlüsoy YS. Prediction of automobile tire cornering force characteristics by finite element modeling and analysis. Comput Struct. 2001;79(13):1219-1232.
[62] Koishi M, Kabe K, Shiratori M. Tire cornering simulation using an explicit finite element analysis code. Tire Sci Technol. 1998;26(2):109-119.
[63] Shiraishi M, Yoshinaga H, Miyori A, et al. Simulation of dynamically rolling tire. Tire Sci Technol. 2000;28(4):264-276.
[64] Hall W, Mottram JT, Jones RP. Tire modeling methodology with the explicit finite element code LS-DYNA. 2004;32(4):236-261.
[65] Olatunbosun OA, Bolarinwa O. FE simulation of the effect of tire design parameters on lateral forces and moments. Tire Sci Technol. 2004;32(3):146-163.
[66] Burke AM, Olatunbosun OA. New techniques in tyre modal analysis usingMSC/NASTRAN. Int J Veh Des. 1997;18(2):203-212.
[67] Chittilla K, Yeola Y, Tiwari A, et al. Effect of excitation methods on experimental modal analysis of passenger car tire. SAE Technical Paper 2013-01-2854. 2013.
[68] Yam L, Guan D, Zhang A. Three-dimensional mode shapes of a tire using experimental modal analysis. Exp Mech. 2000;40:369-375.
[69] Abd-Elsalama AA, Goharyb MA, El-Gamalb HA. Modal analysis on tire with respect to different parameters. Alexandria Eng J. 2017;56(4):345-357.

[70] Patil K, Baqersad J, Bastiaan J. Effects of boundary conditions and inflation pressure on the natural frequencies and 3D mode shapes of a tire. SAE Technical Paper 2017-01-1905. 2017.
[71] Richards TR, Charek LT, Scavuzzo RW. The effects of spindle and patch boundary conditions on tire vibration modes. SAE Transactions. 1986;95:19-30.
[72] Pieters R. Experimental modal analysis of an automobile tire under static load (Report No. DCT 2007.112). Eindhoven University of Technology. 2007.
[73] Potts GR, Csora TT. Tire vibration studies: the state of the art. Tire Sci Technol. 1975;3(3):196-210.
[74] Potts GR. Application of holography to the study of tire vibration. Tire Sci Technol. 1973;1(3):255-266.
[75] Kindt P, Berckmans D, Coninck F, et al. Experimental analysis of the structure-borne tyre/road noise due to road discontinuities. Mech Syst Signal Pr. 2009;23(8):2557-2574.
[76] Kindt P, Sas P, Desmet W. Measurement and analysis of rolling tire vibrations. 2009;47:443-453.
[77] Laine J. Measurements, analysis and modelling of the vibrations of a tyre by using a single embedded accelerometer. [master's thesis]. Espoo: Aalto University; 2016.
[78] Kao BG, Muthukrishnan M. Tire transient analysis with an explicit finite element program. Tire Sci Technol. 1997;25(4):230-244.
[79] Zhang Y, Palmer T, Farahani A. A finite element tire model and vibration analysis: a new approach. Tire Sci Technol. 1998;26(3):149-172.
[80] Olatunbosun OA, Burke AM. Finite element modelling of rotating tires in the time domain. Tire Sci Technol. 2002;30(1):19-33.
[81] Shokouhfar S, Rakheja S, El-Gindy M. Modal analysis of a rolling truck tyre subjected to inflation pressure and vertical deflection. Int J Veh Syst Model Test. 2016;11(2):116-141.
[82] Zegelaar P. Modal analysis of tire in-plane vibration. SAE Technical Paper 971101. 1997.
[83] Huang S, Su C. In-plane dynamics of tires on the road based on an experimentally verified rolling ring model. Vehicel Syst Dyn. 1992;21(1):247-267.
[84] Huang S. The vibration of rolling tyres in ground contact. Int J Vehicle Des. 1992;13(1):78-95.
[85] Soedel W, Prasad MG. Calculation of natural frequencies and modes of tires in road contact by utilizing eigenvalues of the axisymmetric non-contacting tire. J Sound Vib. 1980;70(4):573-584.
[86] Palanivelu S, Rao N, Ramarathnam KK. Determination of rolling tyre modal parameters using finite element techniques and operational modal analysis. Mech Syst Signal Pr. 2015;64-65:385-402.
[87] Kao M, Riesner M, Surulinarayanasami P. Modal analysis of a tire and wheel and its application for vehicle ride evaluation. SAE Technical Paper 860826. 1986
[88] Hunckler CJ, Yang TY, Soedel W. A geometrically nonlinear shell finite element for tire vibration analysis. Comput Struct. 1983;17(2):217-225.
[89] Kung LE, Soedel W, Yang TY, et al. Natural frequencies and mode shapes of an automotive tire with interpretation and classification using 3-D computer graphics. J Sound Vib. 1985;102(3):329-346.
[90] Saigal S, Yang TY, Kim HW, Soedel W. Free vibrations of a tire as a toroidal membrane. J Sound Vib. 1986;107(1):71-82.
[91] Chang YB, Yang TY, Soedel W. Dynamic analysis of a radial tire by finite elements and modal expansion. J Sound Vib. 1984;96(1):1-11.
[92] Wheeler RL, Dorfi HR, Keum BB. Vibration modes of radial tires: measurement, prediction, and categorization under different boundary and operating conditions. SAE Int J Passenger Cars Mech Syst. 2005;114:2823-2837.
[93] Negrus E, Anghelache G, Stanescu A. Finite element analysis and experimental analysis of natural frequencies and mode shapes for a non-rotating tyre. Vehicel Syst Dyn. 1997;27(S1):221-224.
[94] Zhang X, Rakheja S, Ganesan R. Modal analysis of a truck tyre using FE tyre model. Int J Heavy Veh Syst. 2004;11(2):133-154.
[95] ABAQUS 6.14 user's manual. Vélizy-Villacoublay: Dassault Systèmes; 2014.
[96] Liang C, Wang G and Zheng Z. An effect study of passenger car radial tire contour design theory on tire force and moment properties. SAE Technical Paper 2016-01-0446. 2016.

[97] Cho J, Kim K, Jeon D, et al. Transient dynamic response analysis of 3-D patterned tire rolling over cleat. Eur J Mech A-Solid. 2005;24(3):519-531.
[98] Rugsaj R, Suvanjumrat C. Proper radial spokes of non-pneumatic tire for vertical load supporting by finite element analysis. Int J Auto Technol. 2019;20(4):801-812.
[99] Yin Y, Rakheja S, Boileau PE. A roll stability performance measure for off-road vehicles. J Terramechanics. 2016;64:58-68.
[100] Proddaturi A. Robust parameter design and finite element analysis for a non-pneumatic tire with low vibration [master's thesis]. Clemson (SC): Clemson University; 2009.
[101] Roy RK. A primer on the Taguchi method. 2nd ed. Dearbon (MI): Society of Manufacturing Engineers; 2010.
[102] Park GJ, Lee TH, Lee K, et al. Robust design: an overview. AIAA J. 2006;44 (1):181-191.
[103] Myers RH, Khuri AI, Vining G. Response surface alternatives to the Taguchi robust parameter design approach. Am Stat. 1992;46(2):131-139.
[104] Wei C, Olatunbosun OA. Transient dynamic behaviour of finite element tire traversing obstacles with different heights. J Terramech. 2014;56:1-16.
[105] Wei C, Olatunbosun OA. The effects of tyre material and structure properties on relaxation length using finite element method. Mater Des. 2016;102:14-20.
[106] Jang IG, Young HS, Eui JY, et al. Pattern design of a non-pneumatic tyre for stiffness using topology optimization. Engineering Optimization. 2012;44(2):119-131.
[107] Papageorgiou EG, Chatzistergos P, Wang X. The influence of the honeycomb design parameters on the mechanical behaviour of non-pneumatic tyres. Int J Appl Mech. 2020:12(3):1-14.
[108] Zheng Z, Rakheja S, Sedaghati R. A comparative study of static and dynamic properties of honeycomb non-pneumatic wheels and a pneumatic wheel. Proc I Mech Eng, Part D, J Auto Eng, 2021. DOI: 10.1177/09544070211007977
[109] Nair AT, Makwana AR, Ahammed MM. The use of response surface methodology for modelling and analysis of water and wastewater treatment processes: a review. Water Sci Technol. 2014;69(3):464-478.
[110] Bezerra MA, Santelli RE, Oliveira EP, et al. Response surface methodology (RSM) as a tool for optimization in analytical chemistry. Talanta. 2008;76:965-977.
[111] Khuri AI, Mukhopadhyay S. Response surface methodology. Wires Comput Stat. 2010;2(2):128-149.
[112] Ju J, Veeramurthy M, Summers JD, et al. Rolling resistance of a nonpneumatic tire having a porous elastomer composite shear band. Tire Sci Technol. 2013;41(3):154-173.
[113] http://my.tv.sohu.com/us/133251931/ 52639794.shtml.
[114] Myers RH, Montgomery DC, Anderson-Cook CM. Response surface methodology: process and product optimization using designed experiments. New Jersey (NY): John Wiley & Sons; 2016.
[115] Zheng Z, Rakheja S, Sedaghati R. Multi-axis stiffness and road contact characteristics of honeycomb wheels: A parametric analysis using Taguchi method. Compos Struct. 2021;279:1-14.
[116] Gent AN, Walter JD. The pneumatic tire. Washington DC: National Highway Traffic Safety Administration; 2005. p. 395-396.
[117] Deng Y, Zhao Y, Lin B, et al. Influence of structure and material on the vibration modal characteristics of novel combined flexible road wheel. 2021. Advance online publication. DOI:10.1016/j.dt.2021.05.016.
[118] Zheng Z, Rakheja S, Sedaghati R. Cornering stiffness characteristics of honeycomb wheels: A parametric analysis using response surface method. Compos Struct. 2022;288:1-15.